UAB
Universitat Autònoma de Barcelona

Modulating Metabolism and Inflammatory Response with Cerium Oxide Nanoparticles: A Novel Therapeutic Approach

Lena Montaña Ernst

ADVERTIMENT. L'accés als continguts d'aquesta tesi queda condicionat a l'acceptació de les condicions d'ús establertes per la següent llicència Creative Commons: https://creativecommons.org/licenses/?lang=ca

ADVERTENCIA. El acceso a los contenidos de esta tesis queda condicionado a la aceptación de las condiciones de uso establecidas por la siguiente licencia Creative Commons: https://creativecommons.org/licenses/?lang=es

WARNING. The access to the contents of this doctoral thesis it is limited to the acceptance of the use conditions set by the following Creative Commons license: https://creativecommons.org/licenses/?lang=en

Modulating Metabolism and Inflammatory Response with Cerium Oxide Nanoparticles: A Novel Therapeutic Approach

Lena Montaña Ernst

DOCTORAL THESIS

Memòria presentada per optar al grau de Doctor per la Universitat Autònoma de Barcelona

Programa de doctorat en Bioquímica, Biologia Molecular i Biomedicina

Director

Prof. Victor F. Puntes

Tutora

Dra. Julia Lorenzo Rivera

Barcelona, Juny 2024

Table of Contents

List of Abbreviations **8**

Thesis Overview **10**

Chapter 1: General Introduction **12**

1.1 State of the Art: CeO_2 NPs Relevance in Medicine 14

1.1.1 Liver 17

1.1.2 Eye Degeneration 19

1.1.3 Tissue and Cell Preservation 20

1.1.4 Stem Cells 21

1.1.5 Infections (Sepsis) 21

1.2 Dynamic Interplay of ROS and Cellular Redox Balance 22

1.2.1 ROS as Key Mediators of Immune Responses 24

1.3 Hypothesis: ROS Scavenging by CeO_2 NPs Modulates Inflammatory Responses 25

1.4 Challenges and Considerations Assessing the Safety of Nanomaterials 26

1.4.1 Health Impact and Pharmaceutical Product Development 29

1.5 What makes CeO_2 NPs Different from Traditional Antioxidants? 31

1.6 Objectives and Scope 37

1.7 References 38

Chapter 2: Synthesis and Physicochemical Properties of CeO_2 NPs **50**

2.1 Introduction 52

2.2 Scope of the study 55

2.3 Results and Discussion 56

2.3.1 Development and characterization of CeO_2 NPs 56
2.3.2 Stability: Nanoparticle Transformations 56
2.3.3 Efficacy and Safety 85
2.4 References 93
Chapter 3: Pharmacokinetic Profiling of CeO_2 NPs: Absorption, Distribution, Metabolism, and Excretion 99
3.1 Introduction 101
3.2 Scope of the study 102
3.3 Results and discussion 103
3.3.1 Heterogenic distribution of NPs 103
3.3.2 ADME in healthy preclinical models 104
3.4 References 115
Chapter 4: Pharacodynamics of CeO_2 NPs: Immune Modulation and Metabolism 119
Prelude: Energy-Metabolism Concepts 121
4.1 Immunometabolism 123
4.2 Mitochondria: central hub for ATP and ROS generation 124
4.2.1 ROS Generation 126
4.2.2 Metabolic Adaptation to ROS: The Role of HIF-1 and Glycolysis in Cellular Response and Disease 127
4.3 Macrophage Polarization 131
4.4 Scope of the study 134
4.5 Results and Discussion 136
4.5.1 Human THP-1 Macrophage Polarization Model 136
4.5.2 CeO_2 NPs effects on M1 inflammatory macrophages. 139

4.6 Murine RAW 267.4 Macrophage Polarization model 142

4.6.1 ROS, Mitochondria, and Glycolysis in Activated Macrophages 144

4.7 Effect of CeO_2 NPs on Mitochondria Morphology 146

4.8 References 153

Chapter 5: Experimental Section 163

5.1 Chapter 2: Synthesis and Physicochemical Properties of CeO_2 Nanoparticles 165

5.1.1 Chemicals 165

5.1.2 Synthesis of Nanoparticles 165

5.1.3 Nanoparticle Characterization Techniques 166

5.1.4 Aggregation kinetics 173

5.1.5 Bioconjugation protocol 173

5.1.6 CeO_2 NPs Corrosion 173

5.1.7 Amplex Red Assay 174

5.1.8 HEK 293, HeLa, and RAW 267.4 cell culture 174

5.1.9 PrestoBlue: Cell Rescue Assay 174

5.1.10 PrestoBlue: Cell viability 175

5.1.11 PrestoBlue: Albumin cytotoxicity 175

5.1.12 Pacific Blue Annexin V/SYTOX 175

5.1.13 Statistical Analysis 176

5.2 Chapter 3: Pharmacokinetic Profiling of CeO2 NPs: Absorption, Distribution, Metabolism, and Excretion 177

5.2.1 Chemicals 177

5.2.2 Synthesis and characterization 177

5.2.3 Bacterial Endotoxin (LAL) test 177

5.2.4 MSA conjugation 177

5.2.5 In vivo study design 177

5.2.6 Long-term biodistribution in healthy mice 178

5.2.7 CeO_2 NPs excretion in CCl_4-treated rats 178
5.2.8 Brain Distribution after intracranial administration 179
5.2.9 Organ Distribution after oral administration 179
5.2.10 Cerium Content Determination 179
5.2.11 Confocal Imaging in Mice Liver 179
5.2.12 Dissolution of CeO_2 NPs at acidic pH 180
5.2.13 Fitting with traditional pharmacokinetic models 180
5.3 Chapter 4: Pharmacodynamics of CeO_2 NPs: Immune Modulation and Metabolism 182
5.3.1 Chemicals 182
5.3.2 THP-1 cell culture and polarization 182
5.3.3 RAW 267.4 cell culture and polarization 183
5.3.4 CeO_2 NPs treatments 183
5.3.5 Quantitative real-time PCR (RT-qPCR) 183
5.3.6 ELISA 184
5.3.7 Metabolic Profile 184
5.3.8 Mitochondria Polarization 185
5.3.9 Total ROS Assay Kit 185
5.3.10 Confocal Microscopy 185
5.3.11 Computational Analysis 186
5.3.12 Statistical Analysis 188
5.4 References 189
Chapter 6: General Conclusions 190
6.1 Synthesis and Physicochemical Properties of CeO_2 NPs 192
6.2 Pharmacokinetic Profiling of CeO_2 NPs: Absorption, Distribution, Metabolism, and Excretion. 193
6.3 Pharmacodynamics of CeO2 NPs: Immune Modulation and Metabolism 193

Annex **195**

7.1 ANNEX A: List of Publications 197

7.2 ANNEX B: Absorption, Biodistribution, Metabolism, and Excretion (ADME) of CeO2 NPs in Preclinical Models. 198

7.3 ANNEX C: Articles 201

7.3.1 The Interactions between Nanoparticles and the Innate Immune System from a Nanotechnologist Perspective 201

7.3.2 Exploring the Long-Term Tissue Accumulation and Excretion of 3 nm Cerium Oxide Nanoparticles after Single Dose Administration 222

List of Abbreviations

ADME	Absorption, Distribution, Metabolism, and Excretion
AMO	All measured Organs
ATCC	American Type Culture Center
ATP	Adenosine Triphosphate
AuNPs	Gold Nanoparticles
BSA	Bovine Serum Albumin
BW	Body Weight
CeO_2	Cerium Oxide, Nanoceria
DAMPS	Damage-Associated Molecular Patterns
DCFDA	2'-7'-dichlorodihydrofluorescein diacetate
DLS	Dynamic Light Scattering
DMEM	Dulbecco's Modified Eagle's Medium
E°	Electrode potential
ECAR	Extracellular Acidification Rates
EMA	European Medicines Agency
ESFR	European Synchrotron Radiation Facilities
ETC	Electron Transport Chain
FAO	Fatty Acid Oxidation
FBS	Foetal Bovine Serum
FDA	Food and Drug Administration
FWHM	Full Width at Half Maximum
GLUTs	Glucose Transporters
GMP	Good Manufacturing Practices
H2O2	hydrogen peroxide
HAADF-STEM	High-Angle Annular Dark-Field Scanning Transmission Microscopy
HEK 293	Human Embryonic Kidney 293
HeLa	Henrietta Lacks cells
HERFD-XAS	High-Energy Resolution Fluorescence Detected X-ray Absorption Spectroscopy
HMT	Hexamethylenetetramine
HRP	Horseradish Peroxidase
HR-TEM	High-Resolution Transmission Electron Microscopy
HSA	Human Serum Albumin
ICP-MS	Inductively Coupled Plasma Mass Spectrometry
ID	Injected Dose
IL4	Interleukin-4

IV	Intravenous
LPS	Lipopolysaccharides
MSA	Murine Serum Albumin
NAC	N-acetylcysteine
NADH	Nicotinamide Adenine Dinucleotide
NADPH	Nicotinamide Adenine Dinucleotide Phosphate
NAFLD	Non-Alcoholic Fatty Liver Disease
NP	Nanoparticles
O_2•−	Superoxide radical anion
OCR	Oxygen Consumption Rates
OH-	Hydroxides
OH•	Hydroxyl radical
OXPHOS	Oxidative Phosphorylation
PAMPS	Pathogen-Associated Molecular Patterns
PDH	Pyruvate Dehydrogenase
PEG	Polyethene Glycol
PHD	Prolyl Hydroxylase Domain
PMA	Phorbol 12-Mystrate 13-Acetate
RPMI	Roswell Park Memorial Institute
RT-qPCR	Quantitative Real-Time PCR
SC	Sodium Citrate
SLC2a1	Glucose transporter 1
SOD	Superoxide dismutase
TCA	Tricarboxylic Acid Cycle
TGA	Thermogravimetric Analysis
TLR	Toll Like Receptors
TMAOH	Tetramethylammonium Hydroxide
TYR	Tyrosinase
XRD	X-ray Diffraction
Z (ζ)-Pot	Zeta-Potential

Thesis Overview

This thesis investigates the antioxidant properties of Cerium Oxide (CeO_2) nanoparticles (NPs) within biological contexts, focusing on the roles of reactive oxygen species (ROS) in regulating energy metabolism and their intricate involvement in immune responses. ROS, highly reactive free radicals resulting from cellular respiration, play a central role in both metabolism and inflammation, making them an important therapeutic target.

The integration of nanomaterials into biological applications presents challenges that require interdisciplinary expertise and a comprehensive understanding of the material properties. Special attention must be dedicated to nanosafety, particularly when employing metal oxide NPs. Often, poorly soluble, aggregated, polydisperse, and contaminated samples have been linked to increased ROS and inflammation. This work aims to bridge this gap by exploring the synthesis and physicochemical properties of CeO_2 NPs, ensuring they are tailored for their optimal performance in sophisticated therapeutic tasks. The successful application of nanotechnology in biomedicine relies on overcoming these interdisciplinary barriers and developing robust tools for nanomaterial utilization.

Chapter 1 offers an introduction to the current state of biomedical applications of CeO_2 NPs accompanied by an overview of ROS. It also covers fundamental concepts essential for understanding the properties and behaviour of NPs, along with critical safety considerations.

Chapter 2 explores the synthesis and characterisation of CeO_2 NPs, offering a comprehensive understanding of their physicochemical properties, to design and guide them inside biological systems. It also includes an in-depth study of their stability, efficacy, and safety in biological contexts.

Chapter 3 focuses on the pharmacokinetic study of CeO_2 NPs in both healthy and diseased preclinical models. Initially, the long-term absorption, distribution, metabolism, and excretion (ADME) profile is investigated following a single administration of the NPs in healthy animal models. This is followed by detailed distribution and excretion studies in diseased models.

Chapter 4 explores the impact of antioxidant CeO_2 NPs on the innate immune response, specifically focusing on macrophage polarization. The investigation extends to macrophage energy metabolism, mitochondrial function, and cytokine production. The relevance of this work relies on elucidating the precise mechanisms through which effective antioxidants modulate immune responses.

Chapter 5 comprehensively details all the materials and methods utilized in Chapter 2, Chapter 3, and Chapter 4 for their development. It is structured according to the specific methodology employed in each chapter, with an additional section dedicated to the characterization techniques of NPs.

CHAPTER 1

GENERAL INTRODUCTION

“You can know the name of a bird in all the languages of the world, but when you’re finished, you’ll know absolutely nothing whatever about the bird…So let’s look at the bird and see what it’s doing – that’s what counts.”

Richard P. Feynman

Chapter 1

General Introduction

1.1 State of the Art: CeO_2 NPs Relevance in Medicine

Cerium is the most abundant rare earth element [1]. The unique chemistry of rare earth elements stems from the distinctive characteristics of their 4f orbitals, which contribute to their electronic structure and oxidation states. At the nanoscale, CeO_2 presents defects in its crystal structure, leading to the presence of some cerium ions in a Ce^{3+} valence state rather than Ce^{4+}, leading to oxygen vacancies. These Ce^{3+}/Ce^{4+} redox couple on the surface of the NP allows them to act as both electron donors and acceptors, giving cerium and other rare earth materials unique catalytic, magnetic, and electronic properties.

CeO_2 nanoparticles (NPs), indistinctively called nanoceria, have received much attention because of their excellent catalytic activities. CeO_2 NPs were initially employed in various industrial applications, including automotive catalytic converters to improve the conversion of toxic gases into less harmful substances, as catalysts in fuel cells [2] and solar cells [3], as well as serving as polishing agents for glass and optical lenses [4], among other applications [1].

Nanoceria, which has achieved widespread use and maturity within the materials industry, has emerged as a potential candidate for biomedical applications due to its robust antioxidant and anti-inflammatory properties. These attributes stem from its ability to effectively scavenge ROS. This discovery was somewhat serendipitous. Rizigalinski started to use CeO_2 NPs as vehicles for drug delivery, specifically targeting organotypic brain cell cultures. The project was given to a student, who forgot for months the cell cultures in the incubator. After chastising the student, they noticed that control cultures were all dead, whereas NP-treated cultures were very much viable. This sparked a series of extensive experiments, culminating in a remarkable finding:

"CeO_2 NPs, of less than 20 nm in size, prolong the life of mixed brain cell cultures, and the neurons within these cultures, for periods of up to 6-8 months" [5].

In the following years, CeO_2 NPs have been reported beneficial across an impressive array of disease models, particularly in inflammatory-related pathologies, such as cardiac diseases, brain ischemia, diabetes, retinal dysfunction, liver inflammation, cancer, septic shock, acute and chronic glaucoma, radiation-induced injuries, and neurodegeneration, as summarized in **Table 1.1**. This non-exhaustive yet comprehensive compilation of data, focusing solely on preclinical studies, reflects the versatility of these NPs and underscores their potential not only to impede disease progression but also to facilitate disease resolution.

Organ	Pathophysiology	Disease	Reference
Blood	Ageing	Organ preservation	[6]
Bone	Hormonal (Ovariectomy)	Osteoporosis	[7]
Bone marrow	Ageing	Radiation	[8]
Brain	Traumatic Injury	TBI	[9–11]
	Traumatic Injury	Ischemia	[12,13]
	Traumatic Injury	Spinal Cord Injury	[14,15]
	Psychiatric	Depression	[16,17]
	Degeneration	Parkinson	[18,19]
	Degeneration	Alzheimer's	[20]
	Degeneration	ALS	[21]
	Degeneration	Multiple Sclerosis	[22]
	Degeneration	Seizures/Epilepsy	[23]
	Toxicity	Fipronil exposure	[24]
	Metabolic disorder	Diabetic Neuropathy	[25]
Connective Tissue	Cancer	Fibrosarcoma	[26]
Eye	Retinopathy	Diabetes Mellitus	[27]

	Degeneration	Age-related macular degeneration	[28–30]
	Degeneration	Dry eye disease	[31]
	Degeneration	Glaucoma	[32,33]
Gastrointestinal Epithelium	Ageing	Radiation	[34]
Heart	Cardiovascular disorder	Cardiomyopathies	[35]
	Cardiovascular disorder	Heart Failure	[36,37]
	Cardiovascular disorder	Cardiac Hypertrophy	[38]
Kidney	Peritonitis	Acute Kidney Injury	[39,40]
	Chronic Inflammation	Renal Fibrosis	[41]
	Toxicity (cisplatin)	Nephrotoxicity	[42]
Liver	Metabolic Disorder	Liver fibrosis	[43]
	Liver injury	Hepatectomy	[44]
	Liver injury	Acetaminophen overdose	[44]
	Metabolic disorder	Non-alcoholic fatty liver disease	[45]
	Liver injury	Liver Cirrhosis	[46]
	Liver injury	Hepatoxicity	[47]
	Cancer	Hepatocellular carcinoma	[48]
	Ageing	Organ preservation	[49]
Lung	Ageing	Severa radiation Pneumonitis	[50,51]
Multi-organ	Infection	Sepsis	[52,53]
Oocytes	Ageing	Organ preservation	[54]

Pancreas	Enzyme deficiency	Lipase deficiency	[55]
	Inflammation	Pancreatitis	[56]
Skin	Wound healing	Diabetes Mellitus	[57]
	Wound healing	Incisions	[8,58]
Sperm	Ageing	Organ preservation	[54,59–61]
	Intoxication	Organ preservation	[62]
Teeth	Inflammation	Periodontitis	[63,64]
Uterus	Reproductive disorders	Endometriosis	[65]

Table 1.1. Summary of diseases and associated pathologies investigated using CeO_2 NPs in preclinical models, based on literature review.

From the multitude of available preclinical studies, several pivotal examples emphasise the potential of these antioxidants, which will be briefly presented.

1.1.1 Liver

Numerous investigations have focused on assessing the impact of NPs on liver pathologies, likely prompted by the observation that approximately 80-90% of NPs accumulate in the liver following parenteral administration [66]. Based on this evidence, the liver was prioritized as the initial target for CeO_2 NPs testing by our research group. In this section, some results will be presented, where in-house synthesised CeO_2 NPs were evaluated in models of liver pathologies at varying stages of disease progression. These studies were conducted in collaboration with Prof. Wladimiro Jiménez team, from the service of Biochemistry and Molecular Genetics at the Hospital Clinic (Barcelona).

1.1.1.1 Non-alcoholic Fatty Liver Disease – Hepatic Steatosis

Non-alcoholic fatty liver disease (NAFLD) is characterized by the accumulation of fat droplets within the liver (steatosis). While in early stages it may not induce significant liver damage, its progression can lead to inflammation and increased risk of fibrosis. CeO_2 NPs were evaluated in a NAFLD rat model, demonstrating a decrease in the size

and content of liver hepatocyte lipid droplets, a favourable alteration in fatty acid expression, and a direct reduction in ROS and macrophage infiltration, while increasing anti-inflammatory cytokines [67].

1.1.1.2 Liver Fibrosis

Liver fibrosis is considered a chronic liver disease that results from prolonged liver injury and inflammation. If left untreated, it can progress to more severe stages, such as cirrhosis. In a rat model of fibrosis, treatment with CeO_2 NPs resulted in reduced liver steatosis, decreased macrophage infiltration, and lower levels of inflammatory cytokines. Accordingly, these effects contributed to a significant reduction in portal hypertension [43].

1.1.1.3 Cirrhosis

Considered a late-stage fibrosis, cirrhosis can lead to portal hypertension, cancer, and end-stage liver failure. Treatment with CeO_2 NPs in animal models showed a reversal in the pathological hallmarks of the disease. Moreover, results indicated a shift in portal vein macrophage polarization, from M1 (inflammatory) to M2 (anti-inflammatory) activity [46].

1.1.1.4 Hepatocellular Carcinoma

Hepatocellular carcinoma is the most common type of primary liver cancer, often associated with underlying chronic liver diseases. Interestingly, results indicate a significant increase in survival rates among hepatocellular carcinoma rats following treatment with CeO_2 NPs, sorafenib, or NPs plus sorafenib (**Figure 1.1**). Whereas the combination of both NPs and sorafenib showed the highest survival rates, differences did not reach statistical significance [48].

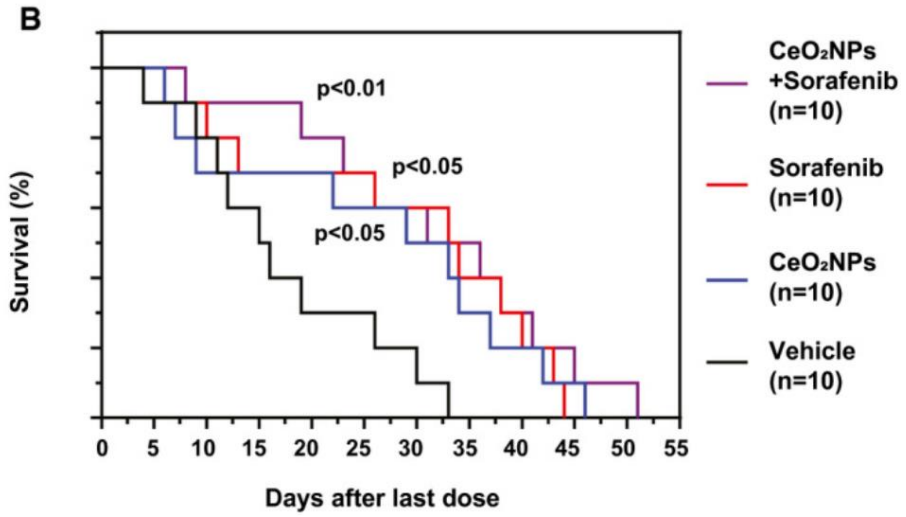


Figure 1.1. Effect of CeO_2 NPs, sorafenib, or the combination of both on survival in hepatocellular carcinoma rats. Extracted from reference [48].

1.1.1.5 Liver Regeneration after Acetaminophen Overdose and Partial Hepatectomy

In both acetaminophen overdose-induced hepatic failure and partial hepatectomy models, the administration of nanoceria enhanced liver regeneration, reducing early liver damage and promoting tissue regeneration [44].

All in all, the above-presented cases, demonstrate the effectiveness of CeO_2 NPs across various stages of liver disease, ranging from mild conditions like NAFLD to severe injuries such as liver failure. These findings underscore the versatility of CeO_2 NPs in addressing diverse aspects of disease pathophysiology. It is important to note that the biological effects of CeO_2 NPs by effectively reducing ROS levels result in diverse positive effects. For instance, in hepatocellular carcinoma, CeO_2 NPs reduce tumour size, while in partial hepatectomy, they promote cell proliferation. This highlights the diverse effects of oxidative stress, which depend on the specific condition of each disease, but involve disruption to the body's natural regulatory processes and functions.

1.1.2 Eye Degeneration

Eyes are constantly exposed to damaging UV light (photons), leading to high levels of ROS. Additionally, the high lipid content makes them more susceptible to oxidative

stress. CeO_2 NPs have been extensively tested in this organ, as reviewed in reference [68]. Here, a study conducted by our group in collaboration with Vall Hebron ophthalmology service is presented. CeO_2 NPs were tested in a model of age-related macular degeneration involving retinal pigment dysfunction and photoreceptor death, leading progressively to blindness with no effective treatment. The published work demonstrates that CeO_2 NPs are capable of reversing the altered gene expression pattern (of almost 500 genes) observed during the disease and related to inflammation and oxidative stress, towards the healthy phenotype [30]. Moreover, decreased signs of inflammation and arrest of degeneration were observed in the animals. The NPs were specially formulated for administration as eye drops, avoiding the much more invasive intravitreal injections, previously used for CeO_2 NPs eye administration [29,69].

1.1.3 Tissue and Cell Preservation

Organs for transplantation have a limited window of viability. Organ viability is highly related to inflammation and oxidative stress-related damage, which provoke their discard. In this section, two remarkable works will be highlighted. First, a pilot study was conducted by Del Turco et. al., where the use of CeO_2 NPs was evaluated in 9 discarded human liver grafts [49]. The objective was ex-situ NP administration during normothermic machine perfusion to mitigate ischemia/reperfusion injury in liver transplantation. Results showed rescue of mitochondrial phenotype, decrease in lipid droplet peroxidation, increase in antioxidant enzymes, and decrease in oxidative stress, demonstrating promising results for enhancing organ viability.

After the serendipitous discovery that CeO_2 increase the life of neuron cell cultures, Rzigalinski and colleagues demonstrated its significant ability to extend the life of red blood cells. This offers a promising approach to improve blood storage and the functional lifespan of these cells in stored whole blood [6]. Similarly, CeO_2 NPs have also been tested to enhance sperm cryopreservation, resulting in enhanced viability and fertility [60–62]. Other studies investigating CeO_2 NPs have reported increased spermatozoa preservation time at 4 ºC [70], as well as enhanced sperm quality in rats with induced testicular toxicity [62]. Moreover, nanoceria has shown promise in improving ovine oocyte development, thereby enhancing in vitro embryo production

[54]. These findings collectively suggest a promising role for CeO_2 NPs in addressing age-related issues and improving the overall health and functionality of biological systems.

1.1.4 Stem Cells

CeO_2 NPs have been studied for their effects on stem cells. Research has shown that CeO_2 NPs can promote the osteogenic differentiation of mesenchymal stem cells, which are critical for fracture repair and bone homeostasis maintenance [71]. Furthermore, studies employing human umbilical cord mesenchymal stem cells have demonstrated the antioxidative properties of CeO_2 NPs, facilitating tendon regeneration and suggesting their potential utility in tissue repair applications [72]. Additionally, CeO_2 NPs have exhibited radioprotective effects on stem cells and tissue regeneration in planarians has also been observed [73]. However, conflicting reports have emerged regarding the impact of CeO_2 NPs on neural stem cells, with some studies suggesting inhibition of neural differentiation [74]. These findings indicate that the effects of CeO_2 NPs on stem cells are complex and can vary depending on the cell type and context. Further research is needed to fully understand the potential benefits and risks associated with the utilization of CeO_2 NPs in stem cell-based applications.

1.1.5 Infections (Sepsis)

Sepsis has a widespread impact across multiple organs and can progress to septic shock, resulting in multi-organ failure and ultimately, death. This pathological condition is characterized by heightened oxidative stress stemming from an exacerbated immune system response. This underscores the crucial need for treatments capable of reducing inflammation and regulating the hyperreactive immune system, all while preserving its essential functions.

In this field, CeO_2 NPs have exhibited promising outcomes in attenuating sepsis-associated pathologies, thereby increasing survival rates in preclinical models. For instance, in a severe sepsis model induced by lipopolysaccharides (LPS) administration, CeO_2 NPs treatment improved rat survival rates from 10% to 73%,

decreased hepatic damage, reduced pro-inflammatory cytokines, and weakened systemic swelling [52]. Furthermore, Nandini et. al. observed increased survival rates, restored body temperature, and decreased systemic and hepatic oxidative stress upon CeO_2 NPs treatment in a peritonitis model induced by intra-abdominal infection [39]. Similarly, CeO_2 NPs treatment in a comparable peritonitis model ameliorated pathologies associated with acute kidney injury [75]. Asano and co-workers demonstrated the efficacy of CeO_2 NPs treatment in a model of sepsis-associated impairment in diaphragmatic contractile function [40]. Finally, in a model of severe sepsis induced by fecal material injection (polymicrobial sepsis), NP treatment significantly reduced sepsis-induced mortality, organ damage, serum IL-6, blood urea nitrogen, and inflammatory markers [53].

In conclusion, traditionally viewed as agents that merely impede oxidation, antioxidants have assumed a more intricate role, as evidenced by these findings, which highlight significant immunomodulatory functions facilitated through the scavenging of ROS. These roles extend beyond the conventional notion of safeguarding cells against damage caused by free radical molecules. Antioxidants are shown to actively participate in modulating immune responses, indicating a wider spectrum of influence on cellular dynamics. This discovery prompts a re-evaluation of the understanding of antioxidants, emphasizing their multifaceted contributions beyond the classical scope of oxidative stress prevention. Further research into the immunomodulatory properties of antioxidants, such as CeO_2 NPs, holds great promise for advancing our understanding of cellular dynamics and developing innovative therapeutic interventions for oxidative stress-related disorders.

1.2 Dynamic Interplay of ROS and Cellular Redox Balance

It has been said that there happen a billion chemical reactions per second in a eukaryotic cell. At any given time, the numerous pathways involved in building up and breaking down cellular components must be monitored and balanced in a coordinated fashion. To achieve this, cells organize reactions into various enzyme-enabled pathways. Indeed, regulation is the most fundamental difference between living and non-living

systems. However, non-enzymatic reactions also play a crucial role in metabolism and are integral to cellular processes. It is noteworthy that in principle, every enzymatic reaction can also occur non-enzymatically [76], but typically they only occur sporadically (as a matter of probability), as they lack the necessary activation energy to proceed (**Figure 1.2**).

As discussed by Atkinson [77], the limited space within a cell restricts the number of enzymes and molecules that can be present. This spatial restriction fosters a remarkable selectivity among enzymes, which, coupled with their inherent catalytic power, allows for the precise selection of one or few reactions for each metabolite from among several that are chemically possible. These selective process helps to avoid random reactions and their associated disadvantages.

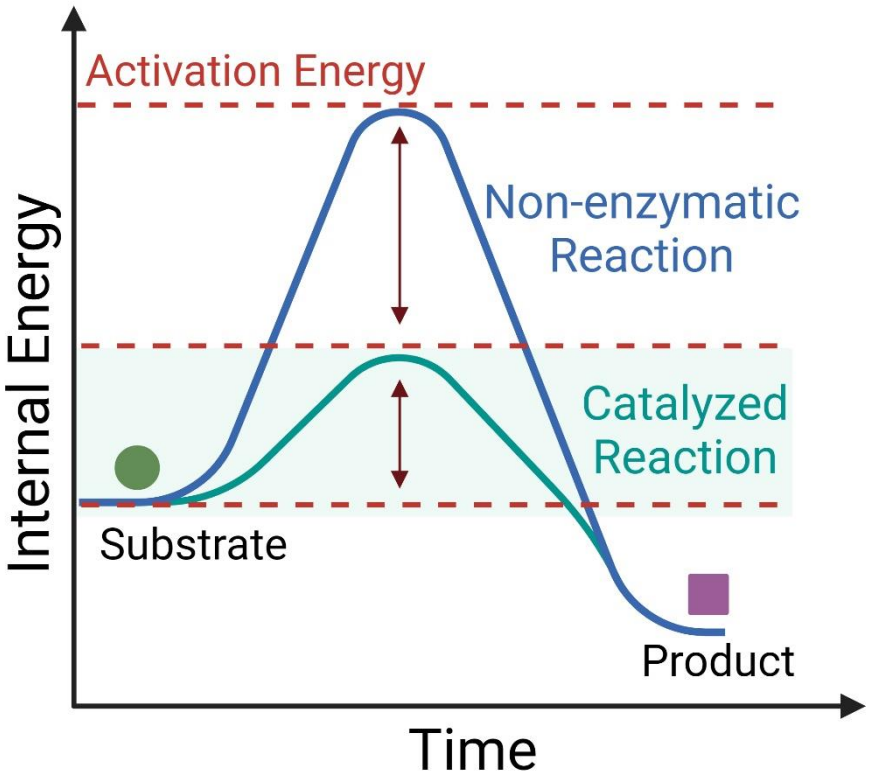


Figure 1.2. Schematic representation of the energy profiles of a catalysed reaction vs. a non-enzymatic reaction over time.

In this context, it is not surprising that in biological systems faster rate reactions are catalysed enzymatically (**Figure 1.2**). Importantly, an increase in internal energy can occur by enhancing the frequency of collisions, which can be accomplished by

elevating reactant concentrations, increasing pressure, or raising the temperature, thereby surpassing the activation energy barrier required to initiate the process. Consequently, maintaining low concentrations of intermediates is crucial to limit non-enzymatic reactions to insignificant rates, thus making enzyme-controlled metabolic systems possible.

Under certain conditions, such as during a rise in temperature (e.g., fever), non-enzymatic reactions may be augmented. Likewise, an increase in ROS boosts non-specific oxidations, causing damage to both substrates and enzymes. Accordingly, evidence has shown how the non-enzymatic oxidation of glucose by the hydroxyl radical (OH•) is largely unselective [78]. Both the enhanced bioavailability of substrate analogues and reduced substrate specificity resulting from enzyme damage can lead to heightened chemical reactivity [79].

In summary, the intricate interplay between ROS, alterations in redox potentials, enzymatic damage, and non-enzymatic reactions highlights the dynamic nature of cellular redox balance and its profound impact on biochemical processes, and consequently, overall health status.

1.2.1 ROS as Key Mediators of Immune Responses

The immune system comprises a complex network of cells, tissues, and molecules, responsible for body integrity, with a high capacity to adapt in response to diverse challenges. The immune system’s intimate connection with nearly every aspect of health and disease positions it as a central player in maintaining the body’s integrity.

ROS can be produced by immune cells, such as macrophages, neutrophils, and dendritic cells, as part of their antimicrobial defence mechanisms. ROS generation is tightly regulated and serves to eliminate invading pathogens through oxidative burst and phagocytosis [80,81]. However, an imbalance between ROS production and the antioxidant defences can lead to oxidative stress, resulting in tissue damage and exacerbation of inflammatory conditions.

The term inflammation finds its origin in Latin, which literally means "setting on fire". Inflammation is a complex biological response of the body’s immune system to

harmful stimuli, such as pathogens (pathogen-associated molecular patterns; PAMPs), damaged cells (damage-associated molecular patterns; DAMPS), or irritants. Inflammation is considered the first line of defence to danger or damage. In 1794, John Hunter concluded that "Inflammation itself is not to be considered as a disease, but a salutary operation, consequent either to some violence or to some diseases" [82]. However, while inflammation is essential for defending the body against infection and injury, dysregulated or excessive inflammation can be harmful and contribute to tissue damage and disease.

Chronic inflammation, driven by persistent oxidative stress, is a hallmark of many diseases, thereby exacerbating their progression. In cardiovascular diseases, for example, ROS-induced oxidative stress contributes to endothelial dysfunction, atherosclerosis, and hypertension [83]. Indeed, it is frequently the robust host response against infection or injury that is responsible for many of the pathophysiologic features of diseases. Strong evidence suggests that failure to restore normal immune function once the danger is neutralized is a key risk factor for adverse outcomes from illness.

Immune cells display remarkable plasticity, dynamically adjusting their metabolic profiles in response to microenvironmental cues and metabolic demands. Immunometabolism delves into the metabolic adaptations that immune cells undergo to fulfil their diverse functions. Metabolic pathways such as glycolysis, oxidative phosphorylation (OXPHOS), and fatty acid metabolism have emerged as key determinants of immune cell function and fate. Recent studies have demonstrated an intricate relationship between ROS levels and metabolic activation. Indeed, enzymes and subcellular compartments that typically produce ROS are associated with metabolic regulation and diseases associated with metabolic dysfunction may be influenced by changes in ROS balance [84]. A deeper insight into the role of ROS regulating immunometabolism will be given in Chapter 4.

1.3 Hypothesis: ROS Scavenging by CeO_2 NPs Modulates Inflammatory Responses

Considering the extensive applications and demonstrated effectiveness of CeO_2 NPs in preclinical models across numerous pathologies, alongside the known role of oxidative

stress in disease progression, an intriguing hypothesis emerges: The effective ROS scavenging activity of CeO_2 NPs protects tissues, regulates metabolism, modulates pro-inflammatory activation, and facilitates inflammation resolution.

1.4 Challenges and Considerations in Assessing the Safety of Nanomaterials

The question of whether CeO_2 NPs are safe does not have a straightforward yes or no answer. Medical NPs are intricately designed to perform sophisticated work within the human body, offering competitive therapeutic benefits compared to other medical approaches while minimizing side effects. The unique behaviour of NPs inside the body distinguishes nanomedicines from conventional drugs. Challenges such as physicochemical precision, biological non-specificity, differential biodistribution and accumulation, and in vivo transformation of NPs, hinder the translation of preclinical potential into clinical efficacy.

The unique properties of NPs pose a specific challenge due to differences in their chemical, physical, or biological properties compared to their molecular or larger-scale counterparts. While these properties hold great promise for scientific and technological advancements, they may also result in unexpected biological effects and environmental risks. Consequently, safety concerns have persisted for decades [85]. Indeed, although CeO_2 NPs have gained tremendous attention for their enormous potential in biomedicine, discrepant reports for either medical benefits or toxicity, as well as the lack of reproducibility of many studies, generate uncertainties delaying their effective implementation.

A primary issue arises from considering NPs with the same active principle as identical products, despite variations in size, shape, surface state, purification degree, and excipients. These differences can lead to dramatically varying biological effects, as well as differences in biodistribution and elimination rates. For example, different reagents and procedures are employed to prepare CeO_2 NPs, yielding NPs with distinct surface states and formulations within the final product. Dowding et al. prepared different samples of CeO_2 NPs using the same precursor and through similar synthesis methods but using different reagents; H_2O_2, NH_4OH, or hexamethylenetetramine

(HMT) [86]. Results showed that HMT-CeO_2 NPs reduced cell viability down to a concentration ten times lower than other CeO_2 NPs preparations, with this effect attributed to HMT. Besides, it was found that CeO_2 NPs with positive surface charge were more toxic to Caenorhabditis elegans than the same neutral or negatively charged NPs [87]. Furthermore, the use of exaggerated large doses, or contaminated materials, such as with endotoxins, is a concern, as most samples are not prepared under sufficient sterile conditions [88]. Concerning morphology, the toxicity of CeO_2 NPs with varying shapes (rods or cubes) was assessed in RAW 264.7 macrophages, revealing dose-dependent toxicity only for rod-like particles [89]. Ji et. al. demonstrated that CeO_2 large nanorods of different lengths, ranging from hundreds of nanometres to micrometres, induced a progressive increase in IL-1β production. In contrast, spherical NPs or shorter nanorods did not elicit the same response, indicating that the toxicity associated with nanorods depends on their length and aspect ratio [90].

In addition, while the relevance of the material characteristics and their ultimate formulation is evident, there remains a lack of standardized characterization methods and assessment guidelines for NPs. Despite the widespread acknowledgement that the biological effects of NPs are determined by their physicochemical properties, many publications do not even include NP characterization. In 2014, Harald Krug examined over a thousand published studies on the toxicity of inorganic NPs [91]. He concluded that a significant majority of these publications lacked sufficient information concerning crucial aspects such as the characterization of the materials under investigation. Moreover, little attention was paid to factors such as solvents and dispersion agents, their concentration and dosage, and the potential interference effects with the system.

The aim is not to criticize papers lacking certain information but to emphasize the importance of associating biological effects with specific NPs features. In general, it makes no sense to classify formulations with the same compositional active principle as either safe or toxic. Despite evaluating the controversy surrounding CeO_2 NPs is challenging due to variations in their physicochemical properties across studies, some insightful reviews have been published [92,93].

On the other hand, the evolution of NPs within a biological system is often underscored. For instance, while the aggregation state of NPs has been associated with their toxicity [94], it has been often neglected that non-aggregated NPs immediately aggregate when administrated. Aggregation is influenced by several factors such as pH, ionic strength, concentration, and protein content in biological environments. This indicates that the biological impact of NPs will depend not only on their intrinsic properties (e.g., size and shape) but also on extrinsic properties (e.g., characteristics of the exposure media). Thus, the composition of the NP core determines its chemical potential and catalytic activity, while the surface coating largely dictates its interactions with the biological systems. NPs can aggregate, either with other NPs or with macromolecules present in the physiological media, or they can dissolve.

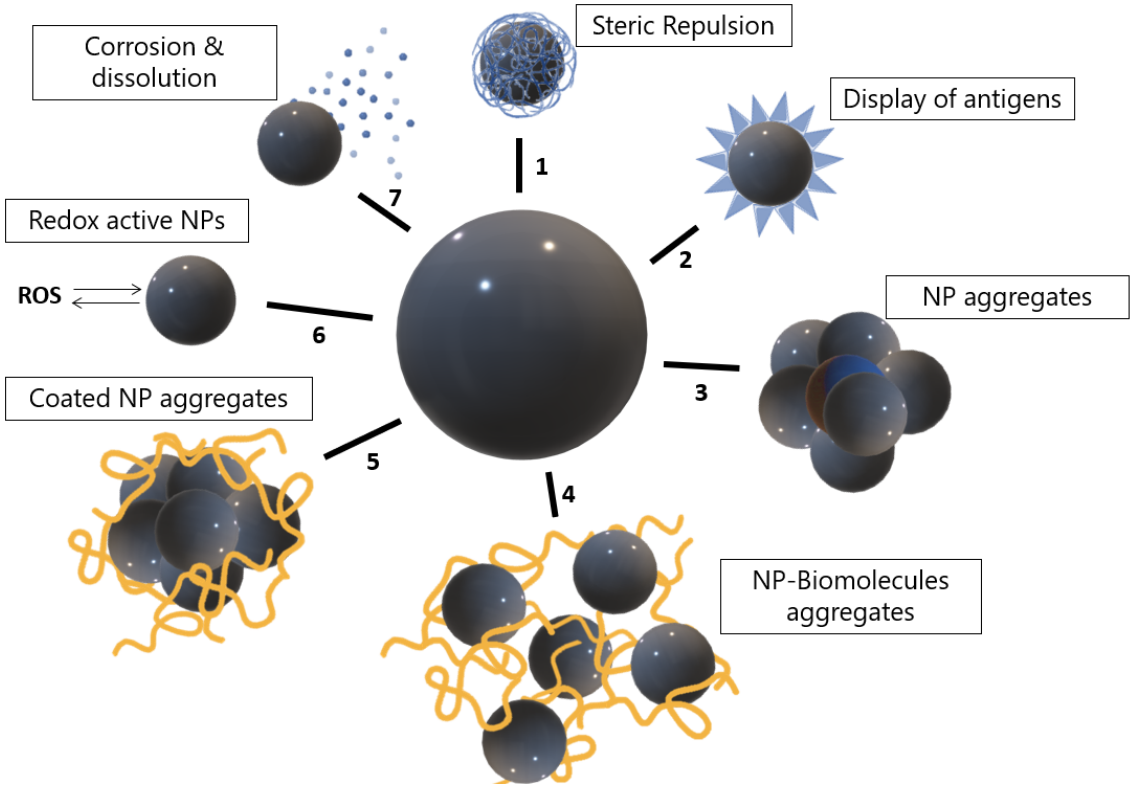


Figure 1.3. Intended or spontaneous NP modifications and their impact on immune responses. Adapted from [95]

Figure 1.3 summarizes the various phenomena NPs can undergo in physiological systems. In brief, NPs can be coated with molecules to try to pass undetected by the immune system or to avoid aggregation (1), but they can also be coated with antigenic molecules to induce an immune response (2). In the opposite direction, when dispersed

in physiological media, NP can aggregate (3) and absorb other molecules present in the medium (e.g., protein corona) (4) or both (5). In addition, depending on the core composition, NP can be used as ROS scavengers, like CeO_2 NPs, thereby down-regulating inflammatory responses (6), or they can dissolve and release bioactive ions, that may increase oxidative stress and generate an inflammatory response (7).

In conclusion, the variability of the nanomaterials and their often poorly described characterization pose significant barriers to the development of this multidisciplinary area. To effectively study NP interactions with biological systems, it is imperative to understand the physicochemical properties of NPs in their final product formulation and to accurately report NP characteristics, as prepared and during storage and use. These features will impact biocompatibility, biodistribution, biodegradation, and interference with cells and normal organ functioning, among other factors. Consequently, they will determine the toxicity of the NPs and the extent of their potential use.

1.4.1 Health Impact and Pharmaceutical Product Development

To overcome the challenges associated with nanomaterials and facilitate the translation of active principles into clinical practice, a new understanding of (nano)structure-activity relationships and standardized characterization techniques are imperative.

Of special relevance are the different interactions of the NPs with the immune system. It is expected that materials in the size range of proteins, protein aggregates, and viruses with different molecular coatings can engage in a sophisticated interaction with the immune system. NPs can be recognized or passed undetected by the immune system. Once detected, they can be tolerated or induce defensive (inflammatory) or anti-inflammatory responses. Throughout this thesis project, we have extensively analysed the main interactions of inorganic NPs and the immune system and published them, which can be found in Annex C section 7.3.1.

Therefore, the development of nanomaterials necessitates a comprehensive understanding of NP pharmacokinetics and pharmacodynamics. Moreover, this development should be framed in the innovation, production, and regulation limits of

our society. This means that proposed NPs must be producible as stable and reliable products, and capable of meeting the regulatory requirements for human application. To develop medical NPs beyond the exploration of the nano-bio interface, it is imperative to align our nanotechnology expertise, tools, and capabilities with practical medical applications and healthcare practitioners. Scientists must contribute to mechanistic understanding, safety assessments, efficacy evaluations, and effective communication. These efforts are essential for fostering public trust and facilitating the integration of novel nanodrugs into healthcare practices.

In pharmaceutical product development, four fundamental parameters should be addressed: understanding drug pharmacology, regulatory compliance, scale-up and industrialization, and social acceptance. Given this, we aimed to contribute to the advancement of the active principle, CeO_2 at the nanoscale, towards a pharmacological product. For these, it is of paramount importance to comprehend how the physicochemical properties of NPs impact their pharmacokinetics and pharmacodynamics.

The relevant differences between small drugs and nanomaterials have boosted regulatory agencies worldwide to establish guidelines ensuring the safe use of nanomaterials in various applications. In 2017, the Food and Drug Administration (FDA) published a guidance document for the industry regarding drug products, including biological products, that contain nanomaterials [96]. This document provides a framework for evaluating potential risks associated with nanomaterials, emphasizing the need for adequate characterization of nanomaterials, understanding their intended use and application, and comprehending how their attributes (physicochemical properties) affect product quality, safety, and efficacy. The recommendations for the correct assessment of nanomaterials include:

1. Adequacy of characterization of the material structure and its function.
2. Complexity of the material structure.
3. Understanding of the mechanism by which the physicochemical properties of the material impact its biological effects (e.g., the effect of particle size on pharmacokinetic parameters).

4. Understanding the in vivo principle of action based on the material's physicochemical properties.
5. Physical and chemical stability.
6. Maturity of the nanotechnology (including manufacturing and analytical methods).
7. The potential impact of manufacturing changes, including in-process controls and the robustness of the control strategy on critical quality attributes of the drug product.
8. Physical state of the material upon administration.
9. Route of administration.
10. Dissolution, distribution, biodegradation, accumulation, and their predictability based on physicochemical parameters and animal studies.

In light of this, synthesized CeO_2 NPs have undergone meticulous design and characterisation to enhance their antioxidant and anti-inflammatory properties, all while evaluating their safety profile. The pharmacokinetics and pharmacodynamics properties of CeO_2 NPs have been thoroughly investigated to exert control over and comprehend the material's attributes. This knowledge is crucial for optimizing the efficiency of NPs for therapeutic applications and predicting safety across various conditions.

1.5 What makes CeO_2 NPs Different from Traditional Antioxidants?

As oxidative stress accelerates and aggravates the pathology of most diseases, antioxidants have shown promise in ameliorating diverse disease conditions. Already in the seventies, the Nobel laureate Linus Pauling advocated for the use of vitamin C, a well-known antioxidant, for treating various diseases ranging from the common cold to cancer [97]. Despite the initial promising results, antioxidants have failed in many clinical trials, primarily due to their poor pharmacokinetics [98].

First, and to fully understand these outcomes, some clarifications regarding ROS are necessary. ROS is an umbrella term encompassing a wide range of chemical species with different properties, reactivity, and interactions. Specifically, ROS refers to species derived from oxygen (O_2) that are more reactive than O_2 itself. This includes

oxygen free radicals, like superoxide radical anion ($O_2^{\bullet -}$), as well as non-radical derivatives such as hydrogen peroxide (H_2O_2) and hypochlorous acid (HOCl), among others [99]. Different ROS have distinct reactivity within biological systems, and thus, they will have different lifetimes and "damaging" power. This variability impacts their ability to diffuse and act as signalling molecules.

The severity of damage caused by ROS can be predicted by a key thermodynamic property: the redox potential. This property gauges a chemical species' tendency to gain or lose electrons. Oxidizing species (high reduction potential) are capable of stealing an electron from any reduced species, while reduced species (with a low redox potential) are willing to donate an electron to any oxidizing species. A summary of reduction potentials of interest is given in **Table 1.2**, listed from highly oxidizing (electron acceptor) to highly reducing (electron donor).

Couple	E0 (V)
OH•, H^+/H_2O	2.33
HOO•, H^+/H_2O_2	1.06
$O_2^{\bullet -}$, $2H^+/H_2O_2$	0.94
RS•/RS- (cysteine)	0.92
H_2O_2, H^+/H_2O, OH•	0.32
O_2/$O_2^{\bullet -}$	-0.33
RSSR/$RSSR^{\bullet -}$ (cysteine or glutathione disulfide, GSSG)	-1.50

Table 1.2. Summary of relevant one-electron reduction potential of molecules relative to the standard hydrogen electrode (1 M, 1 atm, pH 7). Adapted from [100].

Indeed, O_2 with a redox potential of -0.33 V **(Table 1.2.)** is a poor oxidant and relatively fair to biomolecules. In stark contrast, the hydroxyl radical (OH•), with a one-electron reduction potential of +2.33 V, is the most powerful oxidant likely to arise in biological systems [101]. OH• is considered the shortest-lived (10^{-9} seconds at 37ºC) [102] and the most damaging ROS [99]. This means that all the organic compounds within a cell will react with OH• at a similar rate constant, being completely unspecific, so no molecular compound has more scavenging activity for OH• than the thousands of molecules already present in a biological system [103].

In contrast, H_2O_2 exhibits lower reactivity due to its non-radical nature and lower reduction potential (+0.32 V). Its longer lifetime allows these molecules to traverse membranes both by passive diffusion and facilitated transport via channels, such as aquaporins [104], making it an important intra- and extracellular signalling molecule. Specifically, the oxidation of thiol groups of cysteine residues by H_2O_2 is considered an important signalling mechanism [105].

Noteworthily, the redox potential of a molecule is a thermodynamic property that indicates the molecule's tendency to participate in redox reactions and is useful for predictions. However, it does not directly determine the kinetics or rate of the reaction. A reaction may be thermodynamically possible but not kinetically feasible if the rate constant is too small for it to be biologically significant [100]. Actual redox reaction kinetics are influenced by factors such as reactant concentration, temperature, pH, and catalyst presence.

For example, upon protonation of $O_2^{\bullet-}$ (p*K*a = 4.82), the hydroperoxyl radical (HOO•) is obtained. The new specie has an increased reduction potential (+1.06 V) and is a stronger oxidant, but the biological relevance of the HOO• is believed to be minor given its low concentration at physiological pH [101]. Similarly, while one-electron reduction of O_2 to $O_2^{\bullet-}$ (-0.33 V) is thermodynamically less favourable than its direct two-electron reduction to H_2O_2 (+0.33 V), the simultaneous requirement for two electrons in the latter makes it unfavourable [101]. In summary, the most relevant features of ROS are (i) lifetime, directly related to their reactivity, and (ii) concentration, related to its generation and lifetime, which impacts their kinetics.

The principal site for endogenous ROS production is the mitochondrial electron transport chain (ETC), where one-electron reduction of O_2 leads to superoxide radical (O_2•−) [105]. Steady-state levels of O_2•− are typically low because of its spontaneous and enzyme-mediated dismutation with water to H_2O_2 catalysed by superoxide dismutase's (SOD1-3) (**Figure 1.4**). The fate of H_2O_2 is a determinant for ROS control, as it can be neutralized by specific enzymes, resulting in the production of O_2 and water, or it can react to form OH• in presence of metal ions via Fenton chemistry, especially iron, ubiquitous in our biological environment. However, there are no

endogenous enzymes specifically directed at scavenging OH• once formed, likely due to its too-short life. The cellular defence against OH• is controlled by a network of antioxidant molecules and enzymes that oxidize one another propagating the electron donation until finally neutralized. An illustrative example is the tocopherol molecule (a member of the vitamin E family), which acts as a chain-breaking antioxidant by donating two electrons while it gets "consumed". To maintain its antioxidant function, oxidized tocopherol must be recycled (reduced back). Ascorbate, vitamin C, recycles tocopherol, but in this process, ascorbate gets oxidized and generates the ascorbate radical, which can be reduced back by enzyme systems that utilize nicotinamide adenine dinucleotide (NADH) or nicotinamide adenine dinucleotide phosphate (NADPH) [100]. These antioxidant networks require the cooperation of numerous molecules and enzymes at sufficient concentrations to effectively scavenge a single ROS. Failure to complete this process can lead to the leak of highly reactive species, such as the hydroxyl itself, or the ascorbate radical, highly damaging to cellular components.

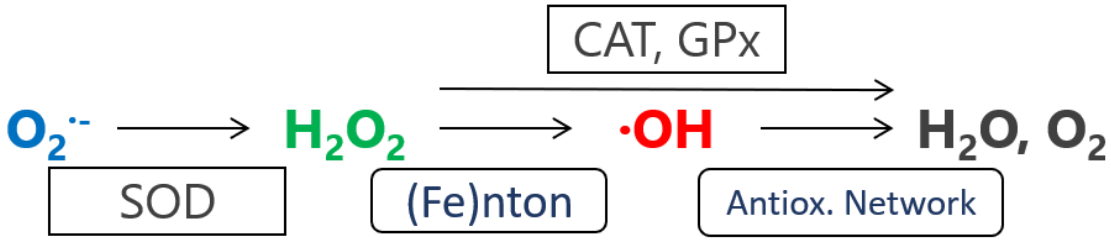


Figure 1.4. Representation of the most relevant ROS species; Superoxide radical (O2•−), hydrogen peroxide (H_2O_2), and hydroxyl radical (OH•), and their interconversion, by endogenous antioxidant systems.

The above-mentioned characteristics of ROS highlight the challenge of developing effective antioxidant substances. In modelling studies, enzymatic antioxidant defences have shown exceptional capacity to scavenge ROS compared to non-enzymatic antioxidants. Besides, it has been concluded that if the concentration of a molecular antioxidant is too low, there is little chance of collision and interaction with a free radical [106], either for enzymes or small molecules. However, within cells, the scavenging of O_2•− by small molecules is negligible compared with the rate of removal by endogenous SODs. These enzymes have rate constants ($\sim 2 \times 10^9\ M^{-1}\ s^{-1}$) that are millions of times faster than those of most other reactions with O_2•− [103].

Antioxidant enzymes possess several sophisticated features that, if not achieved by an exogenous compound, may lead to failure. Some features, such as the reduced activation energy inherent in enzymes cannot be replicated by non-enzymatic compounds. However, parameters like enzyme recyclability are fundamental. For instance, SOD catalyses the dismutation of O_2•− into H_2O_2 and O_2, utilizing transition metals in its active sites, namely copper and zinc (Cu/Zn) for SOD-1 and SOD-3 (cytoplasmic and extracellular, respectively), and manganese (Mn) for SOD-2 (mitochondrial). To scavenge O2•− radicals, the metal core alternates between oxidation states (e.g., Mn alternates between Mn^{+2} and Mn^{+3}) during the catalytic cycle, enabling their recycling while scavenging ROS molecules, whereas molecular antioxidants typically possess few active sites per molecule and are consumed in the process.

In conclusion, the specificity, rate constant, location, and concentration of the antioxidant within the cell should render a chemically plausible antioxidant effect. Therefore, a high concentration of antioxidants at the target site is required, but traditional molecular antioxidants often exhibit poor pharmacokinetics, leading to reduced bioavailability at target sites. Moreover, despite the chemistry of free radical scavenging capacities of several molecules is well documented, just because the chemistry is plausible, it does not guarantee their efficacy in vivo. An effective antioxidant must fulfil two important parameters: (i) recyclability, otherwise, the needed amounts and the produced metabolites would bury the cell (and ideally not dependent on other molecules), and (ii) availability at the target site (pharmacokinetics).

In this scenario, mineral antioxidants, like CeO_2 NPs, present some important properties that make them ideal candidates for mitigating ROS. Foremost among these is their Ce^{3+}/Ce^{4+} duality, which mimics the activity of redox enzymes in its free radical scavenging activity (**Figure 1.5**). CeO_2 NPs also act as catalysts, with the ability to recycle. Additionally, while enzymes have one catalytic site per molecule, a single nanoceria crystal, a few times smaller, may possess dozens, owing to its increased surface-to-volume ratio.

Second, it's important to note that enzymes exhibit high substrate specificity, which is governed by topological restrictions resulting from the interaction of atoms and peptides surrounding the metal ion in the active site, thereby determining its coordination environment. In contrast, the surface availability of CeO_2 NPs, enables them to scavenge any type of ROS, rendering them highly unselective to the type of ROS while only significantly active when ROS concentration is rather high. While specificity offers an evolutionary advantage, there are instances where the ability to process multiple substrates could be beneficial to cells during oxidative stress conditions [79].

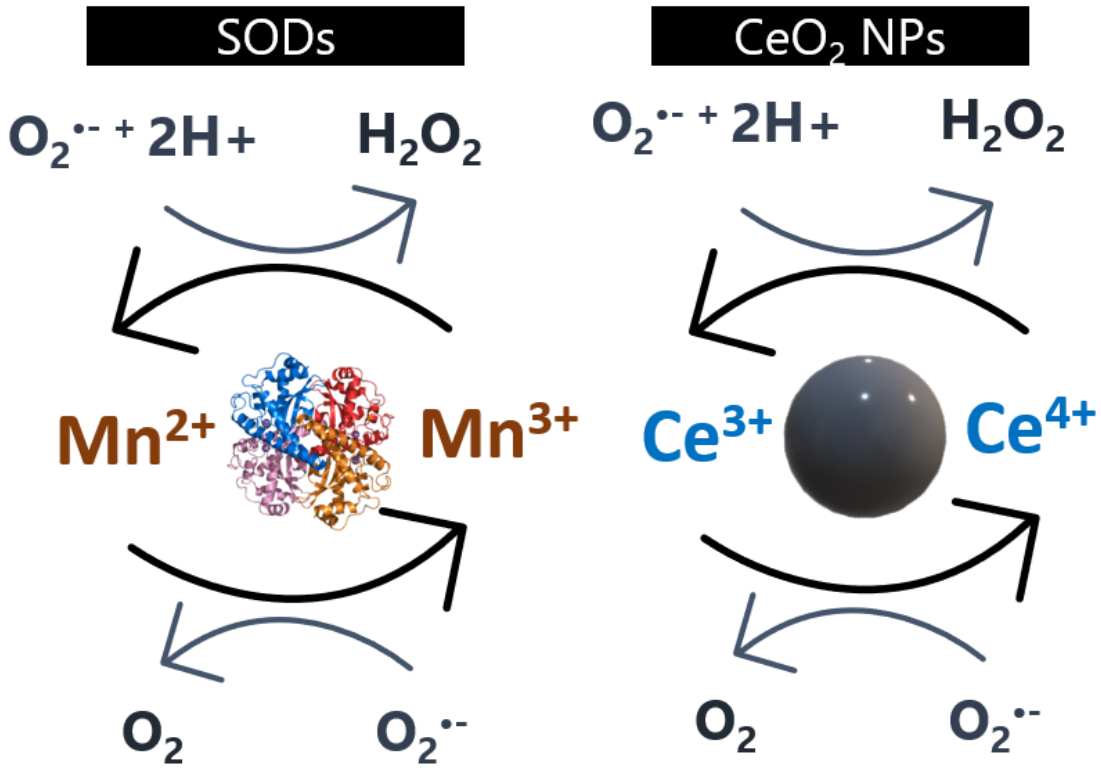


Figure 1.5. Schematic representation comparing the scavenging activity of SOD and CeO_2 NPs, both based on redox pairs.

Furthermore, in biological systems the combination of several enzymes has an advantage over a single enzyme, limiting the effectiveness of compounds mimicking SOD or other types of antioxidant enzymes, although it's important to note that enzyme-mimicking compounds are showing positive results in clinical trials [103].

The multiple enzyme-like catalytic properties exhibited by CeO_2 NPs have positioned them as promising "nanozymes", making them suitable candidates for ROS scavenging and advocating for their use in medicine via pharmaceutical development. Although NPs have been presented as enzyme-likeness, they possess several features such as unspecificity, numerous catalytic sites, and limited reactivity at low ROS concentrations, that distinguish them from natural enzymes. Consequently, in this context, they are better classified as mineral antioxidants.

1.6 Objectives and Scope

This work aims to harness the potential of CeO_2 NPs as ROS scavengers, functioning as mineral antioxidants to promote cellular redox balance. Through the investigation of CeO_2 NPs on inflammatory responses mediated by ROS, we aim to elucidate their potential to enhance immune function and alleviate inflammatory reactions and undesirable metabolic states.

The distinctive features of CeO_2 NPs compared to traditional antioxidants underline the need for a nuanced comprehension of their physicochemical properties and mechanisms of action, given their considerable promise alongside critical safety considerations.

Accordingly, this work has been structured into three main sections:

1. CeO_2 NPs Physicochemical Properties: This section entails the synthesis and characterization of the material, focusing on understanding how its physicochemical properties influence behaviour and therefore efficacy and safety.
2. CeO_2 NPs Pharmacokinetics: This part studies the ADME profile of CeO_2 NPs in healthy and diseased preclinical models.
3. CeO_2 NPs Pharmacodynamics: This section aims to elucidate the mechanism of action of CeO_2 NPs on inflammation by investigating their effects on the energy metabolism of innate immune cells, particularly macrophages. These versatile cells, exhibiting both pro- and anti-inflammatory phenotypes, play a pivotal role in orchestrating the inflammatory response.

1.7 References

1. Montini, T.; Melchionna, M.; Monai, M.; Fornasiero, P. Fundamentals and Catalytic Applications of CeO2-Based Materials. *Chem Rev* **2016**, *116*, 5987–6041.

2. Boudghene Stambouli, A.; Traversa, E. Solid Oxide Fuel Cells (SOFCs): A Review of an Environmentally Clean and Efficient Source of Energy. *Renewable and Sustainable Energy Reviews* **2002**, *6*, 433–455.

3. A, C.; P, A.; H, G.; JY, C.-C. Hierarchically Mesostructured Doped CeO2 with Potential for Solar-Cell Use. *Nat Mater* **2004**, *3*.

4. Cheng, J.; Huang, S.; Lu, X. Preparation of Surface Modified Ceria Nanoparticles as Abrasives for the Application of Chemical Mechanical Polishing (CMP). *ECS Journal of Solid State Science and Technology* **2020**, *9*, 024015.

5. Rzigalinski, B.A. Nanoparticles and Cell Longevity. *http://dx.doi.org/10.1177/153303460500400609* **2005**.

6. Rzigalinski, B.A.; Giovinco, H.M.; Cheatham, B.J. Cerium Oxide Nanoparticles Improve Lifespan of Stored Blood. *Mil Med* **2020**, *185*, 103–109.

7. Vieira, E.; Silva, M.; Maia-Filho, A.; Ferreira, D.; Figuerêdo-Silva, J.; Rovaris, K.; Fialho, A.C.; Leite-Oliveira, A.; de Oliveira, A.L.M.; da Fonseca, M.G.; et al. Effect of Cerium-Containing Hydroxyapatite in Bone Repair in Female Rats with Osteoporosis Induced by Ovariectomy. *Minerals 2021, Vol. 11, Page 377* **2021**, *11*, 377.

8. Popova, N.R.; Andreeva, V. V.; Khohlov, N. V.; Popov, A.L.; Ivanov, V.K. Fabrication of CeO2 Nanoparticles Embedded in Polysaccharide Hydrogel and Their Application in Skin Wound Healing. *Nanosystems: Physics, Chemistry, Mathematics* **2020**, *11*, 99–109.

9. Bailey, Z.S.; Nilson, E.; Bates, J.A.; Oyalowo, A.; Hockey, K.S.; Sajja, V.S.S.S.; Thorpe, C.; Rogers, H.; Dunn, B.; Frey, A.S.; et al. Cerium Oxide Nanoparticles Improve Outcome after In Vitro and In Vivo Mild Traumatic Brain Injury. *J Neurotrauma* **2020**, *37*, 1452–1462.

10. Youn, D.H.; Tran, N.M.; Kim, B.J.; Kim, Y.; Jeon, J.P.; Yoo, H. Shape Effect of Cerium Oxide Nanoparticles on Mild Traumatic Brain Injury. *Sci Rep* **2021**, *11*.

11. Kang, D.W.; Cha, B.G.; Lee, J.H.; Yang, W.; Ki, S.K.; Han, J.H.; Cho, H.Y.; Park, E.; Jeon, S.; Lee, S.H. Ultrasmall Polymer-Coated Cerium Oxide Nanoparticles as a Traumatic Brain Injury Therapy. *Nanomedicine* **2022**, *45*.

12. Estevez, A.Y.; Pritchard, S.; Harper, K.; Aston, J.W.; Lynch, A.; Lucky, J.J.; Ludington, J.S.; Chatani, P.; Mosenthal, W.P.; Leiter, J.C.; et al. Neuroprotective Mechanisms of Cerium Oxide Nanoparticles in a Mouse Hippocampal Brain Slice Model of Ischemia. *Free Radic Biol Med* **2011**, *51*, 1155–1163.

13. Li, X.; Han, Z.; Wang, T.; Ma, C.; Li, H.; Lei, H.; Yang, Y.; Wang, Y.; Pei, Z.; Liu, Z.; et al. Cerium Oxide Nanoparticles with Antioxidative Neurorestoration for Ischemic Stroke. *Biomaterials* **2022**, *291*.

14. Rahimi, B.; Behroozi, Z.; Motamed, A.; Jafarpour, M.; Hamblin, M.R.; Moshiri, A.; Janzadeh, A.; Ramezani, F. Study of Nerve Cell Regeneration on Nanofibers Containing Cerium Oxide Nanoparticles in a Spinal Cord Injury Model in Rats. *J Mater Sci Mater Med* **2023**, *34*, 1–15.

15. Liu, D.; Lu, G.; Shi, B.; Ni, H.; Wang, J.; Qiu, Y.; Yang, L.; Zhu, Z.; Yi, X.; Du, X.; et al. ROS-Scavenging Hydrogels Synergize with Neural Stem Cells to Enhance Spinal Cord Injury Repair via Regulating Microenvironment and Facilitating Nerve Regeneration. *Adv Healthc Mater* **2023**, *12*, 2300123.

16. Zavvari, F.; Nahavandi, A.; Shahbazi, A. Neuroprotective Effects of Cerium Oxide Nanoparticles on Experimental Stress-Induced Depression in Male Rats. *J Chem Neuroanat* **2020**, *106*.

17. Fu, S.; Chen, H.; Yang, W.; Xia, X.; Zhao, S.; Xu, X.; Ai, P.; Cai, Q.; Li, X.; Wang, Y.; et al. ROS-Targeted Depression Therapy via BSA-Incubated Ceria Nanoclusters. *Nano Lett* **2022**, *22*, 4519–4527.

18. Hegazy, M.A.; Maklad, H.M.; Samy, D.M.; Abdelmonsif, D.A.; El Sabaa, B.M.; Elnozahy, F.Y. Cerium Oxide Nanoparticles Could Ameliorate Behavioral and Neurochemical Impairments in 6-Hydroxydopamine Induced Parkinson's Disease in Rats. *Neurochem Int* **2017**, *108*, 361–371.

19. Mohammad; Khan, U.A.; Saifi, Z.; Bora, J.; Warsi, M.H.; Abourehab, M.A.S.; Jain, G.K.; Kesharwani, P.; Ali, A. Intranasal Inorganic Cerium Oxide Nanoparticles Ameliorate Oxidative Stress Induced Motor Manifestations in Haloperidol-Induced Parkinsonism. *Inflammopharmacology* **2023**, *31*, 2571–2585.

20. Danish, S.M.; Gupta, A.; Khan, U.A.; Hasan, N.; Ahmad, F.J.; Warsi, M.H.; Abdelhaleem Ali, A.M.; Zafar, A.; Jain, G.K. Intranasal Cerium Oxide Nanoparticles Ameliorate Cognitive Function in Rats with Alzheimer's via Anti-Oxidative Pathway. *Pharmaceutics* **2022**, *14*.

21. DeCoteau, W.; Heckman, K.L.; Estevez, A.Y.; Reed, K.J.; Costanzo, W.; Sandford, D.; Studlack, P.; Clauss, J.; Nichols, E.; Lipps, J.; et al. Cerium Oxide Nanoparticles with Antioxidant Properties Ameliorate Strength and Prolong Life in Mouse Model of Amyotrophic Lateral Sclerosis. *Nanomedicine* **2016**, *12*, 2311–2320.

22. Heckman, K.L.; Decoteau, W.; Estevez, A.; Reed, K.J.; Costanzo, W.; Sanford, D.; Leiter, J.C.; Clauss, J.; Knapp, K.; Gomez, C.; et al. Custom Cerium Oxide Nanoparticles Protect against a Free Radical Mediated Autoimmune Degenerative Disease in the Brain. *ACS Nano* **2013**, *7*, 10582–10596.

23. Mojarrad, F.; Asadi, A.; Abdolmaleki, A.; Mirzaee, S.; Zahri, S. Preparation of Cinnamon-Coated Cerium Oxide Nanoparticles and Evaluation of Their Anticonvulsant Effect in Rats. *Pharm Chem J* **2023**, *57*, 648–655.

24. Elshony, N.; Nassar, A.M.K.; El-Sayed, Y.S.; Samak, D.; Noreldin, A.; Wasef, L.; Saleh, H.; Elewa, Y.H.A.; Tawfeek, S.E.; Saati, A.A.; et al. Ameliorative Role of Cerium Oxide Nanoparticles Against Fipronil Impact on Brain Function, Oxidative Stress, and Apoptotic Cascades in Albino Rats. *Front Neurosci* **2021**, *15*, 651471.

25. Najafi, R.; Hosseini, A.; Ghaznavi, H.; Mehrzadi, S.; Sharifi, A.M. Neuroprotective Effect of Cerium Oxide Nanoparticles in a Rat Model of Experimental Diabetic Neuropathy. *Brain Res Bull* **2017**, *131*, 117–122.

26. Nourmohammadi, E.; Khoshdel-sarkarizi, H.; Nedaeinia, R.; Darroudi, M.; Kazemi Oskuee, R. Cerium Oxide Nanoparticles: A Promising Tool for the Treatment of Fibrosarcoma in-Vivo. *Materials Science and Engineering: C* **2020**, *109*, 110533.

27. Chen, H.; Li, Z.; Zhou, Z.; Zhuang, J. Cerium Compound-Loaded Poly(Lactic Co Glycolic Acid) Nanospheres in Improving Diabetic Retinopathy. *Sci Adv Mater* **2022**, *14*, 423–429.

28. Tisi, A.; Pulcini, F.; Carozza, G.; Mattei, V.; Flati, V.; Passacantando, M.; Antognelli, C.; Maccarone, R.; Monache, S.D. Antioxidant Properties of Cerium Oxide Nanoparticles Prevent Retinal Neovascular Alterations In Vitro and In Vivo. *Antioxidants* **2022**, *11*, 1133.

29. Chen, J.; Patil, S.; Seal, S.; McGinnis, J.F. Rare Earth Nanoparticles Prevent Retinal Degeneration Induced by Intracellular Peroxides. *Nano-Enabled Medical Applications* **2020**, 525–546.

30. Badia, A.; Duarri, A.; Salas, A.; Rosell, J.; Ramis, J.; Gusta, M.F.; Casals, E.; Zapata, M.A.; Puntes, V.; García-Arumí, J. Repeated Topical Administration of 3 Nm Cerium Oxide Nanoparticles Reverts Disease Atrophic Phenotype and Arrests Neovascular Degeneration in AMD Mouse Models. *ACS Nano* **2023**.

31. Zou, H.; Wang, H.; Xu, B.; Liang, L.; Shen, L.; Lin, Q. Regenerative Cerium Oxide Nanozymes Alleviate Oxidative Stress for Efficient Dry Eye Disease Treatment. *Regen Biomater* **2022**, *9*.

32. Luo, L.J.; Nguyen, D.D.; Lai, J.Y. Harnessing the Tunable Cavity of Nanoceria for Enhancing Y-27632-Mediated Alleviation of Ocular Hypertension. *Theranostics* **2021**, *11*, 5447.

33. Nguyen, D.D.; Lai, J.Y. Synthesis, Bioactive Properties, and Biomedical Applications of Intrinsically Therapeutic Nanoparticles for Disease Treatment. *Chemical Engineering Journal* **2022**, *435*, 134970.

34. Colon, J.; Hsieh, N.; Ferguson, A.; Kupelian, P.; Seal, S.; Jenkins, D.W.; Baker, C.H. Cerium Oxide Nanoparticles Protect Gastrointestinal Epithelium from Radiation-Induced Damage by Reduction of Reactive Oxygen Species and Upregulation of Superoxide Dismutase 2. *Nanomedicine* **2010**, *6*, 698–705.

35. NIU, J.; AZFER, A.; ROGERS, L.; WANG, X.; KOLATTUKUDY, P. Cardioprotective Effects of Cerium Oxide Nanoparticles in a Transgenic Murine Model of Cardiomyopathy. *Cardiovasc Res* **2007**, *73*, 549–559.

36. El Shaer, S.S.; Salaheldin, T.A.; Saied, N.M.; Abdelazim, S.M. In Vivo Ameliorative Effect of Cerium Oxide Nanoparticles in Isoproterenol-Induced Cardiac Toxicity. *Exp Toxicol Pathol* **2017**, *69*, 435–441.

37. Kumari, P.; Saifi, M.A.; Khurana, A.; Godugu, C. Cardioprotective Effects of Nanoceria in a Murine Model of Cardiac Remodeling. *J Trace Elem Med Biol* **2018**, *50*, 198–208.

38. Kolli, M.B.; Manne, N.D.P.K.; Para, R.; Nalabotu, S.K.; Nandyala, G.; Shokuhfar, T.; He, K.; Hamlekhan, A.; Ma, J.Y.; Wehner, P.S.; et al. Cerium Oxide Nanoparticles Attenuate Monocrotaline Induced Right Ventricular Hypertrophy Following Pulmonary Arterial Hypertension. *Biomaterials* **2014**, *35*, 9951–9962.

39. Manne, N.D.P.K.; Arvapalli, R.; Nepal, N.; Shokuhfar, T.; Rice, K.M.; Asano, S.; Blough, E.R. Cerium Oxide Nanoparticles Attenuate Acute Kidney Injury Induced by Intra-Abdominal Infection in Sprague-Dawley Rats. *J Nanobiotechnology* **2015**, *13*, 1–11.

40. Asano, S.; Arvapalli, R.; Manne, N.D.; Maheshwari, M.; Ma, B.; Rice, K.M.; Selvaraj, V.; Blough, E.R. Cerium Oxide Nanoparticle Treatment Ameliorates Peritonitis-Induced Diaphragm Dysfunction. *Int J Nanomedicine* **2015**, *10*, 6215–6226.

41. Saifi, M.A.; Peddakkulappagari, C.S.; Ahmad, A.; Godugu, C. Leveraging the Pathophysiological Alterations of Obstructive Nephropathy to Treat Renal Fibrosis by Cerium Oxide Nanoparticles. *ACS Biomater Sci Eng* **2020**, *6*, 3563–3573.

42. Abdelhamid, A.M.; Mahmoud, S.S.; Abdelrahman, A.E.; Said, N.M.; Toam, M.; Samy, W.; Amer, M.A.E.M. Protective Effect of Cerium Oxide Nanoparticles on Cisplatin and Oxaliplatin Primary Toxicities in Male Albino Rats. *Naunyn Schmiedebergs Arch Pharmacol* **2020**, *393*, 2411–2425.

43. Oró, D.; Yudina, T.; Fernández-Varo, G.; Casals, E.; Reichenbach, V.; Casals, G.; González de la Presa, B.; Sandalinas, S.; Carvajal, S.; Puntes, V.; et al. Cerium Oxide Nanoparticles Reduce Steatosis, Portal Hypertension and Display Anti-Inflammatory Properties in Rats with Liver Fibrosis. *J Hepatol* **2016**, *64*, 691–698.

44. Córdoba-Jover, B.; Arce-Cerezo, A.; Ribera, J.; Pauta, M.; Oró, D.; Casals, G.; Fernández-Varo, G.; Casals, E.; Puntes, V.; Jiménez, W.; et al. Cerium Oxide

Nanoparticles Improve Liver Regeneration after Acetaminophen-Induced Liver Injury and Partial Hepatectomy in Rats. *Journal of Nanobiotechnology 2019 17:1* **2019**, *17*, 1–12.

45. Carvajal, S.; Oró, D.; Fernández-Varo, G.; Yudina, T.; Perramón, M.; Oller, L.; Casals, G.; de la Presa, B.G.; Puntes, V.; Jiménez, W. Therapeutic Effect of Cerium Oxide Nanoparticles (CeO2NPs) in Rats with Diet-Induced Non-Alcoholic Steatohepatitis. *J Hepatol* **2017**, *66*, S608.

46. Ribera, J.; Rodríguez-Vita, J.; Cordoba, B.; Portolés, I.; Casals, G.; Casals, E.; Jiménez, W.; Puntes, V.; Ruiz, M.M. Functionalized Cerium Oxide Nanoparticles Mitigate the Oxidative Stress and Pro-Inflammatory Activity Associated to the Portal Vein Endothelium of Cirrhotic Rats. *PLoS One* **2019**, *14*.

47. Abdel-Karim, R.I.; Hashish, R.K.; Badran, D.I.; Mohammed, S.S.; Salem, N.A. The Ameliorative Effect of Cerium Oxide Nanoparticles on Chlorpyrifos Induced Hepatotoxicity in a Rat Model: Biochemical, Molecular and Immunohistochemical Study. *J Trace Elem Med Biol* **2024**, *81*.

48. Fernández-Varo, G.; Perramón, M.; Carvajal, S.; Oró, D.; Casals, E.; Boix, L.; Oller, L.; Macías-Muñoz, L.; Marfà, S.; Casals, G.; et al. Bespoken Nanoceria: An Effective Treatment in Experimental Hepatocellular Carcinoma. *Hepatology* **2020**, *72*, 1267–1282.

49. Turco, S. Del; Cappello, V.; Tapeinos, C.; Moscardini, A.; Sabatino, L.; Battaglini, M.; Melandro, F.; Torri, F.; Martinelli, C.; Babboni, S.; et al. Cerium Oxide Nanoparticles Administration during Machine Perfusion of Discarded Human Livers: A Pilot Study. *Liver Transplantation* **2022**, *28*, 1173–1185.

50. Colon, J.; Herrera, L.; Smith, J.; Patil, S.; Komanski, C.; Kupelian, P.; Seal, S.; Jenkins, D.W.; Baker, C.H. Protection from Radiation-Induced Pneumonitis Using Cerium Oxide Nanoparticles. *Nanomedicine* **2009**, *5*, 225–231.

51. Xu, P.T.; Maidment, B.W.; Antonic, V.; Jackson, I.L.; Das, S.; Zodda, A.; Zhang, X.; Seal, S.; Vujaskovic, Z. Cerium Oxide Nanoparticles: A Potential Medical Countermeasure to Mitigate Radiation-Induced Lung Injury in CBA/J Mice. *Radiat Res* **2016**, *185*, 516.

52. Chen, G.; Xu, Y. Biosynthesis of Cerium Oxide Nanoparticles and Their Effect on Lipopolysaccharide (LPS) Induced Sepsis Mortality and Associated Hepatic Dysfunction in Male Sprague Dawley Rats. *Materials Science and Engineering C* **2018**, *83*, 148–153.

53. Selvaraj, V.; Manne, N.D.P.K.; Arvapalli, R.; Rice, K.M.; Nandyala, G.; Fankenhanel, E.; Blough, E.R. Effect of Cerium Oxide Nanoparticles on Sepsis Induced Mortality and NF-KB Signaling in Cultured Macrophages. *https://doi.org/10.2217/nnm.14.205* **2015**, *10*, 1275–1288.

54. Ariu, F.; Bogliolo, L.; Pinna, A.; Malfatti, L.; Innocenzi, P.; Falchi, L.; Bebbere, D.; Ledda, S. Cerium Oxide Nanoparticles (CeO2 NPs) Improve the Developmental Competence of in Vitro-Matured Prepubertal Ovine Oocytes. *Reprod Fertil Dev* **2017**, *29*, 1046–1056.

55. Murugan, R.K.; Murugan, C.; Sundaramurthy, A. Collapsible Charge Induced Aggregation Behaviour of Cerium Oxide Nanoparticles for Treating Pancreatic Enzyme Deficiency. *Mater Lett* **2021**, *303*, 130472.

56. Khurana, A.; Saifi, M.A.; Godugu, C. Nanoceria Ameliorates Fibrosis, Inflammation, and Cellular Stress in Experimental Chronic Pancreatitis. *ACS Biomater Sci Eng* **2023**, *9*, 1030–1042.

57. Dewberry, L.C.; Niemiec, S.M.; Hilton, S.A.; Louiselle, A.E.; Singh, S.; Sakthivel, T.S.; Hu, J.; Seal, S.; Liechty, K.W.; Zgheib, C. Cerium Oxide Nanoparticle Conjugation to MicroRNA-146a Mechanism of Correction for Impaired Diabetic Wound Healing. *Nanomedicine* **2022**, *40*.

58. Ahmed, H.E.; Iqbal, Y.; Aziz, M.H.; Atif, M.; Batool, Z.; Hanif, A.; Yaqub, N.; Farooq, W.A.; Ahmad, S.; Fatehmulla, A.; et al. Green Synthesis of CeO2 Nanoparticles from the Abelmoschus Esculentus Extract: Evaluation of Antioxidant, Anticancer, Antibacterial, and Wound-Healing Activities. *Molecules 2021, Vol. 26, Page 4659* **2021**, *26*, 4659.

59. Hosseinmardi, M.; Siadat, F.; Sharafi, M.; Roodbari, N.H.; Hezavehei, M. Protective Effect of Cerium Oxide Nanoparticles on Human Sperm Function During Cryopreservation. *Biopreserv Biobank* **2022**, *20*, 24–30.

60. Feugang, J.M.; Rhoads, C.E.; Mustapha, P.A.; Tardif, S.; Parrish, J.J.; Willard, S.T.; Ryan, P.L. Treatment of Boar Sperm with Nanoparticles for Improved Fertility. *Theriogenology* **2019**, *137*, 75–81.

61. Khalique, M.A.; Andrabi, S.M.H.; Majeed, K.A.; Yousaf, M.S.; Ahmad, N.; Tahir, S.K.; Fayyaz, M.H.; Haider, M.S.; Naz, S.S.; Qureshi, I.Z.; et al. Cerium Oxide Nanoparticles Improve the Post-Thaw Quality and in-Vivo Fertility of Beetal Buck Spermatozoa. *Theriogenology* **2024**, *214*, 166–172.

62. Moridi, H.; Hosseini, S.A.; Shateri, H.; Kheiripour, N.; Kaki, A.; Hatami, M.; Ranjbar, A. Protective Effect of Cerium Oxide Nanoparticle on Sperm Quality and Oxidative Damage in Malathion-Induced Testicular Toxicity in Rats: An Experimental Study. *Int J Reprod Biomed* **2018**, *16*, 261.

63. Yu, Y.; Zhao, S.; Gu, D.; Zhu, B.; Liu, H.; Wu, W.; Wu, J.; Wei, H.; Miao, L. Cerium Oxide Nanozyme Attenuates Periodontal Bone Destruction by Inhibiting the ROS–NFκB Pathway. *Nanoscale* **2022**, *14*, 2628–2637.

64. Ren, S.; Zhou, Y.; Zheng, K.; Xu, X.; Yang, J.; Wang, X.; Miao, L.; Wei, H.; Xu, Y. Cerium Oxide Nanoparticles Loaded Nanofibrous Membranes Promote Bone Regeneration for Periodontal Tissue Engineering. *Bioact Mater* **2022**, *7*, 242–253.

65. Chaudhury, K.; Babu K, N.; Singh, A.K.; Das, S.; Kumar, A.; Seal, S. Mitigation of Endometriosis Using Regenerative Cerium Oxide Nanoparticles. *Nanomedicine* **2013**, *9*, 439–448.

66. Tsoi, K.M.; Macparland, S.A.; Ma, X.Z.; Spetzler, V.N.; Echeverri, J.; Ouyang, B.; Fadel, S.M.; Sykes, E.A.; Goldaracena, N.; Kaths, J.M.; et al. Mechanism of Hard-Nanomaterial Clearance by the Liver. *Nat Mater* **2016**, *15*, 1212–1221.

67. Carvajal, S.; Perramón, M.; Oró, D.; Casals, E.; Fernández-Varo, G.; Casals, G.; Parra, M.; González de la Presa, B.; Ribera, J.; Pastor, Ó.; et al. Cerium Oxide Nanoparticles Display Antilipogenic Effect in Rats with Non-Alcoholic Fatty Liver Disease. *Sci Rep* **2019**, *9*, 1–20.

68. MacCarone, R.; Tisi, A.; Passacantando, M.; Ciancaglini, M. Ophthalmic Applications of Cerium Oxide Nanoparticles. *https://home.liebertpub.com/jop* **2020**, *36*, 376–383.

69. Tisi, A.; Passacantando, M.; Lozzi, L.; Maccarone, R. Cerium Oxide Nanoparticles Reduce the Accumulation of Autofluorescent Deposits in Light-Induced Retinal Degeneration: Insights for Age-Related Macular Degeneration. *Exp Eye Res* **2020**, *199*, 108169.

70. Falchi, L.; Galleri, G.; Dore, G.M.; Zedda, M.T.; Pau, S.; Bogliolo, L.; Ariu, F.; Pinna, A.; Nieddu, S.; Innocenzi, P.; et al. Effect of Exposure to CeO2 Nanoparticles on Ram Spermatozoa during Storage at 4 °C for 96 Hours. *Reproductive Biology and Endocrinology* **2018**, *16*, 1–10.

71. Luo, J.; Zhu, S.; Tong, Y.; Zhang, Y.; Li, Y.; Cao, L.; Kong, M.; Luo, M.; Bi, Q.; Zhang, Q. Cerium Oxide Nanoparticles Promote Osteoplastic Precursor Differentiation by Activating the Wnt Pathway. *Biol Trace Elem Res* **2023**, *201*, 865–873.

72. Ren, X.; Zhuang, H.; Zhang, Y.; Zhou, P. Cerium Oxide Nanoparticles-Carrying Human Umbilical Cord Mesenchymal Stem Cells Counteract Oxidative Damage and Facilitate Tendon Regeneration. *J Nanobiotechnology* **2023**, *21*.

73. Salvetti, A.; Gambino, G.; Rossi, L.; De Pasquale, D.; Pucci, C.; Linsalata, S.; Degl'Innocenti, A.; Nitti, S.; Prato, M.; Ippolito, C.; et al. Stem Cell and Tissue Regeneration Analysis in Low-Dose Irradiated Planarians Treated with Cerium Oxide Nanoparticles. *Materials Science and Engineering: C* **2020**, *115*, 111113.

74. Gliga, A.R.; Edoff, K.; Caputo, F.; Källman, T.; Blom, H.; Karlsson, H.L.; Ghibelli, L.; Traversa, E.; Ceccatelli, S.; Fadeel, B. Cerium Oxide Nanoparticles Inhibit Differentiation of Neural Stem Cells. *Sci Rep* **2017**, *7*.

75. Manne, N.D.P.K.; Arvapalli, R.; Nepal, N.; Thulluri, S.; Selvaraj, V.; Shokuhfar, T.; He, K.; Rice, K.M.; Asano, S.; Maheshwari, M.; et al. Therapeutic Potential of Cerium Oxide Nanoparticles for the Treatment of Peritonitis Induced by Polymicrobial Insult in Sprague-Dawley Rats. *Crit Care Med* **2015**, *43*, e477–e489.

76. Keller, M.A.; Piedrafita, G.; Ralser, M. The Widespread Role of Non-Enzymatic Reactions in Cellular Metabolism. *Curr Opin Biotechnol* **2015**, *34*, 153.

77. Atkinson, D.E. *Cellular Energy Metabolism and Its Regulation*; Academic Press, 1977; ISBN 9780120661503.

78. Gilbert, B.C.; King, D.M.; Thomas, C.B. Radical Reactions of Carbohydrates. Part 2. An Electron Spin Resonance Study of the Oxidation of D-Glucose and Related Compounds with the Hydroxyl Radical. *Journal of the Chemical Society, Perkin Transactions 2* **1981**, 1186–1199.

79. Piedrafita, G.; Keller, M.A.; Ralser, M. The Impact of Non-Enzymatic Reactions and Enzyme Promiscuity on Cellular Metabolism during (Oxidative) Stress Conditions. *Biomolecules* **2015**, *5*, 2101.

80. Gordon, S. Phagocytosis: The Legacy of Metchnikoff. *Cell* **2016**, *166*, 1065–1068.

81. Li, H.; Zhou, X.; Huang, Y.; Liao, B.; Cheng, L.; Ren, B. Reactive Oxygen Species in Pathogen Clearance: The Killing Mechanisms, the Adaption Response, and the Side Effects. *Front Microbiol* **2021**, *11*, 622534.

82. Hunter, J. A Treatise on the Blood, Inflammation, and Gun-Shot Wounds. *Clin Orthop Relat Res* **1794**, *458*, 27–34.

83. Panth, N.; Raj Paudel, K.; Parajuli, K.; Castro, A. Reactive Oxygen Species: A Key Hallmark of Cardiovascular Disease. *Adv Med* **2016**, *2016*, 9152732.

84. Forrester, S.J.; Kikuchi, D.S.; Hernandes, M.S.; Xu, Q.; Griendling, K.K. Reactive Oxygen Species in Metabolic and Inflammatory Signaling. *Circ Res* **2018**, *122*, 877.

85. Barbero, F.; Russo, L.; Vitali, M.; Piella, J.; Salvo, I.; Borrajo, M.L.; Busquets-Fité, M.; Grandori, R.; Bastús, N.G.; Casals, E.; et al. Formation of the Protein Corona: The Interface between Nanoparticles and the Immune System. *Semin Immunol* **2017**, *34*, 52–60.

86. Das, S.; Dowding, J.M.; Klump, K.E.; McGinnis, J.F.; Self, W.; Seal, S. Cerium Oxide Nanoparticles: Applications and Prospects in Nanomedicine. *Nanomedicine* **2013**, *8*, 1483–1508.

87. Collin, B.; Oostveen, E.; Tsyusko, O. V.; Unrine, J.M. Influence of Natural Organic Matter and Surface Charge on the Toxicity and Bioaccumulation of Functionalized Ceria Nanoparticles in Caenorhabditis Elegans. *Environ Sci Technol* **2014**, *48*, 1280–1289.

88. Li, Y.; Fujita, M.; Boraschi, D. Endotoxin Contamination in Nanomaterials Leads to the Misinterpretation of Immunosafety Results. *Front Immunol* **2017**, *8*, 1.

89. Forest, V.; Leclerc, L.; Hochepied, J.F.; Trouvé, A.; Sarry, G.; Pourchez, J. Impact of Cerium Oxide Nanoparticles Shape on Their in Vitro Cellular Toxicity. *Toxicology in Vitro* **2017**, *38*, 136–141.

90. Ji, Z.; Wang, X.; Zhang, H.; Lin, S.; Meng, H.; Sun, B.; George, S.; Xia, T.; Nel, A.E.; Zink, J.I. Designed Synthesis of CeO 2 Nanorods and Nanowires for Studying Toxicological Effects of High Aspect Ratio Nanomaterials. *ACS Nano* **2012**, *6*, 5366–5380.

91. Krug, H.F.; Krug, H.F. Nanosafety Research—Are We on the Right Track? *Angewandte Chemie International Edition* **2014**, *53*, 12304–12319.

92. Casals, E.; Gusta, M.F.; Piella, J.; Casals, G.; Jiménez, W.; Puntes, V. Intrinsic and Extrinsic Properties Affecting Innate Immune Responses to Nanoparticles: The Case of Cerium Oxide. *Front Immunol* **2017**, *8*, 264030.

93. Casals, E.; Zeng, M.; Parra-Robert, M.; Fernández-Varo, G.; Morales-Ruiz, M.; Jiménez, W.; Puntes, V.; Casals, G.; Parra-Robert, M.; Fernández-Varo, G.; et al. Cerium Oxide Nanoparticles: Advances in Biodistribution, Toxicity, and Preclinical Exploration. *Small* **2020**, *16*, 1907322.

94. Röhder, L.A.; Brandt, T.; Sigg, L.; Behra, R. Influence of Agglomeration of Cerium Oxide Nanoparticles and Speciation of Cerium(III) on Short Term Effects to the Green Algae Chlamydomonas Reinhardtii. *Aquatic Toxicology* **2014**, *152*, 121–130.

95. Ernst, L.M.; Casals, E.; Italiani, P.; Boraschi, D.; Puntes, V. The Interactions between Nanoparticles and the Innate Immune System from a Nanotechnologist Perspective. *Nanomaterials 2021, Vol. 11, Page 2991* **2021**, *11*, 2991.

96. Fda; Cder; Yeaton; Ayse Drug Products, Including Biological Products, That Contain Nanomaterials - Guidance for Industry.

97. Pauling, L. Vitamin C and the Common Cold. *Can Med Assoc J* **1971**, *105*, 448.

98. Steinhubl, S.R. Why Have Antioxidants Failed in Clinical Trials? *American Journal of Cardiology* **2008**, *101*, S14–S19.

99. Murphy, M.P.; Bayir, H.; Belousov, V.; Chang, C.J.; Davies, K.J.A.; Davies, M.J.; Dick, T.P.; Finkel, T.; Forman, H.J.; Janssen-Heininger, Y.; et al. Guidelines for Measuring Reactive Oxygen Species and Oxidative Damage in Cells and in Vivo. *Nat Metab* **2022**, *4*, 651–662.

100. Buettner, G.R. The Pecking Order of Free Radicals and Antioxidants: Lipid Peroxidation, α-Tocopherol, and Ascorbate. *Arch Biochem Biophys* **1993**, *300*, 535–543.

101. Krumova, K.; Cosa, G. Overview of Reactive Oxygen Species. **2016**, 1–21.

102. Pryor, W.A. Oxy-Radicals and Related Species: Their Formation, Lifetimes, and Reactions. *https://doi.org/10.1146/annurev.ph.48.030186.003301* **2003**, *VOL. 48*, 657–667.

103. Forman, H.J.; Zhang, H. Targeting Oxidative Stress in Disease: Promise and Limitations of Antioxidant Therapy. *Nature Reviews Drug Discovery 2021 20:9* **2021**, *20*, 689–709.

104. Bienert, G.P.; Chaumont, F. Aquaporin-Facilitated Transmembrane Diffusion of Hydrogen Peroxide. *Biochimica et Biophysica Acta (BBA) - General Subjects* **2014**, *1840*, 1596–1604.

105. Lennicke, C.; Cochemé, H.M. Redox Metabolism: ROS as Specific Molecular Regulators of Cell Signaling and Function. *Mol Cell* **2021**, *81*, 3691–3707.

106. M Davies, A.; G Holt, A. Why Antioxidant Therapies Have Failed in Clinical Trials. *J Theor Biol* **2018**, *457*, 1–5.

CHAPTER 2

SYNTHESIS AND PHYSICOCHEMICAL PROPERTIES OF CeO_2 NANOPARTICLES

“The more closely you look at one thing, the less closely can you see something else.”

Werner Heisenberg

Chapter 2

Synthesis and Physiochemical Properties of CeO_2 Nanoparticles

2.1 Introduction

NP fate belongs to NP pharmacokinetics, the branch of pharmacology that studies drug ADME. NP pharmacokinetics significantly differs from those of the traditional small molecules, and thus emerges the need to create new tools and concepts to assess NP evolution and fate inside the body. Factors such as size, shape, surface state, and aggregation state, significantly influence the biodistribution, degradation, transformations, and excretion profiles of CeO_2 NPs, thereby affecting their therapeutic potential and safety.

This entails understanding how the physiochemical properties of the material determine the nano-bio interface and consequently their efficiency and safety. This crucial preliminary investigation serves as the foundation for gaining a comprehensive understanding of how NPs behave within biological systems. This chapter explores the fundamental importance of elucidating these aspects, laying the groundwork for subsequent discussions on the translation of NP technologies in biomedical applications.

Besides, the safety of engineered NPs is one of the most extensively addressed issues in the context of nanotechnological development and applications. Two paramount considerations are essential for designing safe NPs: the morphology and surface characteristics, determined by their synthesis, and NP transformations when dispersed in biological media.

Synthesis routes will determine the physicochemical features of NPs, encompassing size, shape, surface state (charge and hydrophilicity), and composition. These features

significantly impact the quality of NPs, influencing parameters such as biocompatibility, stability, and potential toxicity. These parameters depend on the intended use and will be determined by the precursor, solvent, and stabilizing agents or surfactants employed during the synthesis process. The presence of contaminants or toxic remnants after synthesis can wield considerable influence over the biological efficacy of the resultant product. A thorough understanding of the most likely by-products, and especially those with pronounced implications for the intended application, is imperative to guarantee their exclusion. Take, for instance, the biologically potent endotoxins, also known as lipopolysaccharides (LPS). These contaminants, originating from the cell membrane of Gram-negative bacteria, are notorious for their potent inflammatory activity and significant impact on the immune system. Moreover, endotoxins are thermoresistant, making them resilient to routine sterilization methods and thus ubiquitous in the environment, including chemicals and glassware used in laboratories [1]. It is highly advisable to consistently assess their presence, ensuring quality control.

Furthermore, the optical properties of nanomaterials differ from those of their bulk counterparts, due to their unique interactions with photons. This distinction allows for the use of characterization techniques based on fundamental principles of physics and chemistry, that provide valuable information about the structure, composition, and properties of the material while allowing for real-time monitoring. Emphasis on adequate and extensive characterization of the material at all stages is essential, as well as the understanding of a material's intended use and application.

NPs may suffer transformations when travelling through different parts of the body, altering their biological identity and behaviour. Understanding the precise evolution of NPs inside the body is essential for their development as medical tools. Upon administration, NPs must overcome different biological barriers before reaching their destination, while they experience processes that transform them towards more stable thermodynamic states, including aggregation, corrosion, dissolution, and interactions with proteins and molecules dispersed in the medium. Indeed, these are strategies to minimize their high surface energy, commonly observed in nature and extensively studied in geochemistry, where a NP is an intermediate state between a micrometric

particle and dissolved ions. These transformations can lead to NP deactivation, while the formation of aggregates or released species can be toxic. Therefore, it is of vital importance to predict the fate of NP in biological media.

In brief, the first natural barrier NPs encounter are biological fluids like blood, lymph, sweat, or tears, and the corresponding extracellular matrix, composed of biological molecules and minerals. These components vary across tissues, compartments, and health conditions [2], potentially promoting NP aggregation and/or corrosion. This occurs because blood and physiological fluids are rich in salts, causing NPs stabilized by electrostatic repulsion to rapidly aggregate in these highly electrolytic media. As a result, large aggregates (hundreds of nanometres) form and sediment, hindering further dispersion. Additionally, proteins in the media will interact with the NP surface. In this case, protein concentration is critical as high protein concentrations will lead to steric stabilization of NPs, while low protein concentrations will lead to agglomeration and aggregation of NPs and proteins [3], a phenomenon known as heteroaggregation. Finally, NPs can undergo chemical transformations, as in the common case of corrosion (reactive chemical dissolution), leading to NP dissolution and the corresponding release of their constituents. These three events – aggregation, interactions with biological components, and chemical transformations– typically coexist, and their rates depend on both NP characteristics and medium composition [4].

The second natural barrier the NPs will encounter, in contrast to small molecules, is the immune system. It is important to note that the immune system can detect molecular and cellular structures with a spatial resolution of a few nanometers. This sensitivity enables the recognition of molecular patterns expressed in a great variety of pathogens, including viral and bacterial proteins, as well as bacterial nucleic acid sequences [5] ranging from a few nanometres to a few hundred nanometres, as colloidal NPs, suggesting an intense interaction between both. Thus, NPs can be recognized or pass undetected by the immune system. Once detected, they can be tolerated or induce defensive (inflammatory) or anti-inflammatory responses. The various immune responses induced by NPs have been recently reviewed and published [6] and can be found in Annex C section 7.3.1. In summary, NPs with poor solubility, large sizes, and cationic charges at the surface or hydrophobic moieties are rather immunogenic, while

small, negatively charged, and highly soluble NPs are relatively undetected and tolerated by the immune system. If NPs are recognized as foreign substances when entering the body, the immune response can diminish their plasma half-life, decreasing their efficiency in targeting different organs. Ideally, NPs should be designed to evade the immune system, allowing for penetration into the different body tissues, unless the target of the NP is the immune system itself.

As a third barrier, the microstructure of blood vessels and tissue also strongly determines NP biodistribution and excretion. Natural barriers restrict the free movement of large molecules or particles. The size of pores in capillaries determines the transit of NPs, but other factors like surface charge also play a role. Typically, NPs with hydrodynamic radii smaller than 6 nm are rapidly excreted through the urine, while those with radii between 6 and 200 nm are readily filtered in the liver. Larger NPs are directly managed by the immune system in blood or lymph and often accumulate in organs such as the liver, spleen, or lung [7].

Summarizing, in the medical field, when considering the application of inorganic NPs, it is essential to understand the processes affecting NP pharmacokinetics. Initially, the synthetic approach will define their physicochemical properties, but as synthesis conditions differ from physiological mediums, NP will suffer transformations directed to lower their surface energy, and this is typically achieved by aggregation, corrosion, and/or interaction with biological molecules. These transformations play a crucial role in shaping the behaviour and fate of NPs within biological systems.

2.2 Scope of the study

The main objective of the study was to design and develop efficient CeO_2 NPs by controlling NP physicochemical properties. This objective involved different aspects: (i) NP synthesis, characterization, and functionalization, (ii) the evaluation of NP efficacy and therapeutic power, and (iii) the study of its potential hazard and risk assessment. All this is directed to assess their potential and weaknesses for future translation to the clinics.

2.3 Results and Discussion

2.3.1 Development and characterization of CeO_2 NPs

It is well known that the redox properties of nanoceria are closely linked to its crystal structure, which, in turn, depends on the synthesis process. Developing high-quality CeO_2 NPs for medical applications involves a clear understanding of the chemical activity of CeO_2. This activity is fundamentally determined by its electronic structure, which is inherently supported by its crystal lattice.

The surfaces of rare earth nanocrystals containing oxygen vacancies hold promise for electron exchange processes. These materials are ideal candidates due to their unique electronic properties, which are influenced by the presence of f-orbitals. cerium exhibits partially filled 4f and 5d subshells of electrons, allowing it to exist either in the 3+ (more reduced) or 4+ (more oxidized) state [8]. CeO_2 crystallises in the cubic fluorite structure (face-centred cubic; fcc), where each cerium atom is surrounded by eight oxygen anions and each oxygen atom occupies a tetrahedral position [9]. It is common to observe a notable concentration of intrinsic defects within the CeO_2 structure, involving a portion of cerium existing in the Ce^{3+} valence state (with unpaired f electrons), linked to oxygen vacancies. This phenomenon can be understood as oxygen being liberated by the reduction of Ce^{4+} to Ce^{3+} and oxygen being reabsorbed during re-oxidation into Ce^{4+}, corresponding to the creation and annihilation of an oxygen vacancy. The presence of crystal defects induces an excess of positive charges that are compensated by crystal expansion [10]. However, despite extensive spectroscopic, microscopic, and diffraction studies, a detailed atomic-level understanding of the local defect structure, defect mobility and clustering, and cerium ion valence remains elusive.

Interestingly, CeO_2 exhibits a high energy requirement for structural rearrangements within its crystal lattice, rendering it highly tolerant to structural defects. This Ce^{4+}/Ce^{3+} duality, along with the stable crystal structure, permits the electron exchange responsible for free radical scavenging, and is crucial for NP regeneration, enabling NPs to act catalytically rather than merely as a reagent.

Understanding the chemistry of CeO_2 NPs permits to design of more effective antioxidant substances. Increasing the number of crystal defects (Ce^{3+}) enhances the catalytic activity of nanoceria, as cerium oxidation within the crystal structure is much faster than reduction[1] [11]. Additionally, oxygen vacancies are crucial for the binding of catalytically active species to ceria [12]. Finally, as Ce^{3+} ions are soluble in water, the higher the Ce^{3+} concentration the more biodegradable (unstable) the NP. One approach to increase crystal defects is to tune NP size, as the number of Ce^{3+} ions increases with decreasing the NP size [13,14], reaching maximum capacity and thermodynamic stability at diameters between 2-5 nm [9]. Other studies state that it's not merely the number of oxygen vacancies (Ce^{3+}), but also their arrangement, meaning that oxygen vacancy clusters have been shown to facilitate oxygen migration, enhancing reduction capacities [11]. However, creating these favourable defects and understanding their roles in the reducibility and activity of nanoceria at the atomic level is still challenging.

2.3.1.1 Synthesis

Over the years, within our group, the synthesis of CeO_2 NPs has been developed and optimized to produce monodisperse, reproducible, and stable NP formulations, which has been followed by a thorough characterization of the NPs in both synthetic and biological settings. This process has provided comprehensive insights, correlating their effectiveness with specific characteristics. Efforts have also been made to mitigate any potential undesired toxicities associated with their usage.

To ensure precise control over the final product, understanding the underlying thermodynamics that govern the synthesis process is essential. This synthesis relies on the behaviour of elements and compounds in different redox states under varying conditions. This can be summarized in a Pourbaix diagram, a graphical representation used in electrochemistry that predicts the stability of different chemical species in a system as a function of the electrode potential (E°) and solution pH. Therefore, by manipulating the chemical environment of cerium ions, we can obtain CeO_2 NPs.

[1] Reduction to Ce^{3+} leads to crystal defects (oxygen vacancies) that induce crystal tensions, which are energetically unfavourable.

CeO_2 NPs are synthesized by basic precipitation of cerium (III) salt using a classical hydrothermal approach. In brief, an aqueous solution containing Ce^{3+} cations is prepared. Raising the pH of the solution via the addition of an alkaline solution facilitates the oxidation of Ce^{3+} cations to Ce^{4+} by dissolved oxygen, as depicted in the Pourbaix diagram of cerium in water (**Figure 2.1**). Since the Ce^{4+} cations are insoluble in water, they precipitate out of the solution with oxygen, forming crystals, which can achieve nanoscale dimensions under carefully controlled precipitation conditions. Furthermore, the NP formation is influenced by adjusting reaction parameters such as the concentration ratio of cerium precursor to base, the choice of base counterion, temperature, or the use of stabilizing agents, among others. These factors can significantly impact their suitability for various applications.

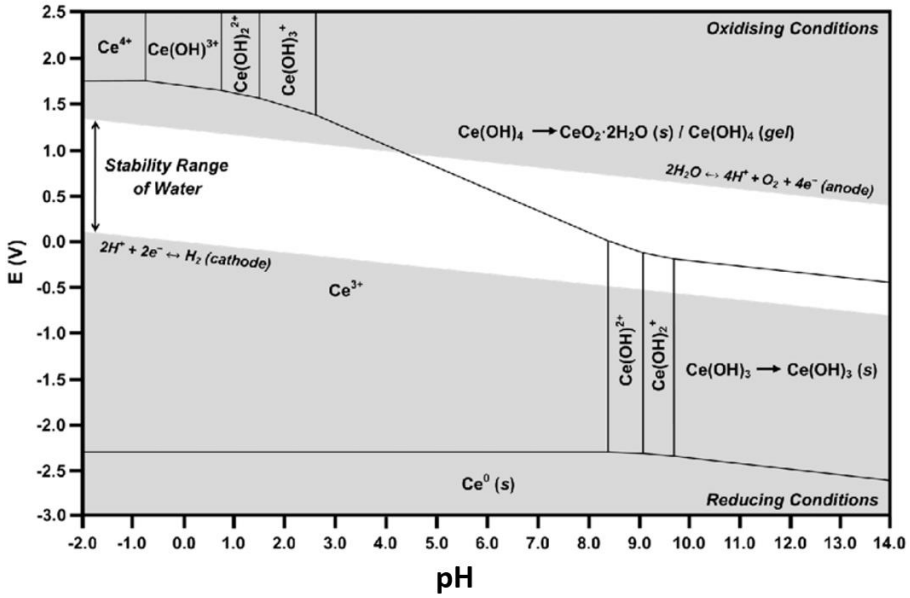


Figure 2.1. Calculated Pourbaix diagram for Ce-H_2O. Reproduced from [15].

Next, the optimized synthesis process will be presented, along with a discussion on some relevant parameters for NP formulation. The synthesis process induces changes in the absorption spectra of the NPs, altering the appearance of the colloid. Thus, the synthetic process can be monitored by UV-vis absorption spectra analysis, as shown in **Figure 2.2**.

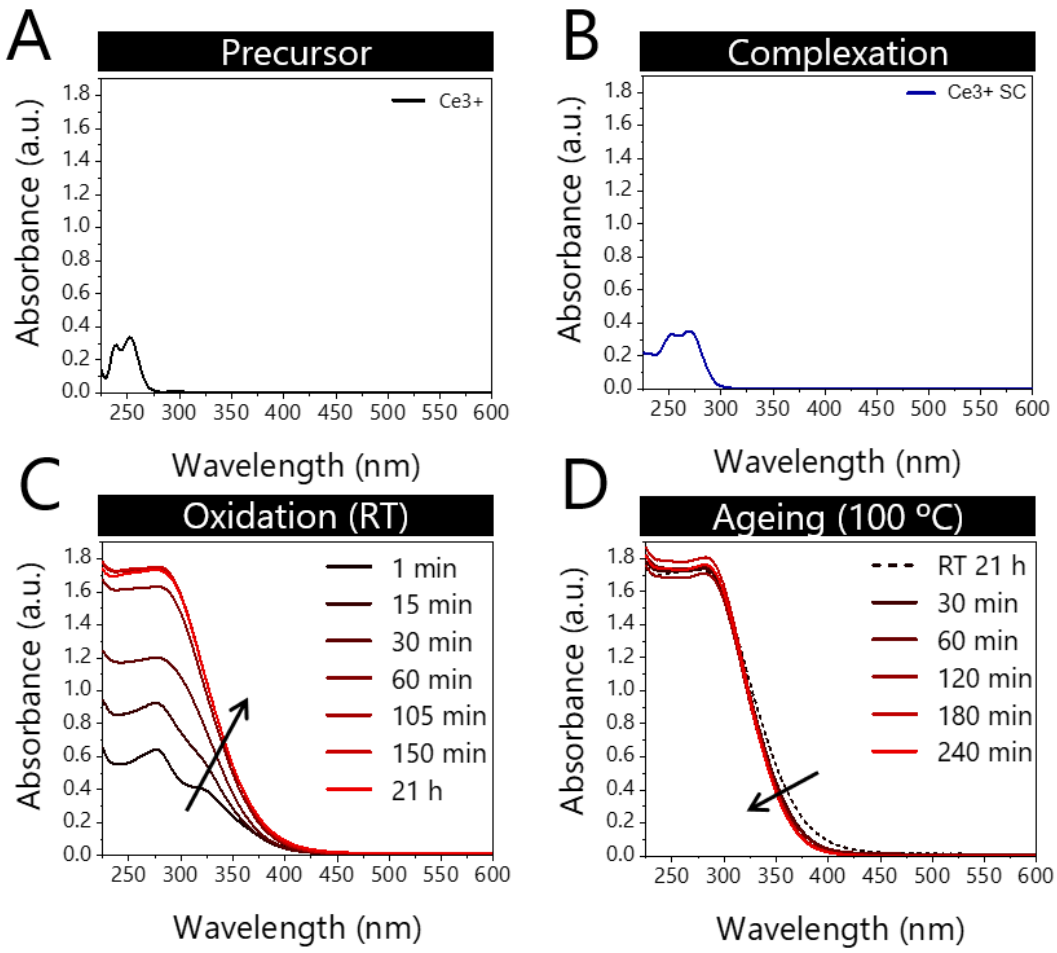


Figure 2.2. Time-evolution of the UV-vis absorption spectra of cerium during synthesis. (A) UV-vis absorption spectra of the Ce^{3+} precursor, corresponding to $CeCl_3$ dissolved in water, (B) complexation of Ce^{3+} with the stabilizing agent, sodium citrate. (C) Time-evolution of Ce^{3+} oxidation to Ce^{4+} after base addition, and (D) time-evolution of NPs during ageing (thermal treatment).

The synthesis begins with the mixture of $CeCl_3 \bullet 7\ H_2O$ precursor (Ce^{3+}) and sodium citrate (SC) in a 1:2 molar ratio, facilitating the formation of the $[Ce(SC)_2]^{3-}$ complex (**Figure 2.2AB**). The role of SC is relevant to (i) control the precipitation of Ce^{4+} and (ii) stabilize the NP surface as soon as it is formed, which will be further discussed later. Following the formation of the complex, tetramethylammonium hydroxide (TMAOH) is added as a base in a 1:2.7 molar ratio, raising the solution's pH to 11-11.5. This initiates the slow oxidation of the Ce^{3+} to Ce^{4+}, discernible in the UV-vis spectra as an increase in light absorption corresponding to NP formation (**Figure 2.2C**). Subsequently, the ageing step takes place, which entails subjecting the NP solution to thermal treatment at 100 ºC for a minimum of 3 hours. This process results in a reduction in the slope of the CeO_2 absorption spectra, indicative of changes in crystal arrangements (**Figure 2.2D**).

2.3.1.2 Synthesis Characterization

Once synthesis is complete, extensive characterization of the material is conducted, which is indispensable to control the material propertiesError! Reference source not f ound.**.** An overview of the principles underlying the employed characterization techniques can be found in Chapter 5, Section 5.3.1. Morphology and size distribution analysed by high-angle annular dark-field scanning transmission microscopy (HAADF-STEM) and high-resolution transmission electron microscopy (HR-TEM) (**Figure 2.3ABCD**) indicate the formation of non-aggregated 2.5 ± 0.5 nm spherical nanoceria particles of high uniformity and narrow size distribution (**Figure 2.3E**).

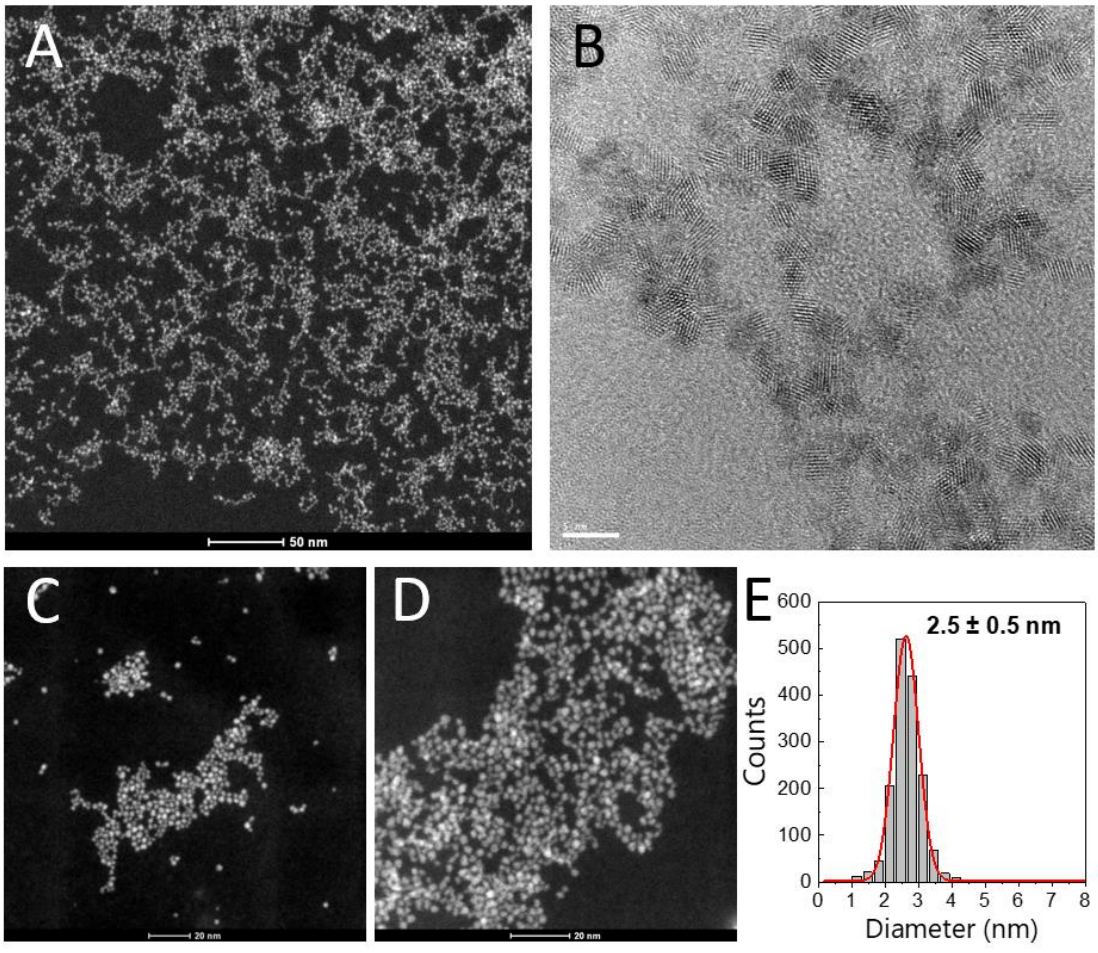


Figure 2.3. Characterization of CeO_2 NPs by microscopy. (A, C, D) Representative HAADF-STEM images. Scale bars are 50, 20, and 20 nm, respectively. (B) HRES-TEM image. Scale bar 5 nm. (E) Size distribution of CeO_2 NPs.

The X-ray diffraction patterns (XRD)[2] of the NPs confirm that the sample displays a pure fluorite single-phase (fcc) crystal structure (**Figure 2.4C**). The broadness of the diffraction peaks indicates an ultra-small crystal size, whereas the Scherrer equation indicates a particle size of 2.9 nm, similar to that obtained from microscopy indicating the existence of single-crystal NPs.

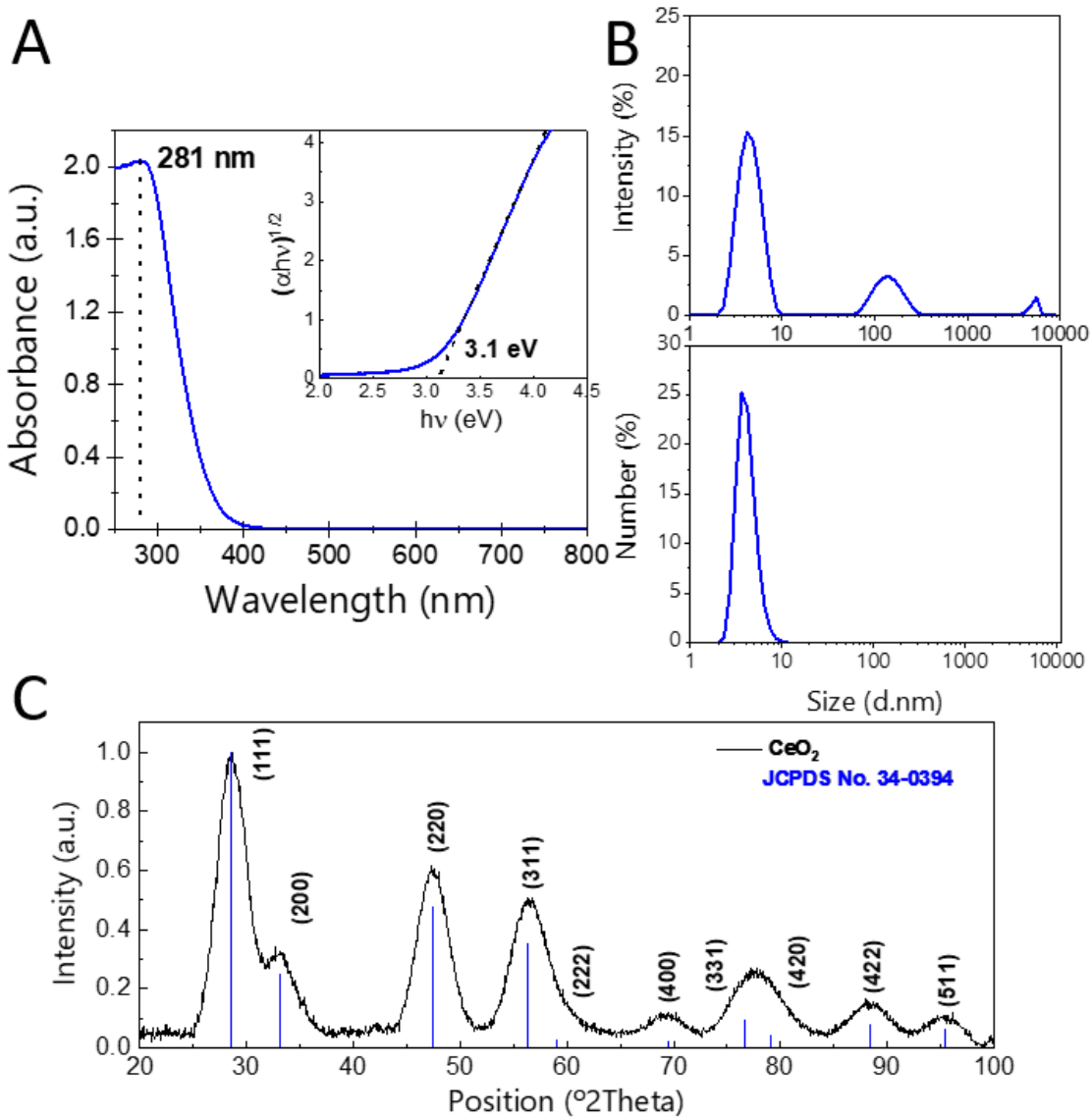


Figure 2.4. CeO_2 NPs characterization. (A) UV-vis spectrum of the CeO_2 NP and optical bandgap energy determined by Tauc equation (insert). (B) The hydrodynamic diameter profile measured by DLS of CeO_2 NPs presented by intensity and number. (C) X-ray diffraction pattern of the as-synthesized nanoceria and JCPDS No. 34-0394 standards.

[2] XRD patterns provide information about the arrangement of atoms within a crystalline material.

The UV-vis spectrum of CeO_2 NPs shows a distinct absorption band at 283 nm, and transparency above 400 nm, also indicating the absence of NP aggregates that would scatter visible light[3]. Moreover, NPs show a characteristic bandgap of 3.1 eV (the bulk is 3.19 eV) (**Figure 2.4A** and inset). As commented above, this reduced bandgap manifests the oxygen vacancies that CeO_2 NPs accumulate at its surface as it decreases in size, and more importantly, these oxygen vacancies (active sites) determine CeO_2 NPs catalytic activity and nanocrystal stability.

The zeta potential indicates that after purification and re-dispersion of nanoceria in 2.2 mM SC, particles are negatively charged (−38.9 ± 16.7 mV, at pH = 8 and a conductivity of 0.33 mS/cm). The hydrodynamic diameter was measured by dynamic light scattering (DLS) and is shown in **Figure 2.4B**, where as-synthesized nanoceria shows monomodal distribution peaking at 3.06 ± 0.76 nm (PDI = 0.35) by number (4.41± 0.76 nm by Intensity).

Finally, the synthesis reaction yield was determined to be 99,6% using Inductively Coupled Plasma Mass Spectrometry (ICP-MS) to measure Ce concentration in both the purified sample and the supernatant. This yields a concentration of CeO_2 NPs of 1.72 mg/mL (10 mM), corresponding to 1.59 x 10^{16} NP/mL, and a total surface area of 4.50x10^{17} nm^2/mL.

As the particles are extremely colloidally stable and cannot be separated by standard centrifugation, the purification process consisted of using a centrifugal concentrator device with a 3 kDa Ultracel® cellulose membrane to separate NP from non-desired synthesis residues, or for media exchange. Long-term storage of synthesized CeO_2 NPs is more stable in the synthesis media due to excess stabilizing compound (citrate) and the pH remaining around 9-10. This pH range is thermodynamically favourable for maintaining Ce^{4+} as the main redox state. However, before use, CeO_2 NPs must be purified and re-suspended in 2.2 mM SC or other biocompatible media. To maintain

[3] NP aggregation broadens the absorption spectrum (absorption of light at multiple wavelengths), typical of bulk materials, where a continuum of energy states and increased degrees of freedom result in a diverse range of energy transitions.

stability during storage, it is advisable to avoid headspace to preserve an inert atmosphere and protect SC from oxidation and degradation. NPs stored for 4 years with headspace showed aggregation, while those stored in an inert atmosphere remained dispersed. Comparing non-purified CeO_2 NPs stored without headspace for 4 years to those stored for 5 months revealed larger aggregates in the older NPs and differences in aggregation kinetics (**Figure 2.5AB**). This is likely due to the degradation of SC over time, underscoring the importance of purification procedures.

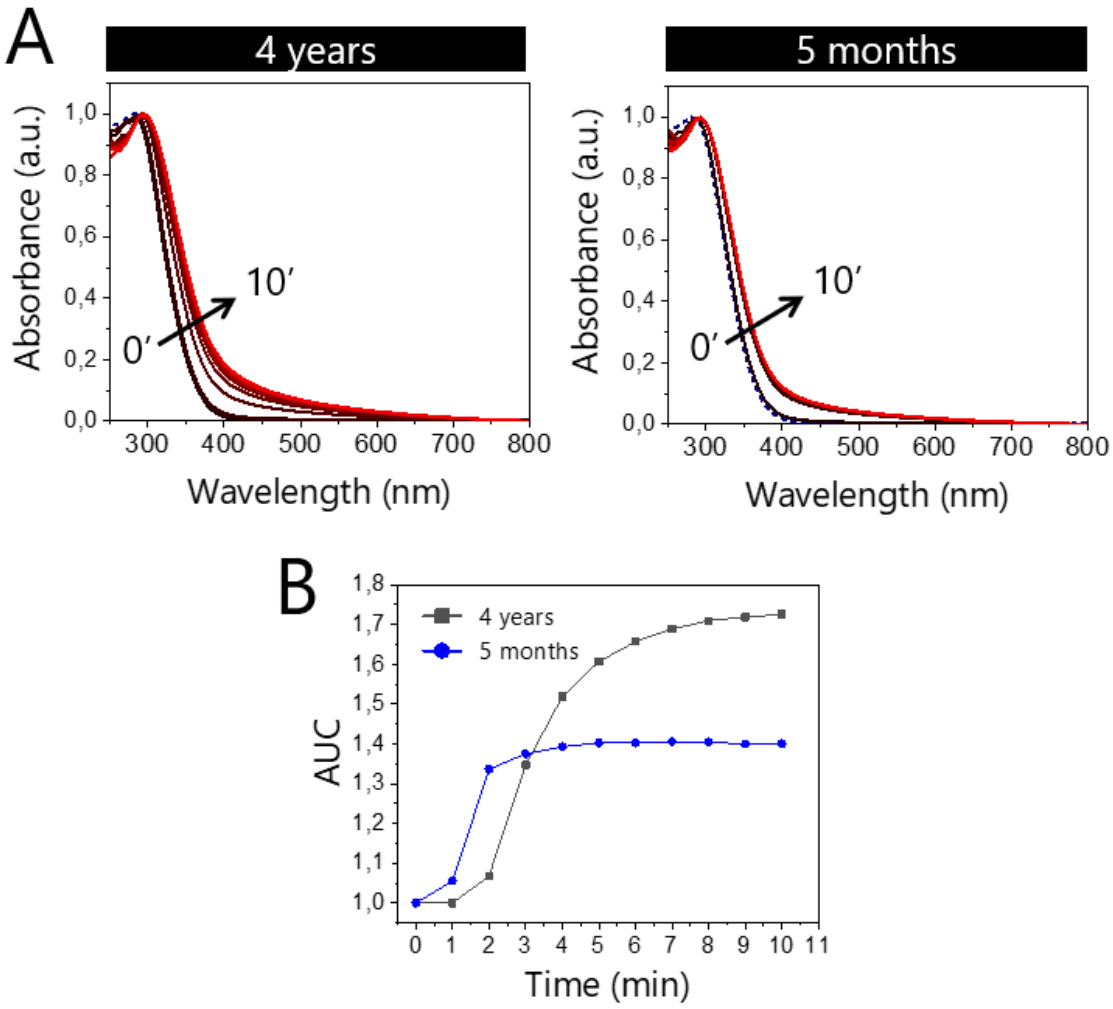


Figure 2.5. Effect of time (ageing) on CeO_2 stability monitored by UV-vis spectroscopy. (A) Absorption spectra comparing two CeO_2 samples of different ages: 4 years vs. 5 months. (B) Normalized Area Under the Curve (AUC) from the UV-vis spectra of CeO_2 NPs aggregation kinetics in cell culture media (DMEM), extracted from (A). UV-vis spectra were recorded every minute for 10 minutes.

2.3.1.2.1 High-Energy Resolution Fluorescence Detected X-ray Absorption Spectroscopy (HERFD-XAS)

To further study the electronic structure of CeO_2 NPs, the conversion of $CeCl_3$ into colloidal CeO_2 NPs was monitored using in situ High-Energy Resolution Fluorescence Detected X-ray Absorption Spectroscopy (HERFD-XAS) at the European Synchrotron Radiation Facilities (ESFR), in collaboration with Prof. Pieter Glatzel. The advantage of using this technique is that the sample set-up allows real-time measurements in liquid media, which is relevant as the electronic structure of CeO_2 NPs has been proven to be very dependent on the environment.

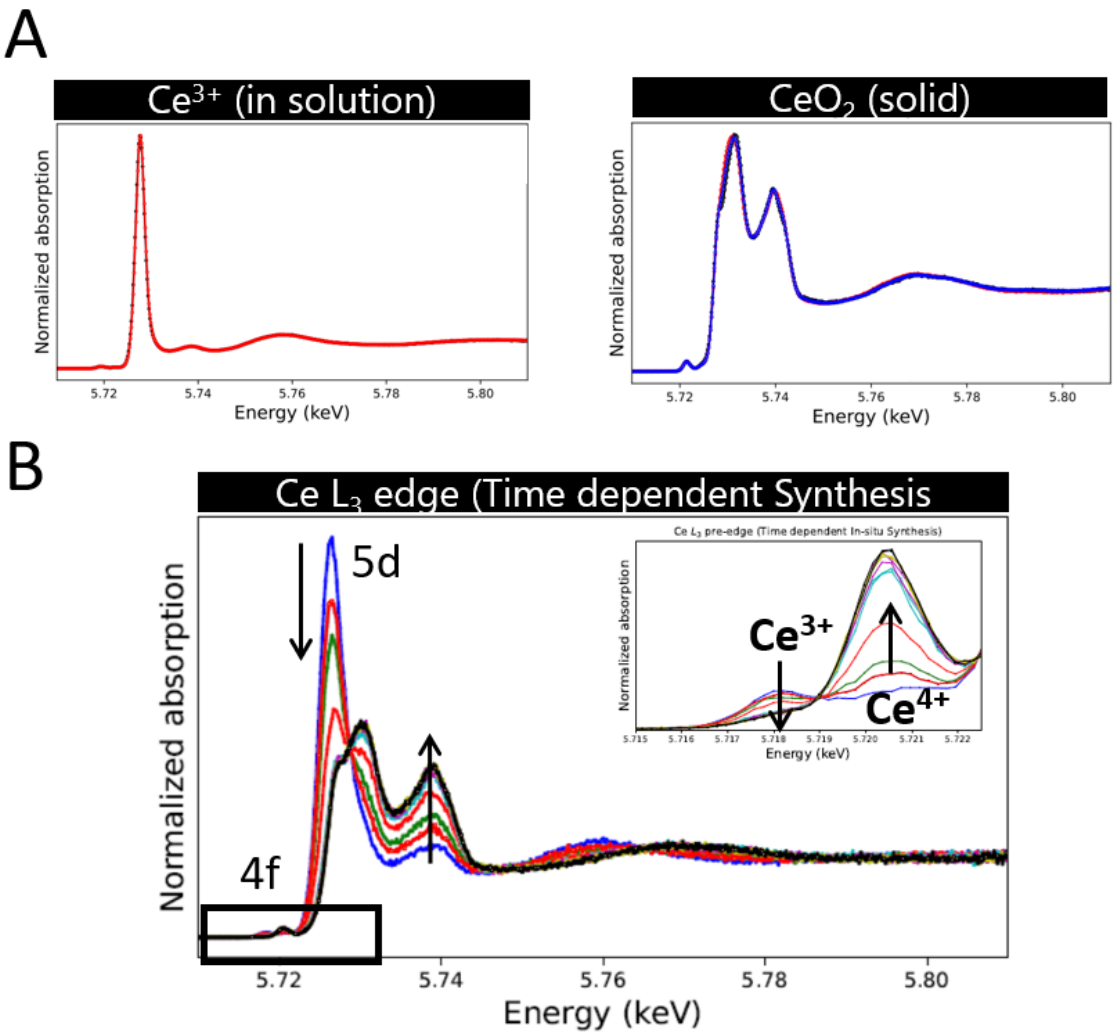


Figure 2.6. XAS spectra of Ce L_3 edge during synthesis of CeO_2. (A) XAS of Ce L_3 Edge for $CeCl_3$ (precursor) and CeO_2 commercial powder solutions used as control. **(B)** Time-dependent high-energy resolution Ce L_3 XAS of. CeO_2 NPs during in-situ synthesis conditions and enlargement of the pre-edge region (insert).

First, X-ray absorption spectra of Ce L_3 edge and pre-edge for the Ce^{3+} ($CeCl_3$ solution) and Ce^{4+} (bulk CeO_2, from a dispersion of CeO_2 commercial powder) are shown in **Figure 2.6A**. **Figure 2.6B** shows HERFD-XAS spectra obtained during the synthesis of CeO_2 NPs. The prominent spectral features are associated with Ce 2p to 5d transitions, whereas the less pronounced pre-edge spectral features (**Figure 2.6B,** insert) can be attributed to Ce 2p to Ce 4f transitions, probing the Ce 4f and 5d orbitals. The initial spectrum recorded during NP synthesis corresponds to the $CeCl_3$ precursor, exhibiting a distinct intense blue line characteristic of the Ce^{3+} ion. Upon the introduction of the oxidizing agent, TMAOH, the intensity of the precursor peak gradually diminishes, while new peaks emerge and intensify over time. Furthermore, the broadness of the peak of the Ce 5d is attributed to smaller particle sizes, as showed in previous studies [10], and explained by an increase of surface to bulk ratio. Moreover, peak broadness can be attributed to lattice expansion, which correlates to a decrease in Ce^{4+} within the NP surface, leading to excess charges on the surface of the NP.

2.3.1.3 Relevant Synthesis Parameters

2.3.1.3.1 The precursor

In general, $Ce(NO_3)_3$ salt has been commonly used as a precursor for NP synthesis [16–19]. However, in this study, $Ce(NO_3)_3$ was substituted by $CeCl_3$ due to different advantages. Nitrate-based salts possess challenges for pharmaceutical translation due to the potential formation of nitrosamines, which can be toxic. Consequently, concerns regarding Good Manufacturing Practices (GMP) have been raised by regulatory agencies such as the FDA [20] and the European Medicines Agency (EMA) [21].

Secondly, chloride salts exhibit higher transparency within the UV-vis region, enabling better data interpretation. (**Figure 2.7**). Moreover, it has been demonstrated that ceria nanorods synthesized using $CeCl_3$ as a precursor exhibit increased catalytic sides (oxygen vacancies) compared to those synthesized using $Ce(NO_3)_3$ [11]. However, this has not been investigated yet in our spherical CeO_2 NP.

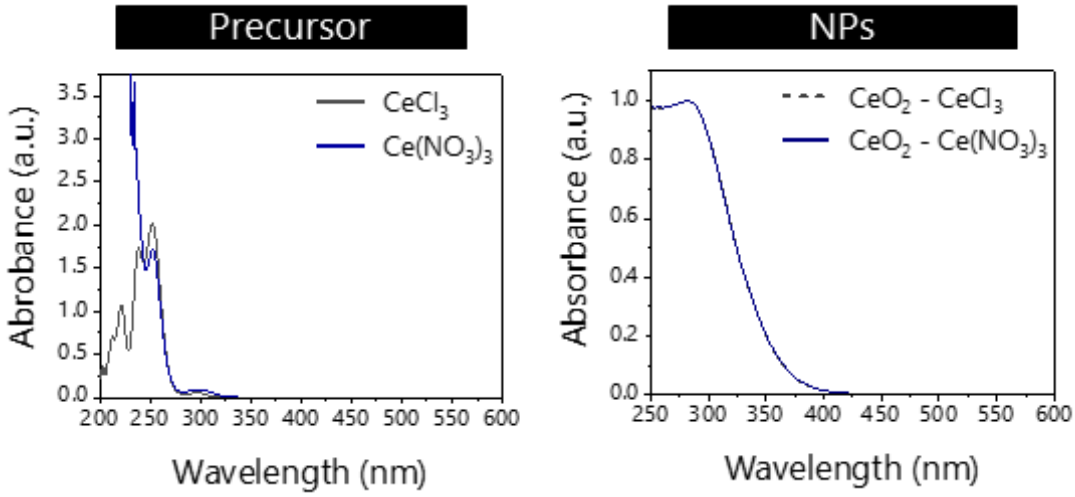


Figure 2.7. Comparison of the UV-vis signature of different cerium salts. UV-Vis spectra of 10 mM $CeCl_3$ and $Ce(NO_3)_3$ salts dissolved in water (left), and UV-Vis spectra of CeO_2 NPs synthesised either with the chloride or nitrate cerium salt (right).

2.3.1.3.2 The Role of Sodium Citrate (SC)

SC is a determinant for achieving small, non-aggregated NPs acting as a stabilizing agent, which in turn can be replaced if surface functionalization is required. Although not directly involved in the chemical reaction, SC significantly influences the final product, providing precise control over size and a versatile surface chemistry.

When the reaction is performed without SC, NPs irreversibly aggregate as shown by UV-Vis spectroscopy, macroscopically, and by DLS measurements (**Figure 2.8ABC**). This reflects the role of SC in protecting the NP surface through electrostatic repulsions. Furthermore, the complexation of the precursor with citrate results in slower reaction kinetics [4], providing greater size control, which is fundamental in the formation of a high number ($1.59x10^{16}$ NP/mL) of small 2.5 nm NPs with a very narrow distribution. Size distribution analysis of TEM images demonstrates an increase in NP size when produced without SC, with sizes averaging 5.2 ± 0.7 nm (**Figure 2.8D**).

Both NP stabilization and reaction kinetics are essential for synthesis reproducibility, as depicted in **Figure 2.9.**

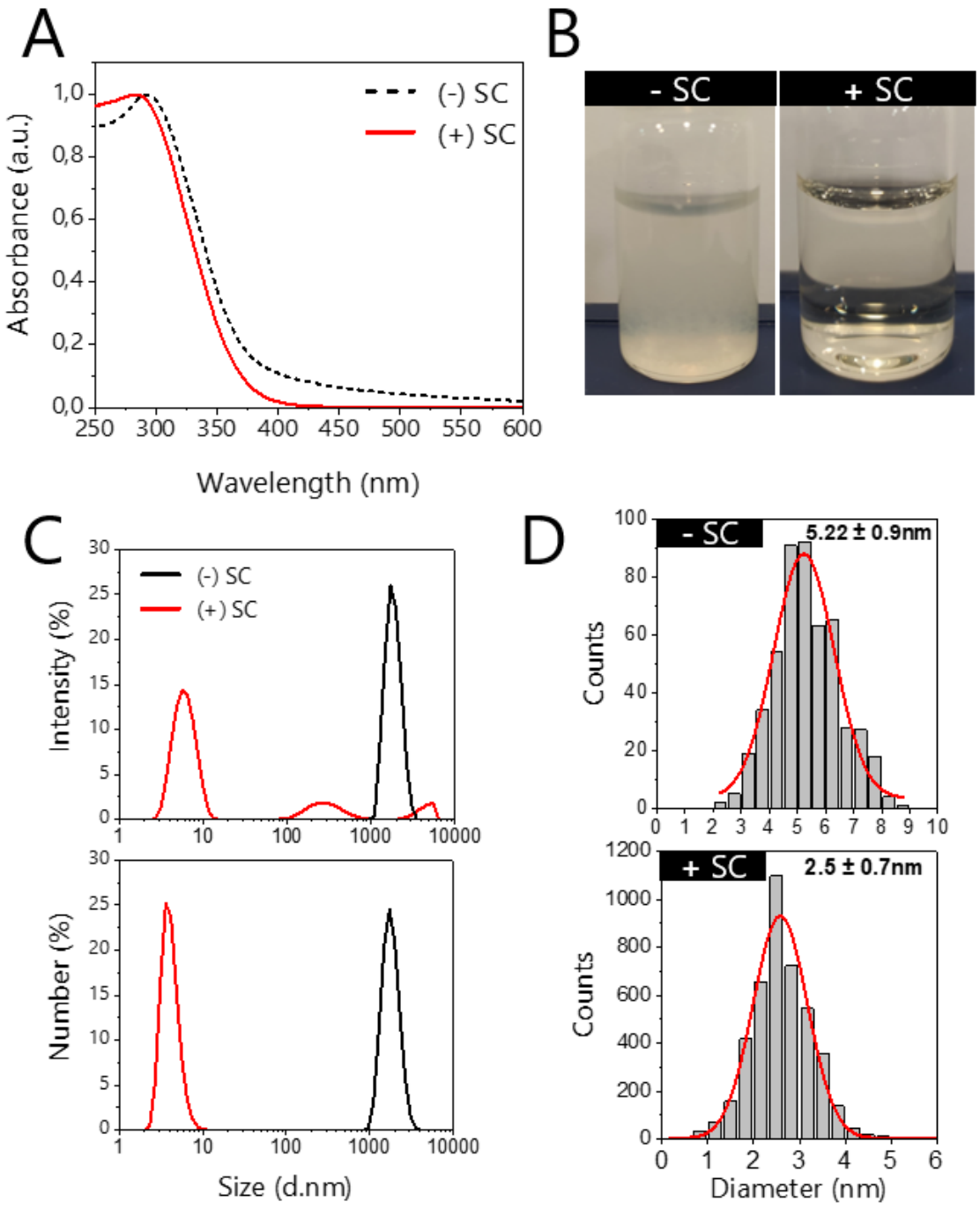


Figure 2.8. The role of sodium citrate (SC) on CeO_2 NPs synthesis and stabilization. **(A)** UV-vis spectrum for CeO_2 NPs with (+) and without (-) SC, and (B) macroscopic appearance. **(C)** Hydrodynamic size (diameter) determined by DLS presented as intensity and number. **(D)** Size distribution analysis of CeO_2 NPs.

Ultimately, the use of SC is relevant in the biological context, given that its pKa values (3.14, 4.76, and 6.4) are lower than physiological pH (around 7.4), being fully deprotonated, providing charge for interaction with the NP surface. For instance, gallic acid, despite its comparable size and number of functional groups, will become more

protonated at physiological pH. This results in reduced interaction with the NP, consequently promoting the aggregation of CeO_2 NPs in 1x PBS medium as illustrated in **Figure 2.10Error! Reference source not found.**.

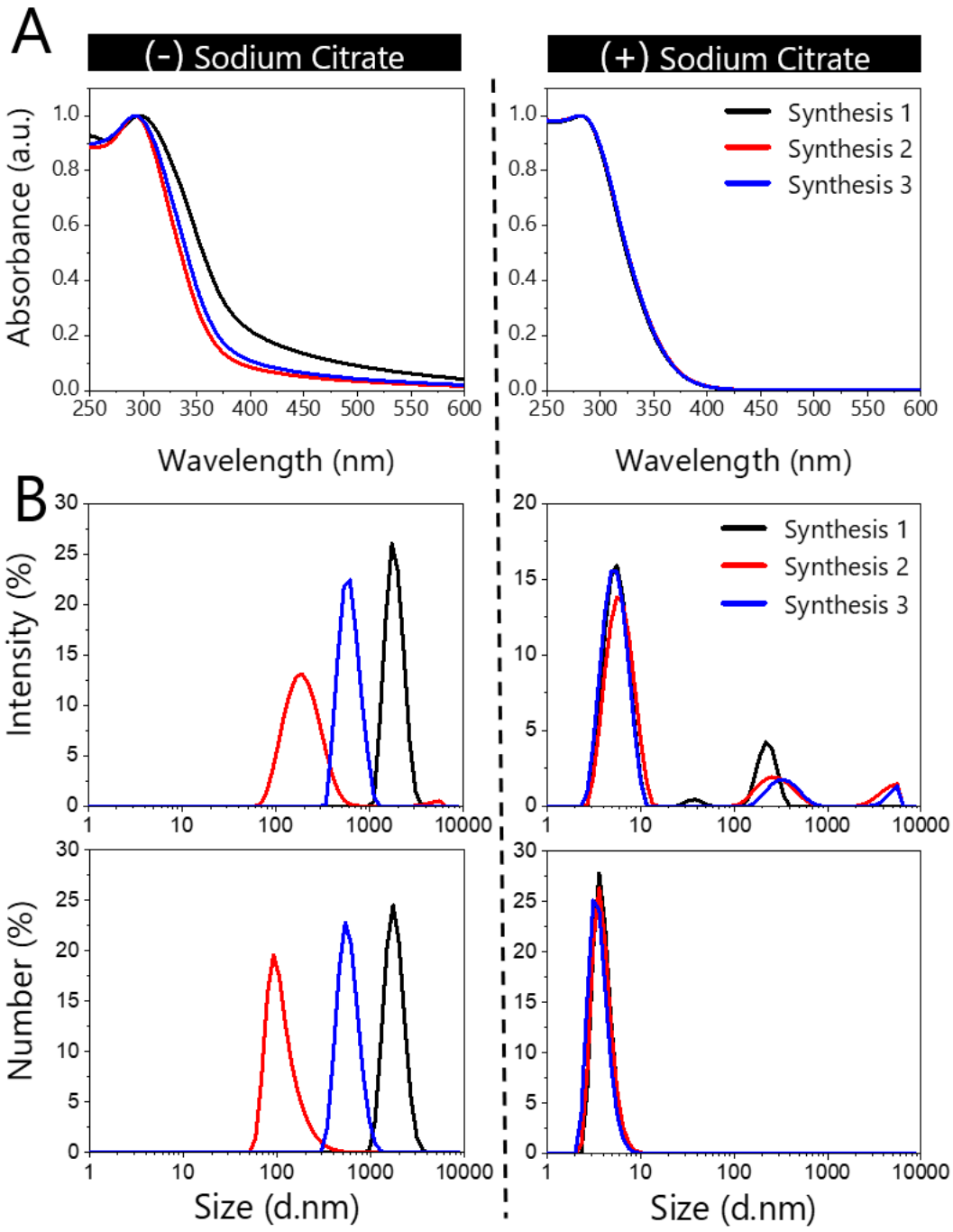


Figure 2.9. Comparison of CeO_2 synthesis reproducibility with and without SC as determined by (A) UV-vis spectroscopy and (B) hydrodynamic diameter presented by Intensity and Number.

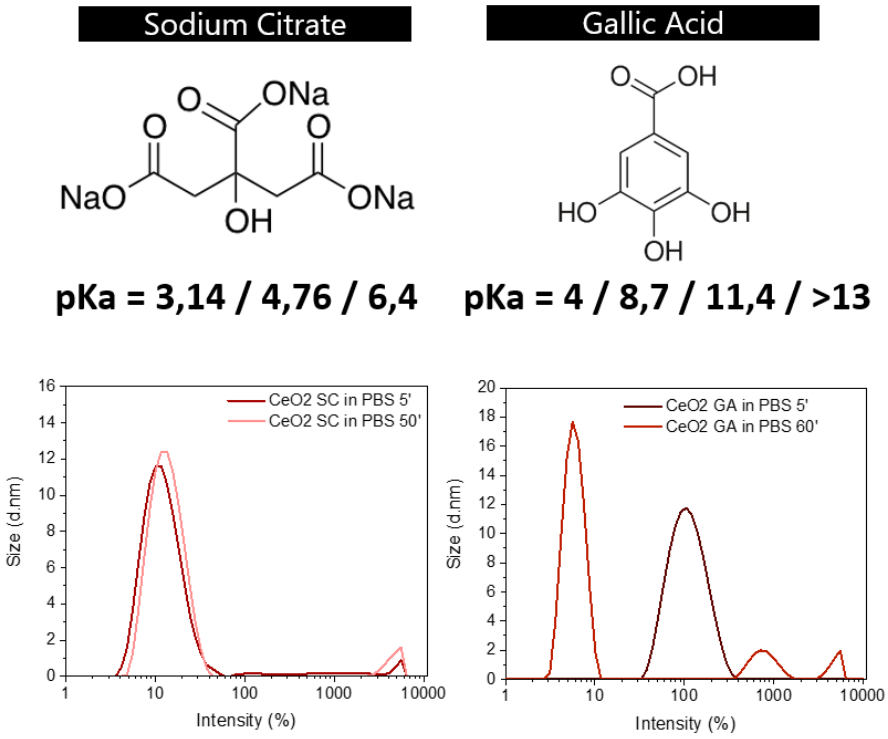


Figure 2.10. Time evolution of intensity size distribution measured by DLS of 0.5 mg/mL CeO_2 NPs conjugated to 5 mM SC (left) or 5 mM gallic acid (right) in 1X PBS solution.

2.3.1.3.3 Ageing: Crystal refinement

A critical factor influencing the performance and stability of CeO_2 NPs is their ageing process, crucial for developing a stable and well-defined product. This process facilitates the NPs to reach a thermodynamic equilibrium, resulting in enhanced stability.

Following the oxidation process and concurrent NP formation, the UV-vis spectra of CeO_2 NPs slowly evolve, as evidenced by an increased slope of the CeO_2 absorption peak, similar to changes observed during the thermal treatment process (**Figure 2.11AB**). This indicates that nanocrystal ageing occurs naturally at standard temperature and pressure conditions, as shown by the UV-vis spectra. However, since this process can take up to two months, it can be accelerated by chemical or physical methods. Here, thermal treatment at 100 °C (boiling) for at least 3 hours, shows an acceleration of the process by physical methods.

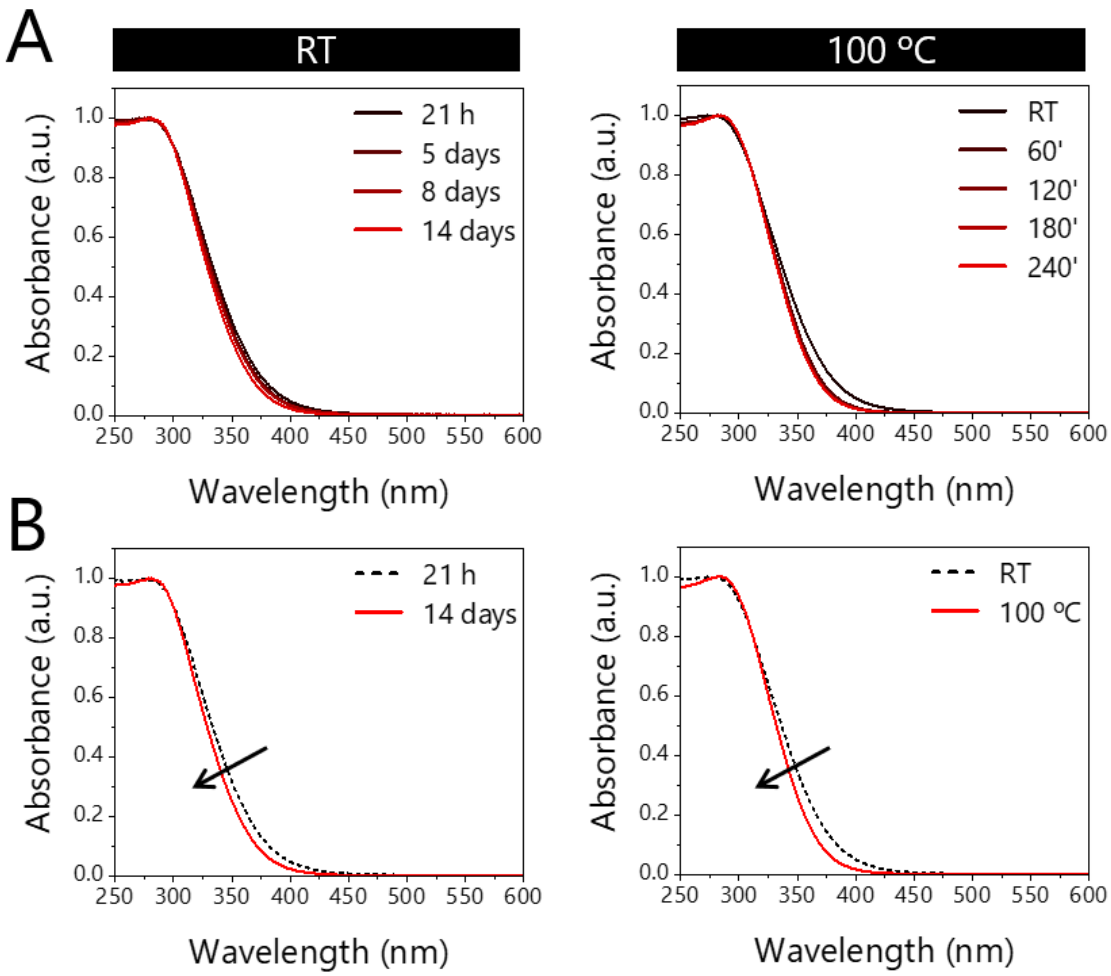


Figure 2.11. Comparison between ageing of CeO_2 NPs at room temperature (RT) vs. 100 °C. (A) Time evolution monitored by UV-vis spectra of CeO_2 NPs kept at RT for 14 days (left) or boiled for 4 hours (right). (B) Comparison between the slope of the first (black scatter line) and the last (red line) UV-vis spectra during the ageing process.

To further investigate this phenomenon, optical band gap[4] energy was calculated from the absorbance spectra following Tauc plot analysis [22]. The results indicate an increase in band gap energy after boiling (thermal treatment), from 2.91 to 3.09 eV (**Figure 2.12**). This increase in band gap energy is associated with a higher Ce^{4+} content within the crystal [23]. The observed optical effect is generated by crystalline

[4] The band gap is the energy difference between the top of the valence band and the bottom of the conduction band. Electrons can transition between bands if they receive the band gap energy. This energy can be determined from the wavelength where absorbance shows a step rise, as it corresponds to the minimum energy required for electron excitation across the band gap.

rearrangement that induces a higher ionic order. This occurs as Ce^{3+} deforms the crystal structure, while an increase in Ce^{4+} content inevitably improves the optical signal by reducing structural defects associated with oxygen vacancies [23].

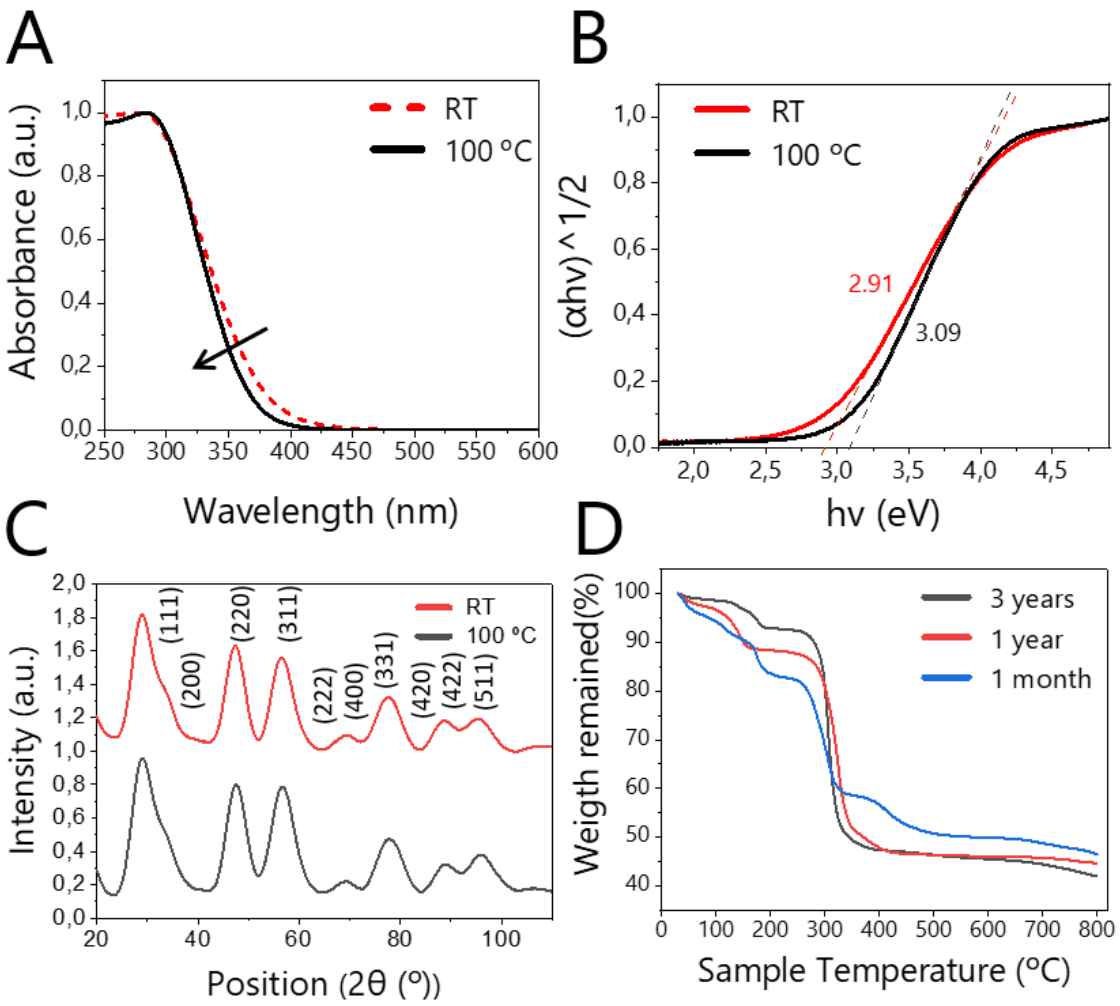


Figure 2.12. Ageing of CeO_2 NPs. (A) Change in the UV-vis slope of CeO_2 NPs after thermal treatment (100 ºC, 4 h), and (B) corresponding band gap calculations by Tauc plot. (C) X-ray diffraction pattern of nanoceria before and after thermal treatment. (D) Thermogravimetric analysis (TGA) of 3 different CeO_2 samples, each representing a different synthesis age: 1 month, 1 year, or 4 years.

XRD pattern before (RT) and after boiling (100°C) was measured and presented in **Figure 2.12C**. The Full Width at Half Maximum (FWHM) values calculated from XRD analysis show significant differences in peak width and relative intensities (**Table 2.1**). These differences indicate changes in the crystalline plane's preferential orientation, suggesting crystal rearrangements. However, the average crystal size, calculated using Scherrer's equation, and the lattice parameter remain unchanged, as shown in **Table 2.2**.

Peak	RT FWHM (Θ)	100°C FWHM (Θ)
(111)	3.7572	3.7107
(220)	3.7521	3.8394
(311)	3.5963	3.6662
(422)	3.7265	3.5316
(511)	4.6207	4.1728

Table 2.1. Calculated FWHM) from XRD data analysis of non-boiled (RT) and boiled (100 ºC) CeO2 NPs samples.

Furthermore, CeO_2 samples aged 1 month, 1 year, and 4 years were analysed to further study the ageing process. Thermogravimetric analysis (TGA) revealed a significant loss of structural water occurring at ~350 ºC in these CeO_2 NPs samples (**Figure 2.12D**).

	RT	100 °C
Crystal Size (d.nm)	2.42 ± 0.19	2.41 ± 0.04
Lattice Parameter (A)	5.4135 ± 0.04	5.4186 ± 0.13

Table 2.2. Calculated Scherrer's Crystal Size and lattice parameter for non-boiled (RT) and boiled CeO_2 NPs samples (100 ºC) from XRD data analysis. The theoretical lattice parameter (standard JCPD) is 5.4113.

The results indicate that "young" CeO_2 NPs (1-month-old) have higher intrinsic water content (the loss of mass at 300°C) compared to older samples. This suggests that particle dehydration occurs over time and may be accelerated by external energy inputs, such as heat. Additionally, the loss of structural water supports an increase in Ce^{4+}

oxidation states within the NP core, as confirmed by UV-vis measurements, thereby enhancing thermodynamic stability. It is well known that the excess electrons left behind by oxygen removal, create localized regions of excess positive charge, and to minimize electrostatic repulsion, adjacent Ce^{3+} ions tend to separate spatially within the crystal lattice, leading to crystal expansion [10,24]. In aqueous environments, thermodynamically unstable oxygen vacancies are suggested to be stabilized through coordination bonds between Ce and molecular and/or dissociated water molecules [25,26]. In this study, the loss of intrinsic water molecules correlates with an increase in Ce^{4+} as shown by UV-vis. Therefore, when Ce^{3+} is oxidized to Ce^{4+}, the water molecules stabilizing the crystal defects are released.

The thermodynamic stability of NPs involves a complex interplay between surface and bulk (core) contributions. While surface electrons may contribute to phenomena related to surface energy minimization, fully coordinated core atoms are more stable in their crystal form, creating a more energetically favourable environment. This suggests that the thermodynamic fate of core atoms within CeO_2 crystals is to oxidise to Ce^{4+}, whereas the atoms at the surface will evolve to minimize their surface energy by aggregation or by reduction to Ce^{3+}, which can be dissolved again in the liquid phase.

In summary, the results suggest that the ageing of CeO_2 NPs promotes particle oxidation, which is correlated to particle dehydration and induces crystal rearrangements necessary for stabilization. The observed increase in band gap energy supports a rise in Ce^{4+} content. Although ageing likely decreases somehow the catalytic activity of the NP, it enhances product stability, which is mandatory for pharmacological development. Additionally, these closed oxygen vacancies will easily form again if the NP environment demands it. Overall, as the behaviour of CeO_2 NPs is influenced by multiple factors and the specific mechanisms involved are complex, further studies are needed.

2.3.2 Stability: Nanoparticle Transformations

NPs can interact with biological systems at the molecular, cellular, and tissue levels, offering opportunities for novel therapeutic and diagnostic applications. However, these interactions are complex and influenced by many factors, including the

physicochemical properties of the NPs, the biological environment, and the dynamic changes that occur over time. Understanding the behaviour of inorganic NPs in biological media is essential for advancing the physical chemistry of inorganic materials as their morphology approaches that of molecular regimes. This knowledge is also crucial for controlling and harnessing the full potential of these materials.

One of the most critical aspects of these interactions is NP instability. The stability of NPs in biological systems is crucial for their function and safety. Understanding the processes that lead to decreased surface energy is pivotal for comprehending the reactivity and associated potential toxicity of NPs. Hence, controlling NP stability is crucial for harnessing their full potential and overcoming hurdles that may arise during synthesis, storage, and use.

The fate of CeO_2 NP in biological systems was explored, focusing on their transformations and interactions at the nano-bio interface. Our investigation provides a comprehensive understanding of the aggregation, corrosion, and protein corona formation (surface chemistry) of CeO_2 NPs.

2.3.2.1 Aggregation

NPs are rendered colloidally stable due to repulsive electrostatic, steric forces, or a combination of both. Aggregability depends on intrinsic NP parameters such as morphology, surface coating, and charge, as well as extrinsic parameters including electrolyte concentration, pH, presence of organic matter, etc.

Aggregation is common in physiological environments, where NPs tend to aggregate to micro- or macro-metric sizes when not properly stabilized. For CeO_2 NPs, although SC provides stability in water environments, an increase in the ionic strength of the media can screen the electrostatic repulsion that stabilizes the NP, leading to rapid aggregation between NPs [3].

Figure 2.13A illustrates the aggregation kinetics of as-synthesized CeO_2 NPs (1 mg/mL) as a function of the ionic strength of the medium. It is evident that higher ionic strengths accelerate aggregation rates. Notably, nanoceria exhibit good stability in 10 mM phosphate buffer (PB), whereas pronounced aggregation is observed in 100 mM

phosphate buffer saline (PBS) containing additional salts such as NaCl. It's crucial to highlight that NP aggregation occurs remarkably fast, with aggregation in physiological media occurring within just a few minutes.

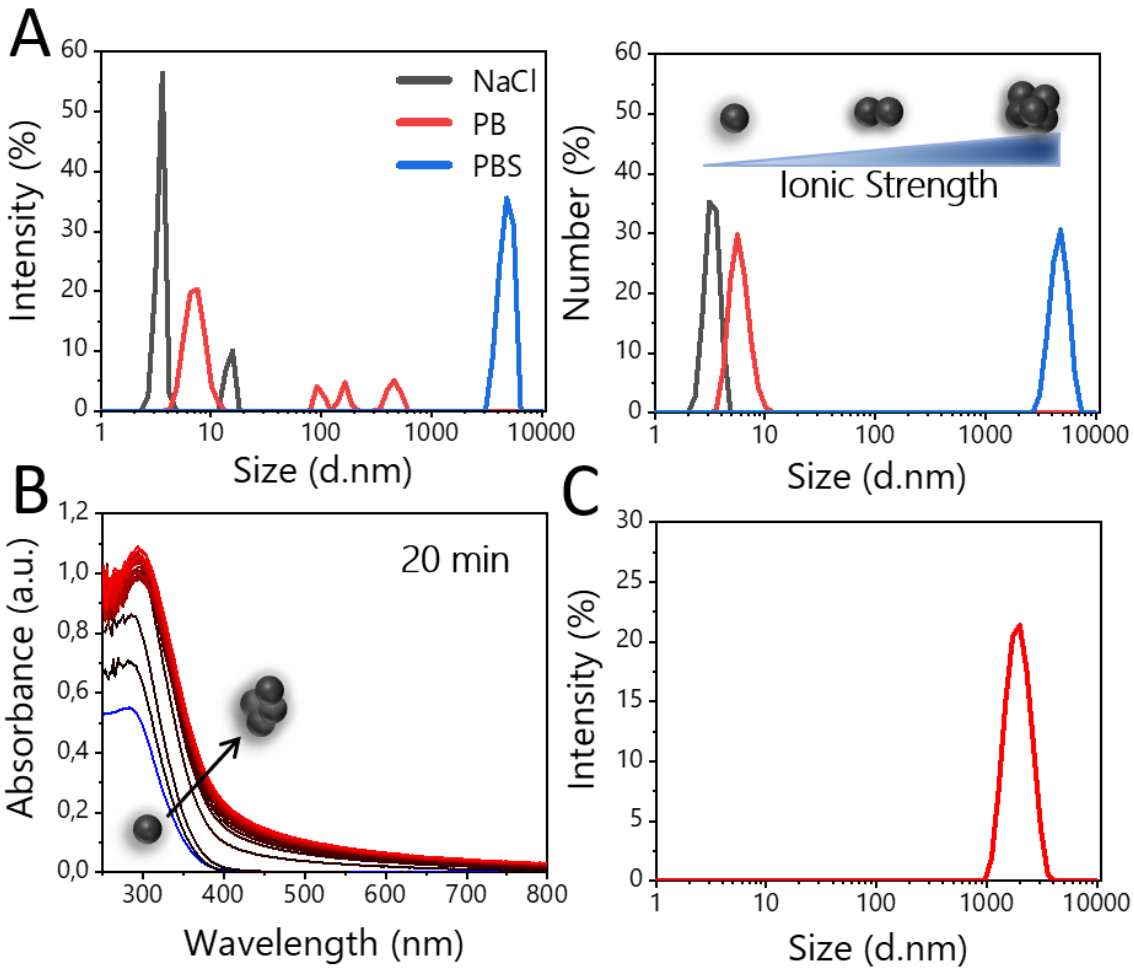


Figure 2.13. Examination of NP aggregation kinetics in various physiological mediums. (A) Measurement of the hydrodynamic diameter of CeO_2 NP by DLS, taken 5 minutes after dispersion in 0.8% NaCl (saline), 10 mM PB, or 100 mM PBS. (B) Time-evolution kinetics of CeO_2 NPs dispersed in DMEM were monitored over 20 minutes using UV-vis spectroscopy (C) and the hydrodynamic diameter of CeO_2 NPs, indicated by the intensity peak corresponding to the final point of the aggregation process.

Exposure of the CeO_2 NPs in a cell culture medium (DMEM) supplemented with 10% fetal bovine serum (FBS) for 20 minutes results in aggregates larger than 1 µm, surpassing the nanoscale range, which results in particle sedimentation (**Figure 2.13BC**).

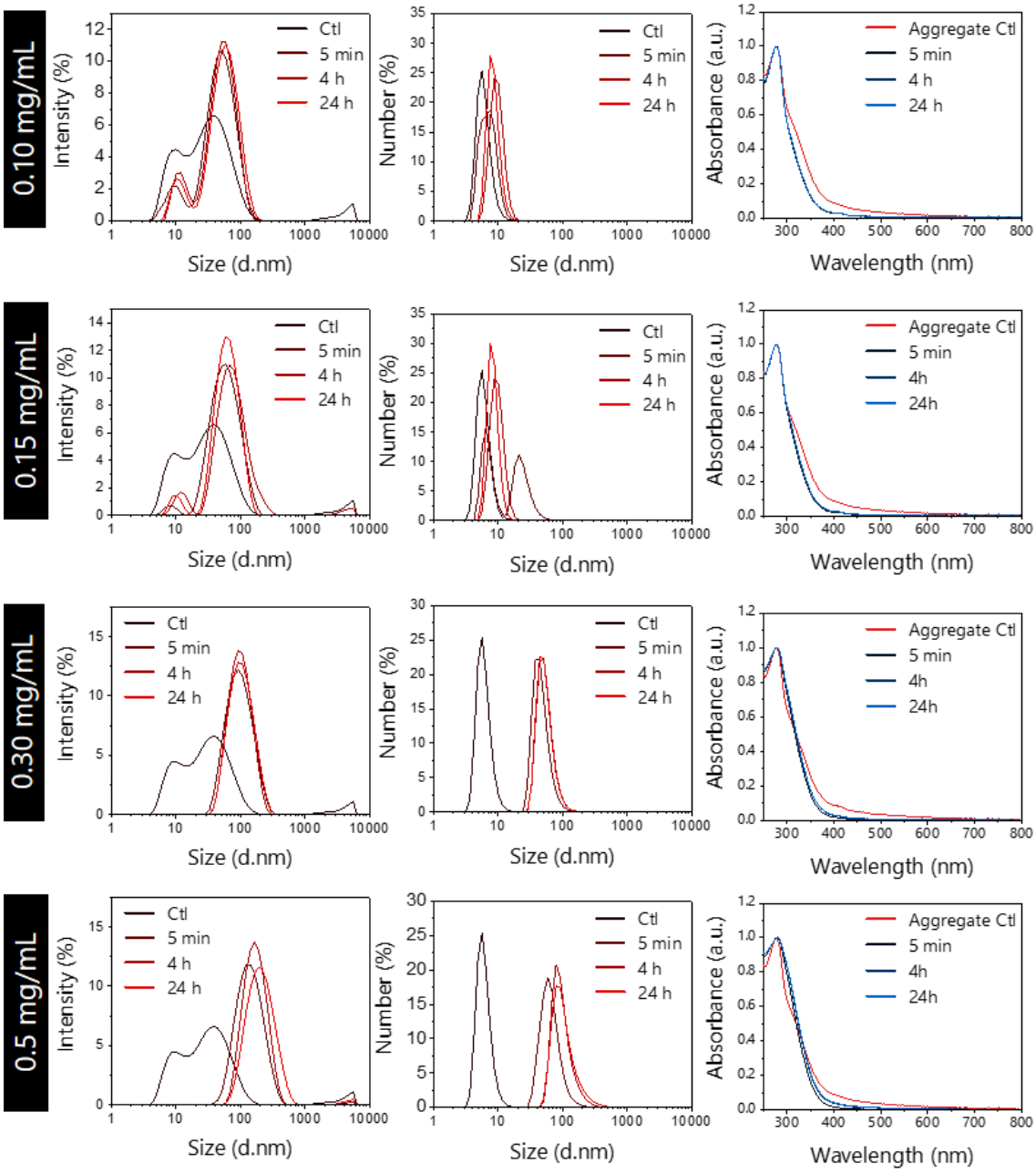


Figure 2.14. Aggregation kinetics of CeO_2 NPs at varying concentrations (0.10, 0.15, 0.30, and 0.50 mg/mL) in DMEM supplemented with 10% FBS, measured over 24 hours. The data was obtained using DLS and UV-vis. Control for DLS corresponds to the peak of DMEM + 10% FBS without NPs, and control for UV-vis shows an aggregated sample of CeO_2 NPs, providing a baseline for comparison.

On the other hand, besides medium composition, the concentration number of NPs plays a significant role in their aggregation. As the concentration increases, so does the likelihood of particle collisions, which is a prerequisite for aggregation. This heightened probability of interactions at elevated concentrations promotes the

formation of aggregates. In this regard, we tested the stability of CeO_2 NPs at different biologically relevant concentrations (0.10, 0.15, 0.30, and 0.50 mg/mL) in DMEM supplemented with 10% FBS over a period of 24 hours (**Figure 2.14**). Our findings, summarized in **Figure 2.15**, reveal that nanoceria particles maintain their stability for at least 24 hours in a complete cell culture medium at concentrations below 0.3 mg/mL, which are within the therapeutic concentrations.

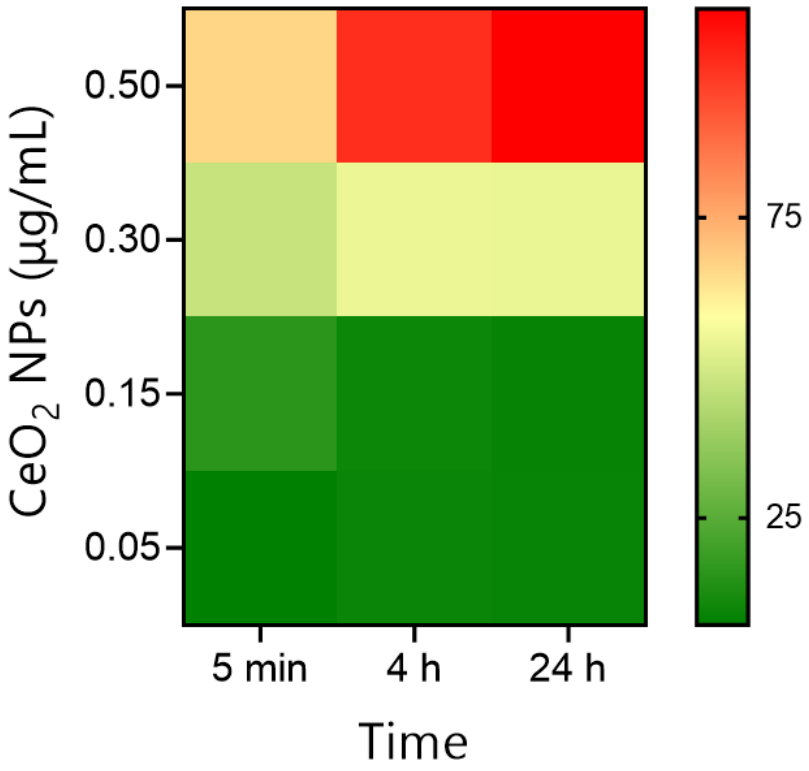


Figure 2.15. Heat Map extracted from Figure 14, showing the aggregation profiles of CeO_2 NPs over time in DMEM supplemented with 10% FBS, based on varying NP concentrations (0.05, 0.15, 0.30, and 0.50 mg/mL). Colour scale and range values indicate the NP hydrodynamic diameter in nm, extracted from the intensity distribution. Green: <30 nm, Yellow: 30-50 nm, Red: > 50nm.

Overall, these results suggest that regardless of the control exerted over NP size during synthesis, these particles can easily lose their stability in biological contexts, as the stability of naked CeO_2 NPs relies on electrostatic interactions. This instability affects their size and consequently alters their nanometric properties. NP toxicity is influenced by size in complex ways. Larger NPs can be more toxic due to greater disruption of biological machinery, while smaller NPs corrode more, which can lead to toxic ions. Conversely, larger NPs are less prone to corrosion but are more likely to trigger

immune responses. There is no simple, universal correlation between NP size and toxicity, as it varies with factors like composition and surface chemistry, leading to non-linear relationships. Therefore, it is essential to explore these aspects for each specific case, not only to design safe nanomaterials but also to gain a comprehensive understanding of the material chemistry.

2.3.2.2 Protein Corona

As shown previously, many materials that are truly nanometric once produced, tend to aggregate rapidly into micrometric particles, thus losing their nanoscale properties. Therefore, if synthesized NPs need to be individually dispersed, surface engineering is required to provide them with repulsion forces to prevent aggregation [27]. This can be achieved either by electrostatic (high surface charge) or steric (entropic) means, usually provided by large soluble molecules associated with the NP surface.

It is well known that once enters a biological environment, NPs will inevitably encounter a vast variety of biomolecules, including proteins and lipids, that will immediately coat the NP surface forming the so-called protein corona, which provides a stabilizing electro-steric effect [3,28]. For instance, the stability of CeO_2 NPs (1 mg/mL) was studied in cell culture medium (DMEM), with and without 10% FBS. The results indicate that the presence of proteins at high enough concentrations offers protection against NP aggregation (**Figure 2.16**), providing valuable insights for surface stabilization.

The interface between the NPs and the biomolecules involves dynamic physicochemical interactions, as well as kinetics and thermodynamic exchanges. These interactions depend on the composition, morphology, and surface state of the NP, as well as the NP-to-protein ratio and the exposure time in the medium. The formation of the protein corona is a dynamic process. Initially, proteins adsorb and desorb on the NP surface, followed by a series of reorganizational arrangements that stabilize the adsorption of more affine proteins, making it eventually irreversible.

In this context, when naked NPs are exposed to complex biological media, they will interact with a mixture of proteins and small organic molecules. This uncontrolled

protein corona formation can lead to NP-biomolecule aggregates (hetero-aggregation) or coated NPs aggregates. The most straightforward strategy to address this issue is to passivate the NP surface beforehand, for example, through albuminization, PEGylation, or the addition of PVP. Albumin, one of the most abundant proteins in blood, plays crucial roles in binding and transporting substances, including ions, molecules, and drugs, making it an ideal candidate for particle stabilization, and ensuring biocompatibility.

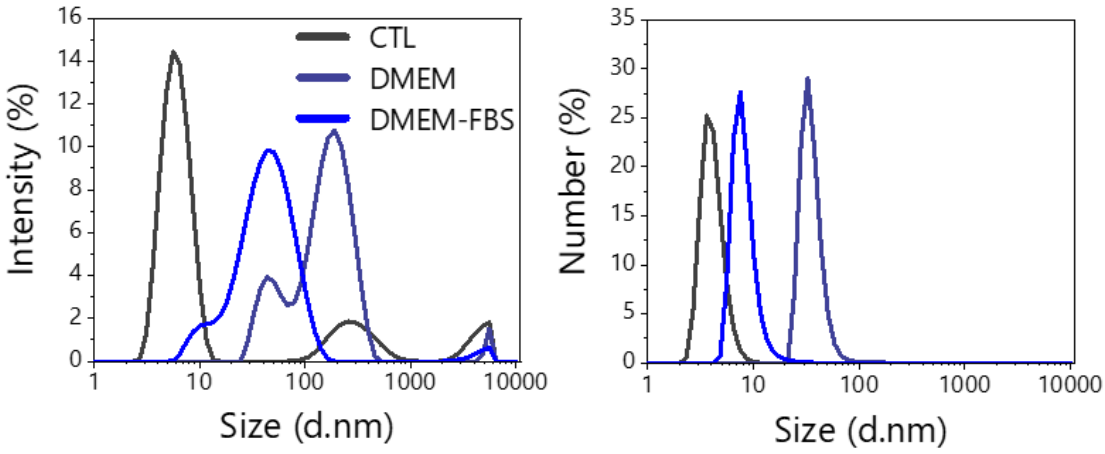


Figure 2.16. The hydrodynamic diameter of CeO_2 NP was measured 5 minutes after dispersion in DMEM supplemented or not with 10% FBS. Control represents the hydrodynamic diameter of as-synthesized CeO_2 NPs.

Building on the previous knowledge of our research group [3,28], the role of albumin in the stabilization and efficacy (ROS scavenging power) of CeO_2 NPs was explored. For the conjugation process, the theoretical number of proteins required to cover the entire NP surface was determined. Considering the surface area of the 2.5 nm CeO_2 NPs as 28.27 nm^2 per particle, and utilizing the surface coverage of albumin, estimated through an equilateral triangular prism model shape for (bovine) serum albumin with dimension 8.0 x 8.0 x 3.5 nm [29]. Under these conditions, the surface area of bovine serum albumin (BSA) is either 28 nm^2 or 32 nm^2, depending on the cross-section[5]. Consequently, it is estimated that around two BSA molecules are needed to cover the NP surface, with approximately two proteins per particle or a few particles per protein.

[5] Given that the BSA molecule is larger than the CeO_2 NP, rather than a protein corona, a NP-protein complex is formed.

Recognizing the impact of protein concentration on effective affinity, CeO_2 NPs were incubated with BSA at a 10-fold excess from the theoretical calculation to force complete coverage of the NP surface. Thus, the final concentrations were set at 1 mg/mL for CeO_2 and 10 mg/mL for BSA. It's noteworthy that during the conjugation process, NPs were always added into the protein solution (containing 10 mM PB) to prevent NP aggregation by guaranteeing that each NP encounters an excess of protein. Additionally, to avoid media exchange, the volume of NPs added was kept at 10% of the volume of the protein solution [28]. The selection of the buffer solution (the nature and concentration of ions) plays a significant role in facilitating the effective conjugation between NPs and proteins, thereby ensuring the integrity of both components during the conjugation process.

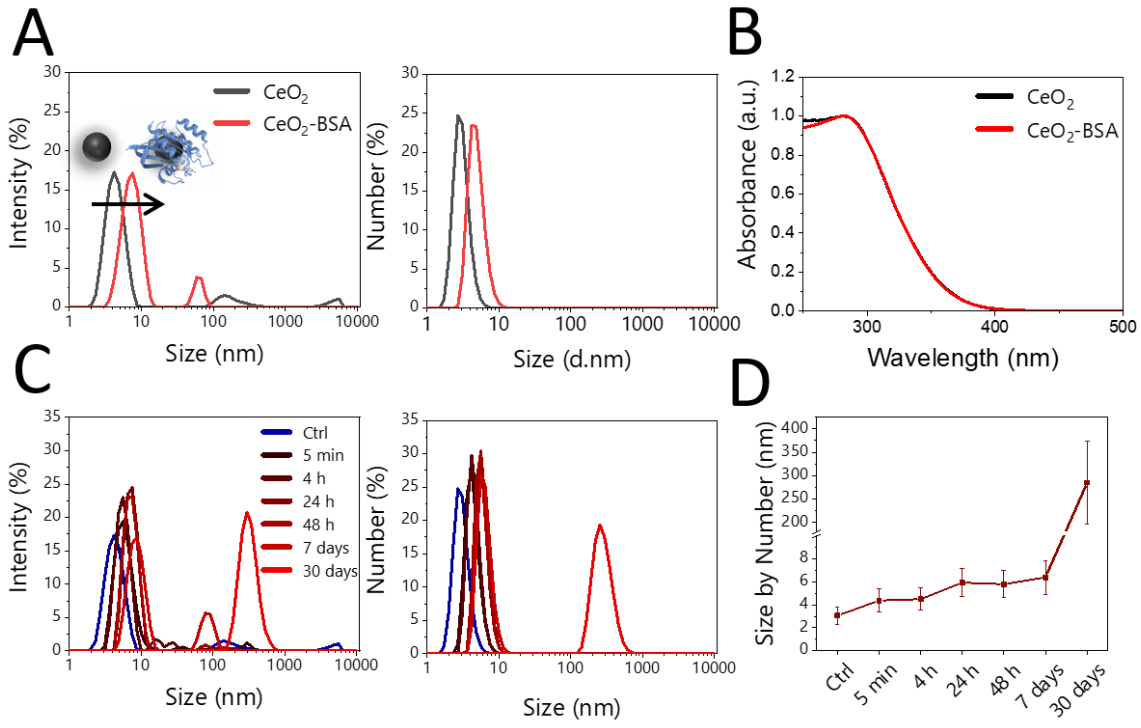


Figure 2.17. Characterization of BSA conjugation to CeO_2 NPs. (A) Comparison of the hydrodynamic diameter of CeO_2 NPs before and after a 24-hour conjugation period with BSA. (B) UV-vis absorbance of the CeO_2-BSA conjugate after 24 hours. (C) The time evolution of the hydrodynamic diameter for the NP-BSA bioconjugate was monitored for 30 days by DLS. (D) Graphical representation of the hydrodynamic size measured by number as a function of time.

As anticipated, the conjugation of CeO_2 NPs to albumin results in an increase of the NP's hydrodynamic diameter, from 3.06 ± 0.76 to 6.28 ± 1.29 nm (**Figure 2.17A**). Z-potential shifted from -18 ± 7.99 to -10 ± 4.31 nm at a conductivity of 0.27 mV (data not shown). Conversely, there were no changes observed in the UV-vis absorption peak 24 hours after conjugation (**Figure 2.17B**). Although proteins are known to absorb light at 280 nm, their refractive index is negligible compared to CeO_2 at these concentrations. The stability of the bioconjugate was assessed by DLS over 30 days at 4 ºC. The results indicate that CeO_2-BSA conjugates are stable for 7 days, but after 30 days, the NPs aggregate, likely due to protein denaturation and aggregation (**Figure 2.17CD**) [30].

Once conjugation conditions were established, the influence of the protein-to-NP ratio was explored in various physiological media with different ionic strengths, including 0.8% NaCl (saline), 100 mM PB, and 100 mM PBS. CeO_2 NPs were conjugated with BSA for 24 hours at different protein concentrations: 10, 20, 40, and 70 mg/mL, corresponding to 8, 15, 30, and 50x excess albumin, respectively. Thereafter, the NP-BSA conjugates were resuspended in the physiological media and monitored for 24 hours using DLS (**Figure 2.18**). As expected (**Figure 2.15**), the results show that the higher the ionic strength of the medium, the higher the protein-to-NP ratio required to avoid aggregation. This indicates that bioconjugation must be optimized for different biological conditions. In the studied case, 30 times excess (40 mg/mL) of BSA was sufficient to protect particles from repulsive charges driven by 100 mM PBS, which is the saltiest tested medium.

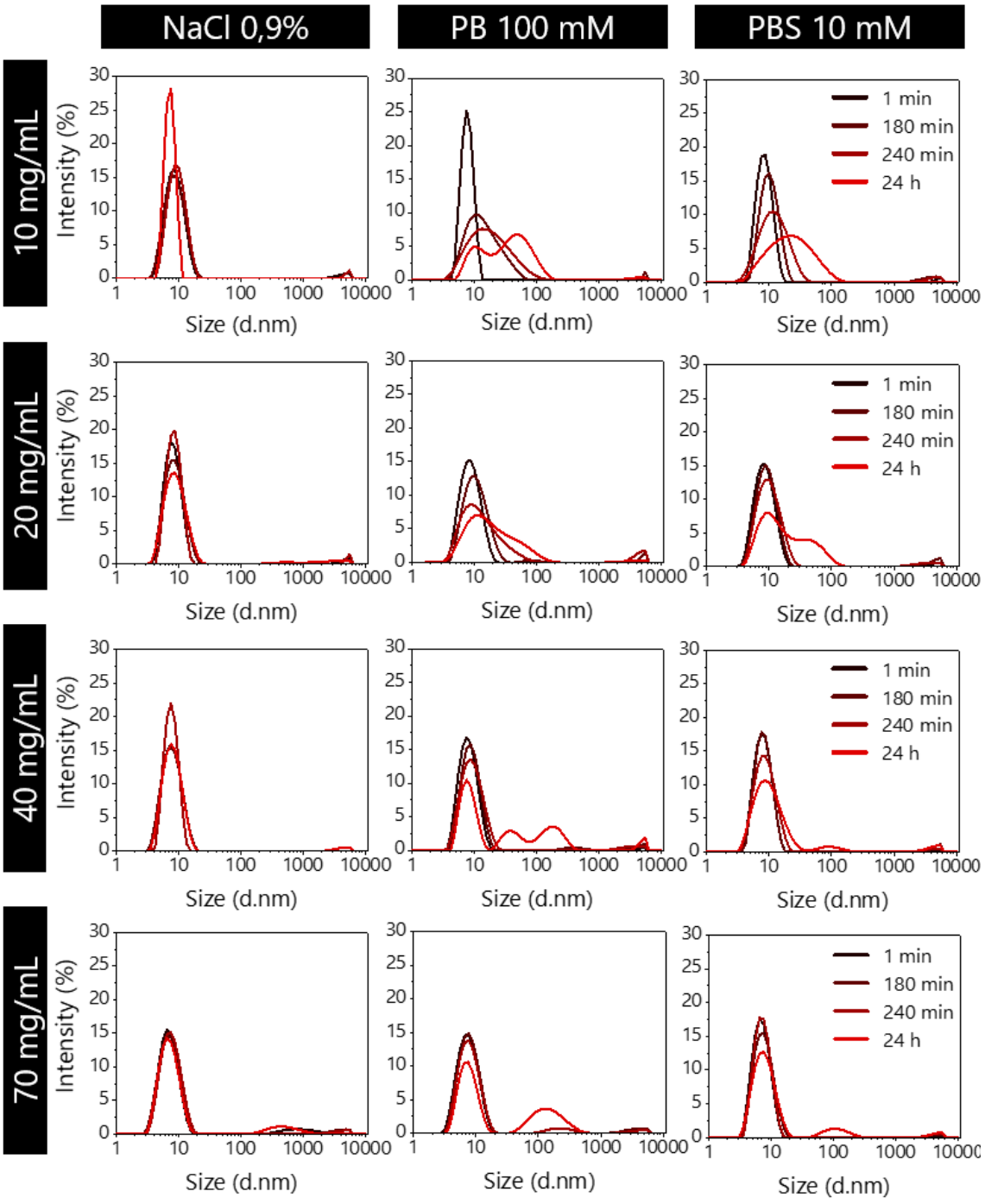


Figure 2.18. Time-evolution of CeO_2 NPs conjugated to BSA in different isotonic solutions: 0.8 % NaCl, 100 mM PB, and 100 mM PBS. Conjugation was tested at different BSA concentrations: 10, 20, 40, and 70 mg/mL, which corresponds to a protein excess of 8, 15, 30, and 50x, respectively.

Finally, the stability of CeO_2-BSA conjugates was evaluated in complete cell culture media (DMEM + 10% FBS), which is one of the most biologically relevant solutions for in vitro testing. As shown in **Figure 2.19AB**, the CeO_2-BSA conjugates with a 40x excess of

protein remain stable for at least 7 days, as indicated by hydrodynamic diameter measurements and UV-vis spectroscopy. The influence of bioconjugation on efficacy and safety will be discussed later.

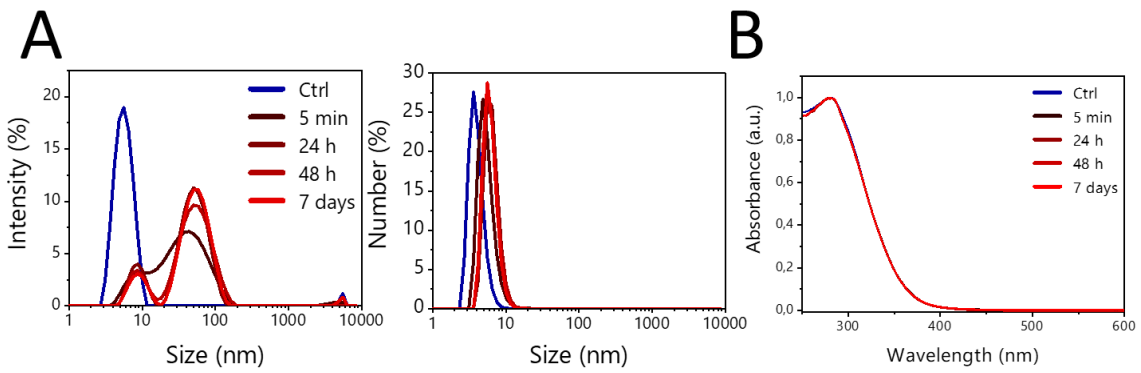


Figure 2.19. Time evolution of CeO_2-BSA conjugates in DMEM supplemented with 10% FBS measured by (A) hydrodynamic diameter (DLS), and (B) UV-vis spectroscopy. Control corresponds to as-synthesized CeO_2 NPs.

2.3.2.3 Corrosion

As shown previously, cerium ions (Ce^{3+}) undergo oxidation at basic pH, rendering them insoluble, while at physiologic pH levels, or below, their thermodynamic fate is to be reduced back and dissolve into Ce^{3+} ions (see the Pourbaix diagram in **Figure 2.1**, page 58). However, this dissolution process is generally hindered by a notably high activation energy required for CeO_2 crystal dissolution [31]. Nevertheless, this barrier diminishes with decreasing particle size. It has been described that the curvature radii of NPs with diameters of 30 nm or less become progressively unstable [32]. Consequently, smaller CeO_2 NPs are more prone to dissolution, thus facilitating their biodegradation. Moreover, the estimated minimal thermodynamically stable nanoceria crystal size is about 1.9 nm in diameter [31], making ~2.5 nm CeO_2 NPs nearly prone to dissolution. This is attributed to the correlation between size and oxygen vacancies, with increased vacancies reflecting more Ce^{3+} ions, and elevated crystal tensions. Considering this, it is highly probable that 2.5 nm CeO_2 NPs, close to the thermodynamic crystal stability limit, are prone to dissolution at neutral or acidic pH, realising Ce^{3+} ions. In fact, rapid dissolution of CeO_2 NPs has been already reported within late endosomes and endolysosomes where physiological pH is decreased below 6 [33].

In collaboration with Prof. Neus Sabaté from the National Institute of Microelectronics (IMB-CNM), in-house synthesized CeO_2 NPs were explored as robust alternatives to natural enzymes for colorimetric detection of analytes. In this study [34], CeO_2 NPs were compared with enzymes during the water oxidation process of ferrocyanide ($[Fe(CN)_6]^{4-}$) to ferricyanide ($[Fe(CN)_6]^{3-}$) at pH 4.4, serving as a model of a redox colorimetric reaction. However, it was observed that under the working conditions (low pH, electron exchange), CeO_2 NPs behaved as a pure stoichiometric reagent rather than a catalyst, being consumed during the reaction of Ce^{4+} to Ce^{3+}.

To examine the evolution of CeO_2 during ferrocyanide oxidation, DLS and ICP-MS measurements were conducted before and after incubating ferrocyanide and CeO_2 NP at different ratios for 3 hours. A solution containing 2.35 mM atomic cerium in the form of CeO_2 NPs was exposed to increased concentrations of ferrocyanide (0.77, 1.16, 1.54 and 2.3 mM). The DLS and corresponding NP concentration analyses revealed the progressive dissolution of the NPs while maintaining a relatively constant NP number until complete disintegration at high ferrocyanide concentrations (**Figure 2.20**).

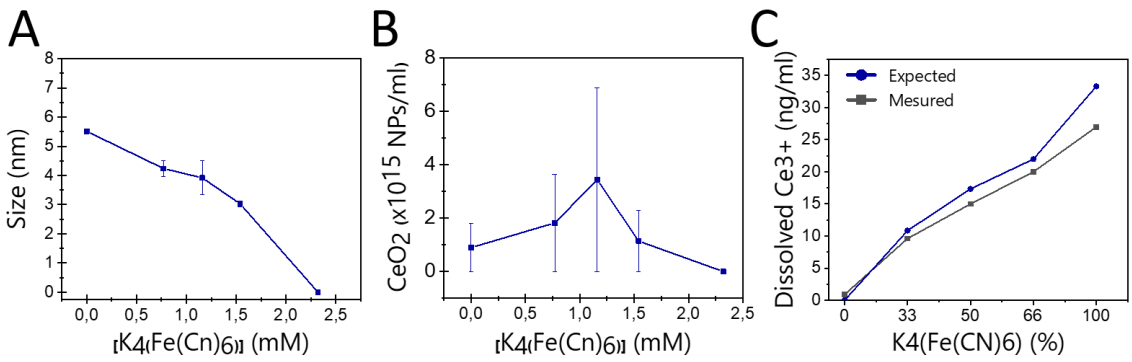


Figure 2.20. CeO_2 NPs at a concentration of 0.4 mg/mL (2.3 mM atomic cerium) reacted for 3 hours with different concentrations of ferrocyanide, ranging from 0 to 2.4 mM. (A) Hydrodynamic diameter by intensity profiles measured by DLS plotted against $K_4[Fe(CN)_6]$ concentrations. (B) CeO_2 NP concentrations measured by DLS. (C) Dissolved cerium ions measured by ICP-MS, plotted against $K_4[Fe(CN)_6]$ concentrations.

For ICP-MS analysis, the samples underwent purification by centrifugation–filtration before analysis to separate NPs from cerium ions. **Figure 2.20** illustrates how the presence of Ce^{3+} ions in solution increases with the addition of ferrocyanide. The discrepancy between the expected and elemental measured values is attributed to some

retention in the purification filters and spontaneous oxidation of ferrocyanide during the experimental time window.

This translates into CeO_2 NP being able to uptake a finite number of electrons while maintaining its fluorite crystal structure and NP integrity before dissolution. Therefore, if Ce^{3+} ions and the corresponding oxygen vacancies are not recycled back to Ce^{4+}, the increasing concentration of crystal defects in the NPs will cause cation repulsion and irreversible disintegration of the NPs in water at pH below 8. Therefore, CeO_2 NPs with sizes around 2–3 nm are very close to the calculated thermodynamically stable crystal size, making them prone to dissolution. This process is influenced by the NP environment and accelerates as pH decreases.

2.3.3 Efficacy and Safety

2.3.3.1 Scavenging Capacity

Testing the efficacy of the synthesised CeO_2 NPs, involved evaluating their ability to scavenge ROS. Measuring ROS within biological systems presents challenges due to their characteristics. Their low concentrations (picomolar to low micromolar), high reactivity, and short lifespan (milliseconds or less) make them challenging to detect [35].

Thus, measuring ROS becomes more complex when attempting to assess ROS levels within cells. Initially, ROS levels were measured in the test tube using the Amplex™ Red commercial probe. This method is based on a fluorometric assay, involving the reaction of Amplex Red (10-acetyl-3,7-dihydroxyphenoxazine) in the presence of horseradish peroxidase (HRP) that reacts with H_2O_2 in a 1:1 stoichiometry, resulting in the formation of a florescent product, resorufin. Importantly, the non-radical nature of H_2O_2, characterized by its low reactivity, grants it longer lifetimes and the ability to exist at higher concentrations compared to other ROS. This property facilitates the detection of H_2O_2 in experimental settings.

The scavenging capacity of CeO_2 NPs was first evaluated by exposing them to increasing concentrations of H_2O_2 for 40 minutes. 5 nm gold (Au) NPs were added as a negative control due to their lack of ROS scavenging activity. Results in **Figure 2.21**

show that CeO_2 NPs significantly decrease H_2O_2 levels by up to 50%, reaching approximately 75% degradation under low H_2O_2 conditions (1 µM) in the experimental window. Minor differences in scavenging capacity at higher H_2O_2 concentrations support their role as catalysts. Notably, naked CeO_2 NPs exhibit higher scavenging power than BSA-coated NPs (CeO_2-BSA) at higher H_2O_2 concentrations (4 and 8 µM), suggesting that the surface coating may affect surface accessibility and reduce scavenging rate.

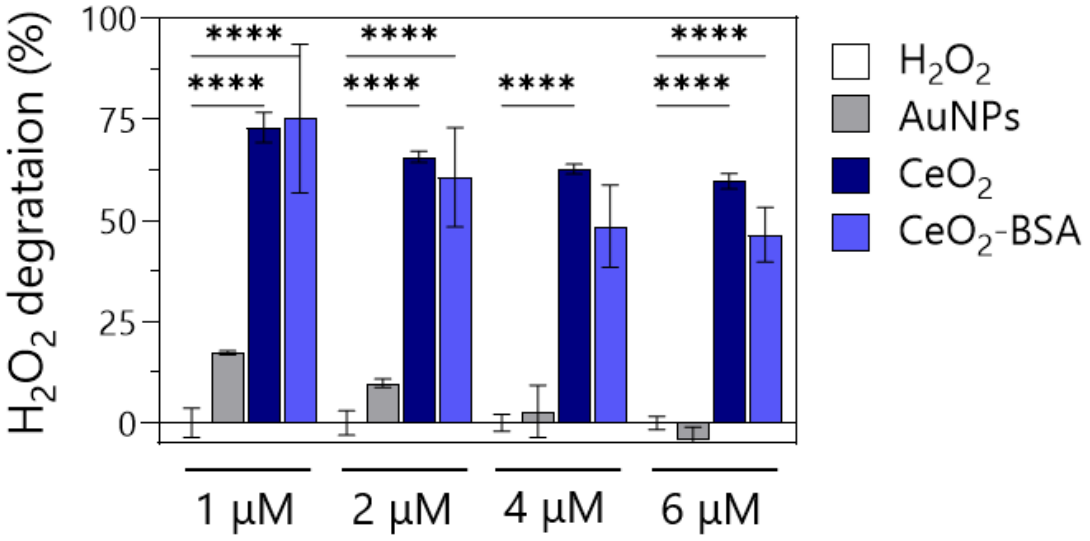


Figure 2.21. CeO_2 NPs (50 µg/mL) catalytic activity measured 40 minutes after incubation with varying H_2O_2 concentrations (1, 2, 4, and 6 µM). Scavenging capacity was assessed depending on their surface coating (naked or BSA-conjugated) with AuNPs as control. H_2O_2 levels were measured by Amplex Red Hydrogen Peroxide kit. Data presented as means ± SEM. n = 3. *p < 0.05, **p<0.01, ***p<0.001, ****p<0.0001

Thereafter, ROS levels were measured in vitro. Despite adding H_2O_2 as a control, the Amplex Red assay did not detect any significant signal. This discrepancy highlights several limitations of Amplex Red in cells. On the one hand, the test can interface with other HRP substrates or be inactivated by O_2•- [35]. On the other hand, extracellular H_2O_2 levels reflect the balance between H_2O_2 production, removal by intracellular enzymes, and diffusion out of the cell. Note that H_2O_2 will rapidly react with metallic ions, forming other types of ROS.

Other commercially available molecular probes were tested, but none produced reliable results (data not shown). For example, 2'-7'-dichlorodihydrofluorescein diacetate (DCFDA) was used, but the results were inconsistent. Control tests showed no linear

response to increasing H_2O_2 concentrations, and some artefactual results were observed.

Thus, the capacity to scavenge ROS was evaluated indirectly by measuring cell survival in response to H_2O_2-induced apoptosis [36,37]. Excess of H_2O_2 (oxidative stress) induces cell death [38–40], which can be delayed or prevented by antioxidants [41–43]. H_2O_2 levels were experimentally determined to mimic acute (500 µM) and chronic (50 µM) oxidative stress models. Human Embryonic Kidney 293 (HEK 293) cells were exposed to determined H_2O_2 concentrations and cell viability was measured using the PrestoBlue reagent after pre-incubation with 150 µg/mL of CeO_2 NPs (naked and BSA-conjugated).

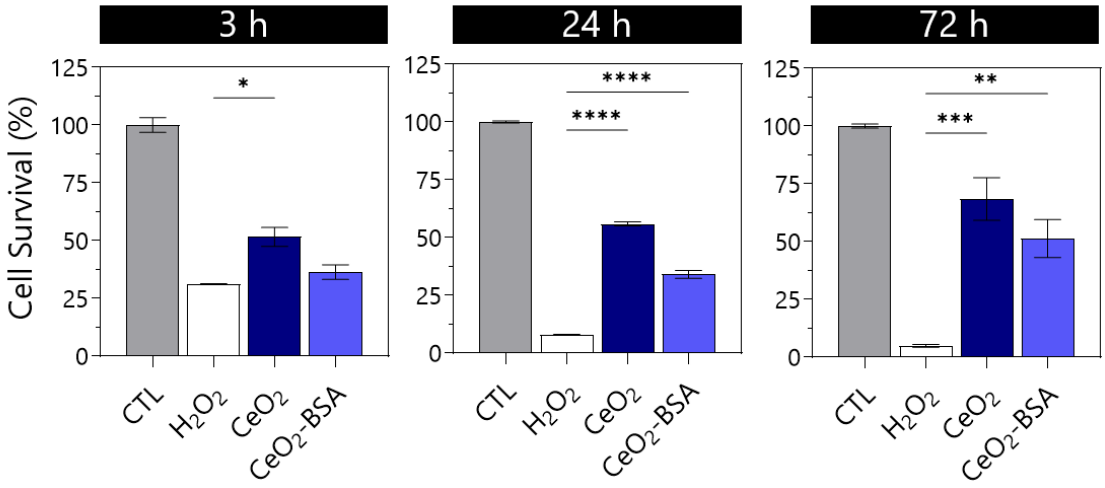


Figure 2.22. Effect of CeO_2 NPs (100 µg/mL) rescuing HEK 293 cells from death induced by 500 µM H_2O_2 exposure for 3, 24, or 72 h. Control cells were incubated with 1X PBS. The data shown are the means ± SEM. n = 3. *p < 0.05, **p<0.01, ***p<0.001, ****p<0,0001.

The viability of cells exposed to high H_2O_2 concentrations (500 µM) was evaluated at 3, 24, and 72 hours (**Figure 2.22**). The high dose of H_2O_2 reduced cell viability to ~31.1 % within 3 hours. At short exposure times, cell viability was significantly increased with naked CeO_2 NPs, whereas BSA-conjugated NPs did not show significant differences. The protective effect of CeO_2 NPs against oxidative stress increased with longer exposure times, significantly raising cell viability from 7.87 to 55.87% at 24 hours and from 4.87 to 68.48% at 72 hours. Although BSA-conjugated NPs significantly increased cell viability under these conditions, they were not as effective as naked NPs.

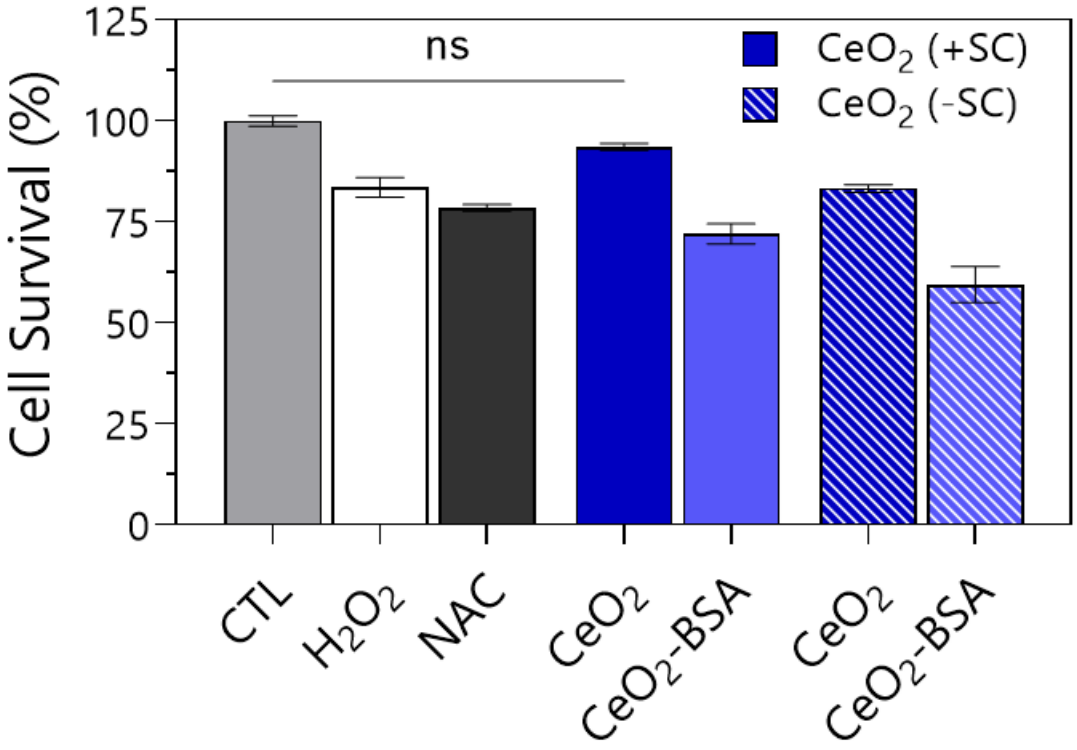


Figure 2.23. Effect of CeO_2 NPs (100 µg/mL) rescuing HEK 293 cells from dead induced by 50 µM H_2O_2 24 h after exposure. Control cells were incubated with vehicle (SC 2.2 mM), and 25 mM N-acetylcysteine (NAC) was used as molecular antioxidant control. Data shown are the means ± SEM. n = 4 (biological replicates). *p < 0.05, **p<0.01, ***p<0.001, ****p<0.0001

Following that, the capacity of CeO_2 NPs to protect HEK 293 cells from ROS-induced apoptosis was further assessed, this time in a chronic oxidative stress model characterized by lower ROS levels. Cells were exposed to 50 µM H_2O_2, resulting in approximately 16% cell dead within 24 hours of exposure. In this study, we also included particles synthesized without citrate (CeO_2 (-SC)), resulting in large aggregates (100-10000 nm) with a reduced surface-to-volume ratio, to further investigate the impact of surface availability. Results indicate that aggregates, unable to prevent cell death, are less effective than well-dispersed particles (**Figure 2.23**). Furthermore, in this model, the conjugation of particles to BSA induces more cell death than H_2O_2 itself, highlighting the need for toxicity studies. Importantly, naked CeO_2 NPs were capable of restoring cell viability levels to those of the control group, showing no significant differences with healthy cells. Interestingly, as we shall see later (see section 2.3.3.2 Effect of CeO_2 NPs on Cell Viability, page 89), the observed NP toxicity is attributed to albumin toxic excipients present in commercial samples, as

Harold Krug already indicated in its seminal work [44]. Moreover, 25 mM of N-acetylcysteine (NAC), a described molecular antioxidant, was used as a positive control but did not show any effect. Importantly, naked CeO_2 NPs were the only treatment capable of restoring cell viability levels to those of the control group, showing no significant differences with healthy cells.

NAC is a standard treatment for acetaminophen overdose, aimed at preventing and mitigating drug-induced liver injury [45,46]. Additionally, NAC has increasingly been regarded as an "antioxidant" in recent years and is one of the most widely used antioxidants in experimental cell and animal biology [47]. However, the use of NAC as a safe antioxidant molecule has come under debate due to a lack of evidence regarding its antioxidant effects [47,48]. The mechanism of action of NAC is unclear and requires further investigation to be established. Moreover, NAC exhibits poor solubility at physiological pH, typically necessitating its provision within HCl to achieve a pH around 2 [49]. Failure to adjust the pH can result in a significant decrease in the pH of physiological media [49,50] while adjusting it can lead to poor bioavailability. Last, the reaction kinetics of NAC with certain ROS molecules was reported in 1989 [51], indicating extremely low reaction rates with H_2O_2 (0.85 M-1s-1), while the reaction with superoxide was undetectable. To date, the paper has been cited 2324 times, and in many cases, paradoxically cited to support the contrary, the scavenging function of NAC in biological systems. Based on the obtained results, particularly where the use of NAC failed to protect cells from ROS-induced apoptosis, I align with the opinion of some authors who emphasize that NAC should not be described as an antioxidant [47]. This term typically implies a compound that directly and efficiently neutralizes oxidants, and the lack of evidence and poor understanding of the mechanisms can lead to misinterpretations.

2.3.3.2 Effect of CeO_2 on Cell Viability

CeO_2 NPs toxicity was first evaluated in two human-derived immortalized cell lines, HEK 293 and Henrietta Lacks (HeLa) cells, chosen for their robustness, rapid growth, and proliferation characteristics. Additionally, both cell lines are well established for

toxicological studies. The distinct nature of these cell lines, with HeLa cells derived from cervical cancer tissue and HEK 293 cells from embryonic kidney tissue, adds relevance to this study.

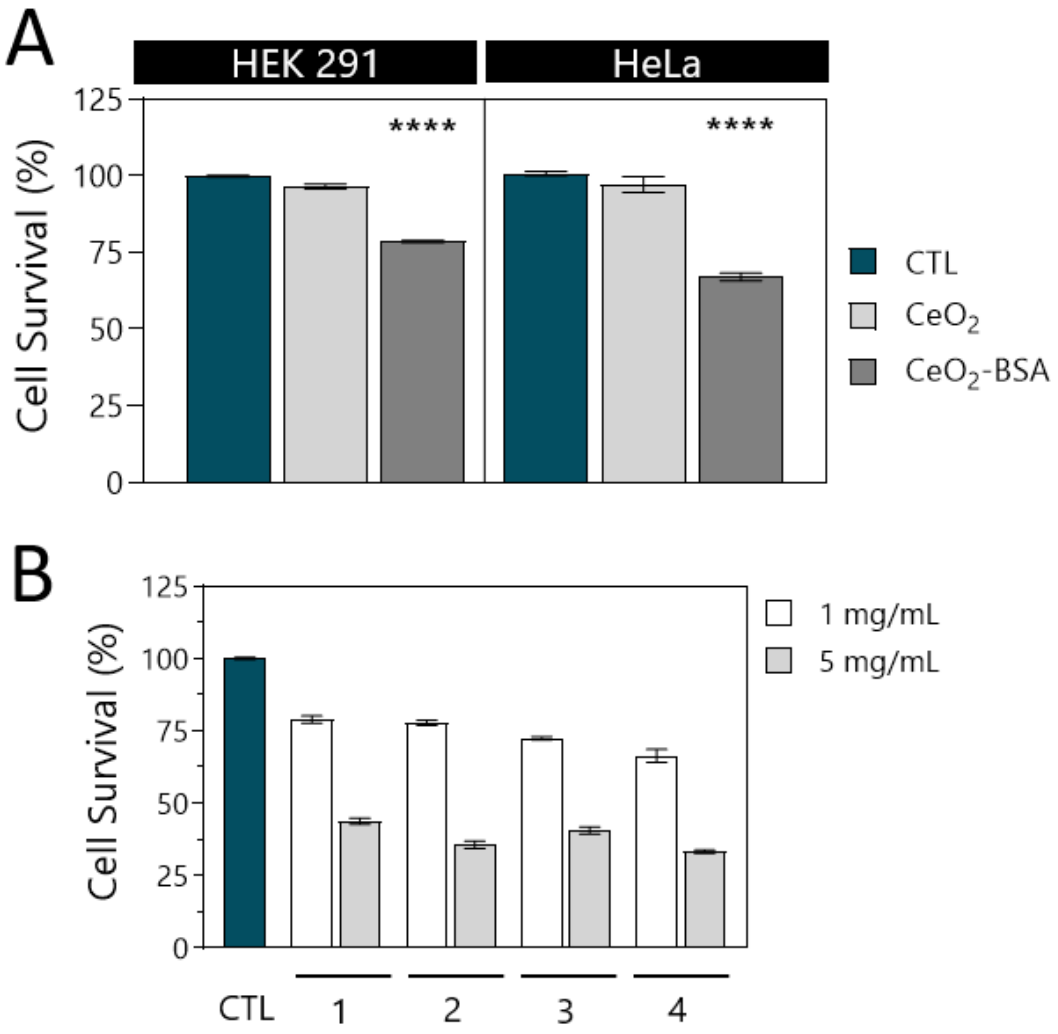


Figure 2.24. Cell viability assessment by PrestoBlue reagent. (A) Cell survival of both HEK 293 and HeLa cell lines, exposed to 100 µg/mL naked and BSA conjugated CeO_2 NPs for 24 hours. Data shown are the means ± SEM. n = 3. *p < 0.05, **p<0.01, ***p<0.001, ****p<0.0001. (B) Toxicity assessment of 1 and 5 mg/mL of four different commercially available albumins in HEK 293 cells. (1) universal grade BSA (≥98% purity), (2) BSA heat shock fraction (≥98% purity), (3) Biochemistry grade BSA (≥98% purity), (4) Human Serum Albumin (HSA) (≥ 97% purity).

To study their susceptibility to NPs, cells were exposed to working concentrations (100 µg/mL) of CeO_2 NPs (naked and BSA-conjugated) for 24 hours. Thereafter, cell viability was determined using the PrestoBlue assay. While cell viability remained unaffected by naked NPs, some toxicities were observed in cells exposed to CeO_2-BSA

NPs, with cell viabilities of 78.45% and 66.91% in HEK 293 and HeLa cells, respectively (**Figure 2.24**A). In consequence, further investigation into albumin toxicity in HEK 293 cells was necessary. To this end, the toxicity of four different commercially available albumins was assessed, including; ***(1)*** universal grade BSA (≥98% purity), ***(2)*** BSA heat shock fraction (≥98% purity), ***(3)*** Biochemistry grade BSA (≥98% purity), and ***(4)*** Human Serum Albumin (HSA) (≥ 97% purity) (**Figure 2.24B**). Albumin was incubated with cells for 24 hours at two different doses: 1 mg/mL and 5 mg/mL. The 1 mg/mL dose corresponds to the standard concentration used in the established working conditions for conjugated CeO_2 NPs. Interestingly, the results showed that albumin, decreased cell viability in all tested conditions, indicating dose-dependent toxicity (**Figure 2.24B**). Species cross-reactivity was ruled out, as both Human Serum Albumin (HSA) and BSA induced toxicity, and it is hypothesized that commercial albumin might contain slightly toxic excipients that induce cell death at high concentrations.

In summary, conjugating NPs to commercial albumin slightly decreases their ROS scavenging capacities while increasing toxicity in vitro. While conjugation is intended to improve cell viability by preventing aggregation, albumin conjugation seems to have the opposite effect at the working conditions, probably due to the presence of toxic excipients. Notably, doses of 100-150 µg/mL of CeO_2 NPs demonstrated significant effectiveness in protecting cells from ROS-induced apoptosis, whereas doses below 300 µg/mL of naked CeO_2 NPs exhibited colloidal dispersion in cell culture medium (**Figure 2.15**, page 77). Hence, while conjugation is mandatory for NP biocompatibility in vivo, caution should be exercised with high doses of albumin or CeO_2 NPs in vitro to address potential toxicity issues. In this context, naked CeO_2 NPs will be used, at doses below 150 µg/mL to prevent any adverse effects stemming from NP aggregation or the presence of toxic excipients.

Next, dose-dependent CeO_2 cell viability was evaluated in RAW 264.7 murine macrophages, chosen for their immune nature whose relevance will be explained later. As previously discussed, the interactions between the NPs and the immune system will determine both their fate and biological effects [6]. Thus, naked CeO_2 NPs were

incubated with the RAW 264.7 cell line for 24 hours at increasing doses, including 50, 150, and 300 µg/mL, followed by cell viability assessment using the Presto Blue assay.

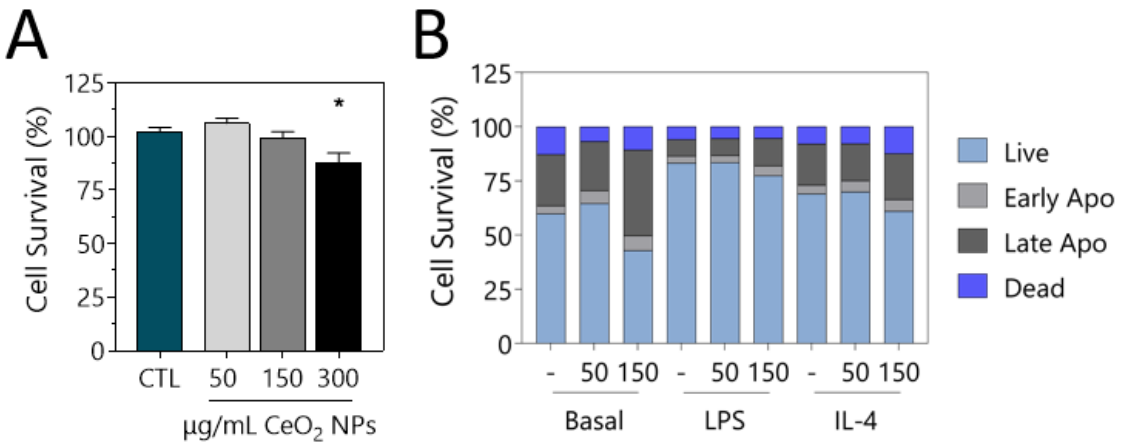


Figure 2.25. Cell viability of RAW 264.7 macrophages exposed to naked CeO_2 NPs. (A) Cell survival 24 hours post-exposure to 50, 150, and 300 µg/mL of CeO_2 NPs. Data shown are the means ± SEM. n = 2. *p < 0.05, **p<0.01, ***p<0.001, ****p<0.0001. (B) Cytotoxicity evaluation by Pacific Blue™ Annexin V/SYTOX™ staining. RAW 264.7 cells were exposed to CeO_2 NPs (50 and 150 µg/mL) for 24 hours, followed by 24 hours of activation with LPS or IL-4. Cells were analysed by flow cytometry, and cell state was classified as live, early or late apoptosis, or dead. n = 1.

Results indicate a notable decrease in cell viability from 100% to 80% at the highest dose (300 µg/mL), likely attributable to NP aggregation (**Figure 2.25A**). Subsequently, CeO_2 toxicity within the working concentration range (50 and 150 µg/mL) was evaluated on immune-activated macrophages (**Figure 2.25B**). Macrophages were exposed to CeO_2 NPs for 24 hours, followed by macrophage activation using either LPS (inflammatory response) or interleukin-4 (IL-4; anti-inflammatory response). Cell viability was assessed 24 hours post-cell activation using flow cytometry and the Pacific Blue Annexin V/SYTOX AADvanced Apoptosis commercial kit. Again, results demonstrate that the use of CeO_2 NPs is safe and does not alter the cell viability, even in immune-activated cells. However, in naïve macrophages (Basal), a dose of 150 µg/mL CeO_2 NPs increased the percentage of late apoptotic cells, which warrants revision.

2.4 References

1. Li, Y.; Fujita, M.; Boraschi, D. Endotoxin Contamination in Nanomaterials Leads to the Misinterpretation of Immunosafety Results. *Front Immunol* **2017**, *8*, 1.

2. Henke, E.; Nandigama, R.; Ergün, S. Extracellular Matrix in the Tumor Microenvironment and Its Impact on Cancer Therapy. *Front Mol Biosci* **2020**, *6*.

3. Barbero, F.; Russo, L.; Vitali, M.; Piella, J.; Salvo, I.; Borrajo, M.L.; Busquets-Fité, M.; Grandori, R.; Bastús, N.G.; Casals, E.; et al. Formation of the Protein Corona: The Interface between Nanoparticles and the Immune System. *Semin Immunol* **2017**, *34*, 52–60.

4. Piella, J.; Bastús, N.G.; Puntes, V. Size-Dependent Protein-Nanoparticle Interactions in Citrate-Stabilized Gold Nanoparticles: The Emergence of the Protein Corona. *Bioconjug Chem* **2017**, *28*, 88–97.

5. Bachmann, M.F.; Jennings, G.T. Vaccine Delivery: A Matter of Size, Geometry, Kinetics and Molecular Patterns. *Nature Reviews Immunology 2010 10:11* **2010**, *10*, 787–796.

6. Ernst, L.M.; Casals, E.; Italiani, P.; Boraschi, D.; Puntes, V. The Interactions between Nanoparticles and the Innate Immune System from a Nanotechnologist Perspective. *Nanomaterials 2021, Vol. 11, Page 2991* **2021**, *11*, 2991.

7. Sonavane, G.; Tomoda, K.; Makino, K. Biodistribution of Colloidal Gold Nanoparticles after Intravenous Administration: Effect of Particle Size. *Colloids Surf B Biointerfaces* **2008**, *66*, 274–280.

8. Xu, C.; Qu, X. Cerium Oxide Nanoparticle: A Remarkably Versatile Rare Earth Nanomaterial for Biological Applications. *NPG Asia Mater* **2014**, *6*, e90–e90.

9. Reed, K.; Cormack, A.; Kulkarni, A.; Mayton, M.; Sayle, D.; Klaessig, F.; Stadler, B. Exploring the Properties and Applications of Nanoceria: Is There Still Plenty of Room at the Bottom? *Environ Sci Nano* **2014**, *1*, 390–405.

10. Cafun, J.-D.; Kvashnina, K.O.; Casals, E.; Puntes, V.F.; Glatzel, P. Absence of Ce3+ Sites in Chemically Active Colloidal Ceria Nanoparticles. *ACS Nano* **2013**, *7*, 10726–10732.

11. Liu, X.; Zhou, K.; Wang, L.; Wang, B.; Li, Y. Oxygen Vacancy Clusters Promoting Reducibility and Activity of Ceria Nanorods. *J Am Chem Soc* **2009**, *131*, 3140–3141.

12. Esch, F.; Fabris, S.; Zhou, L.; Montini, T.; Africh, C.; Fornasiero, P.; Comelli, G.; Rosei, R. Chemistry: Electron Localization Determines Defect Formation on Ceria Substrates. *Science (1979)* **2005**, *309*, 752–755.

13. Deshpande, S.; Patil, S.; Kuchibhatla, S.V.; Seal, S. Size Dependency Variation in Lattice Parameter and Valency States in Nanocrystalline Cerium Oxide. *Appl Phys Lett* **2005**, *87*, 1–3.

14. Hailstone, R.K.; DiFrancesco, A.G.; Leong, J.G.; Allston, T.D.; Reed, K.J. A Study of Lattice Expansion in CeO2 Nanoparticles by Transmission Electron Microscopy. *Journal of Physical Chemistry C* **2009**, *113*, 15155–15159.

15. Channei, D.; Phanichphant, S.; Nakaruk, A.; Mofarah, S.S.; Koshy, P.; Sorrell, C.C. Aqueous and Surface Chemistries of Photocatalytic Fe-Doped CEO2 Nanoparticles. *Catalysts* **2017**, *7*, 45.

16. Heckman, K.L.; Decoteau, W.; Estevez, A.; Reed, K.J.; Costanzo, W.; Sanford, D.; Leiter, J.C.; Clauss, J.; Knapp, K.; Gomez, C.; et al. Custom Cerium Oxide Nanoparticles Protect against a Free Radical Mediated Autoimmune Degenerative Disease in the Brain. *ACS Nano* **2013**, *7*, 10582–10596.

17. Estevez, A.Y.; Pritchard, S.; Harper, K.; Aston, J.W.; Lynch, A.; Lucky, J.J.; Ludington, J.S.; Chatani, P.; Mosenthal, W.P.; Leiter, J.C.; et al. Neuroprotective Mechanisms of Cerium Oxide Nanoparticles in a Mouse Hippocampal Brain Slice Model of Ischemia. *Free Radic Biol Med* **2011**, *51*, 1155–1163.

18. Yokel, R.A.; Tseng, M.T.; Dan, M.; Unrine, J.M.; Graham, U.M.; Wu, P.; Grulke, E.A. Biodistribution and Biopersistence of Ceria Engineered Nanomaterials: Size Dependence. *Nanomedicine* **2013**, *9*, 398–407.

19. Masui, T.; Hirai, H.; Imanaka, N.; Adachi, G.; Sakata, T.; Mori, H. Synthesis of Cerium Oxide Nanoparticles by Hydrothermal Crystallization with Citric Acid. *J Mater Sci Lett* **2002**, *21*, 489–491.

20. FDA Control of Nitrosamine Impurities in Human Drugs Guidance for Industry. **2021**.

21. CHMP Committee for Medicinal Products for Human Use (CHMP). **2020**.

22. Tauc, J.; Grigorovici, R.; Vancu, A. Optical Properties and Electronic Structure of Amorphous Germanium. *physica status solidi (b)* **1966**, *15*, 627–637.

23. Portillo, M.C.; Moreno, O.P.; Mora-Ramírez, M.A.; Santiesteban, H.J.; Avendaño, C.B.; Bernal, Y.P. Optical and Structural Analysis of the Charge Transfer of Ce3++ E-→Ce4+ Ion in the Cerium Oxide (CeO2). *Optik (Stuttg)* **2021**, *248*, 168178.

24. Zhou, Q.; Akber, H.; Zhao, A.; Yang, F.; Liu, Z. Interaction of Water with Ceria Thin Film. *ChemCatChem* **2023**, *15*, e202300318.

25. Mullins, D.R. The Surface Chemistry of Cerium Oxide. *Surf Sci Rep* **2015**, *70*, 42–85.

26. Wu, X.P.; Gong, X.Q. Clustering of Oxygen Vacancies at CeO2 (111): Critical Role of Hydroxyls. *Phys Rev Lett* **2016**, *116*, 086102.

27. Casals, E.; Gonzalez, E.; Puntes, V.F. Reactivity of Inorganic Nanoparticles in Biological Environments: Insights into Nanotoxicity Mechanisms. *J Phys D Appl Phys* **2012**, *45*, 443001.

28. Vitali, M.; Casals, E.; Canals, F.; Colomé, N.; Puntes, V. Simple Spectroscopic Determination of the Hard Protein Corona Composition in AuNPs: Albumin at 75%. *Nanoscale* **2020**, *12*, 15832–15844.

29. He, X.M.; Carter, D.C. Atomic Structure and Chemistry of Human Serum Albumin. *Nature 1992 358:6383* **1992**, *358*, 209–215.

30. Almeida, F.C.L.; Sanches, K.; Pinheiro-Aguiar, R.; Almeida, V.S.; Caruso, I.P. Protein Surface Interactions—Theoretical and Experimental Studies. *Front Mol Biosci* **2021**, *8*, 706002.

31. Plakhova, T. V.; Romanchuk, A.Y.; Yakunin, S.N.; Dumas, T.; Demir, S.; Wang, S.; Minasian, S.G.; Shuh, D.K.; Tyliszczak, T.; Shiryaev, A.A.; et al. Solubility of Nanocrystalline Cerium Dioxide: Experimental Data and Thermodynamic Modeling. *Journal of Physical Chemistry C* **2016**, *120*, 22615–22626.

32. Auffan, M.; Rose, J.; Bottero, J.Y.; Lowry, G. V.; Jolivet, J.P.; Wiesner, M.R. Towards a Definition of Inorganic Nanoparticles from an Environmental, Health and Safety Perspective. *Nature Nanotechnology 2009 4:10* **2009**, *4*, 634–641.

33. Muhammad, F.; Wang, A.; Qi, W.; Zhang, S.; Zhu, G. Intracellular Antioxidants Dissolve Man-Made Antioxidant Nanoparticles: Using Redox Vulnerability of Nanoceria to Develop a Responsive Drug Delivery System. *ACS Appl Mater Interfaces* **2014**, *6*, 19424–19433.

34. Galyamin, D.; Ernst, L.M.; Fitó-Parera, A.; Mira-Vidal, G.; Bastús, N.G.; Sabaté, N.; Puntes, V. Nanoceria Dissolution at Acidic PH by Breaking off the Catalytic Loop. *Nanoscale* **2022**, *14*, 14223–14230.

35. Murphy, M.P.; Bayir, H.; Belousov, V.; Chang, C.J.; Davies, K.J.A.; Davies, M.J.; Dick, T.P.; Finkel, T.; Forman, H.J.; Janssen-Heininger, Y.; et al. Guidelines for Measuring Reactive Oxygen Species and Oxidative Damage in Cells and in Vivo. *Nat Metab* **2022**, *4*, 651–662.

36. Kannan, K.; Jain, S.K. Oxidative Stress and Apoptosis. *Pathophysiology* **2000**, *7*, 153–163.

37. Slater, A.F.G.; Stefan, C.; Nobel, I.; Van Den Dobbelsteen, D.J.; Orrenius, sten Signalling Mechanisms and Oxidative Stress in Apoptosis. *Toxicol Lett* **1995**, *82–83*, 149–153.

38. Xin, X.; Gong, T.; Hong, Y. Hydrogen Peroxide Initiates Oxidative Stress and Proteomic Alterations in Meningothelial Cells. *Scientific Reports 2022 12:1* **2022**, *12*, 1–10.

39. Park, W.H. The Effects of Exogenous H2O2 on Cell Death, Reactive Oxygen Species and Glutathione Levels in Calf Pulmonary Artery and Human Umbilical Vein Endothelial Cells. *Int J Mol Med* **2013**, *31*, 471–476.

40. Anasooya Shaji, C.; Robinson, B.D.; Yeager, A.; Beeram, M.R.; Davis, M.L.; Isbell, C.L.; Huang, J.H.; Tharakan, B. The Tri-Phasic Role of Hydrogen Peroxide in Blood-Brain Barrier Endothelial Cells. *Sci Rep* **2019**, *9*.

41. Zamzami, N.; Susin, S.A.; Marchetti, P.; Hirsch, T.; Gómez-Monterrey, I.; Castedo, M.; Kroemer, G. Mitochondrial Control of Nuclear Apoptosis. *Journal of Experimental Medicine* **1996**, *183*, 1533–1544.

42. Delia, D.; Aiello, A.; Meroni, L.; Nicolini, M.; Reed, J.C.; Pierotti, M.A. Role of Antioxidants and Intracellular Free Radicals in Retinamide-Induced Cell Death. *Carcinogenesis* **1997**, *18*, 943–948.

43. Voehringer, D.W. BCL-2 and Glutathione: Alterations in Cellular Redox State That Regulate Apoptosis Sensitivity. *Free Radic Biol Med* **1999**, *27*, 945–950.

44. Krug, H.F.; Krug, H.F. Nanosafety Research—Are We on the Right Track? *Angewandte Chemie International Edition* **2014**, *53*, 12304–12319.

45. Licata, A.; Minissale, M.G.; Stankevičiūtė, S.; Sanabria-Cabrera, J.; Lucena, M.I.; Andrade, R.J.; Almasio, P.L. N-Acetylcysteine for Preventing Acetaminophen-Induced Liver Injury: A Comprehensive Review. *Front Pharmacol* **2022**, *13*, 828565.

46. Smilkstein, M.J.; Bronstein, A.C.; Linden, C.; Augenstein, W.L.; Kulig, K.W.; Rumack, B.H. Acetaminophen Overdose: A 48-Hour Intravenous N-Acetylcysteine Treatment Protocol. *Ann Emerg Med* **1991**, *20*, 1058–1063.

47. Pedre, B.; Barayeu, U.; Ezeriņa, D.; Dick, T.P. The Mechanism of Action of N-Acetylcysteine (NAC): The Emerging Role of H2S and Sulfane Sulfur Species. *Pharmacol Ther* **2021**, *228*.

48. Lowe, D. N-Acetyl Cysteine: A Warning Shot. *Science (1979)* 2019.

49. Fazary, A.E.; Awwad, N.S.; Ibrahium, H.A.; Shati, A.A.; Alfaifi, M.Y.; Ju, Y.H. Protonation Equilibria of N-Acetylcysteine. *ACS Omega* **2020**, *5*, 19598.

50. Kundukad, B.; Udayakumar, G.; Grela, E.; Kaur, D.; Rice, S.A.; Kjelleberg, S.; Doyle, P.S. Weak Acids as an Alternative Anti-Microbial Therapy. *Biofilm* **2020**, *2*, 100019.

51. Aruoma, O.I.; Halliwell, B.; Hoey, B.M.; Butler, J. The Antioxidant Action of N-Acetylcysteine: Its Reaction with Hydrogen Peroxide, Hydroxyl Radical, Superoxide, and Hypochlorous Acid. *Free Radic Biol Med* **1989**, *6*, 593–597.

CHAPTER 3

PHARMACOKINETIC PROFILING OF CeO_2 NPs: ABSOPRTION, DISTRIBUTION, METABOLISM, AND EXCRETION

“Theory attracts practice as the magnet attracts iron”

Carl Friedrich Gauss

Chapter 3

Pharmacokinetic Profiling of CeO_2 NPs: Absorption, Biodistribution, Metabolism, and Excretion

3.1 Introduction

The research discussed herein was originally published in 2021 and can be referenced in Annex C Section 7.3.2. Next, a selection of the most relevant parts will be presented.

ADME studies provide crucial insights into how NPs interact with biological systems, including cellular uptake mechanisms, biodistribution within organisms, metabolic transformations, and elimination pathways. These studies not only elucidate the potential toxicity and safety profiles of NPs but also guide the design and optimization of NPs for targeted delivery, controlled release, and enhanced therapeutic efficacy. Furthermore, ADME considerations are vital for regulatory approval and clinical translation of NP-based products. Therefore, comprehensive ADME characterization is fundamental for harnessing the full potential of inorganic NPs in diverse applications and ensuring their safe and effective use in real-world settings.

Despite the appealing therapeutic observations of CeO_2 NPs presented in Chapter 1, there is still a fundamental open question: nanoceria's end of life inside the body and in the environment. To some extent, inorganic NPs are supposed to be non-biodegradable and have a tendency to accumulate in various tissues, persisting there for extended periods. The slow and inefficient clearance rates displayed by inorganic materials raise concerns regarding the long-term toxicity resulting from their accumulation. An example is the case of the so-called frustrated phagocytosis where inorganic matter triggers chronic inflammation preluding cancer, as in the cases of silicosis or asbestosis, where large inorganic particles, induce chronic granulomatosis

[1]. Even if the inorganic matter causing these diseases is orders of magnitude larger than the currently employed NPs, this raises concerns about NP accumulation, aggregation, and excretion from the organism over extended periods.

Today, there are plenty of short-term NP biodistribution studies in the literature, but there is a lack of fate and excretion studies. Excretion is paramount in the development of a drug. The primary natural excretion pathways from the organism are via the liver to faces, and kidneys to urine. Regarding kidney clearance, several studies show how very small NPs, smaller than 6 nm (hydrodynamic diameter), can be readily cleared from the body via the urinary tract [2,3]. Note that glomerular filtration not only depends on size but also depends on molecule charge [4]. Thus, Kobayashi and co-workers [5] showed that glomerular filtration depended on whether the charge was positive or negative, showing enhanced filtration for cationic molecules. Other researchers reported similar observations on NP charge and size effects [3]. Clearance from the liver is more complex, leading to a slower elimination rate than urine excretion. This slow clearance rate is mediated by the hepatobiliary route. The clearance of NPs from the blood into the liver, and from the liver into faeces has been well described in the studies of Pr. Warren Chan [6,7].

3.2 Scope of the study

This study investigates the long-term accumulation and excretion of ~3 nm CeO_2 NPs in healthy mice following a single intravenous (IV) administration. It also compares these findings with related experiments. Additionally, the study examines the shorter-term accumulation and renal and fecal excretion of CeO_2 NPs in model rats administered via IV, oral, and intracranial routes.

3.3 Results and discussion

3.3.1 Heterogenic distribution of NPs

According to our experience and the current literature, CeO_2 NPs accumulate largely in the liver (85-90%) and spleen (~10%). Interestingly, this occurs both in healthy and liver-diseased models, as in hepatocellular carcinoma [8] or liver steatosis [9]. Indeed, liver accumulation of NPs has been extensively described in the scientific literature. An extended work can be found in reference [6], where the clearance of the NPs from blood to the liver is reported. In all those cases, the administered NPs were given at different doses and administration schedules, and despite originating from similar synthesis methods, they had different formulations mainly in terms of surface state and aggregation states yet ended up in similar locations. Moreover, it often seems assumed that NPs are homogeneously distributed within organs, but organs are complex and host different tissues and cell types, and therefore biodistribution inside the organs is expected to be heterogeneous. A particularly interesting study examined blood clearance mechanisms in relation to flow dynamics, cellular phenotype, and vessel microstructure [6]. They found that slower blood flow within organs enhances the possibility of NP retention, which can aid in predicting accumulation regions inside an organ. Here, in model cirrhotic rats, injected CeO_2 NPs (5 nm aggregated in 30 nm clusters as described in Ref. [9]), were found heterogeneously distributed in the liver, as shown in **Figure 3.1A**, indicating that organs must be fully digested or homogenized before analysing a fraction for elemental analysis.

Besides, once in a particular organ, NPs can be processed by different types of cells. For instance, in the liver, NPs can be taken up by hepatocytes, described as the main cells responsible for hepatic filtration [10], or by Kupffer cells, the resident macrophages in the liver, responsible for the elimination of apoptotic bodies, protein aggregates, and foreign matter [7]. However, we recently observed selective capture of NPs by hepatic stellate cells in the mice liver after a single IV injection (**Figure 3.1BC**). In this work, we employed 50 nm AuNPs so they could be observed in reflectance mode in the confocal microscope without the need for labels at the NP surface [11], which could affect their biodistribution. This is not expected to be a general trend or

applicable to CeO_2 NPs, but this selective NP uptake illustrates a most likely widespread event.

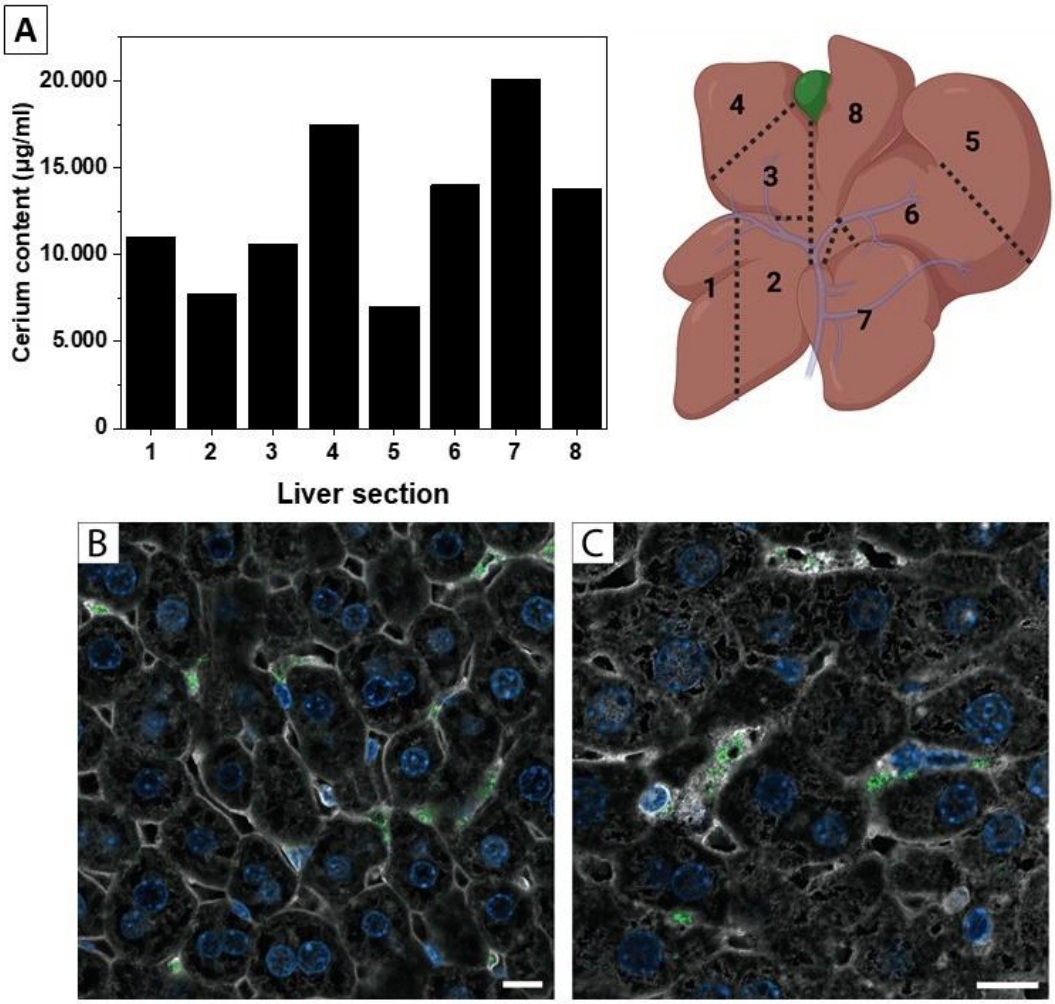


Figure 3.1. Heterogeneity in organ distribution. (A) Liver biodistribution of nanoceria 24 hours after IV administration, and liver schema of the digested tissue sections. The liver was divided into 8 parts (schema), and the Cerium content of each section is represented in the graph. (B, C) Confocal images of 50 nm AuNPs in reflectance mode of a liver thin cut after IV administration of NPs to healthy mice at (B) 40x magnification and (C) 60x magnification. Actin (white), Hoechst (blue), and NPs (green). Scale bar = 10 µm.

3.3.2 ADME in healthy preclinical models

Next, the fate of synthesized ~3 nm CeO_2 NPs IV administered in healthy mice was assessed. Size is one of the parameters that has been the focus of understanding NPs' biodistribution, accumulation, and clearance. As a first observation, it has been postulated that the bigger the NPs are, the narrower their organ distributions [12]. Size may also have a substantial impact on NP integrity. As shown previously, small CeO_2

NPs, particularly those with a diameter of 30 nm or below, are more prone to dissolution due to lower activation energy [13], leaving NPs of 3 nm on the verge of dissolution. Once dispersed in neutral pH, in the redox conditions of living systems, their thermodynamic fate is to reduce back and dissolve into Ce^{3+} ions. Indeed, as commented before, rapid dissolution of CeO_2 NPs has been reported inside late endosomes and endolysosomes [14], and at acidic pH during colorimetric detection of analytes [15] (Chapter 2, section 2.3.2.3 Corrosion).

Once CeO_2 NPs were produced under sterile conditions, tested for endotoxin content, and albuminized with murine serum albumin (MSA), a single dose of CeO_2 NPs was administered IV at 5.7 mg/kg of body weight (BW), and animals were euthanized at different times points after injection: 1, 9, 30, and 100 days (n = 5 mice per time point). Although the lateral tail vein is commonly used for administration, we opted for retro-orbital injection in the ophthalmic venous sinus at the back of the eye socket. The reason is that administration in the secondary vein network improves biocompatibility and prevents adverse infusion reactions. During the experiments, all animals maintained a healthy weight and appearance and exhibited normal activity without lethargy or apathy after NP administration (see **Figure 7.1**, Annex B, section 7.2).

Thereafter, cerium concentrations in various organs including the liver, spleen, kidney, lung, brain, lymph nodes, ovaries, bone marrow, urine, and faeces were determined using ICP-MS. As expected, the results revealed the primary accumulation of CeO_2 in the liver and spleen (82% and 5% of the injected dose (ID), respectively) (**Figure 3.2**). cerium was not detected in the brain and showed extremely low levels in the other organs, although its presence could be observed in the kidneys, lungs, lymph nodes, ovaries, and bone marrow.

Over time, the concentration of Ce in the different organs progressively diminished. The most significant elimination was observed in the liver, with a decrease from 82% to 40% of ID between day 1 and day 100. The spleen exhibited the second-highest accumulation, but the clearance rate was slower (see the excretion rates for the different organs in **Figure 7.2**, Annex B, section 7.2).

In the kidney, lung, bone marrow, and ovaries there was low accumulation, and slow clearance rates. Interestingly, on day 30, cerium concentration increased in the lymph nodes, which may suggest some re-distribution over longer times. Traditionally, the spleen has received little attention in pharmacology due to its minor role in the disposition and excretion of "classical" drugs, but this is changing for "new" generation drugs (NPs, recombinant proteins, and monoclonal antibodies) [16]. For example, Demoy et al. demonstrated the pivotal role of spleen marginal zone macrophages in the uptake of polystyrene NPs [17]. We hypothesize that in our study, a small portion of CeO_2 NPs may have been retained in spleen macrophages, which are known for their slower clearance rate, as discussed below.

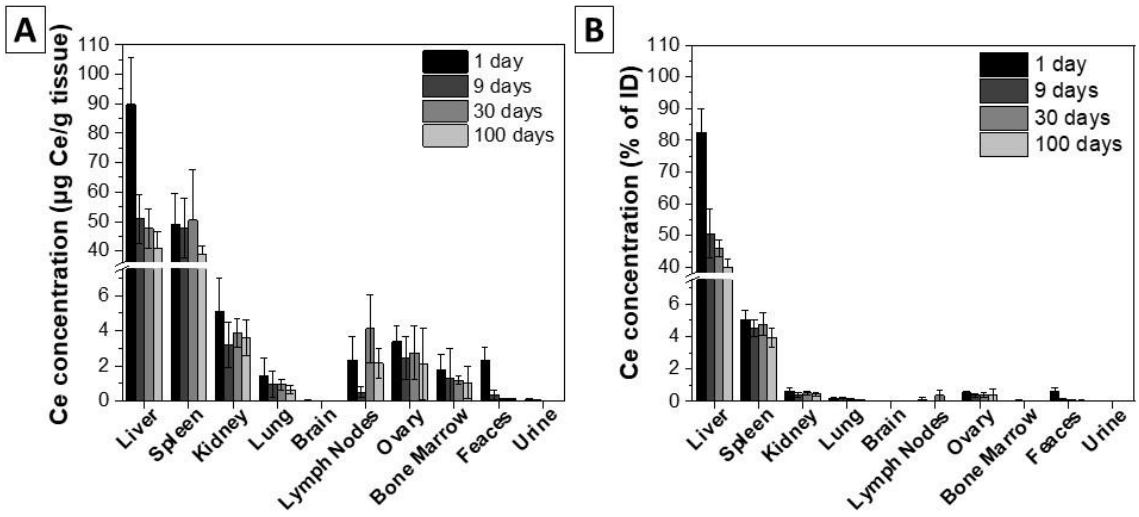


Figure 3.2. Organ cerium concentration was measured by ICP-MS 1, 9, 30, and 100 days after a single CeO_2 IV administration (5.7 mg/Kg BW). (A) Cerium concentration (µg Ce/g tissue). (B) Cerium as a percentage of the injected dose. n = 5.

The results suggest that the primary clearance route is hepatobiliary elimination, with a ~60% decrease in the liver and ~50% reduction in the whole body 100 days after injection. This hypothesis is also supported by the observed cerium content in the faecal samples. Interestingly, excretion is most pronounced within the first 24 hours post-injection, showing the highest peak of cerium content in the collected faeces. With time, cerium is also detected in urine. Given the hydrodynamic diameter (6.28 ± 1.6 nm; PDI = 0.47), surface charge (-38.9 ± 16.7 mV), and core density of CeO_2 NPs, it is improbable that particles undergo renal clearance. Additionally, other studies have not reported significant urine excretion [18]. Therefore, these traces found in urine are

likely ionic cerium coming from CeO_2 dissolution. All in all, this suggests elimination by the two main described mechanisms: (i) renal excretion of cerium ions (Ce^{3+}) and (ii) hepatobiliary elimination of CeO_2 NPs.

Despite the limited number of time points in **Figure 3.2**, we fitted the evolution of cerium content in the liver and in all measured organs (AMO) vs. time to standard pharmacokinetic models. These models assume that small drugs diffuse rather passively through the body, following first-order reaction kinetics, which can be described by an exponential decay of cerium concentration over time. These models help predict NP concentrations over time and optimize drug dosing regimens. Here, one exponential term was used for the one-compartment model, and two exponential terms were used for the two-compartment model [19,20]. The one-compartment model assumes that the NPs are rapidly and uniformly distributed throughout the body, with the rate of NPs elimination proportional to the amount of drug present and describes a simple exponential decay of drug concentration over time. The two-compartment model assumes that NPs are distributed into two compartments: a central compartment (such as blood) and a peripheral compartment (such as tissues), typically involving two exponential terms to describe the distribution and elimination phases separately. As shown in **Figure 3.3**, deviation from the two-compartment model indicates how the system eliminates cerium in a more active form, with peripheral distribution making no significant contribution, thus exhibiting a monomodal exponential decay pattern.

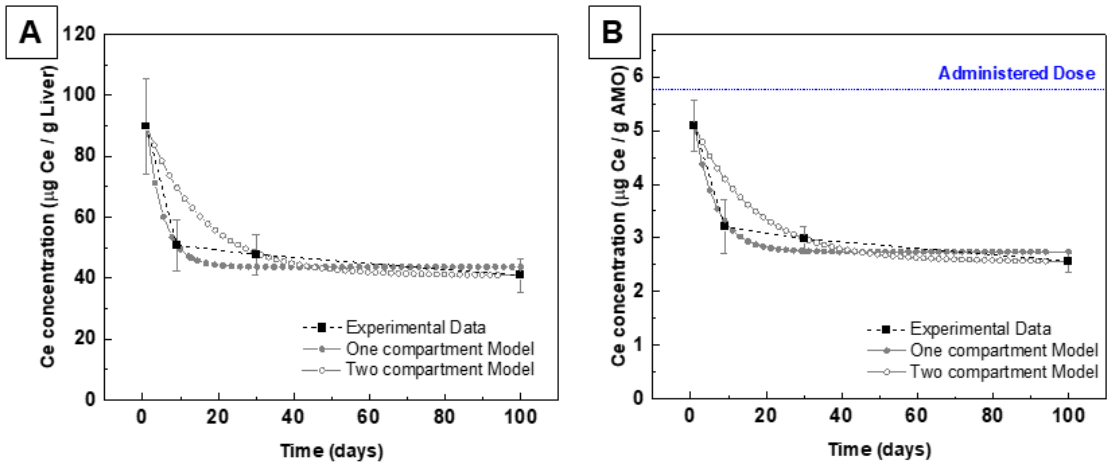


Figure 3.3. Pharmacokinetics of CeO_2 NPs at 1, 9, 30, and 100 days post-injection: (A) in the liver and (B) in all measured organs (AMO). Black squares are experimental data, solid grey circles are the one-compartment

model fitting, and hollow grey circles are the two-compartment model fitting. Blue lines correspond to the administered dose.

In addition, it appears that after the ninth day and beyond, there is a rather monotonous decrease in the cerium concentration, which may indicate a slow excretion of cerium ions generated over time. On one hand, different fractions of nanoceria may coexist, with some CeO_2 NPs potentially remaining permanently in the body, captured inside tissue macrophages or blood monocytes. On the other hand, CeO_2 NPs should completely dissolve over time in biological conditions, regardless of location, accounting for the slow monotonous decrease in ceria concentration observed at long times. A physiologically based pharmacokinetic modelling of CeO_2 systemic distribution in rats [21] showed similar results, particularly regarding the different fates of NPs depending on administration route, surface, size, and physicochemical properties.

3.1.1.1 Excretion of CeO_2 NPs in CCl_4-Treated Rats

In collaboration with Prof. Wladimiro Jiménez from the service of Biochemistry and Molecular Genetics at the Hospital Clinic, cerium recovery in urine and faeces was monitored during the experimental timeline by placing the animals in metabolic cages. This study used Wistar rats with hepatic fibrosis induced by repetitive CCl_4 inhalation and phenobarbital-containing drinking water. These animals received IV injections of CeO_2 NPs (0.1 mg/Kg BW) twice a week for two consecutive weeks, starting in the seventh week after CCl_4 administration began [9]. To prioritize animal welfare, the time spent in metabolic cages was minimized. Thus, following the last dose of CeO_2 NPs, animals were monitored in metabolic cages for 24 hours to measure cerium concentration in urine and faeces at intervals of 3, 21, 42, and 56 days. As depicted in **Figure 3.4**, while the faecal content of cerium decreased exponentially, a rather monotonous cerium concentration was observed in urine, suggesting slow and progressive dissolution of CeO_2 into cerium ions and its corresponding renal excretion [22].

These findings are consistent with other studies where IV injection of CeO_2 NPs with similar size and surface coating resulted in localization within both Kupffer cells and

hepatocytes [23]. It is worth noting that both cell types possess phagocytic capacities, although hepatocytes are directly implicated in the pathway for biliary excretion (NPs found here will be potentially excreted to the bile), whereas Kupffer cells can only eliminate CeO_2 NPs via intracellular degradation. Importantly, the uptake of CeO_2 NPs by Kupffer cells often leads to mild and transient activation of the immune system [23], calling for a careful examination of the immunogenic properties of designed NPs.

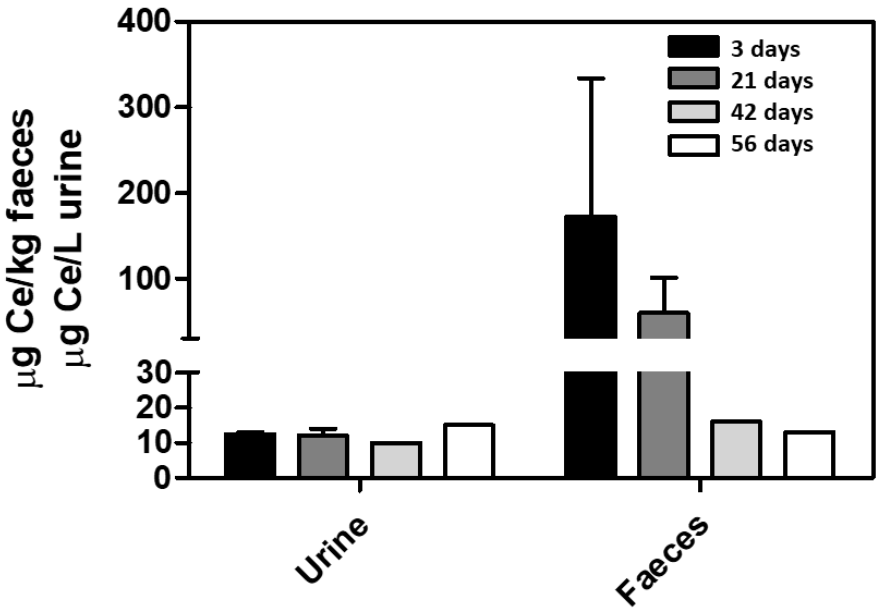


Figure 3.4. CeO_2 NPs excretion in rats. Cerium concentration was measured by ICP-MS in urine and faeces from CCl_4-treated rats 3, 21, 42, and 56 days after IV nanoceria administration (0.1 mg/Kg BW) twice weekly for two weeks. n = 3.

Regarding long-term accumulation of CeO_2 NPs, it's worth mentioning the studies conducted by Yokel et al. [24,25], where a large dose of 30 nm cubic CeO_2 NPs (87 mg/Kg BW) was IV administered to rats, followed by exhaustive accumulation and excretion assessments on days 1, 7, 30, and 90. In these studies, CeO_2 NPs were once again primarily accumulated in the liver, spleen, and bone marrow. Interestingly, the clearance of NPs from blood was examined for two weeks, revealing that less than 1% of the CeO_2 NPs were removed, with only a slight decrease observed in any tissue over the course of 90 days. In addition, although significant NP presence in the blood a few hours after injection was not observed in our previous studies (data not shown), this study revealed a significant cerium blood content after 90 days, suggesting potential particle endocytosis by blood cells. This disparity in results is likely attributable to

differences in the physicochemical properties of the CeO_2 NPs used, such as size (large vs. small), aggregated state (aggregated vs. non-aggregated), and morphology (cubic vs. spherical).

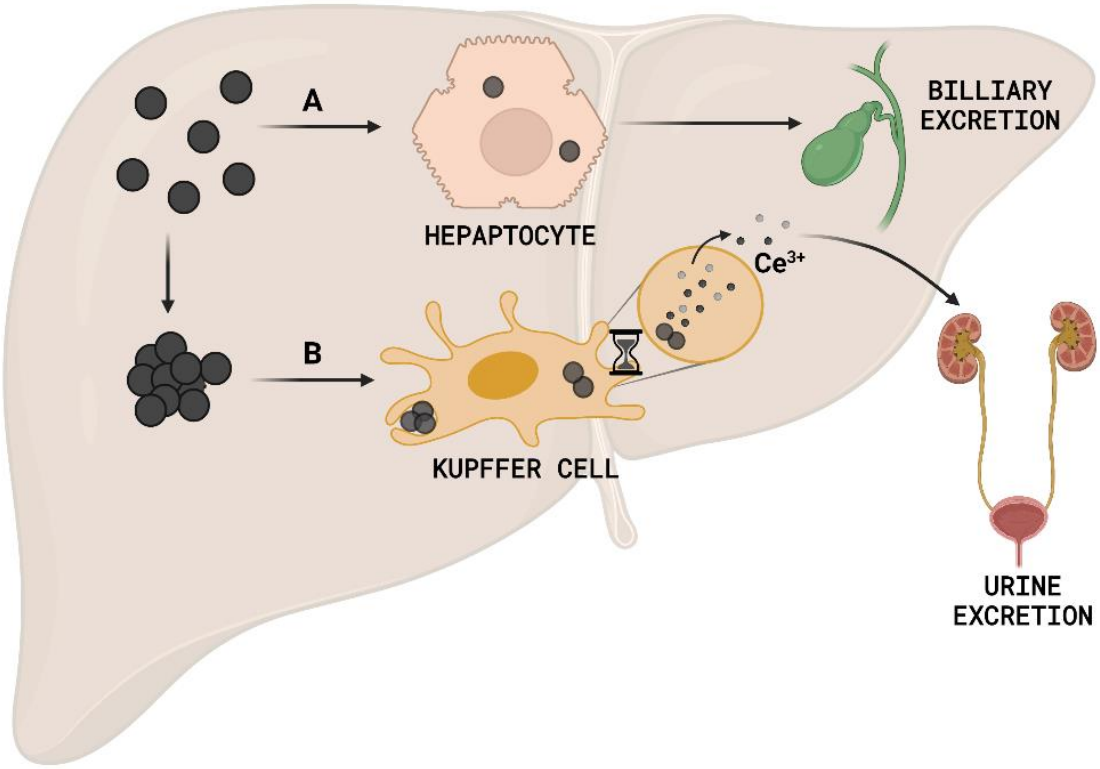


Figure 3.5. Hypothetical in vivo management of 3 nm CeO_2 NPs. After liver accumulation, (A) hepatocytes rapidly process non-immunogenic CeO_2 NPs to the biliary excretion, (B) while CeO_2 NPs detected by Kupffer cells will remain inside the cell until they completely dissolve, and the produced Ce^{3+} ions are then excreted via the urine.

Interestingly, despite similarities in biodistribution and target organs, excretion profiles seem to differ widely. One could hypothesize that NPs reaching the liver and processed by hepatocytes will be eliminated from the body via the hepatobiliary route, leading to fast excretion rates. In contrast, NPs phagocytosed by resident macrophages like Kupffer cells in the liver may remain within macrophages indefinitely, while NPs may slowly dissolve, generating Ce^{3+} ions that are eventually excreted via the urinary tract, resulting in slower excretion rates (**Figure 3.5**).

3.1.1.2 Distribution of CeO_2 NPs in the brain after intracranial injection

In collaboration with Dr. Miquel Vila from the neurodegenerative diseases group at Vall Hebron Research Institute, CeO_2 NPs were tested in a rat model of Parkinson's disease. The model utilizes viral vector-mediated expression of the melanin-producing enzyme tyrosinase (TYR) in the substantia nigra of rats [26]. This humanized neuromelanin-producing animal model exhibits enhanced features of Parkinson's disease.

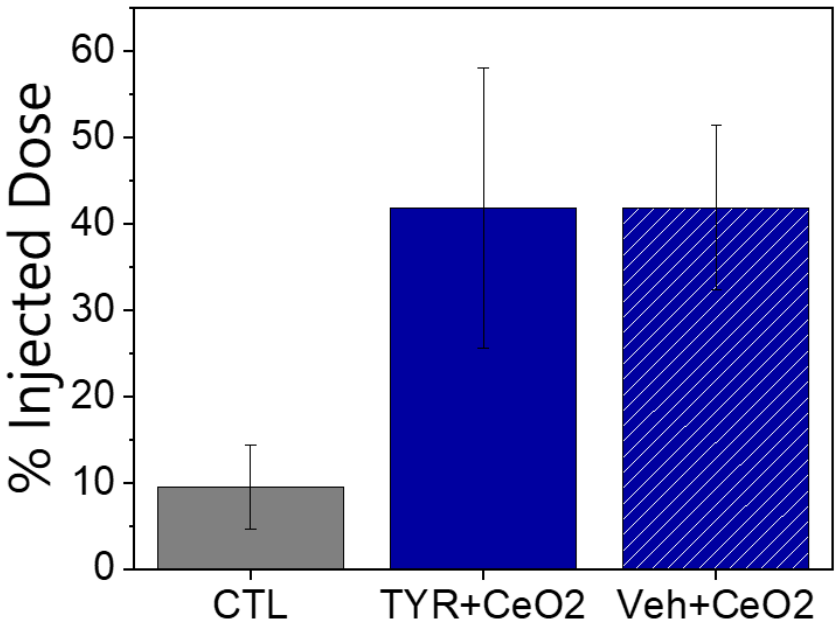


Figure 3.6. Cerium content, measured by ICP-MS, in the brains of healthy animals (control and CeO_2-injected) and Parkinson's model rats (TYR) 120 days after intracranial injection of 2 µg of CeO_2 NPs per brain.

The animals received an intracranial injection of 2 µg CeO_2 NPs. Remarkably, 120 days post-injection, a notable ~50% reduction in total cerium content within the brain was observed (**Figure 3.6**). This finding suggests a gradual excretion process of CeO_2 NPs from the cerebral tissue, likely attributable to the slow dissolution kinetics of the NPs.

3.1.1.3 Organ Distribution of CeO_2 after Oral Administration in Healthy Rats

Last, the impact of oral administration was also investigated. CeO_2 NPs dispersed in a PEG solution, were orally administered to healthy Wistar rats (10 mg CeO_2/Kg BW)

for 14 days. Although most of the cerium was excreted in faeces, a portion entered the body and was detected in various organs, albeit at different concentrations than in the case of parenteral administration (**Figure 3.7**). Despite PEG coating, exposure to rat gastrointestinal fluid facilitated rapid NP dissolution into Ce^{3+} ions, which have been reported to mimic Ca^{2+} and can be absorbed in the body without long-term accumulation, thus being excreted through the urine [27].

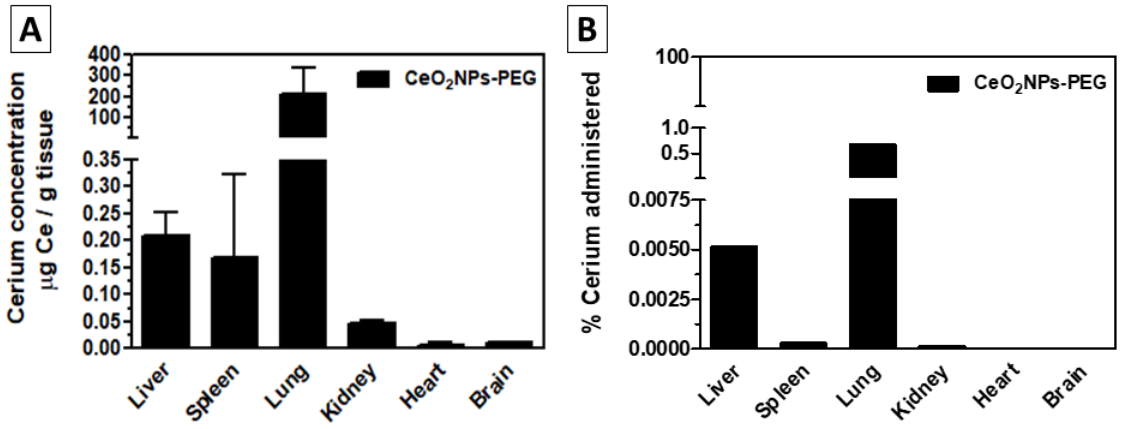


Figure 3.7. Organ biodistribution after oral administration of CeO_2-PEG coated NPs (CeO_2NPs-PEG) in healthy rats. CeO_2NPs-PEG were delivered daily by intragastric administration (10 mg CeO_2/Kg BW) for 14 days. Major organs and serum were collected 72 hours after the last administration. ICP-MS measured cerium concentration. (A) Cerium concentration in µg Ce/g tissue. (B) Cerium as a percentage of the administered dose. n = 3.

Dispersion of CeO_2 NPs in simulated acidic solution (pH 1.7) showed both NP aggregation, due to the protonation of SC at stomach pH, and dissolution of the NPs. Assuming an average residence time in the stomach of about two hours, it appears that after a rapid agglomeration, nearly half of the CeO_2 NPs dissolve while the rest remain as aggregates (see **Figure 3.8**). Furthermore, the dissolution of particles into ions could account for their elimination through the kidneys and their notable accumulation in the lungs. Note that $CeCl_3$ (Ce^{3+}) administered IV to mice has been reported to accumulate in the lungs before renal excretion [22]. Moreover, there is a case report of an individual who accidentally ingested about 1000 mL of a nanoceria-containing solution while working in an industrial setting where CeO_2 NPs (aggregated 20–40 nm NPs) were utilized as a polishing agent [28]. Cerium was detected in both her blood and urine. Surprisingly, the only symptoms he presented were transient scattered red petechial, mainly in her face, and decreased plasma coagulation factors. Although anticoagulant

properties have been attributed to cerium ions and other rare earth materials [22,29], there have been no reports of similar effects associated with their nanoscale counterparts, as far as we know.

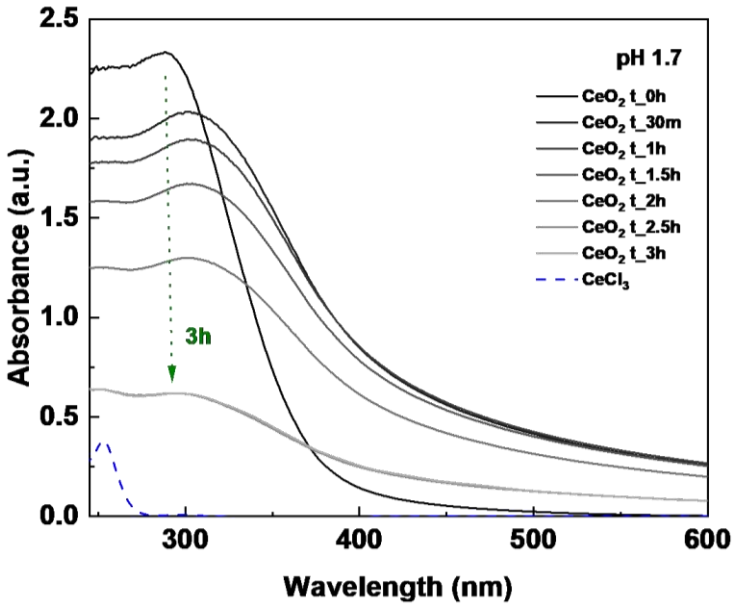


Figure 3.8. Dissolution of CeO_2 NPs at pH 1.7. CeO_2 NPs were exposed to acidic media. A decrease in UV-vis absorbance maximum with time confirms that NPs gradually dissolve.

In conclusion, while it seems universal that NPs are primarily captured in the liver, followed by the spleen, regardless of their difference in dose, morphology, aggregation, and surface state, or whether they are taken up by immune or filtering cells. However, the clearance rates from the body appear to be extremely dependent on those NP characteristics.

In this model, NPs that evade the immune system may be eliminated through the hepatobiliary route, while nanoceria captured by circulating monocytes or resident macrophages can dissolve, with cerium ions subsequently excreted through the urinary tract. The slow excretion of CeO_2 NPs from the body holds promise for its medical development; however, the low excretion rates raise concerns about potential toxic accumulation with repeated dosing [30]. Interestingly, in toxicity studies, no adverse effects were found at concentrations significantly higher than therapeutic doses, even after CeO_2 NPs oral administration at 1000 mg/Kg BW for 14 days [31], suggesting the possibility of repeated administration despite slow excretion. Accumulation in the

spleen also deserves special attention since much slower clearance rates have been observed.

It is remarkable that until now, CeO_2 NPs have been known to persist in the body for extended periods without being excreted and have also been linked to mild pro-inflammatory activation. However, our study demonstrates that non-immunogenic, small, highly soluble, non-aggregated CeO_2 NPs can indeed be excreted and degraded, paving the progress towards converting nanoceria into an active pharmaceutical ingredient. All this data and considerations should help to better understand the pharmacokinetics of CeO_2 NPs to enable its successful translation to clinical use.

3.4 References

1. Mossman, B.T.; Churg, A. Mechanisms in the Pathogenesis of Asbestosis and Silicosis. *https://doi.org/10.1164/ajrccm.157.5.9707141* **2012**, *157*, 1666–1680.

2. Longmire, M.; Choyke, P.L.; Kobayashi, H. Clearance Properties of Nano-Sized Particles and Molecules as Imaging Agents: Considerations and Caveats. *Nanomedicine (Lond)* **2008**, *3*, 703.

3. Soo Choi, H.; Liu, W.; Misra, P.; Tanaka, E.; Zimmer, J.P.; Itty Ipe, B.; Bawendi, M.G.; Frangioni, J. V. Renal Clearance of Quantum Dots. *Nat Biotechnol* **2007**, *25*, 1165–1170.

4. Comper, W.D.; Glasgow, E.F. Charge Selectivity in Kidney Ultrafiltration. *Kidney Int* **1995**, *47*, 1242–1251.

5. Kobayashi, H.; Le, N.; Kim, I.-S.; Kim, M.-K.; Pie, J.-E.; Drumm, D.; Paik, D.S.; Waldmann, T.A.; Paik, C.H.; Carrasquillo, J.A.; et al. The Pharmacokinetic Characteristics of Glycolated Humanized Anti-Tac Fabs Are Determined by Their Isoelectric Points. *Cancer Res* **1999**, *59*, 422–430.

6. Tsoi, K.M.; Macparland, S.A.; Ma, X.Z.; Spetzler, V.N.; Echeverri, J.; Ouyang, B.; Fadel, S.M.; Sykes, E.A.; Goldaracena, N.; Kaths, J.M.; et al. Mechanism of Hard-Nanomaterial Clearance by the Liver. *Nat Mater* **2016**, *15*, 1212–1221.

7. W, P.; YN, Z.; B, O.; BR, K.; JLY, W.; S, W.; WCW, C. Elimination Pathways of Nanoparticles. *ACS Nano* **2019**, *13*, 5785–5798.

8. Fernández-Varo, G.; Perramón, M.; Carvajal, S.; Oró, D.; Casals, E.; Boix, L.; Oller, L.; Macías-Muñoz, L.; Marfà, S.; Casals, G.; et al. Bespoken Nanoceria: An Effective Treatment in Experimental Hepatocellular Carcinoma. *Hepatology* **2020**, *72*, 1267–1282.

9. Oró, D.; Yudina, T.; Fernández-Varo, G.; Casals, E.; Reichenbach, V.; Casals, G.; González de la Presa, B.; Sandalinas, S.; Carvajal, S.; Puntes, V.; et al. Cerium Oxide Nanoparticles Reduce Steatosis, Portal Hypertension and Display Anti-Inflammatory Properties in Rats with Liver Fibrosis. *J Hepatol* **2016**, *64*, 691–698.

10. Kuntz, E.; Kuntz, H.-D. *Hepatology Textbook and Atlas*; 3rd edition.; Springer Berlin Heidelberg: Graz, Austria, 2008;

11. Gusta, M.F.; Ernst, L.M.; Moriones, O.H.; Piella, J.; Valeri, M.; Bastus, N.G.; Puntes, V. Long-Term Intracellular Tracking of Label-Free Nanoparticles in Live Cells and Tissues with Confocal Microscopy. *Small Methods* **2024**.

12. Sonavane, G.; Tomoda, K.; Makino, K. Biodistribution of Colloidal Gold Nanoparticles after Intravenous Administration: Effect of Particle Size. *Colloids Surf B Biointerfaces* **2008**, *66*, 274–280.

13. Auffan, M.; Rose, J.; Bottero, J.Y.; Lowry, G. V.; Jolivet, J.P.; Wiesner, M.R. Towards a Definition of Inorganic Nanoparticles from an Environmental, Health and Safety Perspective. *Nature Nanotechnology 2009 4:10* **2009**, *4*, 634–641.

14. Muhammad, F.; Wang, A.; Qi, W.; Zhang, S.; Zhu, G. Intracellular Antioxidants Dissolve Man-Made Antioxidant Nanoparticles: Using Redox Vulnerability of Nanoceria to Develop a Responsive Drug Delivery System. *ACS Appl Mater Interfaces* **2014**, *6*, 19424–19433.

15. Galyamin, D.; Ernst, L.M.; Fitó-Parera, A.; Mira-Vidal, G.; Bastús, N.G.; Sabaté, N.; Puntes, V. Nanoceria Dissolution at Acidic PH by Breaking off the Catalytic Loop. *Nanoscale* **2022**, *14*, 14223–14230.

16. Cataldi, M.; Vigliotti, C.; Mosca, T.; Cammarota, M.R.; Capone, D. Emerging Role of the Spleen in the Pharmacokinetics of Monoclonal Antibodies, Nanoparticles and Exosomes. *Int J Mol Sci* **2017**, *18*.

17. Demoy, M.; Andreux, J.P.; Weingarten, C.; Gouritin, B.; Guilloux, V.; Couvreur, P. In Vitro Evaluation of Nanoparticles Spleen Capture. *Life Sci* **1999**, *64*, 1329–1337.

18. Park, K.; Park, J.; Lee, H.; Choi, J.; Yu, W.J.; Lee, J. Toxicity and Tissue Distribution of Cerium Oxide Nanoparticles in Rats by Two Different Routes: Single Intravenous Injection and Single Oral Administration. *Arch Pharm Res* **2018**, *41*, 1108–1116.

19. Dubaj, T.; Kozics, K.; Sramkova, M.; Manova, A.; Bastús, N.G.; Moriones, O.H.; Kohl, Y.; Dusinska, M.; Runden-Pran, E.; Puntes, V.; et al. Pharmacokinetics of PEGylated Gold Nanoparticles: In Vitro-In Vivo Correlation. *Nanomaterials (Basel)* **2022**, *12*.

20. Ahmed, T.A.; Ahmed, T.A. Pharmacokinetics of Drugs Following IV Bolus, IV Infusion, and Oral Administration. *Basic Pharmacokinetic Concepts and Some Clinical Applications* **2015**.

21. Carlander, U.; Moto, T.P.; Desalegn, A.A.; Yokel, R.A.; Johanson, G. Physiologically Based Pharmacokinetic Modeling of Nanoceria Systemic Distribution in Rats Suggests Dose- and Route-Dependent Biokinetics. *Int J Nanomedicine* **2018**, *13*, 2631–2646.

22. Kawagoe, M.; Ishikawa, K.; Wang, S.C.; Yoshikawa, K.; Arany, S.; Zhou, X.P.; Wang, J.S.; Ueno, Y.; Koizumi, Y.; Kameda, T.; et al. Acute Effects on the Lung and the Liver of Oral Administration of Cerium Chloride on Adult, Neonatal and Fetal Mice. *J Trace Elem Med Biol* **2008**, *22*, 59–65.

23. Yokel, R.A.; Hussain, S.; Garantziotis, S.; Demokritou, P.; Castranova, V.; Cassee, F.R. The Yin: An Adverse Health Perspective of Nanoceria: Uptake, Distribution, Accumulation, and Mechanisms of Its Toxicity. *Environ Sci Nano* **2014**, *1*, 406.

24. Yokel, R.A.; Au, T.C.; MacPhail, R.; Hardas, S.S.; Butterfield, D.A.; Sultana, R.; Goodman, M.; Tseng, M.T.; Dan, M.; Haghnazar, H.; et al. Distribution, Elimination, and Biopersistence to 90 Days of a Systemically Introduced 30 Nm Ceria-Engineered Nanomaterial in Rats. *Toxicol Sci* **2012**, *127*, 256–268.

25. Yokel, R.A.; Tseng, M.T.; Dan, M.; Unrine, J.M.; Graham, U.M.; Wu, P.; Grulke, E.A. Biodistribution and Biopersistence of Ceria Engineered Nanomaterials: Size Dependence. *Nanomedicine* **2013**, *9*, 398–407.

26. Gonzalez-Sepulveda, M.; Compte, J.; Cuadros, T.; Nicolau, A.; Guillard-Sirieix, C.; Peñuelas, N.; Lorente-Picon, M.; Parent, A.; Romero-Gimenez, J.; Cladera-Sastre, J.M.; et al. In Vivo Reduction of Age-Dependent Neuromelanin Accumulation Mitigates Features of Parkinson's Disease. *Brain* **2023**, *146*, 1040.

27. Liang, Q.; Yin, H.; Li, J.; Zhang, L.; Hou, R.; Wang, S. Investigation of Rare Earth Elements in Urine and Drinking Water of Children in Mining Area. *Medicine* **2018**, *97*.

28. Lu, Y.Q. Coagulation Disorders Following an Accidental Ingestion of Cerium Dioxide Nanoparticles. *Environ Toxicol Pharmacol* **2021**, *82*.

29. Funakoshi, T.; Furushima, K.; Shimada, H.; Kojima, S. Anticoagulant Action of Rare Earth Metals. *Biochem Int* **1992**, *28*, 113–119.

30. Casals, E.; Gusta, M.F.; Piella, J.; Casals, G.; Jiménez, W.; Puntes, V. Intrinsic and Extrinsic Properties Affecting Innate Immune Responses to Nanoparticles: The Case of Cerium Oxide. *Front Immunol* **2017**, *8*, 264030.

31. Lee, J.; Jeong, J.S.; Kim, S.Y.; Lee, S.J.; Shin, Y.J.; Im, W.J.; Kim, S.H.; Park, K.; Jeong, E.J.; Nam, S.Y.; et al. Safety Assessment of Cerium Oxide Nanoparticles: Combined Repeated-Dose Toxicity with Reproductive/Developmental Toxicity Screening and Biodistribution in Rats. *https://doi.org/10.1080/17435390.2020.1751322* **2020**, *14*, 696–710.

CHAPTER 4

PHARMACODYNAMICS OF CeO_2 NPs: IMMUNE MODULATION AND METABOLISM

“To ask the right question is harder than to answer it.”

Georg Cantor

Chapter 4

Pharmacodynamics of CeO_2 NPs: Immune Modulation and Metabolism

Prelude: Energy-Metabolism Concepts

In emerging fields like immunometabolism, inconsistent nomenclature for biochemical pathways has complicated the construction of knowledge. Here, to ensure communication and to align with the scientific community, we aim to briefly explain the main catabolic pathways and the nomenclature that will be used in this study. Catabolic processes generate the energy and intermediates required for anabolism, which drives biosynthesis and growth, and there exists a variety of complex reactions and interrelations between them. Cells require energy (adenosine triphosphate; ATP) and starting materials for biosynthesis to sustain thousands of metabolic pathways. In eukaryotic organisms, two primary catabolic pathways fulfil these needs: (i) glycolysis and (ii) the tricarboxylic acid (TCA) cycle.

Glycolysis, the conversion of glucose to pyruvate, is the initial step in both fermentation and TCA cycle. The TCA cycle is the primary pathway in aerobic organisms for the oxidation of biofuels (carbohydrates, lipids, and proteins), and it is the most efficient energy production pathway in eukaryotic cells. Within the mitochondria, smaller molecules derived from glucose, fatty acids, and amino acids are transformed into acetyl-CoA. Acetyl-CoA enters the TCA cycle, where it is further oxidated to CO_2 and water, producing reducing equivalents (NADH and $FADH_2$). These reducing equivalents are oxidized through the ETC, leading to ATP production in a process known as oxidative phosphorylation (OXPHOS)[6]. Alternatively, pyruvate can undergo partial oxidation to lactate in the cytosol through a process known as

[6] OXPHOS refers to the process by which ATP is synthesized using the energy released by the transfer of electrons through the ETC.

fermentation. While fermentation does not directly produce ATP it plays a crucial role in regenerating NAD+, which is essential for maintaining glycolysis and diverting glucose flux away from the mitochondria.

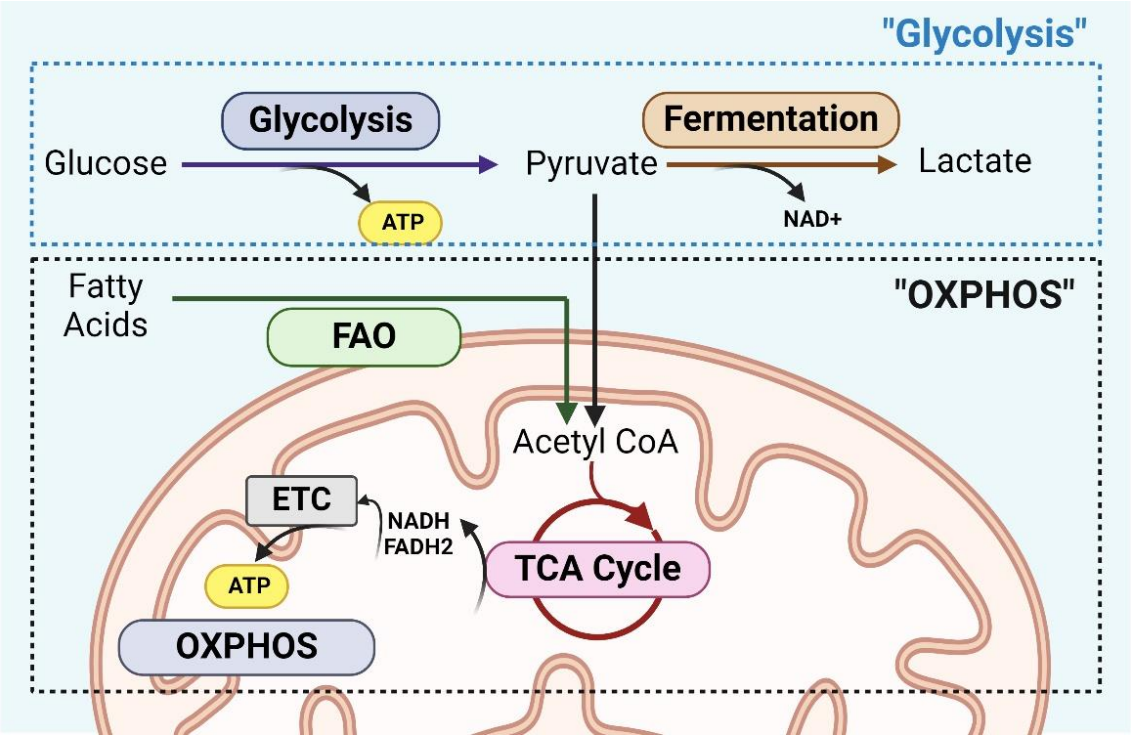


Figure 4.1. Main catabolic pathways in eukaryotic organisms and their nomenclature.

Here, the standard nomenclature of the immunometabolism field will be used. Hereto, the term "glycolysis" will refer to the oxidation of glucose to lactate, and "OXPHOS" or "mitochondrial respiration" will refer to all mitochondrial reactions driving ATP production, including the TCA cycle, ETC, and OXPHOS (**Figure 4.1**).

It's important to note that glycolysis is an anaerobic process, but it also occurs when oxygen is available. Thus, many authors refer to glycolysis as either aerobic or anaerobic, but in some contexts, this nomenclature may mistakenly suggest the involvement of different metabolic pathways, whereas the pathway itself remains unchanged. Oxygen serves as a regulatory factor, yet its presence does not deactivate fermentation. Interestingly, if anaerobic glycolysis is upregulated in oxygen-depleted environments, leads to the suggestion that oxygen may act as a negative regulator of glycolytic flux. But, if an increase in the glycolytic rate occurs in high oxygen concentrations, it indicates that oxygen is not the only factor influencing glycolysis. It

is a fallacy to consider any proposed regulatory input as the only factor affecting a control system. The fact that when a system or process is regulated by several inputs there can be no one-to-one relationship between the response and any single input unless all other variables are fixed.

4.1 Immunometabolism

The adaptability of immune cells emerges from their plasticity – the ability to change their phenotype – that is directly related to metabolic reprogramming. The integration of immunology and metabolism, known as immunometabolism, has revealed crucial insights into the regulation of immune cell activation, differentiation, and function. This relies on the fact that different cellular functions have distinct energy demands, and changes in metabolism drive to different energy production rates, as well as the obtention of important metabolites for anabolic reactions needed for biosynthesis and growth.

Metabolic shifts from mitochondrial respiration to glycolysis are frequently observed during critical diseases, and lactate levels in blood appear to be a chemical predictor of sickness severity in many circumstances [1–3]. For instance, researchers in the 1920s reported a switch from OXPHOS to glycolysis in tumour cells, where they observed a heightened glucose consumption and lactate production [4,5], a phenomenon later labelled as the Warburg effect. The Warburg effect reflects a metabolic reprogramming of cancer cells towards glycolysis, driving sustained proliferation and accelerating malignant progression. Additionally, this metabolic shift is associated with the suppression of immunosurveillance within the tumour microenvironment [6,7]. However, the exact mechanisms causing tumour cells to use this pathway are still to be explained, although it has been extensively studied since then, with thousands of papers trying to elucidate its causes or its functions.

Initially thought to be unique to cancer cells, the Warburg effect is observed in a wide range of inflammatory immune cells. Evidence suggested that during peak inflammation, immune cells preferentially use glycolysis for energy production, while during the resolution phase, they rely mainly on OXPHOS, acquiring a pro-resolving phenotype to restore tissue homeostasis. This involves the clearance of damaged cells,

repair mechanisms, and in some instances the generation of memory cells. Glycolysis is typically predominant in pro-inflammatory M1 macrophages, NK cells, activated B cells, and effector T cells. OXPHOS on the other hand, in general supports anti-inflammatory phenotypes, such as in activated M2 macrophages or regulatory T cells.

Besides, oxidative stress is a common observation in disease and inflammation. During oxidative stress conditions, cells often exhibit higher glucose uptake and a metabolic shift towards glycolysis. Activation of T cells and macrophages towards inflammatory settings rapidly upregulates the levels of glucose transporters (GLUTs) [8,9], indicating increased glucose metabolism. Initially, this metabolic shift was thought necessary for the activation, proliferation, and differentiation of effector cells. However, GLUT deficiency did not affect T cell activation but reduced T effector cell survival, differentiation, expansion, and inflammatory response, while increasing regulatory T cells, which remained functional and could suppress T effector cells [9]. Furthermore, glycolytic inhibition in macrophages suppresses their specific inflammatory immune response [10] but does not affect the M2 response as long as OXPHOS and fatty acid oxidation (FAO) remain intact [11].

This has driven to the perception of glycolysis as a detrimental pathway, associated with inflammation and aberrant immune responses. Here, we propose that glycolysis becomes activated when mitochondrial ATP production is impaired, providing essential energy for cell function. Thus, glycolysis appears as a consequence of mitochondrial dysfunction, and ROS is proposed as a key modulator of this metabolic shift. To better understand this hypothesis, we will first review the role of mitochondria in metabolic reprogramming.

4.2 Mitochondria: central hub for ATP and ROS generation

Approximately one to two billion years ago, a significant event likely occurred when a bacterium merged with an Archaea-type host [12]. While many initial specifics remain elusive, it is evident that these original adversaries gradually formed a symbiotic relationship, becoming increasingly interdependent. The bacteria are theorized to have evolved into what we now recognize as mitochondria. As it adapted to its new environment, the responsibility for its replication increasingly fell to the host.

Concurrently, the host began to heavily rely on its former invader, gathering benefits from specialization and compartmentalization, [13] a defining event in the evolution of eukaryotic cells. These once-unwanted invaders, now transformed into specialized organelles, enabled remarkable efficiency in energy production through OXPHOS, hinting at the potential for the development of robust muscles or vigorous hearts, and facilitating an increase in complexity within living organisms. This agreement between host and bacteria has endured, largely unchanged, to the present day.

Despite being marvels of energy production, mitochondria also have a less favourable impact within the cell: they are the primary source of ROS [13]. The "oxygen paradox" proposes that although oxygen is essential for aerobic beings, it is also inherently dangerous to the very same lifeforms [14]. Life on Earth has adapted to thrive in an oxygen-rich environment by mitigating the risks associated with oxidation. This suggests that evolutionary pressures have promoted mechanisms that minimize the harmful effects of ROS, driving the development of robust enzymatic and non-enzymatic antioxidant systems, as well as repair mechanisms that mitigate oxidative damage. Overall, the preservation of mitochondria through evolutionary history aims for a favourable benefit for both the host and the former invader.

However, an imbalance between ROS production and the cellular antioxidant system, leads to oxidative stress, disrupting the system's redox state. Despite their potential detrimental effects, ROS are recognized as important signalling molecules regulating chemical reactions in a specific and controlled manner. These oxygen-derived species participate in signal transduction by inducing reversible oxidative modifications in redox-sensitive proteins, thereby initiating phosphorylation cascades that alter gene transcription and influence cellular functions [15]. Moreover, ROS exhibit bactericidal activities that are important for pathogen elimination [16,17]. Therefore, a slight elevation of ROS could be either beneficial or detrimental depending on the conditions, recalling the Paracelsus toxicology maxim "*sola dosis facit venenum*" (the dose makes the poison; Paracelsus, 1538).

4.2.1 ROS Generation

Comprehending the regulation of ROS starts with understanding their generation, which takes place in multiple compartments and by multiple enzymes within the cell. Important ROS generators include proteins such as the family of the NADPH oxidases [13], as well as lipid metabolism within the peroxisomes [18], among others [19]. Although all these sources contribute to the overall oxidative burden, the vast majority of cellular ROS can be traced back to the mitochondria [13,20], where approximately 95% of cellular oxygen is consumed [21].

The ETC, located within the inner mitochondrial membrane, exhibits increasing oxidation potentials, ultimately reducing molecular oxygen to water. This exergonic[7] process is used to pump protons from the mitochondrial matrix into the intermembrane space, creating an electrochemical gradient known as the proton motive force. The proton motive force drives protons back into the mitochondrial matrix through the ATP synthase enzyme, catalysing the conversion of ADP and inorganic phosphate to ATP, coupling substrate oxidation and ADP phosphorylation. Despite the high efficiency of this process, electron leakage can occur when electrons prematurely exit the respiratory chain and combine with oxygen to form superoxide (O_2•−).

Although the generation of superoxide by respiration is a well-established phenomenon, it is poorly understood mechanistically. Experimental manipulations altering the redox potential at sites I or III of the ETC have demonstrated increased ROS generation rates, highlighting the critical role of these reactive sites in free radical formation [13]. Additionally, mitochondrial membrane potential[8] shows a strong correlation with ROS production [22]. However, caution is warranted due to significant experimental limitations in studies using isolated mitochondria, where redox states of many elements are often non-physiological and can destabilize the kinetic and thermodynamic conditions of regular electron flow. This can lead to artefactual results,

[7] An exergonic process is a chemical reaction characterized by a negative change in free energy, indicating a spontaneous reaction accompanied by the release of energy.

[8] The mitochondria membrane potential is primarily determined by the balance between the movement of protons (H+ ions) across the inner mitochondrial membrane and the flow of electrons trough the ETC.

as exemplified by initial overestimations suggesting 2% of total oxygen consumption is directed towards ROS production [23], later corrected to 0.2% under more physiological conditions [24]. These discrepancies underscore the methodological influence on understanding the mitochondrial respiratory chain as a source of radicals.

Moreover, comparisons between mitochondria within cardiomyocytes and isolated mitochondria by Aon et al. [25] indicate that isolated mitochondria exhibit heightened oxidative stress at high reduction potentials. In contrast, mitochondria within intact cardiac cells exhibit oxidative stress under both high oxidation (low membrane potential) and maximal reduction conditions. This underscores the importance of carefully regulating mitochondria redox potential, as both reducing and oxidizing conditions can be harmful.

Thus, when the energy requirements of the cell rise, as it happens during immune cell activation, fuel oxidation rates increase (e.g., glucose consumption), resulting in a higher electron flow through the ETC and a subsequent increase in mitochondria membrane potential. At some point, this heightened mitochondrial workload causes more electrons to leak from the ETC, elevating ROS production. When ROS production exceeds the cell's antioxidant defence capacity, oxidative stress occurs. This increased oxidant production, both by damaging components of the ETC (or associated proteins and molecules) and by altering their redox potential, can lead to ETC dysfunction. This dysfunction impairs mitochondrial work, reduces ATP production, and further increases ROS generation, creating a detrimental feedback loop. Over time, this can result in mitochondrial dysfunction, which can contribute to cellular injury, ultimately leading to apoptosis.

4.2.2 Metabolic Adaptation to ROS: The Role of HIF-1 and Glycolysis in Cellular Response and Disease

Interestingly, several studies show that excess ROS derived from mitochondria triggers the activation of the glycolytic pathway by increasing the levels of hypoxia-inducible factor (HIF-1) [26–34] (**Figure 4.2**). HIF-1 is a heterodimeric transcription factor with two subunits, HIF-1α and HIF-1β [35]. HIF-1α is hydroxylated by prolyl hydroxylase domain (PHD) enzymes in an oxygen-dependent manner. This hydroxylation targets

HIF-1α for degradation, keeping its levels low. However, ROS can inhibit the activity of PHD enzymes, reducing hydroxylation activity [36]. This leads to an accumulation of HIF-1, which drives the expression of target genes, including GLUTs, LDH, and other important glycolytic genes.

In this scenario, the activation of glycolysis acts as a biological mechanism to counter-regulate mitochondrial workload, thereby reducing ROS production, while maintaining essential ATP production for cellular functions.

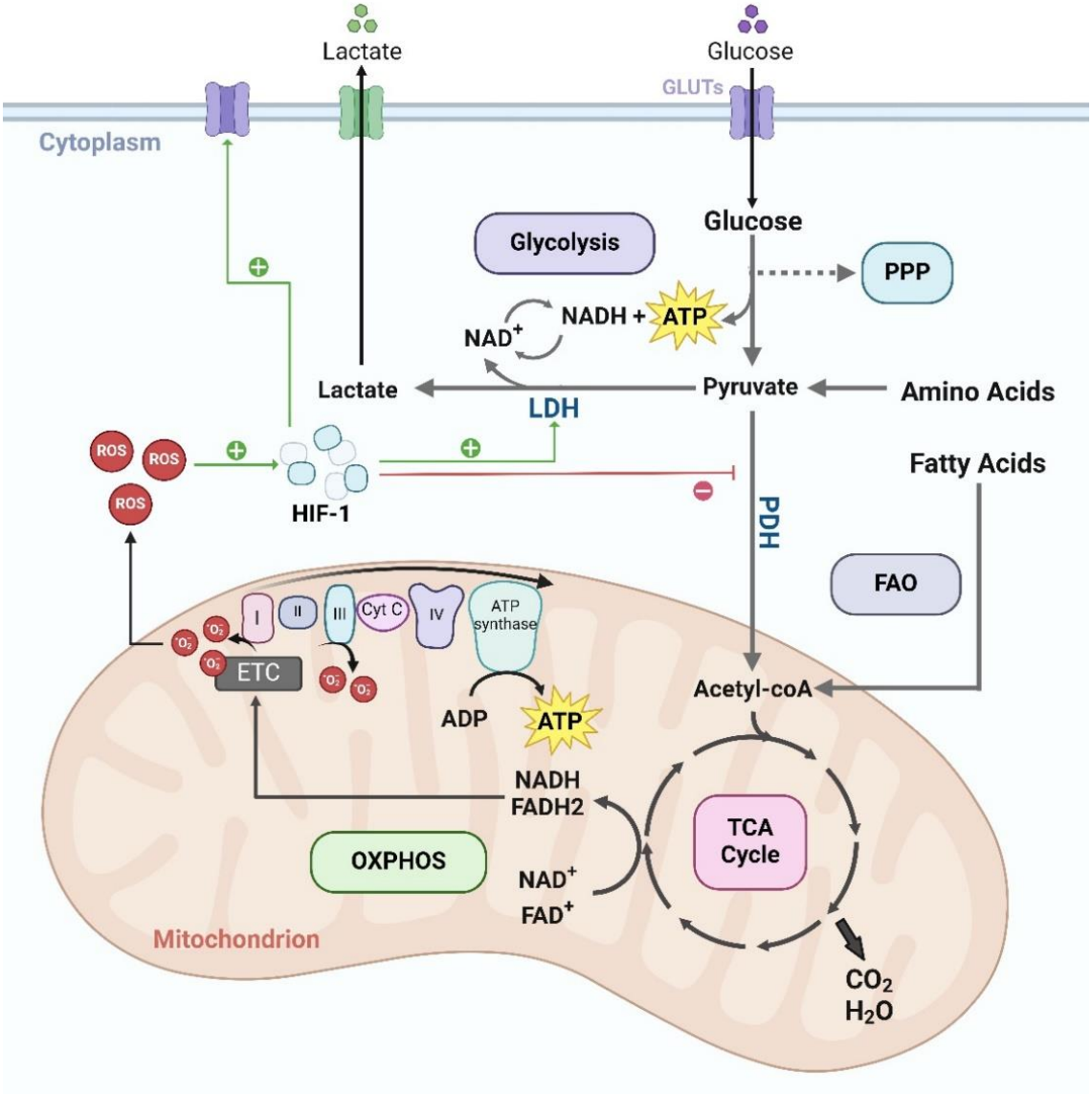


Figure 4.2. Main catabolic pathways and their regulation in response to increased HIF-1 levels due to excess ROS. Glycolytic genes such as GLUTs and LDH are upregulated, whereas others like pyruvate dehydrogenase (PDH) are downregulated.

In summary, the proposed process begins with an increase in energy demand, such as during immune activation or in highly proliferating cells. Elevated energy demand stimulates increased mitochondrial metabolism, leading to enhanced biofuel consumption. If not tightly regulated, this heightened mitochondrion workload can lead to excessive ROS production and subsequent mitochondrial dysfunction. Elevated ROS levels activate glycolysis, diverting glucose away from the mitochondria to sustain ATP production, thereby moderating OXPHOS rates and preventing further ROS generation.

There are some relevant studies that reinforce this hypothesis. For instance, the investigation of erythrocytes (red blood cells) in mammals is intriguing given their distinctive lack of both nucleus and mitochondria. Their primary function of oxygen transport requires minimal energy expenditure. The absence of mitochondria in these cells remains an enigmatic aspect, as there exists no compelling rationale for their exclusion in living cells. Initially, it was theorized that nucleated erythrocytes might be too large to pass through narrow capillaries, but subsequent research disapproved this theory. Zhang et al. demonstrated that mammalian erythrocytes maintain stable ROS levels even under conditions of diabetes, ischemia-reperfusion injury, malaria infection, and exposure to in vitro sugar/heme treatments [37]. In contrast, avian erythrocytes, which retain mitochondria, exhibit significantly higher ROS levels under these same conditions. This suggests that the lack of mitochondria in mammalian erythrocytes may enhance their adaptation to stress by minimizing ROS generation.

Growing evidence links diabetes, characterized by chronic hyperglycemia and impaired mitochondria electron transport, to elevated ROS production, which contributes to disease progression. Epidemiological studies show that individuals with diabetes have a 1.5- to 4-fold increased risk of infection [38], highlighting the detrimental effects of hyperglycemia on the immune response. Notably, metformin, a biguanide derivate, has demonstrated efficacy in preventing diabetes in high-risk individuals and reducing complications. Large cohort studies have associated metformin use with reduced mortality rates across multiple diabetic-related conditions, including infections [39], cardiovascular diseases [40], as well as reduced risk of cancer [41]. Moreover, metformin exhibits promising outcomes in treating inflammatory

disorders, promoting ongoing research into its therapeutic potential for various conditions such as cancer, rheumatoid arthritis, neurodegenerative diseases, cardiovascular diseases, polycystic ovary syndrome, and infections [42,43].

While studies consistently indicate that metformin can modulate cellular redox balance and reduce ROS production [44–47], its precise mechanism remains debated. Despite its generally regarded as safe with few side effects, metformin can lead to a serious condition called lactic acid acidosis, characterized by elevated lactate levels in the blood. This suggests that metformin may enhance glycolytic flux. It is plausible that metformin, by promoting glycolysis, may lower blood sugar levels by increasing glucose consumption to produce equivalent ATP levels via glycolysis compared to OXPHOS[9]. Moreover, this reduction in mitochondrial fuel consumption may contribute to decreased ROS production.

On the other hand, Kondoh and collaborators found that immortalized mouse embryonic fibroblasts and mouse embryonic stem cells that exhibit higher glycolytic flux are more resistant to oxidative damage, suggesting that glycolytic flux might influence cellular life span [48]. Another study explored the effects of ischemia-reperfusion on cells with different metabolic pathways. It revealed that cells with higher rates of glycolysis exhibited reduced ROS levels, protecting against ischemia-reperfusion injury compared to cells with heightened TCA cycle turnover [49]. Similarly, other researchers have demonstrated that glycolysis serves as a protective mechanism against ROS in highly proliferating cells [50]. Overall, these findings highlight the significance of metabolic adjustments mitigating ROS generation and preserving cell viability, while maintaining the energy supply.

Fiorillo and coworkers demonstrated that within breast cancer cells, the most aggressive ones (metastatic) were the cells producing higher ATP rates [51], indicating that those tumoral cells that develop a higher ATP production rate are the more aggressive. In accordance, inhibition of LDH in cancer cells, significantly reduced ATP levels, increased ROS, and promoted cell death [52]. Therefore, inhibition of LDH has

[9] Note that glycolysis produces 2 ATP molecules, whereas complete oxidation of glucose through mitochondrial respiration yields approximately 36 ATP molecules.

been proposed as an adjuvant therapy that may promote the sensitization of tumour cells [53].

In conclusion, while heightened glycolytic flux has been linked to several pathologies, disease progression, and elevated ROS levels, it has often been perceived as a "detrimental" metabolic pathway. Nevertheless, this correlation may warrant reconsideration, as evidence suggests that activation of glycolysis under certain circumstances can be beneficial for cell survival during stress conditions. Glycolysis may arise as a consequence of altered mitochondrial metabolism, stemming either from high mitochondrial workloads or mitochondrial dysfunction (notably, higher mitochondrial flux will lead to dysfunction if not tightly regulated). Be that as it may, both situations would lead to an increase in ROS, which appear as the main regulators of this metabolic shift. Of note, it is important to consider that this metabolic re-programming is crucial for energy generation, making ATP an important player, as well as a regulatory factor that should be carefully considered.

4.3 Macrophage Polarization

The value of a hypothesis, it is said, lies in its ability to propose new experiments, accompanied by the rationale of promoting understanding. Here, macrophages have been chosen as a model to explore this hypothesis due to their immunoregulatory capabilities and their involvement in the inflammatory response.

As detailed in Chapter 1, CeO_2 NPs have shown significant efficacy in various diseases associated with inflammatory settings. To gain insights into how CeO_2 functions as an anti-inflammatory agent within biological systems, we focus on macrophages, fundamental cells orchestrating inflammatory responses. Their multifaceted roles encompass recognition of PAMPS and DAMPS, phagocytosis, antigen presentation, cytokine production, recruitment of other immune cells, tissue repair, and immunomodulation, where their different functions are fuelled by reprogramming cell metabolism.

Activated macrophages are classically divided into LPS and/or IFNγ-elicited inflammatory (M1) and IL-4-induced anti-inflammatory (M2) cells. The M1/M2

classification is useful as it describes two major and opposing activities of macrophages. These polarization states have been extensively studied for their associations with disease progression. M1 inflammatory response is considered the first line of defence to fight against pathogens, characterized by the production of elevated ROS levels and secretion of pro-inflammatory cytokines, but M1 activation causes collateral tissue damage and chronic inflammation if not properly regulated. In contrast, M2 activity promotes inflammation resolution, cell proliferation and tissue repair to restore tissue homeostasis.

The polarization of macrophages in various physiological and pathological contexts is characterized by a continuum, reflecting high plasticity and heterogeneity among these effector cells. This is manifested as a spectrum encompassing distinct polarization states that do not fit in the oversimplified M1/M2 dichotomy, but for clarity, we will hereafter refer to macrophages as M1 or M2 activation states.

In general, naïve macrophages are first polarized to the pro-inflammatory M1 phenotype to assist the host against DAMPS and PAMPS. Once the danger signals have been neutralized, macrophages shift towards the M2 phenotype to initiate an anti-inflammatory response directed to repair and restore normal function. Note that M2 macrophages foster proliferation and growth, thereby implicating them in tumour progression under certain circumstances [54].

Macrophage activation and function require high energy rates, but the distinct polarization states have been associated with different energetic pathways. Specifically, M1 inflammatory macrophages are linked to enhanced glycolytic rates and mitochondria dysfunction, while M2 macrophages exhibit elevated OXPHOS, often relying on FAO (**Figure 4.3**). Although glycolysis occurs in the cytosol, mitochondria still play a central role by sustaining a broken TCA cycle that produces important metabolic intermediates (e.g., citrate and succinate) [55] and reduced equivalents that sustain the ETC. This mode of work increases electron leakage and results in elevated ROS levels. Additionally, mitochondrial dysfunction has been shown to impede the repolarization towards M2 macrophages [33,56,57], suggesting fundamental roles of mitochondria respiration in sustaining the M2 response.

In this scenario, emerging research has highlighted the importance of mitochondrial dynamics: the ability to fuse together to form larger mitochondria or to undergo fission to break up into smaller bodies. The ability to change number and morphology (size and shape) ultimately controls the power output and concomitant ROS production. An increase in mitochondrial volume and consequent activity appears when cells must do some extra work. Yet, high mitochondria workloads can lead to damage to their components due to elevated ROS production, resulting in mitochondrial fragmentation and loss of membrane potential. This disruption impairs the TCA cycle, increases ROS release, and promotes glycolysis. Consequently, mitochondrial dynamics extend beyond mere structural adjustments, actively shaping cellular metabolism [58].

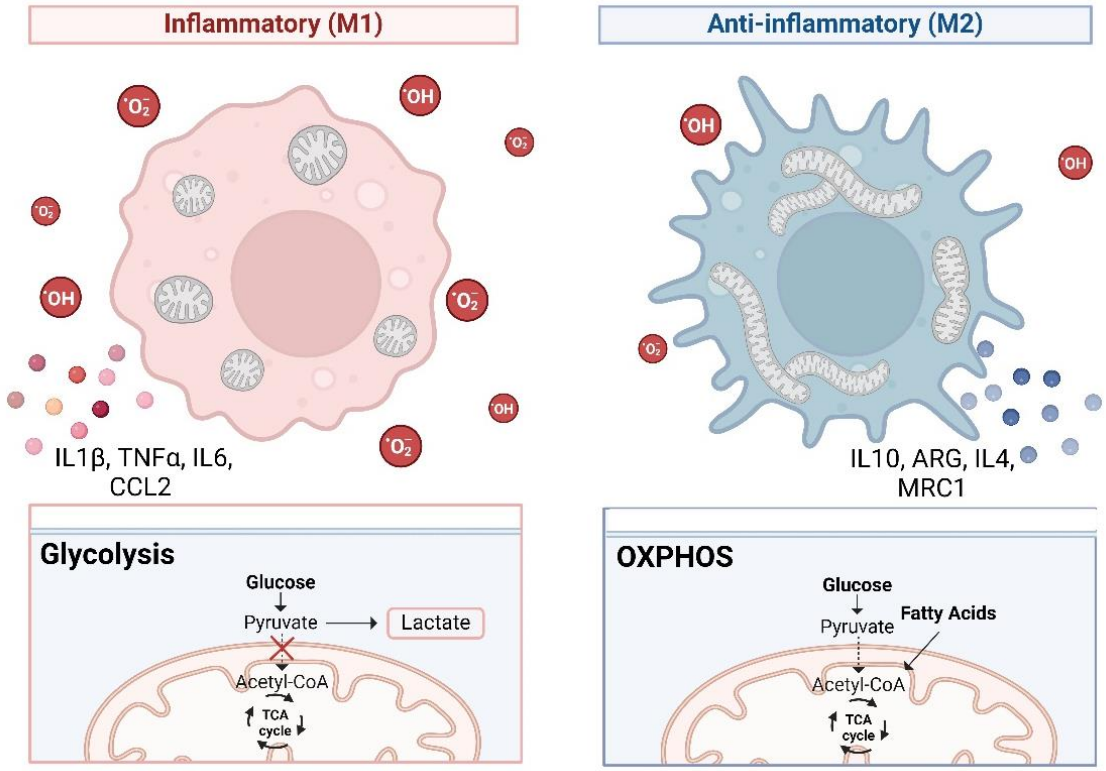


Figure 4.3. Main features of macrophage polarization states. M1 macrophages, activated by LPS and/or IFNγ, are characterized by high ROS production, predominantly utilize glycolysis for energy production, and release pro-inflammatory cytokines such as IL1β, TNFα, IL6, and CCL2. Conversely, M2 macrophages, induced by IL-4, rely on OXPHOS, producing anti-inflammatory cytokines like IL10, ARG, IL4, and MRC1, which promote tissue repair and homeostasis.

In summary, M1 activation is linked to disrupted mitochondrial function, characterized by fragmented mitochondria with low membrane potentials (**Figure 4.3**), which can

lead to immune system exhaustion and impact disease progression. In contrast, M2 macrophages are associated with elongated mitochondrial networks with increased membrane potentials. These cells rely on an intact TCA cycle, supplied by glucose and/or FAO, for sustained energy production (**Figure 4.3**). Since fatty acids are more reduced than carbohydrates, they contain more energy per molecule, representing a more efficient fuel than glucose, for sustained high energy – but slower – responses. Thus, although fatty acids are the preferred energy source during the M2 response, their utilization depends on their availability.

As shown in various contexts, the inhibition of glycolysis dampens the inflammatory response of macrophages (M1) in vitro and in vivo, [33,59,60] suggesting that glycolysis is essential to sustain M1 macrophage function when mitochondria are damaged. As an example, in vivo suppression of glycolysis through the HIF-1 pathway, suppressed the M1 response aggravating infection by *L. monocytogens* in mice [33].

Furthermore, despite exhibiting elevated rates of mitochondrial respiration, M2 macrophages have shown lower levels of ROS compared to M1 macrophages, attributed to their higher levels of antioxidant defences [61]. However, the role of ROS in M2 macrophage activation remains unclear. Some studies state that certain levels of ROS are necessary for M2 activation [61,62], while others do not. Generally, antioxidant treatments have been shown to promote M2 polarization [45,56,63]. The study of M2 macrophages is more challenging due to their multifaced functions. Indeed, the M2 response is sometimes divided into multiple subgroups, each determined by the specific stimuli for their activation and characterized by distinct cell functions [64].

4.4 Scope of the study

Given the dual role of ROS as both cause and consequence of metabolic reprogramming, we hypothesize that CeO_2 NPs, by effectively lowering ROS levels, can restore mitochondria function and potentially modulate the inflammatory response. This modulation may promote macrophage repolarization towards the anti-inflammatory M2 phenotype, thereby facilitating the resolution of inflammation.

To test this hypothesis, two immortalized macrophage cell lines were employed: (i) human THP-1 monocytes and (ii) murine RAW 267.4 macrophages. To this end, we focused on evaluating cytokine production, mitochondria membrane potential and morphology, ROS levels, and energy metabolism in these cell lines.

4.5 Results and Discussion

4.5.1 Human THP-1 Macrophage Polarization Model

Human THP-1 monocytes were first differentiated into macrophages using phorbol 12-myristate 13-acetate (PMA). Subsequently, the cells were exposed to LPS + IFNγ to induce M1 macrophages or IL-4 to induce M2 macrophages. The polarization capacity was assessed though analysis of mRNA and protein secretion of specific differentiation markers [65].

Inflammatory M1 macrophages exhibit significant upregulation of M1 marker genes, including *IL1B* and *CCL2* (**Figure 4.4A**). In accordance, IL-1β cytokine secretion increased after exposure to LPS + IFNγ (**Figure 4.4B**). In contrast, exposure to IL-4 did not affect the expression of M2-related genes, *IL10* and *ARG*, nor the secretion of the IL-10 cytokine.

Given the importance of mitochondrial metabolism on immune cell activation, the polarization capacity of THP-1 macrophages was further determined by analysing the mitochondria membrane potential by using the MitoTracker Orange probe (**Figure 4.4C**). An increase in MitoTracker^{TM} Orange fluorescence signal indicates an increase in mitochondrial membrane potential. Accordingly, exposure to LPS + IFNγ produced an important decrease in mitochondrial membrane potential, suggesting organelle dysfunction and concomitant ETC uncoupling [66], while cells exposed to the anti-inflammatory cytokine IL-4 show an increase in mitochondrial membrane potential, indicating higher OXPHOS rates.

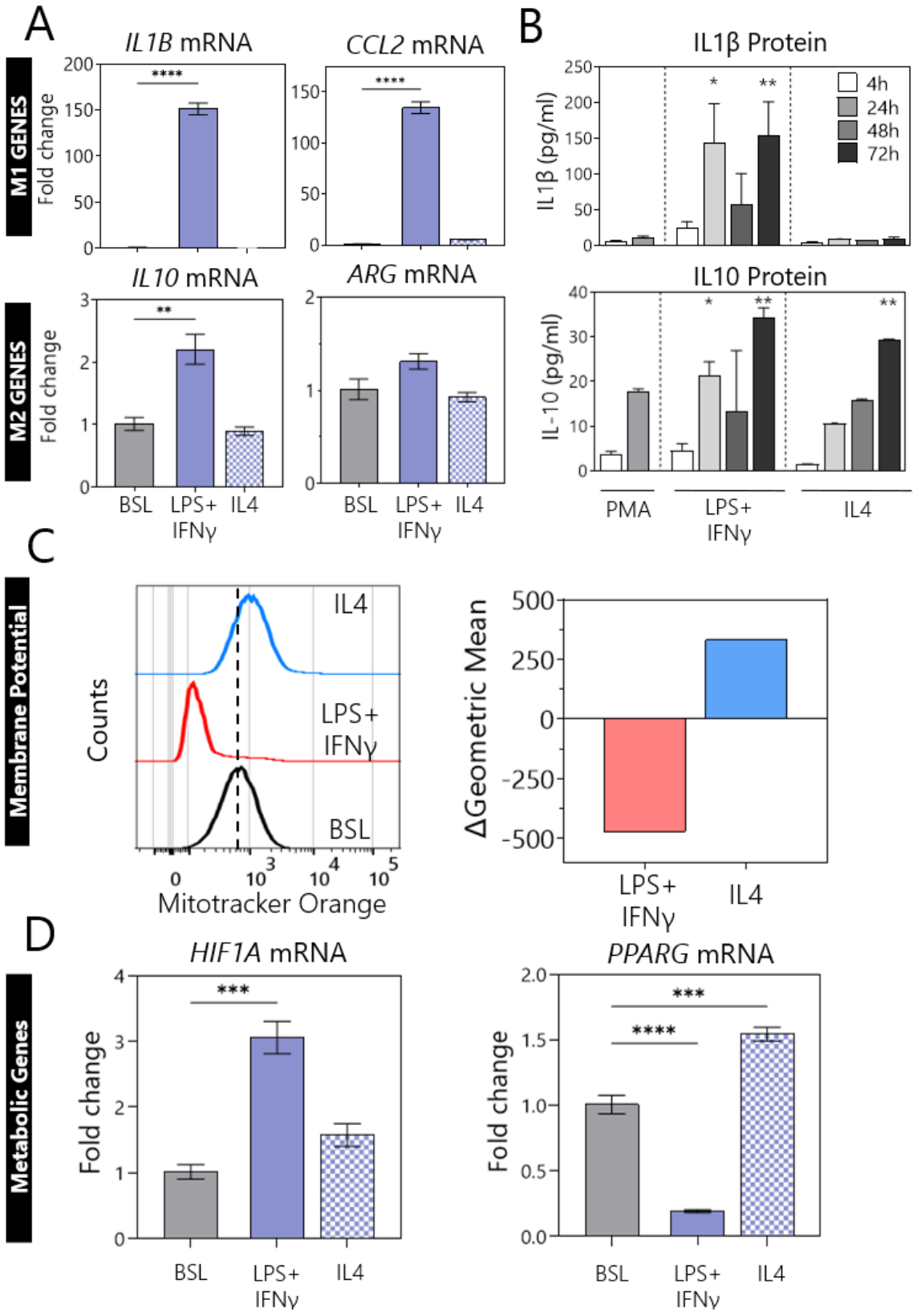


Figure 4.4. Polarization capacity of the THP-1 macrophages induced by LPS or IL-4. (A) Gene expression levels of macrophages were determined following 12 hours of stimulation with LPS+IFNγ or IL-4. n = 3. **(B)** Quantification of IL-1β and IL-10 secretion was conducted at various time points (4, 24, 48, 72 hours) using

ELISA assay. n = 2 (biological duplicates). (C) Mitochondrial membrane potential was assessed using MitoTracker Orange and flow cytometry after 24-hour exposure to LPS + IFNγ or IL-4. Membrane potential is presented as ΔGMF = $(\text{Geometric mean fluorescence})_{\text{experimental sample}}$ - $(\text{Geometric mean fluorescence})_{\text{control sample}}$. n = 1. (D) Gene expression levels of important metabolic regulators (*HIF1A*, *PPARG*) were determined following 12 hours of stimulation with LPS + IFNγ or IL-4. n = 3. Data are presented as means ± SEM. *p < 0.01, **p<0.001, ***p<0.0001, ****p<0.00001

Next, to further assess the metabolic reprogramming of macrophages, *HIF1A* (M1) and *PPARG* (M2) were included as metabolic markers. HIF-1 promotes the transcription of important glycolytic genes [55,67], and the peroxisome proliferator-activated receptor (PPARγ) has been shown to promote macrophage differentiation towards the M2 phenotype by promoting FAO and suppressing the pro-inflammatory phenotype, being an important contributor to inflammation resolution [68–70]. In accordance with previous results, M1 cells show increased levels of *HIF1A*, indicating an increased glycolytic metabolism, while IL-4 exposure led to elevated *PPARG* expression, which has important roles in promoting both FAO and OXPHOs.

Overall, these results indicate that activation of toll-like receptors (TLRs) in macrophages by exposure to LPS + IFNγ effectively induced an M1 response, whereas differentiation towards the M2 phenotype was not clearly observed. For this reason, we concluded an extensive assessment of M2 marker gene expression under diverse experimental conditions, including varied exposure timings to IL-4 (4, 12, 24 hours), increasing IL-4 concentrations (20, 50, 60 ng/mL), utilization of two distinct cell lines (ATCC, DSMZ), use of different IL-4 proteins (R&D systems, PeproTech), and even the combination of IL-4 and IL-13 for M2 stimulation. Despite this comprehensive exploration, the expression levels of M2 marker genes remained unchanged across all tested conditions (data not shown).

While the literature reports the polarization of THP-1 cells to the M2 phenotype [71–74], contrasting results are apparent in other investigations. For example, Tedesco and colleagues revealed that PMA-derived THP-1 macrophages failed to fully replicate the response spectrum observed in primary macrophages [75]. Additionally, Chanput et al. also found that THP-1 M2 cells did not express many M2 markers, like Arginase, although they had others [76]. It has been suggested that the differentiation process of these cell lines with PMA could significantly influence the THP-1 M2 response [77–

80], as PMA has been shown to induce pro-inflammatory cytokine release in THP-1 cells independently [81]. Thus, the use of high PMA concentrations has been linked to undesirable responses, particularly those mediated by NF-kB, [73] which impede the M2 activation [79]. PMA might attenuate certain M2-like phenotypes without completely suppressing their function, as evidenced by heightened mitochondrial activity and upregulation of *PPARG* following exposure to IL-4.

In this study, as recommended in the literature, PMA levels were consistently maintained at low concentration (20 ng/mL) and with extended resting periods (> 48 h), with no success. Recognizing the limitations of this model, we focused only on investigating the effects of antioxidants on the M1 inflammatory response.

4.5.2 CeO_2 NPs effects on M1 inflammatory macrophages.

Next, the effect of antioxidant CeO_2 NPs in M1-activated cells was investigated. First, we studied the administration schedule of CeO_2 NPs. Cells received the same dose of CeO_2 NPs (150 μg/mL) under different conditions: prophylaxis, prophylaxis + treatment, or treatment alone. **Figure 4.5A** shows that CeO_2 NPs effectively reduced the inflammatory response across all treatment regimes, with the prophylactic administration having the most significant effects. Therefore, this schedule was chosen for further testing of the NPs' effects.

Indeed, as shown in **Figure 4.5B**, pre-treatment with 150 μg/mL of CeO_2 NPs reduced mRNA expression levels of the M1 marker genes *IL1B* and *CCL2*, suggesting that nanoceria can attenuate the inflammatory response. Additionally, CeO_2 NPs decreased *HIF1A* expression in M1 macrophages, indicating a pivotal role in metabolic reprogramming, likely mediated through ROS attenuation (**Figure 4.5B**). The downregulation of glycolytic genes correlates with restored mitochondrial function. Importantly, CeO_2 NP treatment did not alter the gene expression of naïve macrophages, indicating that these NPs do not trigger an undesired immune response.

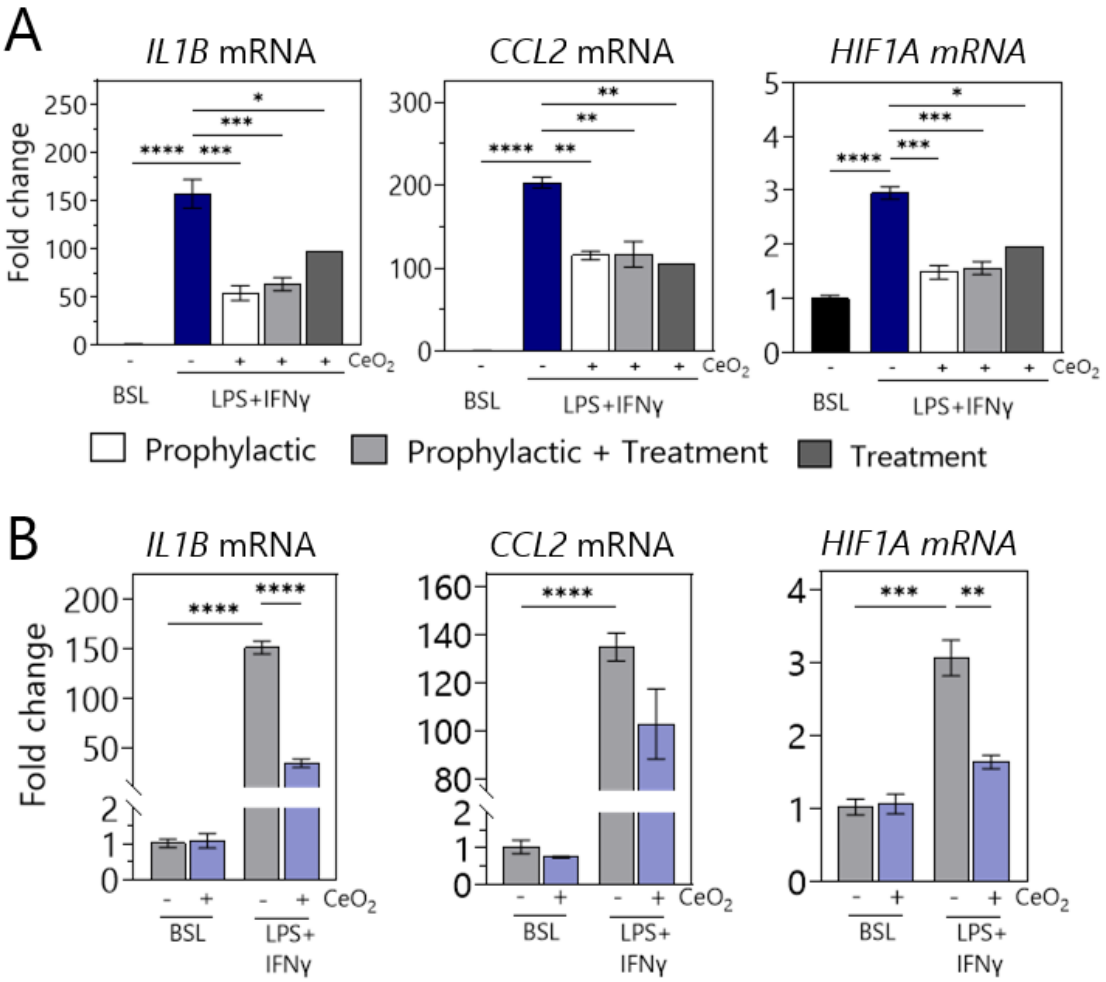


Figure 4.5. Effect of CeO_2 NPs on the M1 inflammatory response in THP-1 macrophages. **(A)** Evaluation of the expression levels of M1 marker genes depending on the administration schedule of CeO_2 NPs. Macrophages were exposed to CeO_2 NPs under three different regimens: (i) prophylaxis (150 µg/mL for 24 hours), (ii) prophylaxis (75 µg/mL for 24 hours) + treatment (75 µg/mL for 2 hours), or (iii) treatment alone (150 µg/mL for 2 hours). n = 3 (biological replicates). **(B)** Expression levels of representative M1 marker genes including signalling molecules (*IL1B*, *CCL2*) and metabolic markers (*HIF1A*), 12 hours after LPS + IFNγ stimulation. n = 3. Data are represented as means ± SEM. *p < 0.01, **p<0.001, ***p<0.0001, ****p<0.00001

To further elucidate if antioxidant treatments directly influence the metabolic reprogramming of immune cells, the metabolic signature of macrophages was assessed by extracellular flux analyses. The following experiments were conducted during a research stay in the Laboratory of Neurogenesis, Neuroinflammation and Network Dynamics led by Dr. Juan Manuel Encinas. The cellular metabolic profile was determined by measuring the oxygen consumption rates (OCR) and extracellular acidification rates (ECAR), which provides insights into whether glucose is oxidized in the mitochondria (OXHPOS) or the cytosol (glycolysis).

Results confirm that naive cells (basal) exhibit low metabolic rates, indicating a quiescent state. Exposure to LPS + IFNγ triggers a shift towards glycolysis within one hour and becomes more pronounced 3 hours later (**Figure 4.6A**). This glycolytic shift is also reflected in ATP production, with half of the ATP being produced through glycolysis 3 hours after LPS exposure (**Figure 4.6B**).

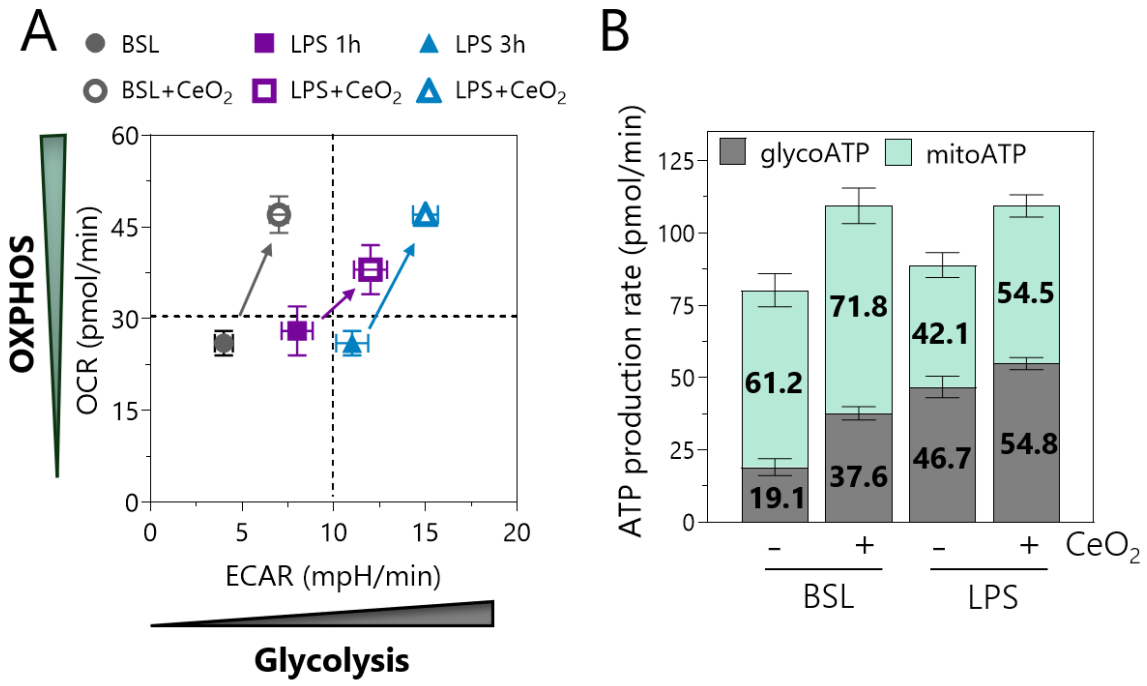


Figure 4.6. Metabolic profile of M1 macrophages treated with CeO_2 NPs. (A) Bioenergetic profile of M1 macrophages (1 – 3 hours after LPS exposure) and the effect of 150 µg/mL CeO_2 NPs, based on the rates of OCR vs. ECAR measured via Seahorse extracellular flux analyser. (B) ATP production rates determined by real-time ATP production rate assay kit for Seahorse extracellular flux analyser. THP-1-derived macrophages were pretreated or not with CeO_2 NPs for 24 hours and thereafter activated by exposure to LPS for 3 hours. Mean values ± SEM are presented.

Interestingly, treatment with CeO_2 NPs boosted mitochondrial respiration (OXPHOS) in both naïve and LPS-stimulated macrophages, with a more pronounced increase in the latter (**Figure 4.6A**). Furthermore, CeO_2 NPs increased ATP production rates in both naïve and M1 cells, despite glycolysis remaining a significant contributor (**Figure 4.6B**). The rise in ATP levels, accompanied by a lack of corresponding increase in ROS, likely enhances overall cellular functions. However, it is important to consider that the increased ATP production could also be attributed to cellular responses such phagocytosis of NPs, which might elevate energy demands without provoking an

inflammatory response. This aspect warrants further investigation to elucidate the precise mechanisms.

Overall, these results indicate that M1 macrophages have reduced mitochondrial function, evidenced by lower mitochondrial membrane potential. This dysfunction leads to an elevated glycolytic rate, likely caused by excess mitochondrial ROS boosting HIF-1 levels. The use of CeO_2 NPs, by scavenging ROS, restores mitochondrial function and increases the OXPHOS rates. Mitochondria restoration by antioxidant treatment allows for a milder inflammatory response, as demonstrated by the decreased expression of M1 marker genes without complete suppression. These findings suggest promising prospects for controlling macrophage reprogramming and highlight the important roles of antioxidants in preserving efficient mitochondrial respiration.

4.6 Murine RAW 267.4 Macrophage Polarization model

As excessive ROS has been demonstrated to dampen macrophage repolarization to the M2 phenotype, and ROS inhibition has been shown to influence reprogramming towards M2 macrophages [56], the effect of antioxidant NPs was assessed in murine RAW 267.4 macrophages. This change in the cell model aims to achieve a more robust evaluation of CeO_2 NPs potential therapeutic applications in modulating macrophage polarization and mitigating associated risks. Understanding the M2 response, which is pivotal for resolving inflammation, is crucial in exploring macrophage reprogramming effectively.

First, the polarization capacity of RAW 267.4 macrophages towards the M1 and M2 phenotypes was assessed by evaluating specific marker genes characteristic for the M1 (*Il1b*, *Ccl2*) or the M2 (*Arg*, *Mrc1*) responses (**Figure 4.7**). 12 hours upon TLR activation by LPS, a notable upregulation of pro-inflammatory cytokines was observed. Interestingly, in this model, priming cells with the anti-inflammatory cytokine IL-4 efficiently induced the expression of M2-associated genes *Arg* and *Mrc1*. Importantly, as observed in THP-1-derived macrophages, treatments with CeO_2 NPs in naive RAW 267.4 macrophages did not induce any response, corroborating that CeO_2 NPs are well

tolerated by the immune system. Additionally, pretreatment of cells with CeO_2 NPs resulted in a significant reduction of M1-associated genes. However, CeO_2 NPs significantly downregulated the expression levels of key M2 marker genes, potentially indicating a reduced anti-inflammatory response. This decreased expression of M2 markers raises concerns about potential immune suppression associated with CeO_2 NPs use.

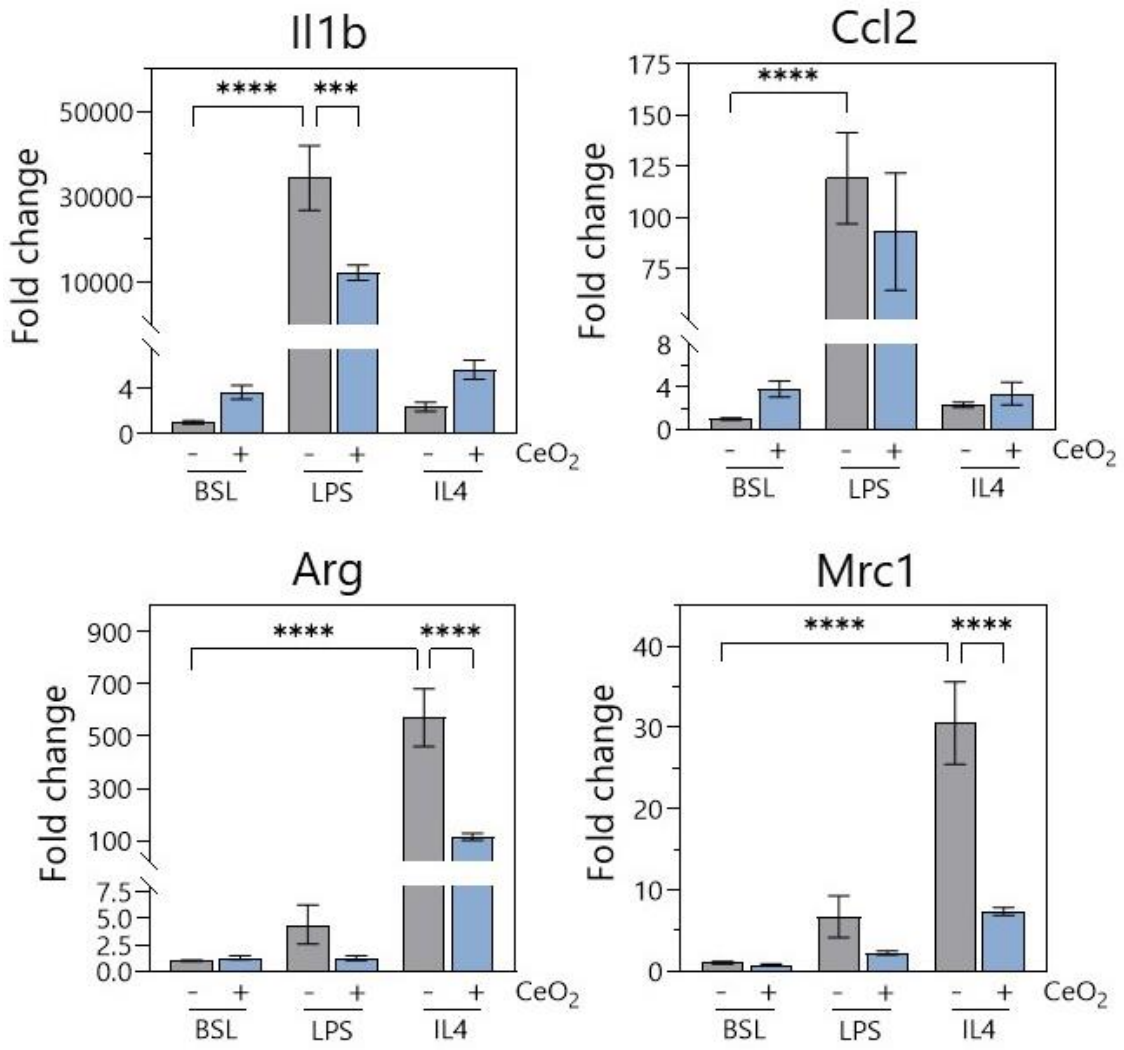


Figure 4.7. Effect of CeO_2 NPs on RAW 267.4 macrophage polarization. Gene expression levels of cells treated with 150 µg/mL CeO_2 NPs for 24 hours followed by stimulation with LPS or IL-4 for 12 hours. Data are represented as mean ± SEM. n = 3. * p <0.05, ** p <0.01, *** p <0.001, 0.0001

4.6.1 ROS, Mitochondria, and Glycolysis in Activated Macrophages

Next, we aimed to assess the role of ROS in modulating the inflammatory response in RAW 267.4 macrophages. Macrophages were pre-treated with CeO_2 NPs followed by exposure to LPS or IL-4 and thereafter ROS levels, mitochondria membrane potential, and metabolic markers were assessed.

As shown in **Figure 4.8A**, upon exposure to LPS, macrophages exhibited a significant increase in ROS levels, concomitant with a notable reduction in mitochondrial function, as evidenced by a pronounced decrease in the mitochondrial membrane potential (**Figure 4.8B**). Correspondingly, the heightened ROS levels in M1 macrophages correlated with the upregulation of *Hif1a* and the glucose transporter 1 (*Slc2a1*), which are key promoters of glycolysis (**Figure 4.8C)**.

The attenuation of ROS levels by CeO_2 NPs (**Figure 4.8A**) restored mitochondrial function (**Figure 4.8B**). The restoration of mitochondrial function was accompanied by significant reductions in *Hif1a* and *Slc2a1,* indicating glucose consumption shifts away from glycolysis towards mitochondrial respiration.

It is noteworthy that, RAW 264.7 M2 macrophages exhibit enhanced mitochondrial membrane potentials, reflecting their reliance on OXPHOS as the primary energy source. In accordance, the expression levels of glycolytic genes remained constitutive (**Figure 4.8C**), indicating a low glycolytic rate. Treatment with CeO_2 NPs led to further enhancement of mitochondrial membrane potentials, potentially altering cell function. Despite M2 macrophages typically maintaining higher levels of OXPHOS, their antioxidant systems are known to mitigate oxidative stress. Yet, the significant increase in membrane potential following CeO_2 NPs treatment may result in higher levels of ROS than the ones that can be managed by endogenous antioxidants, or it may affect mitochondrial function through alternative metabolic pathways.

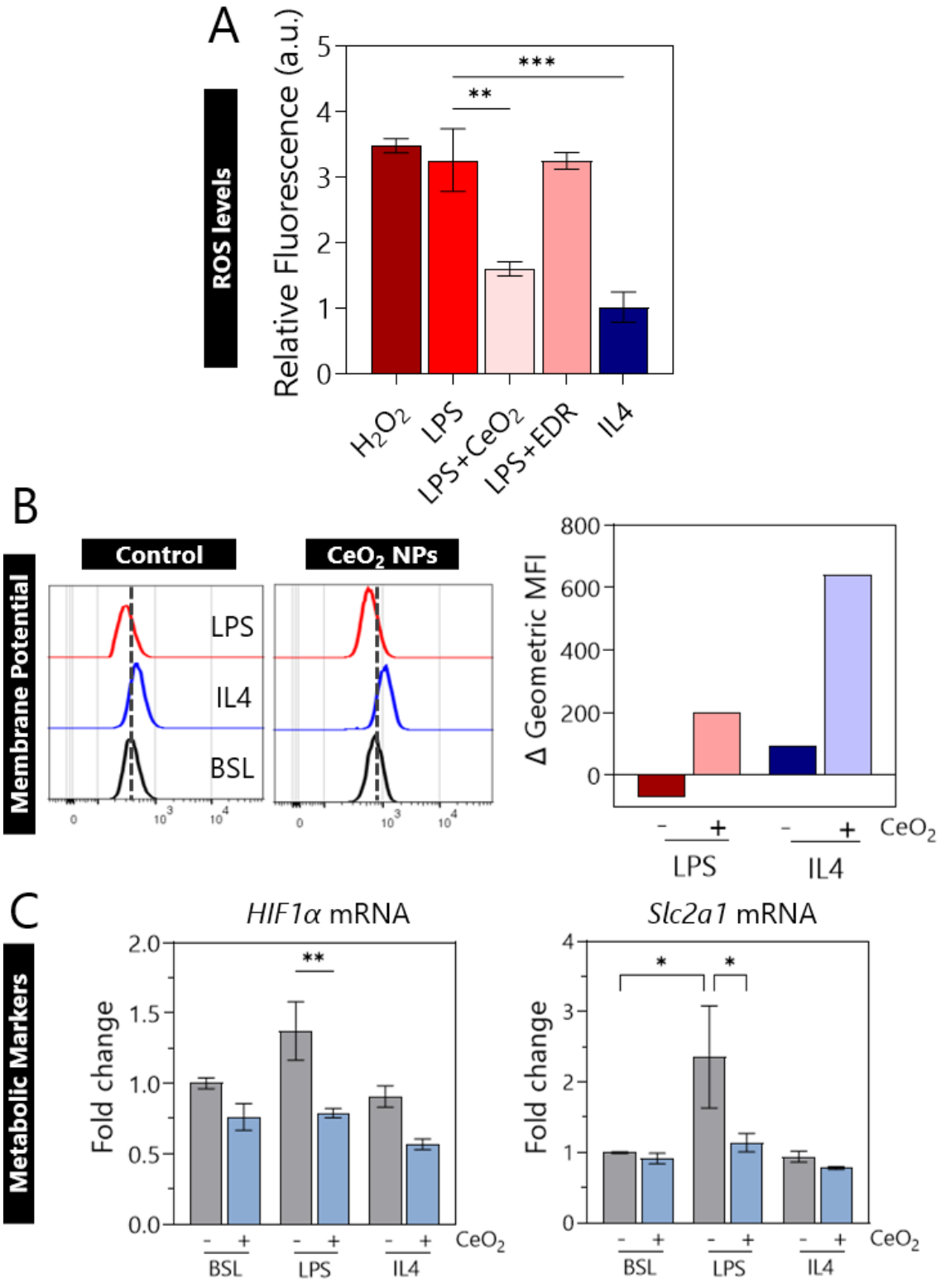


Figure 4.8. ROS promotes macrophage polarization towards M1 macrophages. RAW 267.4 macrophages were treated with 150 µg/mL of CeO_2 NPs and thereafter stimulated either with LPS or IL-4. **(A)** ROS determined 24 hours after cell activation using flow cytometry and the ROS assay kit. 50 nM Edaravone was used as molecular antioxidant control. Relative fluorescence was calculated from basal measurements. n = 3. **(B)** Mitochondria membrane potential was evaluated through cellular staining with MitoTracker Orange

followed by flow cytometry analysis. Staining was conducted 24 hours after cell activation. Membrane potential is presented as ΔGMFI = (Geometric mean fluorescence intensity)$_{experimental\ sample}$ - (Geometric mean fluorescence intensity)$_{control\ sample}$. n = 1. (C) Gene expression levels of cells after stimulation for 12 hours. n = 3. Data are represented as mean ± SEM. * p <0.05, ** p <0.01, *** p <0.001, ****p <0.0001

Although ROS quantification indicated no significant levels in M2-activated cells, the effect of CeO_2 NPs on M2 macrophage ROS levels was not assessed. To avoid speculation and strengthen the findings, further study on this is necessary. Additionally, since ROS levels may not directly correlate with oxidative stress, it is essential to concurrently assess antioxidant systems.

4.7 Effect of CeO_2 NPs on Mitochondria Morphology

Given the important role of mitochondria metabolism in macrophage polarization, we further investigated mitochondria morphology by imaging analysis. By combining advanced imaging with quantitative analysis, we sought to unravel patterns of mitochondrial dynamics and overall morphology alterations that may be linked to immune cell activation, differentiation, or pathological states. Mitochondria are often classified as spherical, short to elongated tubules, and reticular networks [82], but they present a dynamic behaviour that allows them to respond to cellular energy demands and contribute to the overall cell bioenergetics.

Thus, rapid changes in mitochondria number, morphology, and membrane potential have an impact on biofuel oxidation. Enhanced OXPHOS is associated with both increased membrane potential and mitochondrial elongation [83], consistent with the proposal that elongation of these organelles results in higher energy production [84]. Mitochondrial fragmentation and decreased membrane potentials have been related to a broken TCA cycle, decreased ATP synthesis, and elevated ROS production [85], which has been generally associated with oxidative stress conditions and diseases. The interconnectedness between mitochondrial and metabolic pathways has unveiled a reciprocal relationship: alterations in metabolism influence mitochondrial morphology, and conversely, the dynamic state of mitochondria impacts cellular bioenergetics and consequent everything.

During the M1 response, dysfunctional mitochondria have been related to highly fragmented and spherical structures, that can be linked to impaired OXPHOS, high ROS levels and increased glycolysis, whereas M2 cells frequently present elongated and hyperpolarized mitochondrial structures that correspond to increased OXPHOS rates coupled to high ATP production rates [86]. Thus, mitochondria morphology and membrane potential can be correlated to OXPHOS activity and efficiency, which is directly linked with ROS production and consequent metabolic reprogramming.

Here, RAW 267.4 macrophages were stained with the mitochondrial marker MitoTracker™ Orange and observed by confocal imaging. Representative images are depicted in **Figure 4.9**. 3D mitochondria imaging revealed typical arrangement of mitochondria in naive macrophages is mainly elongated although subsets of separated short tubular mitochondria or even individual spherical organelles were also observed, reflecting heterogeneity in mitochondrial morphology. Different structural features were observed in cells exposed either to LPS or IL-4. As expected, LPS stimulation led to a reduced mitochondrial volume and marked mitochondrial fragmentation, whereas M2 macrophages showed an intensely branched network of elongated organelles.

Next, to test CeO_2 NPs' effects on mitochondria morphology, cells were treated for 24 hours with CeO_2 NPs before cell activation. Confocal images showed no significant differences between CeO_2 NPs treated cells in both basal and IL-4 stimulated cells, whereas, in M1 macrophages, nanoceria increased mitochondria elongation and networking.

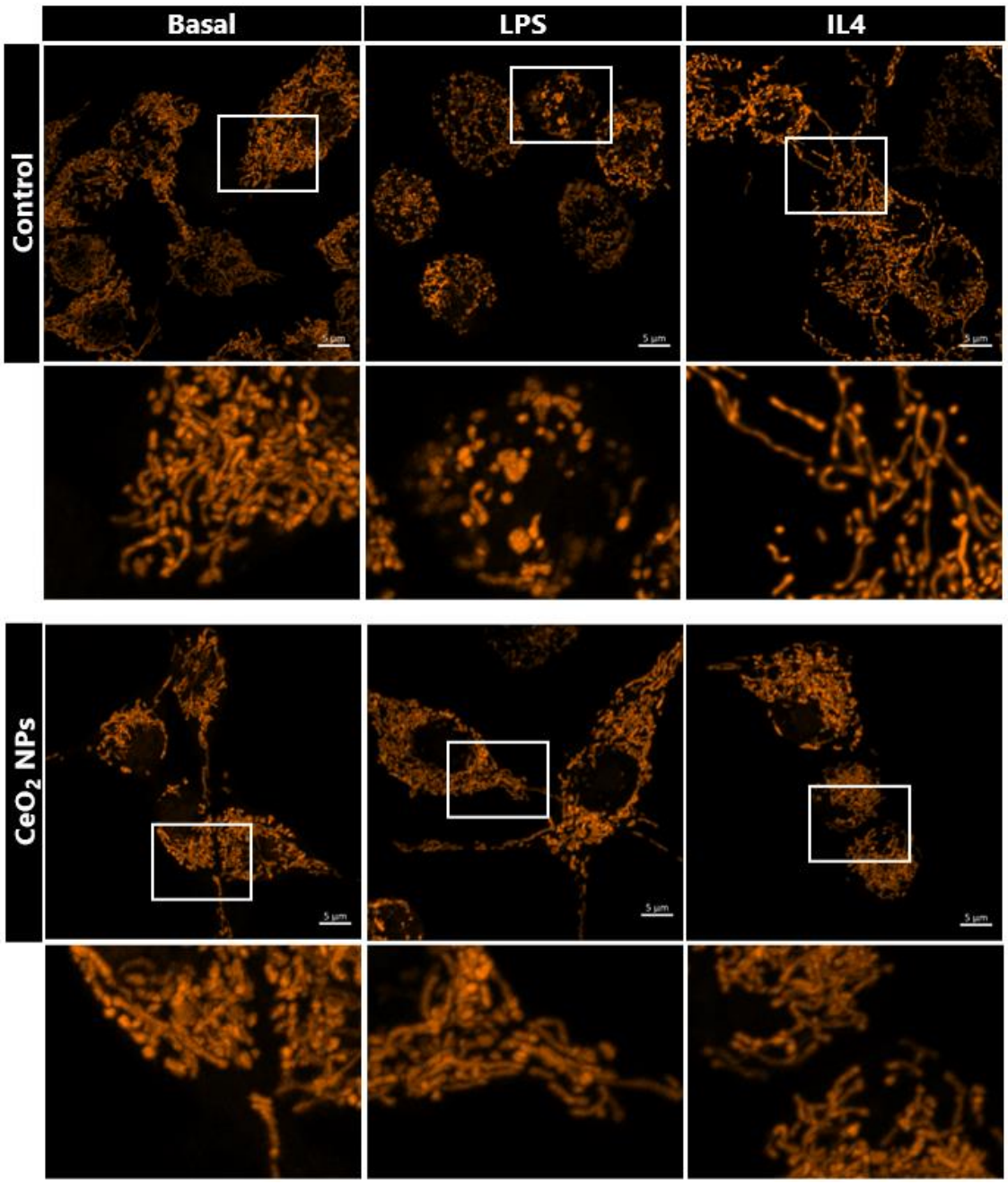


Figure 4.9. CeO_2 NPs treatment restores mitochondria morphology in M1 macrophages. RAW 267.4 cells were stimulated either with LPS (M1) or IL-4 (M2) (upper panel) and treated with 150 µg/mL CeO_2 NPs (lower panel) and then stained with MitoTracker Orange. Confocal Z-stacks were acquired using a Zeiss LSM980 confocal microscope and a maximum projection image was generated using Zen Blue software. Scale bar 5 µm. Representative images of each phenotype.

As visual methods for morphology classification are more dependent on subjective interpretations, next, to quantitatively evaluate the mitochondrial structure, confocal images were processed and analysed using imaging software. In brief, 3D images underwent pre-processing to enhance contrast and remove non-specific signals by using Image J software. To remove background, image segmentation was performed by using Ilastik software, employing machine learning algorithms. Finally, after the removal of outliers, mitochondrial number and volume were quantified using the "3D object counter" plugin, while branching was analysed using the "Analyse skeleton" plugin, both available in Image J. A minimum of 40 cells were analysed for each cell phenotype and the entire mitochondrial network was analysed for each cell. The complete workflow can be found in Chapter 5, section 5.3.11.

As shown in **Figure 4.10A**, image analysis reveals that while there are no significant differences in mitochondrial number, notable changes in mitochondrial volume are evident, suggesting a potential role of mitochondrial dynamics in regulating macrophage function, rather than mitochondria biogenesis. Interestingly, CeO_2 NPs increased the total mitochondrial volume in both LPS and IL-4-treated cells, which correlates with the previously reported increase in mitochondrial membrane potential. Further analysis of mitochondrial branching (**Figure 4.10B**) reveals that M1 cells have significantly decreased mitochondrial branching, suggesting mitochondria fragmentation and decreased networking, while the treatment with antioxidants like CeO_2 NPs, significantly improves mitochondrial network.

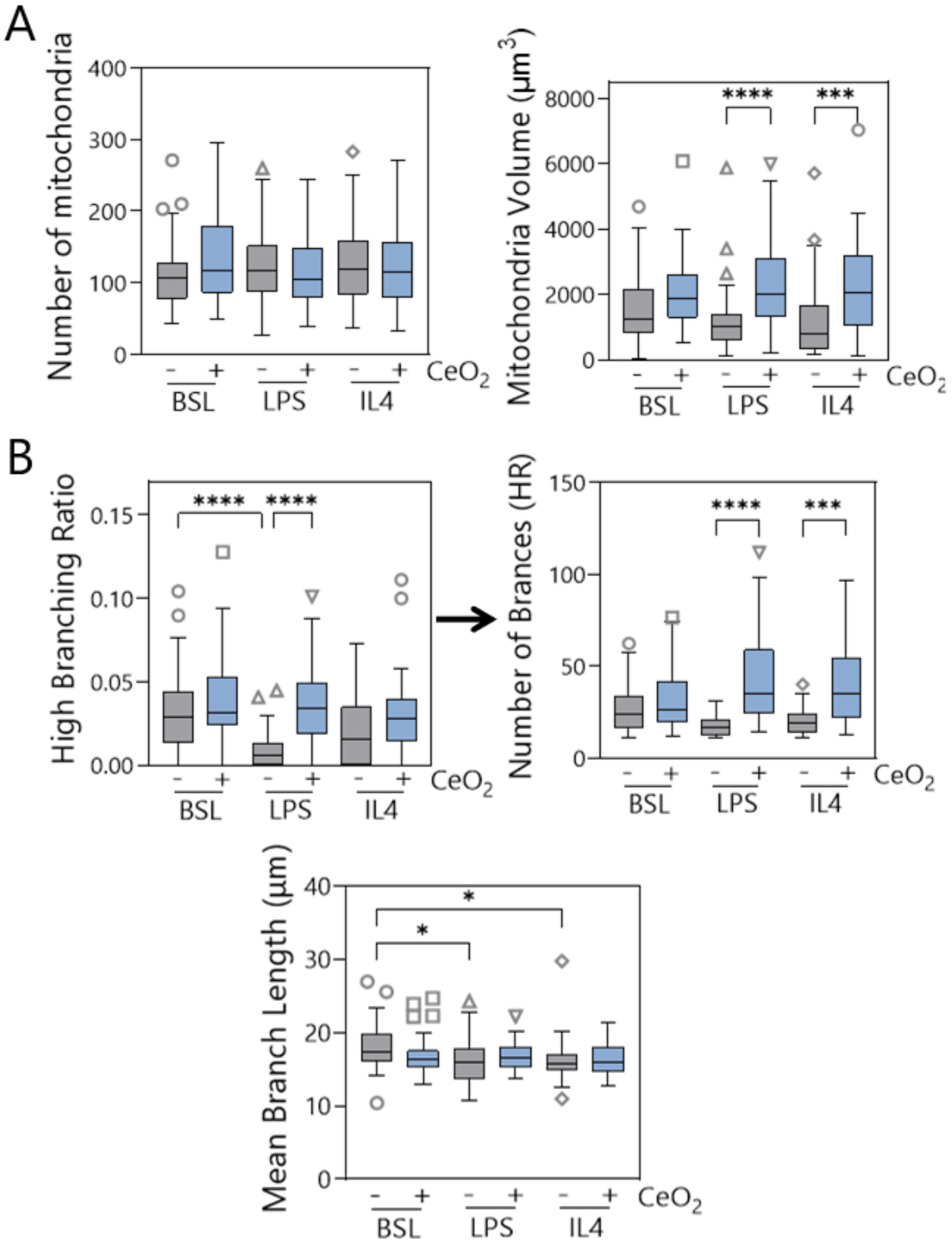


Figure 4.10. Analysis and quantification of mitochondrial structure. Z-stacks (3D) were pre-processed and analysed with ImageJ to determine the total number, volume, and branching of mitochondria. The high branching ratio was calculated by dividing the number of mitochondria with more than 10 branches by the total number of branches. Data are represented as mean ± SEM. n ≥ 40 cells for each condition. *p < 0.01, **p<0.001, ***p<0.0001, ****p<0.00001

Moreover, CeO_2 NPs increase the total number of branches in both LPS or IL-4 stimulated macrophages, while no significant effects are observed regarding the length of the branches (**Figure 4.10**). All in all, these results suggest that mitochondrial dynamics can be important markers of cell function and immune responses.

Because image analysis can be subjected to some technical errors, like image processing, the imaging analysis method was evaluated by measuring fractal dimension and lacunarity. Fractal geometry provides a useful framework for revealing the complexity inherent to structures that define living organisms [87], and lacunarity, as an extension of fractal geometry, offers a quantitative measure of the distribution and size of gaps within an image, which is related to texture.

Recently, some authors have proposed and validated fractal dimension and lacunarity measurements as a sensitive and objective method to quantify mitochondria morphology and have shown to be more resolutive in some circumstances [88,89], as these measurements take into account subtle differences in mitochondrial structure and their distribution within the cell. In general, mitochondrial elongation and networking, by increasing complexity, results in a higher fractal dimension, while highly fragmented and punctuated organelles (lower density) have high lacunarity.

In this scenario, the fractal dimension and lacunarity of each cell were measured using the Image J plugin FracLac. Results shown in **Figure 4.11** reveal that M1 cells present significantly lower fractal dimension (complexity) and higher lacunarity (gaps) values, which correlate with previous results showing increased mitochondrial fragmentation and lower membrane potentials, all in all indicating mitochondrial dysfunction in M1 inflammatory macrophages. Interestingly, the use of CeO_2 NPs significantly restored mitochondrial complexity and density as demonstrated by higher fractal dimension and reduced lacunarity. For M2 cells, fractal dimension measurement indicates a tendency towards higher complexity compared to control cells, and the use of CeO_2 NPs seems to further increase mitochondrial networking.

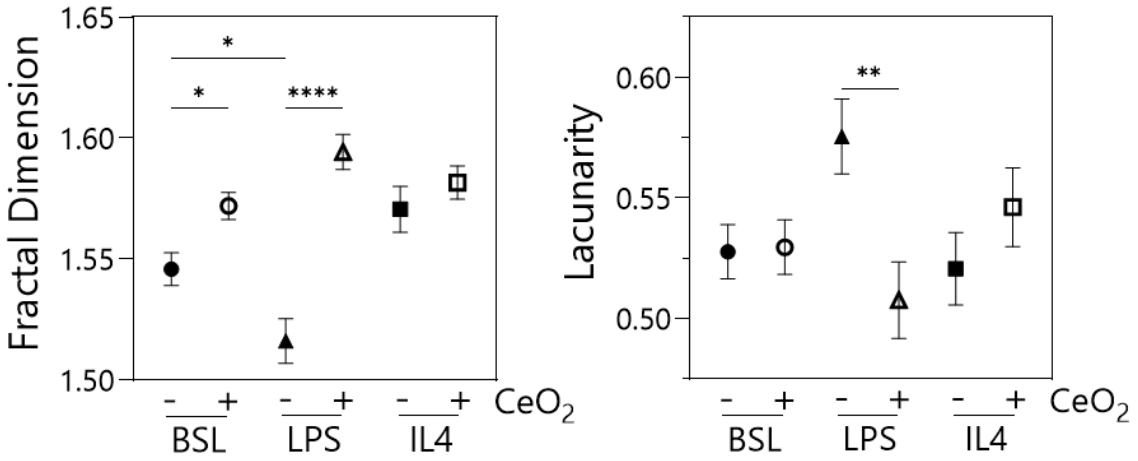


Figure 4.11. Maximum projection images (2D) were generated using Image J, followed by the calculation of fractal dimension and lacunarity with Image J software. Data are presented as mean ± SEM. n ≥ 40 cells for each condition. *p < 0.01, **p<0.001, ***p<0.0001, ****p<0.00001

Our results indicate that macrophages show a spectrum of mitochondrial morphologies ranging from elongated to highly reticulated in naïve and M2 macrophages, to more fragmented and spherical morphologies in pro-inflammatory cells. The use of antioxidants promotes mitochondria elongation which implies important structural adjustments within these organelles that correlate with restore of mitochondrial activity in M1 macrophages.

In summary, these findings indicate that mitochondrial activity is lost progressively after activation by TLR agonists (LPS) in M1 inflammatory macrophages. We found that this is because of the inhibition of OXPHOS by ROS and that the switch to glycolysis is a survival response that serves to maintain ATP levels when OXPHOS is inhibited. Scavenging ROS with the use of antioxidant CeO_2 NPs restores mitochondrial function, which drives the reduction of important inflammatory markers. Although modulating ROS levels presents a promising avenue for therapeutic intervention, the effects on the M2 response should be further evaluated because they may attenuate some specific functions, which could indicate that ROS might have a dual role in both immune activation and inflammatory resolution.

4.8 References

1. Ma, Y.L.; Ke, J.F.; Wang, J.W.; Wang, Y.J.; Xu, M.R.; Li, L.X. Blood Lactate Levels Are Associated with an Increased Risk of Metabolic Dysfunction-Associated Fatty Liver Disease in Type 2 Diabetes: A Real-World Study. *Front Endocrinol (Lausanne)* **2023**, *14*, 1133991.

2. Kushimoto, S.; Akaishi, S.; Sato, T.; Nomura, R.; Fujita, M.; Kudo, D.; Kawazoe, Y.; Yoshida, Y.; Miyagawa, N. Lactate, a Useful Marker for Disease Mortality and Severity but an Unreliable Marker of Tissue Hypoxia/Hypoperfusion in Critically Ill Patients. *Acute Medicine & Surgery* **2016**, *3*, 293.

3. Marecaux, G.; Pinsky, M.R.; Dupont, E.; Kahn, R.J.; Vincent, J.L. Blood Lactate Levels Are Better Prognostic Indicators than TNF and IL-6 Levels in Patients with Septic Shock. *Intensive Care Med* **1996**, *22*, 404–408.

4. Cori, C.F.; Cori, G.T. THE CARBOHYDRATE METABOLISM OF TUMORS: I. THE FREE SUGAR, LACTIC ACID, AND GLYCOGEN CONTENT OF MALIGNANT TUMORS. *Journal of Biological Chemistry* **1925**, *64*, 11–22.

5. Warburg, O.; Wind, F.; Negelein, E. THE METABOLISM OF TUMORS IN THE BODY. *J Gen Physiol* **1927**, *8*, 519.

6. Reinfeld, B.I.; Rathmell, W.K.; Kim, T.K.; Rathmell, J.C. The Therapeutic Implications of Immunosuppressive Tumor Aerobic Glycolysis. *Cellular & Molecular Immunology 2021 19:1* **2021**, *19*, 46–58.

7. Cohen, I.J.; Pareja, F.; Socci, N.D.; Shen, R.; Doane, A.S.; Schwartz, J.; Khanin, R.; Morris, E.A.; Sutton, E.J.; Blasberg, R.G. Increased Tumor Glycolysis Is Associated with Decreased Immune Infiltration across Human Solid Tumors. *Front Immunol* **2022**, *13*, 880959.

8. Freemerman, A.J.; Johnson, A.R.; Sacks, G.N.; Milner, J.J.; Kirk, E.L.; Troester, M.A.; Macintyre, A.N.; Goraksha-Hicks, P.; Rathmell, J.C.; Makowski, L. Metabolic Reprogramming of Macrophages: Glucose Transporter 1 (GLUT1)-Mediated Glucose Metabolism Drives a Proinflammatory Phenotype. *Journal of Biological Chemistry* **2014**, *289*, 7884–7896.

9. Macintyre, A.N.; Gerriets, V.A.; Nichols, A.G.; Michalek, R.D.; Rudolph, M.C.; Deoliveira, D.; Anderson, S.M.; Abel, E.D.; Chen, B.J.; Hale, L.P.; et al. The Glucose Transporter Glut1 Is Selectively Essential for CD4 T Cell Activation and Effector Function. *Cell Metab* **2014**, *20*, 61–72.

10. Lefere, S.; Tacke, F. Macrophages in Obesity and Non-Alcoholic Fatty Liver Disease: Crosstalk with Metabolism. *JHEP Reports* **2019**, *1*, 30.

11. Sun, J.X.; Xu, X.H.; Jin, L. Effects of Metabolism on Macrophage Polarization Under Different Disease Backgrounds. *Front Immunol* **2022**, *13*, 880286.

12. Archibald, J.M. Endosymbiosis and Eukaryotic Cell Evolution. *Current Biology* **2015**, *25*, R911–R921.

13. Balaban, R.S.; Nemoto, S.; Finkel, T. Mitochondria, Oxidants, and Aging. *Cell* **2005**, *120*, 483–495.

14. Davies, K.J. Oxidative Stress: The Paradox of Aerobic Life. *Biochem Soc Symp* **1995**, *61*, 1–31.

15. Lennicke, C.; Cochemé, H.M. Redox Metabolism: ROS as Specific Molecular Regulators of Cell Signaling and Function. *Mol Cell* **2021**, *81*, 3691–3707.

16. Li, H.; Zhou, X.; Huang, Y.; Liao, B.; Cheng, L.; Ren, B. Reactive Oxygen Species in Pathogen Clearance: The Killing Mechanisms, the Adaption Response, and the Side Effects. *Front Microbiol* **2021**, *11*, 622534.

17. Sena, L.A.; Chandel, N.S. Physiological Roles of Mitochondrial Reactive Oxygen Species. *Mol Cell* **2012**, *48*, 158.

18. Fransen, M.; Nordgren, M.; Wang, B.; Apanasets, O. Role of Peroxisomes in ROS/RNS-Metabolism: Implications for Human Disease. *Biochimica et Biophysica Acta (BBA) - Molecular Basis of Disease* **2012**, *1822*, 1363–1373.

19. Snezhkina, A. V.; Kudryavtseva, A. V.; Kardymon, O.L.; Savvateeva, M. V.; Melnikova, N. V.; Krasnov, G.S.; Dmitriev, A.A. ROS Generation and Antioxidant Defense Systems in Normal and Malignant Cells. *Oxid Med Cell Longev* **2019**, *2019*.

20. Jastroch, M.; Divakaruni, A.S.; Mookerjee, S.; Treberg, J.R.; Brand, M.D. Mitochondrial Proton and Electron Leaks. *Essays Biochem* **2010**, *47*, 53.

21. Pittman, R.N. Tissue Gas Transport. **2011**.

22. Suski, J.M.; Lebiedzinska, M.; Bonora, M.; Pinton, P.; Duszynski, J.; Wieckowski, M.R. Relation between Mitochondrial Membrane Potential and ROS Formation. *Methods Mol Biol* **2012**, *810*, 183–205.

23. Chance, B.; Sies, H.; Boveris, A. Hydroperoxide Metabolism in Mammalian Organs. *Physiol Rev* **1979**, *59*, 527–605.

24. St-Pierre, J.; Buckingham, J.A.; Roebuck, S.J.; Brand, M.D. Topology of Superoxide Production from Different Sites in the Mitochondrial Electron Transport Chain. *J Biol Chem* **2002**, *277*, 44784–44790.

25. Aon, M.A.; Cortassa, S.; O'Rourke, B. Redox-Optimized ROS Balance: A Unifying Hypothesis. *Biochimica et Biophysica Acta (BBA) - Bioenergetics* **2010**, *1797*, 865–877.

26. Jung, S.N.; Yang, W.K.; Kim, J.; Kim, H.S.; Kim, E.J.; Yun, H.; Park, H.; Kim, S.S.; Choe, W.; Kang, I.; et al. Reactive Oxygen Species Stabilize Hypoxia-Inducible Factor-1 Alpha Protein and Stimulate Transcriptional Activity via AMP-Activated Protein Kinase in DU145 Human Prostate Cancer Cells. *Carcinogenesis* **2008**, *29*, 713–721.

27. Zou, H.; Wang, H.; Xu, B.; Liang, L.; Shen, L.; Lin, Q. Regenerative Cerium Oxide Nanozymes Alleviate Oxidative Stress for Efficient Dry Eye Disease Treatment. *Regen Biomater* **2022**, *9*.

28. Zhao, T.; Zhu, Y.; Morinibu, A.; Kobayashi, M.; Shinomiya, K.; Itasaka, S.; Yoshimura, M.; Guo, G.; Hiraoka, M.; Harada, H. HIF-1-Mediated Metabolic Reprogramming Reduces ROS Levels and Facilitates the Metastatic Colonization of Cancers in Lungs. *Scientific Reports 2014 4:1* **2014**, *4*, 1–7.

29. Chandel, N.S.; McClintock, D.S.; Feliciano, C.E.; Wood, T.M.; Melendez, J.A.; Rodriguez, A.M.; Schumacker, P.T. Reactive Oxygen Species Generated at Mitochondrial Complex III Stabilize Hypoxia-Inducible Factor-1α during Hypoxia: A

MECHANISM OF O2 SENSING *. *Journal of Biological Chemistry* **2000**, *275*, 25130–25138.

30. Bell, E.L.; Emerling, B.M.; Chandel, N.S. Mitochondrial Regulation of Oxygen Sensing. *Mitochondrion* **2005**, *5*, 322–332.

31. Liu, L.; Luc, Y.; Martinez, J.; Bi, Y.; Lian, G.; Wang, T.; Milasta, S.; Wang, J.; Yang, M.; Liu, G.; et al. Proinflammatory Signal Suppresses Proliferation and Shifts Macrophage Metabolism from Myc-Dependent to HIF1α-Dependent. *Proc Natl Acad Sci U S A* **2016**, *113*, 1564–1569.

32. Forrester, S.J.; Kikuchi, D.S.; Hernandes, M.S.; Xu, Q.; Griendling, K.K. Reactive Oxygen Species in Metabolic and Inflammatory Signaling. *Circ Res* **2018**, *122*, 877.

33. Yu, Q.; Wang, Y.; Dong, L.; He, Y.; Liu, R.; Yang, Q.; Cao, Y.; Wang, Y.; Jia, A.; Bi, Y.; et al. Regulations of Glycolytic Activities on Macrophages Functions in Tumor and Infectious Inflammation. *Front Cell Infect Microbiol* **2020**, *10*, 287.

34. Everts, B.; Amiel, E.; Van Der Windt, G.J.W.; Freitas, T.C.; Chott, R.; Yarasheski, K.E.; Pearce, E.L.; Pearce, E.J. Commitment to Glycolysis Sustains Survival of NO-Producing Inflammatory Dendritic Cells. *Blood* **2012**, *120*, 1422–1431.

35. Masoud, G.N.; Li, W. HIF-1α Pathway: Role, Regulation and Intervention for Cancer Therapy. *Acta Pharm Sin B* **2015**, *5*, 378.

36. Fong, G.H.; Takeda, K. Role and Regulation of Prolyl Hydroxylase Domain Proteins. *Cell Death & Differentiation 2008 15:4* **2008**, *15*, 635–641.

37. Zhang, Z.W.; Cheng, J.; Xu, F.; Chen, Y.E.; Du, J.B.; Yuan, M.; Zhu, F.; Xu, X.C.; Yuan, S. Red Blood Cell Extrudes Nucleus and Mitochondria against Oxidative Stress. *IUBMB Life* **2011**, *63*, 560–565.

38. Holt, R.I.G.; Cockram, C.S.; Ma, R.C.W.; Luk, A.O.Y. Diabetes and Infection: Review of the Epidemiology, Mechanisms and Principles of Treatment. *Diabetologia 2024* **2024**, 1–13.

39. Bramante, C.T.; Ingraham, N.E.; Murray, T.A.; Marmor, S.; Hovertsen, S.; Gronski, J.; McNeil, C.; Feng, R.; Guzman, G.; Abdelwahab, N.; et al. Metformin and Risk of

Mortality in Patients Hospitalised with COVID-19: A Retrospective Cohort Analysis. *Lancet Healthy Longev* **2021**, *2*, e34–e41.

40. Han, Y.; Xie, H.; Liu, Y.; Gao, P.; Yang, X.; Shen, Z. Effect of Metformin on All-Cause and Cardiovascular Mortality in Patients with Coronary Artery Diseases: A Systematic Review and an Updated Meta-Analysis. *Cardiovasc Diabetol* **2019**, *18*, 1–16.

41. Bradley, M.C.; Ferrara, A.; Achacoso, N.; Ehrlich, S.F.; Quesenberry, C.P.; Habel, L.A. A Cohort Study of Metformin and Colorectal Cancer Risk among Patients with Diabetes Mellitus. *Cancer Epidemiol Biomarkers Prev* **2018**, *27*, 525.

42. Bai, B.; Chen, H. Metformin: A Novel Weapon Against Inflammation. *Front Pharmacol* **2021**, *12*, 622262.

43. Triggle, C.R.; Marei, I.; Ye, K.; Ding, H.; Anderson, T.J.; Hollenberg, M.D.; Hill, M.A. Repurposing Metformin for Vascular Disease. *Curr Med Chem* **2023**, *30*, 3955.

44. Lascu, A.; Ionică, L.N.; Merce, A.P.; Dănilă, M.D.; Petrescu, L.; Sturza, A.; Muntean, D.M.; Streian, C.G. Metformin Acutely Mitigates Oxidative Stress in Human Atrial Tissue: A Pilot Study in Overweight Non-Diabetic Cardiac Patients. *Life 2022, Vol. 12, Page 2058* **2022**, *12*, 2058.

45. Nassif, R.M.; Chalhoub, E.; Chedid, P.; Hurtado-Nedelec, M.; Raya, E.; Dang, P.M.C.; Marie, J.C.; El-Benna, J. Metformin Inhibits ROS Production by Human M2 Macrophages via the Activation of AMPK. *Biomedicines* **2022**, *10*.

46. Hartwig, J.; Loebel, M.; Steiner, S.; Bauer, S.; Karadeniz, Z.; Roeger, C.; Skurk, C.; Scheibenbogen, C.; Sotzny, F. Metformin Attenuates ROS via FOXO3 Activation in Immune Cells. *Front Immunol* **2021**, *12*.

47. Algire, C.; Moiseeva, O.; Deschênes-Simard, X.; Amrein, L.; Petruccelli, L.; Birman, E.; Viollet, B.; Ferbeyre, G.; Pollak, M.N. Metformin Reduces Endogenous Reactive Oxygen Species and Associated DNA Damage. *Cancer Prev Res (Phila)* **2012**, *5*, 536–543.

48. Kondoh, H.; Lleonart, M.E.; Bernard, D.; Gil, J. Protection from Oxidative Stress by Enhanced Glycolysis; a Possible Mechanism of Cellular Immortalization. *Histol Histopathol* **2007**, *22*, 85–90.

49. Beltran, C.; Pardo, R.; Bou-Teen, D.; Ruiz-Meana, M.; Villena, J.A.; Ferreira-González, I.; Barba, I. Enhancing Glycolysis Protects against Ischemia-Reperfusion Injury by Reducing ROS Production. *Metabolites* **2020**, *10*.

50. Brand, K.A.; Hermfisse, U. Aerobic Glycolysis by Proliferating Cells: A Protective Strategy against Reactive Oxygen Species 1 . *The FASEB Journal* **1997**, *11*, 388–395.

51. Fiorillo, M.; Ózsvári, B.; Sotgia, F.; Lisanti, M.P. High ATP Production Fuels Cancer Drug Resistance and Metastasis: Implications for Mitochondrial ATP Depletion Therapy. *Front Oncol* **2021**, *11*.

52. Le, A.; Cooper, C.R.; Gouw, A.M.; Dinavahi, R.; Maitra, A.; Deck, L.M.; Royer, R.E.; Vander Jagt, D.L.; Semenza, G.L.; Dang, C. V. Inhibition of Lactate Dehydrogenase A Induces Oxidative Stress and Inhibits Tumor Progression. *Proc Natl Acad Sci U S A* **2010**, *107*, 2037–2042.

53. Korga, A.; Ostrowska, M.; Iwan, M.; Herbet, M.; Dudka, J. Inhibition of Glycolysis Disrupts Cellular Antioxidant Defense and Sensitizes HepG2 Cells to Doxorubicin Treatment. *FEBS Open Bio* **2019**, *9*, 959–972.

54. Wang, S.; Wang, J.; Chen, Z.; Luo, J.; Guo, W.; Sun, L.; Lin, L. Targeting M2-like Tumor-Associated Macrophages Is a Potential Therapeutic Approach to Overcome Antitumor Drug Resistance. *npj Precision Oncology 2024 8:1* **2024**, *8*, 1–19.

55. O'Neill, L.A.J. A Broken Krebs Cycle in Macrophages. *Immunity* 2015, *42*, 393–394.

56. Van den Bossche, J.; Baardman, J.; Otto, N.A.; van der Velden, S.; Neele, A.E.; van den Berg, S.M.; Luque-Martin, R.; Chen, H.J.; Boshuizen, M.C.S.; Ahmed, M.; et al. Mitochondrial Dysfunction Prevents Repolarization of Inflammatory Macrophages. *Cell Rep* **2016**, *17*, 684–696.

57. Song, Y.J.; Kim, A.; Kim, G.T.; Yu, H.Y.; Lee, E.S.; Park, M.J.; Kim, Y.J.; Shim, S.M.; Park, T.S. Inhibition of Lactate Dehydrogenase A Suppresses Inflammatory Response in RAW 264.7 Macrophages. *Mol Med Rep* **2019**, *19*, 629–637.

58. Rambold, A.S.; Pearce, E.L. Mitochondrial Dynamics at the Interface of Immune Cell Metabolism and Function. *Trends Immunol* **2018**, *39*, 6–18.

59. Michl, J.; Ohlbaum, D.J.; Silverstein, S.C. 2-Deoxyglucose Selectively Inhibits Fc and Complement Receptor-Mediated Phagocytosis in Mouse Peritoneal Macrophages II. Dissociation of the Inhibitory Effects of 2-Deoxyglucose on Phagocytosis and ATP Generation. *J Exp Med* **1976**, *144*, 1484.

60. Francis, R.; Singh, P.K.; Singh, S.; Giri, S.; Kumar, A. Glycolytic Inhibitor 2-Deoxyglucose Suppresses Inflammatory Response in Innate Immune Cells and Experimental Staphylococcal Endophthalmitis. *Exp Eye Res* **2020**, *197*, 108079.

61. Griess, B.; Mir, S.; Datta, K.; Teoh-Fitzgerald, M. Scavenging Reactive Oxygen Species Selectively Inhibits M2 Macrophage Polarization and Their Pro-Tumorigenic Function in Part, via Stat3 Suppression. *Free Radic Biol Med* **2020**, *147*, 48–60.

62. Covarrubias, A.; Byles, V.; Horng, T. ROS Sets the Stage for Macrophage Differentiation. *Cell Research 2013 23:8* **2013**, *23*, 984–985.

63. Zhang, B.; Yang, Y.; Yi, J.; Zhao, Z.; Ye, R. Hyperglycemia Modulates M1/M2 Macrophage Polarization via Reactive Oxygen Species Overproduction in Ligature-Induced Periodontitis. *J Periodontal Res* **2021**, *56*, 991–1005.

64. Huang, X.; Li, Y.; Fu, M.; Xin, H.B. Polarizing Macrophages In Vitro. *Methods Mol Biol* **2018**, *1784*, 119–126.

65. Mills, C.D. Anatomy of a Discovery: M1 and M2 Macrophages. *Front Immunol* **2015**, *6*.

66. Miyazono, Y.; Hirashima, S.; Ishihara, N.; Kusukawa, J.; Nakamura, K.I.; Ohta, K. Uncoupled Mitochondria Quickly Shorten along Their Long Axis to Form Indented Spheroids, Instead of Rings, in a Fission-Independent Manner. *Scientific Reports 2017 8:1* **2018**, *8*, 1–14.

67. Corcoran, S.E.; O'Neill, L.A.J. HIF1α and Metabolic Reprogramming in Inflammation. *J Clin Invest* **2016**, *126*, 3699–3707.

68. Yao, Q.; Liu, J.; Zhang, Z.; Li, F.; Zhang, C.; Lai, B.; Xiao, L.; Wang, N. Peroxisome Proliferator-Activated Receptor γ (PPARγ) Induces the Gene Expression of Integrin AVβ5 to Promote Macrophage M2 Polarization. *J Biol Chem* **2018**, *293*, 16572–16582.

69. Bouhlel, M.A.; Derudas, B.; Rigamonti, E.; Dièvart, R.; Brozek, J.; Haulon, S.; Zawadzki, C.; Jude, B.; Torpier, G.; Marx, N.; et al. PPARgamma Activation Primes Human Monocytes into Alternative M2 Macrophages with Anti-Inflammatory Properties. *Cell Metab* **2007**, *6*, 137–143.

70. Tian, Y.; Yang, C.; Yao, Q.; Qian, L.; Liu, J.; Xie, X.; Ma, W.; Nie, X.; Lai, B.; Xiao, L.; et al. Procyanidin B2 Activates PPARγ to Induce M2 Polarization in Mouse Macrophages. *Front Immunol* **2019**, *10*, 471348.

71. Genin, M.; Clement, F.; Fattaccioli, A.; Raes, M.; Michiels, C. M1 and M2 Macrophages Derived from THP-1 Cells Differentially Modulate the Response of Cancer Cells to Etoposide. *BMC Cancer* **2015**, *15*, 1–14.

72. Shiratori, H.; Feinweber, C.; Luckhardt, S.; Linke, B.; Resch, E.; Geisslinger, G.; Weigert, A.; Parnham, M.J. THP-1 and Human Peripheral Blood Mononuclear Cell-Derived Macrophages Differ in Their Capacity to Polarize in Vitro. *Mol Immunol* **2017**, *88*, 58–68.

73. Chanput, W.; Mes, J.J.; Wichers, H.J. THP-1 Cell Line: An in Vitro Cell Model for Immune Modulation Approach. *Int Immunopharmacol* **2014**, *23*, 37–45.

74. Baxter, E.W.; Graham, A.E.; Re, N.A.; Carr, I.M.; Robinson, J.I.; Mackie, S.L.; Morgan, A.W. Standardized Protocols for Differentiation of THP-1 Cells to Macrophages with Distinct M(IFNγ+LPS), M(IL-4) and M(IL-10) Phenotypes. *J Immunol Methods* **2020**, *478*, 112721.

75. Tedesco, S.; De Majo, F.; Kim, J.; Trenti, A.; Trevisi, L.; Fadini, G.P.; Bolego, C.; Zandstra, P.W.; Cignarella, A.; Vitiello, L. Convenience versus Biological Significance: Are PMA-Differentiated THP-1 Cells a Reliable Substitute for Blood-Derived Macrophages When Studying in Vitro Polarization? *Front Pharmacol* **2018**, *9*.

76. Chanput, W.; Mes, J.J.; Savelkoul, H.F.J.; Wichers, H.J. Characterization of Polarized THP-1 Macrophages and Polarizing Ability of LPS and Food Compounds. *Food Funct* **2013**, *4*, 266–276.

77. Daigneault, M.; Preston, J.A.; Marriott, H.M.; Whyte, M.K.B.; Dockrell, D.H. The Identification of Markers of Macrophage Differentiation in PMA-Stimulated THP-1 Cells and Monocyte-Derived Macrophages. *PLoS One* **2010**, *5*, e8668.

78. Park, E.K.; Jung, H.S.; Yang, H.I.; Yoo, M.C.; Kim, C.; Kim, K.S. Optimized THP-1 Differentiation Is Required for the Detection of Responses to Weak Stimuli. *Inflamm Res* **2007**, *56*, 45–50.

79. Maeß, M.B.; Wittig, B.; Cignarella, A.; Lorkowski, S. Reduced PMA Enhances the Responsiveness of Transfected THP-1 Macrophages to Polarizing Stimuli. *J Immunol Methods* **2014**, *402*, 76–81.

80. Starr, T.; Bauler, T.J.; Malik-Kale, P.; Steele-Mortimer, O. The Phorbol 12-Myristate-13-Acetate Differentiation Protocol Is Critical to the Interaction of THP-1 Macrophages with Salmonella Typhimurium. *PLoS One* **2018**, *13*.

81. Kim, Y.K.; Hwang, J.H.; Lee, H.T. Differential Susceptibility to Lipopolysaccharide Affects the Activation of Toll-like-Receptor 4 Signaling in THP-1 Cells and PMA-Differentiated THP-1 Cells. *Innate Immun* **2022**, *28*, 122–129.

82. Galloway, C.A.; Yoon, Y. Perspectives on: SGP Symposium on Mitochondrial Physiology and Medicine: What Comes First, Misshape or Dysfunction? The View from Metabolic Excess. *J Gen Physiol* **2012**, *139*, 455.

83. Mishra, P.; Chan, D.C. Metabolic Regulation of Mitochondrial Dynamics. *J Cell Biol* **2016**, *212*, 379.

84. Skulachev, V.P. Mitochondrial Filaments and Clusters as Intracellular Power-Transmitting Cables. *Trends Biochem Sci* **2001**, *26*, 23–29.

85. Wai, T.; Langer, T. Mitochondrial Dynamics and Metabolic Regulation. *Trends Endocrinol Metab* **2016**, *27*, 105–117.

86. Kawano, I.; Bazila, B.; Ježek, P.; Dlasková, A. Mitochondrial Dynamics and Cristae Shape Changes During Metabolic Reprogramming. *Antioxid Redox Signal* **2023**, *39*, 684–707.

87. Losa, G.A.; Nonnenmacher, T.F. Self-Similarity and Fractal Irregularity in Pathologic Tissues. *Mod Pathol* **1996**, *9*, 174–182.

88. Lennon, F.E.; Cianci, G.C.; Kanteti, R.; Riehm, J.J.; Arif, Q.; Poroyko, V.A.; Lupovitch, E.; Vigneswaran, W.; Husain, A.; Chen, P.; et al. Unique Fractal Evaluation

and Therapeutic Implications of Mitochondrial Morphology in Malignant Mesothelioma. *Scientific Reports 2016 6:1* **2016**, *6*, 1–15.

89. Zahedi, A.; On, V.; Phandthong, R.; Chaili, A.; Remark, G.; Bhanu, B.; Talbot, P. Deep Analysis of Mitochondria and Cell Health Using Machine Learning. *Scientific Reports 2018 8:1* **2018**, *8*, 1–15.

CHAPTER 5

EXPERIMENTAL SECTION

Chapter 5

Experimental Section

5.1 Chapter 2: Synthesis and Physicochemical Properties of CeO_2 Nanoparticles

5.1.1 Chemicals

Cerium (III) chloride heptahydrate ($CeCl_3 \bullet 7\ H_2O$), Tetramethylammonium hydroxide (TMAOH), Sodium Citrate (SC), cerium (III) nitrate hexahydrate ($Ce(NO_3)_3 \bullet 6\ H_2O$), bovine serum albumin (BSA), human serum albumin (HAS; A9511), NaCl, Ferrocyanide ($[Fe(CN)_6]^{4-}$), ferricyanide ($[Fe(CN)_6]^{3-}$), HNO_3, LPS (from Escherichia coli, serotype O111), BSA heat shock fraction (A4161) were purchased at Sigma-Aldrich.

Phosphate Buffer (PB), Phosphate Buffered Saline (PBS), Dulbecco's modified Eagle's medium (DMEM), Heat-inactivated Foetal Bovine Serum (FBS), N-acetyl Cysteine (NAC), Amplex™ Red Hydrogen Peroxide Assay Kit (A22188), Hydrogen Peroxide 30% (H_2O_2), PrestoBlue reagent (A13261), Amplex™ Red Hydrogen Peroxide Assay Kit (A22188), Pacific Blue™ Annexin V/SYTOX™ AADvanced™ Apoptosis kit (A35136) were purchased from Thermo Fisher Scientific.

Mouse recombinant IL-4 was purchased from PeproTech, Universal Grade BSA (810033) from Millipore, and Biochemistry grade BSA (268131000) from Acros.

5.1.2 Synthesis of Nanoparticles

CeO_2 NPs were synthesized using a wet chemistry method based on the basic precipitation of cerium (III) chloride heptahydrate ($CeCl_3 \bullet 7\ H_2O$) in the presence of sodium citrate (SC). In detail, a TMAOH solution (50 mL, 81 mM) was added to a 100 ml solution containing $CeCl_3 \bullet 7\ H_2O$ (30 mM) and SC (60 mM). The final concentration was: 27 mM TMAOH, 10 mM $CeCl_3 \bullet 7\ H_2O$, and 20 mM SC. The

reaction mixture was left under stirring overnight at room temperature. Later, the mixture was transferred to a three-necked round bottom flask (250 mL) and left under refluxing at 100 ºC for 4 hours (thermal treatment). The resulting mixture was a stable, well-dispersed solution of 3 nm CeO_2 NPs at a concentration of 1.72 mg/mL CeO_2.

Note that synthesis with cerium (III) nitrate hexahydrate ($Ce(NO_3)_3 \bullet 6\ H_2O$) was also tested.

Before use, the NPs solution was purified with 3 kDa centrifugal filter units (Amicon-Ultra-15 3K) at 5000g for 20 minutes and then re-suspended in 2.2 mM SC unless otherwise specified.

5.1.2.1 Synthesis without Sodium Citrate (SC)

Synthesis without the use of SC followed the same protocol but omitted thermal treatment. The resulting mixture was composed of 5 nm aggregated CeO_2 NPs at a concentration of 1.72 mg/mL CeO_2.

Before use, the NPs solutions were purified by standard centrifugation at 5000g for 5 minutes and re-suspended in 10 mM TMAOH.

5.1.3 Nanoparticle Characterization Techniques

5.1.3.1 Bacterial Endotoxin (LAL) test

Both synthesis and purification of NPs were performed under sterile conditions and with non-pyrogenic material. To ensure safe CeO_2 NPs were routinely tested for endotoxin levels at the *Echevarne* analysis laboratory (Barcelona).

5.1.3.2 High-Resolution Scanning Transmission Electron Microscopy (HRES-TEM) and High-Angle Annular Dark Field Scanning Transmission Electron Microscopy (HAADF-STEM)

CeO_2 NPs were visualized using HRES-TEM (Tecnai F20 S/TEM) and HAADF-STEM (Magellan 400L). 10 µl of the as-synthesized solutions were drop-casted onto a carbon-coated 200 mesh copper grid and left to dry for at least 24 hours in the air at

room temperature. The samples' average size and distribution were measured using Image J Analysis software by counting at least 500 particles.

TEM is a powerful imaging technique that uses a beam of electrons to produce high-resolution images. The basic principle involves transmitting electrons through a very thin specimen. As the electrons interact with the sample, they get scattered and create an image or diffraction pattern. The high energy of the electrons and the short wavelength associated with them enable TEM to achieve much higher resolution compared to light microscopy. However, while CeO_2 NPs can be visualized by TEM, their small size and density pose limitations on resolution.

HRES-TEM further enhances the capabilities of conventional TEM by achieving even higher resolution. HRES-TEM utilizes advanced electron lenses and aberration-corrected optics to minimize distortions and improve image clarity. This technique is crucial for studying CeO_2 NPs, especially when dealing with extremely small particles, such as those around 2.5 nm in size. HRES-TEM's ability to provide high-resolution images and resolve the fine details of small NPs, such as crystal planes, makes it an indispensable tool for material characterization.

Unlike conventional TEM, which relies on imaging using scattered electrons in general, HAADF-STEM focuses on capturing electrons scattered at high angles. In HAADF-STEM, a finely focused electron beam scans across the sample, and an annular detector collects electrons scattered at these high angles. These high-angle scattered electrons contribute to the annular dark field signal, with intensity correlated to the atomic number (Z) of the sample's elements. Consequently, heavier elements produce brighter regions in the HAADF-STEM image. HAADF-STEM enables direct imaging of CeO_2 NPs ($Z = 58$) and facilitates the assessment of their size distribution (polydispersity) and morphology.

5.1.3.3 X-ray Diffraction (XRD)

CeO_2 NPs sample preparation included the purification and posterior drying of the material suspension. Once dried, the solid is carefully milled and deposited onto a Si holder.

XRD diffraction experiments were performed on a Malvern Panalytical Xpert Pro diffractometer equipped with a Cu radiation source operating at 40kV and 40mA, producing Kα X-rays with a wavelength (λ) of 1.5406 Å. The diffraction patterns were collected in the angle region between 20° and 95°(2θ). All the obtained diffractograms matched with the reference pattern for CeO_2 (00-034-0394).

XRD is based on the principle of analyzing the scattering of X-rays by the crystal lattice of a material. When X-rays strike a crystalline sample, they undergo constructive interference as they scatter off the regularly spaced atoms within the crystal lattice. By measuring the angles at which these scattered X-rays are diffracted, known as Bragg angles, XRD can determine the spacing between atomic planes within the crystal lattice. This information is then used to identify the crystal structure and phase composition of the material, providing valuable insights into its atomic arrangement and properties.

To determine the crystallite size using the Scherrer equation, one typically measures the FWHM of a diffraction peak in radians (θ) and the wavelength (λ) of the X-ray source. The Scherrer equation is as follows:

$$D = \frac{K\lambda}{\beta \cos(\theta)}$$

Here, D is the average crystal size, K is the Scherrer constant, λ is the wavelength of the X-ray source, β is the FWHM of the diffraction peak, and θ is the Bragg angle corresponding to the diffraction peak.

For calculating the lattice parameter, Bragg's law is employed:

$$2dsin(\theta) = n\lambda$$

Where *d* is the interplanar spacing, and *n* is the order of the diffraction peak. Subsequently, the lattice parameter (*a*) is derived from the interplanar spacing *d* using the equation:

$$a = \frac{d\sqrt{h^2 + k^2 + l^2}}{\sqrt{h^2 + k^2 + l^2}}$$

Here, h, k, and l represent the Miller indices of the diffraction peak.

5.1.3.4 UV-vis Spectroscopy

UV-vis spectra were acquired with a Cary 60 spectrophotometer (Agilent Technologies) in the 250-800 nm range at room temperature, using 1.5 ml plastic cuvettes.

UV-vis spectroscopy measures the extinction of light, which comprises the scattering light and the absorption contributions to the loss of light, in part of the ultraviolet (UV) and the full visible (vis) regions of the electromagnetic spectrum, that passes through a sample. The absorption spectrum obtained reveals the amount of light absorbed at different wavelengths, providing information about the electronic structure and chemical composition of the sample.

5.1.3.4.1 *Band Gap: Tauc Plot Calculations*

The band gap is defined as the energy difference between the top of the valence band and the bottom of the conduction band. Electrons can transition from one band to another if the band gap energy, the minimum energy required, is provided. This energy can be determined from the wavelength at which a steep rise in absorbance occurs, as this wavelength represents the minimum photon energy required for electron excitation across the band gap.

Tauc et al. proposed a method for determining the band gap using optical absorbance data plotted against energy [1]. The optical absorption strength depends on the difference between the photon energy and the band gap, as described by the equation:

$$\alpha h\nu^{(\frac{1}{n})} = A(h\nu - Eg)$$

where *h* is Planck's constant, *v* is the photon's frequency, α is the absorption coefficient, *Eg* is the band gap, and A is a proportionality constant. The absorption coefficient (α) can be calculated using Beer–Lambert's relation:

$$\alpha = \frac{2.303A}{d}$$

where *d* is the path length of the cuvette and *A* is the absorbance from the UV–vis spectrum.

The value of the exponent *n* indicates the nature of the electronic transition:

- for direct allowed transitions: $n = 1/2$,
- for direct forbidden transitions: $n = 3/2$,
- for indirect allowed transitions: $n = 2$,
- for indirect forbidden transitions: $n = 3$.

For CeO_2 NPs, the transitions can be direct or indirect allowed. The maximum absorption peak at 320 nm is assigned to the charge transfer transition from O^{2-} in O2p to Ce^{4+} in Ce 4f. Therefore, we will fit the curve to indirect (n=2) transitions.

5.1.3.5 Dynamic Light Scattering (DLS)

Malvern ZetaSizer Nano ZS (Malvern instruments) operating at a light source wavelength of 532 nm and fixed scattering angle of 173º was used to measure NPs hydrodynamic size. Measurements were conducted in 1 cm path cell and 25 ºC. Three independent measures were performed.

DLS is a non-invasive technique employed to measure the size distribution of particles and molecules in solution, usually within the submicron range. The technique relies on the observation of the Brownian motion of particles suspended in a liquid medium, which induces fluctuations in the intensity of laser light scattered by the sample.

By analysing these fluctuations in scattered light intensity, DLS provides insights into the velocity of Brownian motion, allowing for the determination of particle size

through the application of the Stokes-Einstein relationship. This relationship links the diffusion coefficient of particles to their size, enabling the calculation of particle size distribution based on the observed intensity fluctuations. Note that the diameter that is measured is a value that refers to how particle diffuses within a fluid so it is referred to as a hydrodynamic diameter. The diameter that is obtained by this technique is the diameter of a sphere that has the same translational diffusion coefficient as the particle. The translational diffusion coefficient will depend not only on the size of the particle core, but also on any surface structure, as well as the concentration and type of ions in the medium. Thus, the value of the hydrodynamic diameter is also determined by factors extrinsic to the NP's properties, as temperature and viscosity of the medium. All in all, the DLS measurement value gives us information about the hydrodynamic size of NPs in colloidal suspension, the polydispersity of a sample and its aggregation state [2].

Different methods exist for analysing scattered light signals: intensity and number distributions. The intensity distribution is weighted according to the scattering intensity of each particle fraction or family, with larger particles yielding stronger signals (as they scatter more light). Conversely, the number distribution adjusts the scattering intensity as a function of particle size, Thus, in some cases, peaks may become "lost" or disappear during the transformation from intensity to number, as the relative contributions of particles regarding its size is taken into account.[2]. Both distributions are typically provided as complementary information.

5.1.3.6 Zeta-potential (Z-Pot; ζ)

A Malvern ZetaSizer Nano ZS instrument (Malvern Instruments) was used to measure NP's surface charge. An aliquot of NP solution was placed in a folded capillary cell and zeta potential analysis was performed under controlled temperature (25 °C).

Z-Pot measurement is a technique for determining the surface charge of NPs in a colloidal solution. The Z-Pot of particles is typically measured by electrophoretic light scattering. An electric field is applied, and the electrophoretic mobility of particles is used to calculate the Z-Pot. In the presence of an electric field, particles will move at

different speeds: highly surface-charged particles will move faster than those with lower charges [3]. The magnitude of the Z-Pot indicates the potential stability of the colloidal system, correlated to the electrostatic repulsion of the particles in the sample. Generally, suspensions with zeta potential values greater than +30 or less than -30 mV are considered stable. However, a Z-Pot value alone is meaningless without defining the solution conditions such as pH, buffer concentration, temperature and ionic strength.

5.1.3.7 High-Energy Resolution Fluorescence-Detected X-ray Absorption Spectroscopy (HERFD-XAS) Measurements

Measurements were performed at beamline ID26 of the European Synchrotron Radiation Facility (ESRF) in Grenoble. Technical aspects of the setup are taken from the work of Cafun et al. [4]. The incident energy was selected using the (111) reflection from a double Si crystal monochromator, with higher harmonics rejected by three Si mirrors operating under total reflection. The incident photon flux was monitored by detecting the X-rays scattered from a foil using a photodiode. Five spherically bent Ge crystal analyzers (R = 1 m) in (331) reflection mode were used to detect the Lα1 emission line of Ce (4839 eV), providing a combined energy bandwidth of 0.9 eV. The sample, analyser crystal, and photon detector (avalanche photodiode) were arranged in a vertical Rowland geometry. HERFD-XAS spectra were recorded at scattering angles covering 70 – 110º in the horizontal plane. Measurement conditions were optimised by Dr. Vinod Paidi and Prof. Pieter Glatzel, to avoid radiation damage to the CeO_2 NPs.

HERFD-XAS is based on the principle of measuring the fluorescence emitted by a sample after it absorbs X-rays. By detecting the emitted fluorescence with high energy resolution, HERFD-XAS minimizes the background noise and enhances the spectral features of the absorption edge, allowing for a more precise analysis of the electronic structure and local environment of specific elements within a material. This technique is particularly advantageous for studying inorganic NPs such CeO_2 NPs due to its superior spectral resolution compared to conventional XAS. It enables the precise detection of subtle electronic and structural features, allowing for differentiation between oxidation states (e.g., Ce^{3+} and Ce^{4+}). Additionally, HERFD-XAS provides

detailed insights into the local atomic environment and electronic structure around specific elements, while minimizing background noise and enhancing the signal-to-noise ratio.

5.1.4 Aggregation kinetics

To test the aggregation kinetics of CeO_2 NPs in physiological media, 100 µL of CeO_2 NPs were mixed with 900 µL of tested media, ensuring that the NP volume did not exceed 10% of the total volume to avoid media exchange. The final concentration of CeO_2 NPs was maintained at 1 mg/mL, except for investigations involving varying concentrations, where final CeO_2 NPs concentrations were: 0.1, 0.15, 0.30, and 0.50 mg/mL.

Subsequently, aggregation kinetics were assessed using DLS and UV-vis spectroscopy. The tested media included 0.8% NaCl, 10 mM PB, or 100 mM PBS, DMEM, and DMEM supplemented with 10 % FBS.

5.1.5 Bioconjugation protocol

Albumin concentration for conjugation was determined by the theoretical number of proteins required to cover the entire NP surface, as outlined in Chapter 2, page X.

A stock solution of BSA was prepared at the desired concentration in PB 10 mM buffer. CeO_2 NPs were added dropwise onto the BSA solution to a final relative volume concentration of 90-10% (Albumin:NPs), and incubated overnight at 4 ºC. Conjugation was characterized by UV-vis spectroscopy, DLS, and Z-Pot.

To test CeO_2-BSA conjugate stability, the conjugates were exposed to physiological media including 0.8% NaCl, 10 mM PB, 100 mM PBS, and DMEM supplemented with 10 % FBS.

5.1.6 CeO_2 NPs Corrosion

A solution of 0.4 mg/mL of CeO_2 NPs (2.4 mM cerium) was exposed to increasing concentrations of ferrocyanide, ranging from 0 to 2.4 mM, for 3 hours. The hydrodynamic size and NP concentrations were assessed using DLS. Elemental cerium

levels were analysed using ICP-MS (7900 ICPMS, Aligent), in Servei d'Anàlisi Química (UAB, Barcelona). To prepare the samples, they were centrifuged with 3 kDa centrifugal filter units to separate ionic dissolved cerium ions from the NP fraction. Following this, microwave-assisted digestion (Metrohm, Milestone Ethos Easy) using HNO_3 at 200ºC was performed.

5.1.7 Amplex Red Assay

The H_2O_2 scavenging capacity of CeO_2 NPs was determined using the Amplex™ Red Hydrogen Peroxide Assay Kit according to the manufacturer's instructions. Briefly, 50 µg/mL CeO_2 NPs were incubated with varying concentrations of H_2O_2 (1, 2, 4, and 6 µM) for 40 minutes. 50 µg/mL of 5 nm AuNPs were used as a negative control. Subsequently, the Amplex Red reagent/HRP working solution was added and the mixtures were incubated for 30 minutes at room temperature. Fluorescence was measured using Varioskan™ LUX multimode microplate reader (Thermo Fisher Scientific) with excitation/emission wavelengths set at 540/590 nm.

5.1.8 HEK 293, HeLa, and RAW 267.4 cell culture

HeLa and HEK 293 cell culture was maintained in culture in a 75 cm^2 tissue culture flask using DMEM with heat-inactivated FBS at 10% at 37 °C and humidified 5% CO_2.

RAW 267.7 cell culture was maintained in culture in a 35 mm cell culture dish using DMEM with heat-inactivated FBS at 10%, and 1% penicillin/streptomycin, at 37 °C and humidified 5% CO_2.

RAW 264.7 cells were activated by adding 60 ng/mL LPS or with 40 ng/mL mouse recombinant IL-4.

5.1.9 PrestoBlue: Cell Rescue Assay

HEK 293 cells were seeded at a density of $1x10^5$ cells per well in 96-well plates and allowed to incubate for 24 hours before exposure to 100 µg/mL CeO_2 NPs. The CeO_2 NPs were conjugated to BSA at a 30-fold excess, corresponding to 40 mg/mL. Prior to H_2O_2 exposure, the cell medium was replaced to remove non-internalized NPs. For the

acute oxidative stress model, cells were treated with 500 µM H_2O_2 for 3, 24, or 72 hours. For the chronic oxidative stress model, cells were exposed to 50 µM H_2O_2 for 24 hours. To assess cell viability, 10 µL of PrestoBlue reagent was added to each well, followed by a 2-hour incubation period. Fluorescence was measured (λ_{ex}531nm, λ_{em}572) using the Varioskan™ LUX multimode microplate reader (Thermo Fisher Scientific).

5.1.10 PrestoBlue: Cell viability

HEK 293 and HeLa cells were seeded at a density of $1x10^5$ cell/well and allowed to incubate for 24 hours prior to exposure to 100 µg/mL CeO_2 NPs naked or conjugated to BSA at a 30-fold excess (40 mg/mL). After 24 hours of NPs exposure, the cell medium was replaced to remove non-internalized NPs. After the 24-hour exposure period, cell viability was evaluated using the PrestoBlue assay as described previously.

To determine cell viability in RAW 267.4, the cells were seeded at a density of $1x10^5$ cell/well in 96-well plates and allowed to incubate for 24 hours before exposure to 50, 150, and 300 µg/mL naked CeO_2 NPs. 24 hours after NPs exposure, the cell medium was replaced to remove non-internalized NPs. After the 24-hour exposure period, cell viability was evaluated using the PrestoBlue assay as described previously.

5.1.11 PrestoBlue: Albumin cytotoxicity

HEK 293 and HeLa cells were seeded at a density of $1x10^5$ cells per well and allowed to incubate for 24 hours prior to exposure to different types of albumins. These included universal grade BSA, BSA heat shock fraction, Biochemistry grade BSA, Human Serum Albumin (HSA). After the 24-hour exposure period, cell viability was evaluated using the PrestoBlue assay as described previously.

5.1.12 Pacific Blue Annexin V/SYTOX

RAW 267.4 cells were seeded at a density of $2.5x10^5$ cells/well in 12-well plates and allowed to incubate for 24 hours, before exposure to 50 and 150 µg/mL naked CeO_2 NPs naked. 24 hours after NPs exposure, the cell medium was replaced to remove non-

internalized NPs, followed by additional incubation for 24 hours with LPS or IL4 for cell activation. Cells were collected by scrapping, washed with 1X PBS, and pelleted via centrifugation at 200g for 5 min. Staining was performed in DMEM containing Pacific Blue™ Annexin V/SYTOX™ AADvanced™ Apoptosis dies and cells were analysed using a flow cytometer (LSRF FortessaTM equipment, BD Biosciences). A total of at least 10.000 events were acquired and analyzed. Data was analysed with FlowJoTM V10 software.

5.1.13 Statistical Analysis

Data analysis and calculations were performed with OriginLab Software or GraphPad Prism 9. Differences between groups were determined using one-way ANOVA for comparisons involving more than two groups. Tukey's test was applied for pairwise comparisons between all group means, while Dunnett's test was used for comparisons between each group mean and the control mean.

Results are presented as mean ± SEM unless specified otherwise. Statistical significance levels are indicated as follows: *p < 0.05, **p<0.01, ***p<0.001, ****p<0.0001. The numbers of experimental or biological replicates are provided in the figure legends. No statistical methods were used to predetermine sample size.

5.2 Chapter 3: Pharmacokinetic Profiling of CeO2 NPs: Absorption, Distribution, Metabolism, and Excretion

5.2.1 Chemicals

All chemicals were purchased from Thermo Fisher Scientific unless otherwise specified.

Mouse Serum Albumin (MSA), Isoflurane, Carbon tetrachloride (CCl_4), polyethene glycol (PEG), 4% formalin, paraformaldehyde (PFA), paraffin, Triton-X, Hoechst 3342 (H1399), Prolong antifade mounting medium (11559306), goat anti-mouse Alexa Fluor568 (A110199), Phalloidin Alexa Fluor 568 (A11019). Anti-β-actin mouse monoclonal antibody (MAB8929) was purchased from R&D systems.

5.2.2 Synthesis and characterization

The synthesized CeO2 NPs were fully characterized by TEM, DLS, XRD, and UV-vis spectroscopy (see section 5.1.2 for methodological details).

5.2.3 Bacterial Endotoxin (LAL) test

Both synthesis and purification of NPs were performed under sterile conditions and with non-pyrogenic material. To ensure safe NPs for animal administration, CeO_2 NPs were tested for endotoxin levels at the *Echevarne* analysis laboratory (Barcelona).

5.2.4 MSA conjugation

To prevent aggregation of the NPs in the bloodstream, and to avoid hypotonic shock, CeO_2 NPs were conjugated with MSA (Merck) in 10 mM PB at 4 ºC for 24 hours prior to injection.

5.2.5 In vivo study design

All experimental procedures were conducted in strict accordance with the European (Directive 2010/63/UE) and Spanish laws and regulations (Real Decreto 53/2013; Generalitat de Catalunya Decret 214/97) on the protection of animals used for

experimental and other scientific purposes and approved by the Vall d'Hebron Research Institute Ethical Experimentation Committee (CEEA: 19/20), and further validated by the authorized body of Generalitat de Catalunya.

The experimental procedures conducted in Wistar rats were approved and performed according to the criteria of the Investigation and Ethics Committee of the Hospital Clínic Universitari (Barcelona).

Animals received humane care according to the criteria outlined in the "Guide for the Care and Use of Laboratory Animals".

5.2.6 Long-term biodistribution in healthy mice

For long-term biodistribution study, 30 adult female BALB/C mice (Charles River Laboratories) weighing 25 g and aged 7 months at the time of NP administration, were housed in three to four per cage with ad libitum access to food and water during a 12 h light/dark cycle. Mice were randomly divided into 4 groups. On day 0, each group of 6 mice received a single IV injection of 7.2 mg/Kg BW CeO_2 NPs, via retro-orbital route in the ophthalmic venous sinus under general anaesthesia induced by 5% Isoflurane and maintained at 2%. Animals were euthanised at specified intervals after injection: 1, 9, 30 and 100 days. The liver, spleen, kidneys, lung, brain, lymph nodes, ovaries, bone marrow, faecal content, and urine were removed and stored at -20ºC before elemental Cerium content analysis.

5.2.7 CeO_2 NPs excretion in CCl_4-treated rats

The study was conducted in male Wistar rats (Charles River Laboratories) with hepatic fibrosis induced by repeated inhalation CCl_4, following established protocols [5]. Rats were provided ad libitum access to standard chow and water containing phenobarbital (0.3 g/L) as drinking fluid. Animals were exposed to CCl_4 vapour twice weekly for 16 weeks. CeO_2 NPs at a dose of 0.1 mg/kg BW were injected IV twice weekly for 2 consecutive weeks, beginning in the seventh week of CCl_4 administration. Following the final CeO_2 NPs dose, animals were placed in metabolic cages, and urine and feces were collected and measured 24 hours after administration at 3, 21, 42, and 56 days post-nanoceria injection.

5.2.8 Brain Distribution after intracranial administration

In this study, a single dose of 2 µg of CeO_2 NPs was administered in a rat model of Parkinson's disease [6] via intracranial injection. Cerium concentrations were measured using ICP-MS, and brains were collected 120 days after administration for analysis.

5.2.9 Organ Distribution after oral administration

In this study, polyethene glycol (PEG)-coated CeO_2 NPs (CeO_2NPs-PEG) conjugates were administered to healthy Wistar rats via daily intragastric gavage (3 mg/mL; 10 mg CeO_2/kg of BW) for 14 consecutive days. Cerium concentrations were measured using ICP-MS, and major organs and serum were collected 72 hours after the final administration for analysis.

5.2.10 Cerium Content Determination

Digestions were carried out in Ethos™ Easy (Milestone), an advanced microwave digestion system. First, samples were defrosted and mixed in the digestion solution containing one part concentrated nitric acid (HNO_3) and two parts of water. Subsequently, the digestions were performed under a 200 °C cycle for one hour and a half. Thereafter, elemental cerium in tissue was analysed using ICP-MS (7900 ICPMS, Agilent), in the Chemical analysis service (UAB, Barcelona).

5.2.11 Confocal Imaging in Mice Liver

0.1 mL of 7 µg/mL of albuminized Au@SiO2-FITC@PS NPs were IV injected via tail-vein injection (n=2). At 24 hours, mice were euthanized, and organ samples were collected (including liver, spleen, and kidney). The organs were briefly washed with normal saline, slightly dried with blotting paper, and immersed for 4 h in 4% formalin for tissue fixation. Next, tissues were embedded in paraffin following a standard protocol. For immunohistochemistry, paraffin-embedded samples were sectioned at 4 µm using a microtome and transferred to a poly-lysine-coated glass slide. The paraffin was then removed with xylene and the samples were rehydrated. For immunostaining, Samples were permeabilized with Triton-X 0.2% for 10 min. Sections were incubated

with anti-β-Actin mouse monoclonal antibody (dilution 1:100) overnight at 4 °C, followed by incubation with a secondary antibody goat anti-mouse Alexa Fluor568 (dilution 1:500). Nuclei were stained with Hoesch 3342 (dilution 1:10000). Fading was controlled using the Prolong antifade mounting medium (11559306). Samples were observed on the Confocal Laser Scanning Microscope (Zeiss LSM 980 Airyscan). Hoescht 33342 (em350⁄ex461), Alexa Fluor-568 (ex578/em603) and FITC (em490/ex525) were observed using the standard fluorescence mode and pre-defined settings.

5.2.12 Dissolution of CeO_2 NPs at acidic pH

CeO_2 NPs (500 μL, 1.72 mg/mL) were exposed to 2.85 mL of HCl. The final pH of the solution was 1.7. Aliquots were extracted at different time points as labelled and measured by UV-visible.

5.2.13 Fitting with traditional pharmacokinetic models

Experimental data were compared with the two principal pharmacokinetic models, the one-compartment and two-compartment models.

The one-compartment model assumes that the NPs are rapidly and uniformly distributed throughout the body and that the rate of NPs elimination is proportional to the amount of drug in the body. Therefore, the mathematical equation for a one-compartment model is:

$$C = Ae^{-k_1 t}$$

where C is the concentration of the NPs in the body, A is a constant that depends on the dose and volume of distribution, k_1 is the elimination rate constant, and t is the time after administration.

A two-compartment model assumes that the NPs are distributed into two compartments: a central compartment (such as blood) and a peripheral compartment (such as tissues). The mathematical equation for a two-compartment model is:

$$C = Ae^{-k_1 t} + Be^{-k_2 t}$$

where C is the NPs concentration in the body, A a constant that depends on the amount of NPs in the central compartment and the volume of the central compartment, k1 is the rate constant for distribution from the central compartment to the peripheral compartment, and t is time. B is a constant that depends on the number of NPs in the peripheral compartment and the volume of the peripheral compartment, and k2 is the rate constant for elimination from the peripheral compartment.

In both models, the concentration of the drug in the body can be predicted based on the dose and elimination rate constant. These models help predict NPs concentrations over time and optimize drug dosing regimens.

5.3 Chapter 4: Pharmacodynamics of CeO_2 NPs: Immune Modulation and Metabolism

5.3.1 Chemicals

All the reagents were purchased at Thermo Fisher Scientific if not otherwise specified. RPMI 1640 GlutaMAX™ (72400047), 1% penicillin/streptomycin, heat-inactivated Foetal Bovine Serum (FBS), phosphate-buffered saline (PBS), 4-(2-hydroxyethyl)-1-piperazineethanesulfonic acid (HEPES), recombinant human IFN-γ (285-IF; R&D Systems), LPS (L2630; from Escherichia coli, serotype O111, Sigma-Aldrich), recombinant human IL-4 (200-04; PeproTech), DMEM GlutaMAX™ (10564-011), recombinant murine IL-4 (214-14; PeproTech), RNeasy Mini Kit with DNase protocol (50974104, Qiagen), High Capacity cDNA transcription kit (4387406), MitoTracker Orange CMTMRos (M7510), Total ROS Assay kit (88593074), edaravone, and hydrogen peroxide (H_2O_2).

RT-qPCR probes included RPL37A (Hs06050959_g1; Ms), IL-1B (Hs01555410_m1; Mm00434228_m1), CCL2 (Hs00234140_m1; Mm00441242_m1), SLC2A1 (Hs00892681_m1: Mm00441480_m1), HIF1-a (Hs00153153_m1; Mm00468869), ARG1 (Hs00163660_m1; Mm00475988_m1), IL-10 (Hs00961622_m1; Mm01288386_m1), PPAR-y (Hs01115513_m1; Mm00440940_m1), MRC1 (Mm01329359_m1).

Reagents for metabolic assessment were purchased from Agilent, including, glucose, sodium pyruvate, glutamine, and Seahorse XF RPMI assay medium pack (103681100). Olygomicine (495455) Rotenone (R8875), and Antymicine A (J63522) were purchased from Thermo Fisher Scientific.

Of note, the same batch of FBS was maintained throughout the macrophage polarization experiments.

5.3.2 THP-1 cell culture and polarization

The human THP-1 monocyte cell line was cultured in RPMI 1640 GlutaMAX™ (72400047). The culture medium was further supplemented with 10% heat-inactivated

FBS and 1% penicillin/streptomycin. Cells were maintained at 37°C in a humidified atmosphere containing 5% CO_2.

THP-1 monocytes were differentiated into macrophages by incubating them with 20 ng/mL PMA for 24 hours, followed by a 48-hour incubation in RPMI medium. To polarize the macrophages to M1 phenotype, cells were treated with 20 ng/mL recombinant human IFN-γ and 20 ng/mL LPS for 12 hours. For M2 polarization, macrophages were treated with 40 ng/mL recombinant human IL-4 for 12 hours.

5.3.3 RAW 267.4 cell culture and polarization

The murine RAW 264.7 macrophage cell line was cultured in DMEM GlutaMAX™, with 10% FBS, and 1% penicillin/streptomycin. Cells were maintained at 37°C in a humidified atmosphere with 5% CO_2.

To polarize RAW 264.7 cells, M1 macrophages were induced by adding 60 ng/mL LPS for 24 hours. Alternatively, M2 macrophages were induced by adding 40 ng/mL recombinant murine IL-4 for 24 hours.

5.3.4 CeO_2 NPs treatments

In all the experiments, unless otherwise specified, 150 µg/mL naked CeO_2 NPs were added to cells for 24 hours prior to cell activation. After incubation, the cell culture medium was replaced to remove non-internalized NPs. This standardized procedure was followed consistently across experimental setups to evaluate the effects of CeO_2 NPs on cellular responses under various conditions.

5.3.5 Quantitative real-time PCR (RT-qPCR)

Cells were seeded at a density of $5x10^5$ cells per well for THP-1 and $2.5x10^5$ cells per well for RAW 264.7 in 12-well plates. After incubating for 24 hours, the cells were treated with CeO_2 NPs and differentiated into macrophages as previously described.

Total RNA was extracted using the RNeasy Mini Kit with DNase protocol (Qiagen), and RNA quantity and quality were assessed using a NanoPhotometer NP80 (Implen). Subsequently, 2 µg of total RNA was reverse transcribed using the High-Capacity

cDNA Reverse Transcription Kit (Applied Biosystems) following the manufacturer's instructions. RT-qPCR was performed using TaqMan Fast Universal PCR Master Mix (Applied Biosystems). Reference genes *RPL37A* (THP-1) and *STX5A* (RAW 264.7) were used for normalization. M1 markers included *IL-1B*, *CCL2*, *SLC2A1*, and *HIF1α*, while M2 markers included *ARG1*, *IL-10*, *PPARγ*, and *MRC1*. All probes were purchased from Thermo Fisher Scientific. RT-qPCR analysis was conducted using a LightCycler 480 II instrument (Roche).

5.3.6 ELISA

THP-1 cells were seeded at a density of $5x10^5$ cells per well in 12-well culture plates and treated as described above. The cell culture supernatants were collected at different time points (4, 12, 24, 48 h) and centrifuged at 300g for 10 min. Cytokine levels were detected using specific ELISA kits from Biolegend: ELISA MAX Deluxe Set Human IL-1β (437004) and ELISA MAX Deluxe Set Human IL-10 (430604), according to the manufacturer's instructions.

5.3.7 Metabolic Profile

A Seahorse Bioscience XF96 Extracellular Flux Analyzer was utilized to measure Oxygen Consumption Rate (OCR) and Extracellular Acidification Rate (ECAR). THP-1 cell lines were cultured in normal growth media and seeded onto a 96-well XF Flux Analyzer assay plate at a density of $2x10^4$ cells per well 24 hours prior to the assay. The cells were treated and polarized as described previously.

For the assay, cells were switched to XF assay media containing 10 mM glucose, 1 mM sodium pyruvate, and 2 mM glutamine. The plate was then placed in a CO_2-free incubator for at least 1 hour prior to the start of the assay to equilibrate. The Seahorse XF96 analyser was used to measure basal metabolic profiles and ATP production rates. For ATP production measurements, baseline measurements were recorded before and after the injection of oligomycin, followed by an injection of rotenone + antimycin A.

5.3.8 Mitochondria Polarization

RAW 264.7 cells were seeded at a density of $5x10^5$ cells per well in 12-well plates and treated as described. 24 hours after cell activation, cells were washed three times with 1X PBS and stained with 500 nM MitoTracker Orange CMTMRos for 10 minutes at 37°C in a 5% CO_2 atmosphere. Subsequently, cells were washed with PBS and analyzed using a flow cytometer (LSRF Fortessa™ equipment, BD Biosciences). At least 10000 cells were analyzed per experiment. The data was processed using FlowJo™ v10 Software.

5.3.9 Total ROS Assay Kit

ROS detection was done using a Total ROS Assay kit. First, RAW 267.4 cells were seeded in 12-well plates at a density of $1x10^5$ cells/well and kept in the incubator overnight, then cells were treated as described, but in this case, 50 nM of Edaravone was added as negative control at the same time than NPs. Cells were resuspended in 1x ROS assay stain and kept at 37ºC, 5% CO_2 for one hour. Then stimulation with LPS or IL-4 was done as previously described. At this point, 50 µM H_2O_2 was used as a positive control. Cell stimulation was tested at 1 and 24 hours. Finally, cells were collected by scraping and analysed using a BD LSRF FortessaTM flow cytometer. At least 10000 cells were analyzed per experiment. The flow cytometry data were analysed by using FlowJo V10 software.

5.3.10 Confocal Microscopy

RAW 264.7 macrophages were seeded in 8-well µ-slides chambered coverslips coated with Poly-L-Lysine (80824; Ibidi) at a density of $1.5x10^5$ cells per well. Cells were treated as previously described. Subsequently, cells were stained with 500 nM MitoTracker Orange CMTMRos for 10 minutes at 37°C in 1X PBS supplemented with 10% HEPES.

Live cell imaging was performed using a confocal laser scanning microscope (Zeiss LSM980 with Airyscan 2) equipped with a micro-incubator system to maintain a humidified environment at 37°C and 5% CO_2. For 3D imaging, z-stacks were obtained

using a 100x oil immersion objective (1.46 NA), with the pinhole size set to 1 Airy unit. Bidirectional scanning was enabled. Laser power, detector filtering/gating, and gain were adjusted to maximize signal without saturation while minimizing background signal, cross-fluorescence, and photobleaching. MitoTracker images were acquired at λ_{ex}551nm, λ_{em}575 nm. The refractive index of the immersion oil used was 1.518.

5.3.11 Computational Analysis

5.3.11.1 Image Deconvolution

Deconvolution of Z-stacks was performed using the Zen Blue software (Zeiss) deconvolution toolkit, utilizing the Fast Iterative (Meinel) algorithm. This process reduces blur and increases contrast, enhancing the clarity and detail of the 3D images.

5.3.11.2 Image Pre-Processing

The entire mitochondrial network of each individual cell was selected and saved as a separate image. Preprocessing alters the rate of detection of mitochondrial objects, improving the ability of the segmentation algorithm to discern between mitochondrial objects and the background. Using ImageJ/Fiji, 3D image stacks (operating on each slice in the stack) were processed using the following commands: “Subtract Background” (rolling = 10 stack) to remove background noise, “Enhance Local Contrast (CLAHE)” (block size = 64, histogram = 256, maximum = 1.25) to enhance areas with lower intensity (dim areas) while minimizing noise amplification, “Gamma Correction” (value = 1.10 stack) to correct any remaining dim areas, mainly focused on correcting the brightness between the first and last stacks, as the intensity of the laser diminishes.

These preprocessing steps improve the quality and accuracy of the segmentation algorithm for subsequent analysis.

5.3.11.3 Image Segmentation: Pixel Classification

Processed images were subjected to pixel classification and segmentation using Ilastik software. A training dataset was generated by manually annotating regions of interest

(ROIs) representing both stained mitochondria and background. The pixel classifier within Ilastik was trained using these annotated samples, incorporating features such as intensity, texture, and shape. Subsequently, the trained classifier was applied to the entire image stack to classify pixels as belonging to either mitochondria or background. The accuracy of the segmentation was validated through manual inspection.

5.3.11.4 Post-Processing of Segmented Images

Image segmentation was post-processed in ImageJ/Fiji to remove non-specific signals. The segmented image was first converted to binary using the "Make Binary" command. Then, two commands were used for further image processing: "Fill Holes" to connect or fill existing gaps, and "Remove Outliers..." (radius = 2.5, threshold = 50) to eliminate small non-specific signals.

These steps ensured a cleaner and more accurate segmentation of the mitochondrial network.

5.3.11.5 Mitochondria Analysis

Last, the images were processed with ImageJ/Fiji software. To measure the number, volume, and total surface area of mitochondria, the “3D Object Counter” plugin was used with the following settings: threshold = 255, min. = 0, max. = Infinity. The segmented image was then skeletonized using the "Skeletonize (2D/3D)" command. Subsequently, the skeleton was analyzed with the "Analyze Skeleton (2D/3D)" plugin to obtain branching information, including the number of branches, junctions, and branch length. Results were visually inspected by redirecting both the object counter map and skeleton mask to the original image. Data was analyzed using R commander and Graph Pad Prism software.

5.3.11.6 Fractal Dimension and Lacunarity

The entire mitochondrial network of each individual cell was selected and saved as a separate image. Initially, a maximum projection was generated from the original images, which were cropped to isolate individual cells using ImageJ. Subsequently, 2D images were processed to subtract nonspecific background signals using the ImageJ

command “Subtract Background” with a rolling ball radius of 10. The images were then converted to grayscale.

Fractal dimension and lacunarity were analysed using the ImageJ plugin FracLac. The analysis employed a box-counting method for binary images, where fractal dimension estimation is based on the distribution of object pixels across different scales. This involved using 12 grid positions and varying box sizes from a minimum of 2 x 2 pixels up to a maximum size of 45% of the selected image area. The fractal dimension was estimated for each grid position from the regression line of a log-log plot of intensity versus box size. Lacunarity was calculated based on the number of positive pixels within each box at different box sizes, providing additional information about the texture and spatial distribution of the mitochondrial network.

5.3.12 Statistical Analysis

Data analysis and calculations were performed with R studio or GraphPad Prism 9. Differences between groups were determined using one-way ANOVA for comparisons involving more than two groups. Tukey’s test was applied for pairwise comparisons between all group means, while Dunnett’s test was used for comparisons between each group mean and the control mean.

Results are presented as mean ± SEM unless specified otherwise. Statistical significance levels are indicated as follows: *p < 0.05, **p<0.01, ***p<0.001, ****p<0.0001. The numbers of experimental or biological replicates are provided in the figure legends. No statistical methods were used to predetermine the sample size.

5.4 References

1. Tauc, J.; Grigorovici, R.; Vancu, A. Optical Properties and Electronic Structure of Amorphous Germanium. *physica status solidi (b)* **1966**, *15*, 627–637.

2. Dynamic Light Scattering DLS | Malvern Panalytical Available online: https://www.malvernpanalytical.com/en/products/technology/light-scattering/dynamic-light-scattering#whatisdls (accessed on 12 June 2024).

3. Electrophoretic Light Scattering ELS | Measure Electrophoretic Mobility | Malvern Panalytical Available online: https://www.malvernpanalytical.com/en/products/technology/light-scattering/electrophoretic-light-scattering (accessed on 12 June 2024).

4. Cafun, J.-D.; Kvashnina, K.O.; Casals, E.; Puntes, V.F.; Glatzel, P. Absence of Ce3+ Sites in Chemically Active Colloidal Ceria Nanoparticles. *ACS Nano* **2013**, *7*, 10726–10732.

5. Clària, J.; Jiménez, W. Experimental Models of Cirrhosis and Ascites. *Ascites and Renal Dysfunction in Liver Disease: Pathogenesis, Diagnosis, and Treatment: Second Edition* **2007**, 215–226.

6. Gonzalez-Sepulveda, M.; Compte, J.; Cuadros, T.; Nicolau, A.; Guillard-Sirieix, C.; Peñuelas, N.; Lorente-Picon, M.; Parent, A.; Romero-Gimenez, J.; Cladera-Sastre, J.M.; et al. In Vivo Reduction of Age-Dependent Neuromelanin Accumulation Mitigates Features of Parkinson's Disease. *Brain* **2023**, *146*, 1040.

CHAPTER 6

GENERAL CONCLUSIONS

Chapter 6

General Conclusions

6.1 Synthesis and Physicochemical Properties of CeO_2 NPs

This chapter delves into the physicochemical properties of synthesized CeO_2 NPs, with a focus on their application in the biomedical field. The key findings are as follows:

1. **Refined Synthesis:** The synthesis of CeO_2 NPs has been optimized to yield monodisperse, reproducible, and stable NPs formulations, with precise control over size and surface chemistry, which are crucial for effectiveness and biocompatibility. This involves considerations of the thermodynamic principles governing cerium ions mineralization.

2. **Biological Transformations:** Mechanistic studies reveal the transformations experienced by CeO_2 NPs within biological environments, including aggregation, corrosion (chemical dissolution), and interaction with biomolecules (specifically proteins). This research has provided valuable insights into predicting the fate of these NPs in biological settings and developing strategies to control physicochemical modifications, enhancing their stability and efficacy.

3. **Antioxidant Efficacy:** CeO_2 NPs exhibit potent ROS scavenging capabilities in vitro, exhibiting minimal toxicity even in immune-activated cells. These properties highlight their potential as antioxidant therapeutic agents.

6.2 Pharmacokinetic Profiling of CeO_2 NPs: Absorption, Distribution, Metabolism, and Excretion.

This section explores the ADME profile of CeO_2 NPs. The main conclusions are summarized as follows:

1. **Liver and Spleen Accumulation:** Intravenous administration leads to major accumulation of NPs in the liver and spleen, regardless of dose, morphology, aggregation, and surface state. However, their accumulation and excretion are extremely dependent on these NP characteristics.

2. **CeO_2 NPs Excretion:** Contrary to previous reports, this study demonstrates that non-immunogenic, small, highly soluble, and non-aggregated CeO_2 NPs can be excreted and are biodegradable.

3. **Elimination Pathways:** It is hypothesized that CeO_2 NPs that escape the immune system are eliminated via the hepatobiliary route, while those captured by monocytes or resident macrophages slowly dissolve, with cerium ions being excreted through the urinary tract. Although promising for medical development, the slow excretion rates indicate that repeated dosing could lead to toxic accumulation.

6.3 Pharmacodynamics of CeO2 NPs: Immune Modulation and Metabolism

This chapter investigates the capacity of CeO_2 NPs to modulate immune responses in macrophages by lowering ROS levels and restoring energy metabolism. Key findings include:

1. **In vitro macrophage polarization:** M1 macrophages exhibit elevated ROS levels, mitochondrial dysfunction (low membrane potentials and fragmentation), a shift towards glycolytic metabolism, and rapid pro-inflammatory cytokine expression. In contrast, M2 macrophages display

enhanced mitochondrial respiration and a less pronounced glycolytic phenotype, with anti-inflammatory cytokine expression observed only in RAW 267.4 macrophages.

2. **Mitochondrial dysfunction and Glycolysis:** Elevated ROS levels in M1 macrophages impair mitochondrial function and enhance HIF-1 expression, leading to increased glycolysis. This switch to glycolysis acts as a survival mechanism to maintain high ATP levels when OXPHOS is being inhibited by excess ROS.

3. **ROS Modulation and Mitochondrial Restoration:** CeO_2 NPs effectively attenuate the M1 inflammatory response by restoring mitochondrial function, sustaining OXPHOS and preventing glycolysis. However, while mitochondrial function and metabolism of M2 macrophages are not significantly altered by the presence of CeO_2 NPs, they appear to suppress M2 markers gene expression, indicating a potential limitation that warrants further exploration.

4. **Therapeutic Implications:** These findings highlight the complex interplay between ROS modulation, mitochondrial function, metabolism, and macrophage polarization. CeO_2 NPs demonstrate significant potential in modulating macrophage reprogramming and inflammatory outcomes, highlighting their promise for further antioxidant-based therapeutic strategies.

ANNEX

ANNEX

7.1 ANNEX A: List of Publications

Articles Published during the doctoral studies:

1. Casals E, Gusta MF, **Ernst LM**, Mendoza M, Maiz N, Carreras E, Puntes V., Nanotechnology for Maternal Foetal Medicine. *Int J Pediatr Neonat Health*, **2018** May

2. **Ernst LM**, Casals E, Italiani P, Boraschi D, Puntes V., The interactions between nanoparticles and the innate immune system from a nanotechnologist prespective. *Nanomaterials*, **2021** Nov

3. Galyamin D, **Ernst LM**, Fitó-Parera A, Mira-Vidal G, Bastús NG, Sabaté N, Puntes V. Nanoceria dissolution at acidic pH by breaking off the catalytic loop. *Nanoscale,* **2022** Sep

4. **Ernst LM**, Puntes V., How does immunomodulatory nanoceria work? ROS and Immunometabolism. *Front Immunol*, **2022** Oct

5. **Ernst LM**, Mondragón L, Ramis J, Gusta MF, Yudina T, Casals E, Bastús NG, Fernández-Varo G, Casals G, Jiménez W, Puntes V., Exploring the Long-Term Tissue Accumulation and Excretion of 3 nm Cerium Oxide Nanoparticles after Single Dose Administration. *Antioxidants*, **2023** Mar

6. Gusta MF, **Ernst LM**, Moriones OH, Piella J, Valeri M, Bastus NG, Puntes V., Long-Term Intracellular Tracking of Label-Free Nanoparticles in Live Cells and Tissues with Confocal Microscopy. *Small Methods*, **2024** Apr

7.2 ANNEX B: Absorption, Biodistribution, Metabolism, and Excretion (ADME) of CeO_2 NPs in Preclinical Models.

Contents

Table **7.1**---------- 199

Figure 7.1---------- 201

Figure **7.2**---------- 201

Table 7.1. Cerium content by organs and days, given in µg/g tissue and % of injected dose

Organ	*Time post-injection*	*Ce quantity per organ (µg/g tissue)*		*Ce quantity per organ (%ID)*	
		Mean	**Standard deviation**	**Mean**	**Standard deviation**
Liver	24 h	89,818	15,763	82,46	7,45
	9 days	50,827	8,351	50,67	7,78
	30 days	47,727	6,637	46,03	2,53
	100 days	40,945	5,535	40,00	2,44
Spleen	24 h	48,969	10,595	5,05	0,57
	9 days	47,688	10,035	4,51	0,54
	30 days	50,448	17,160	4,75	0,70
	100 days	38,814	2,834	4,08	0,62
Kidney	24 h	5,064	1,927	0,629	0,178
	9 days	2,868	1,358	0,385	0,138
	30 days	3,880	0,792	0,508	0,091
	100 days	3,603	1,041	0,452	0,106
Lung	24 h	1,006	1,016	0,189	0,076

	9 days	0,962	0,766	0,140	0,119
	30 days	0,939	0,318	0,120	0,040
	100 days	0,638	0,239	0,097	0,027
Brain	24 h	0,033	0,020	0,009	0,005
	9 days	0,031	0,006	0,016	0,015
	30 days	0,017	0,005	0,005	0,002
	100 days	0,025	0,007	0,008	0,002
Lymph Nodes	24 h	2,333	1,357	0,098	0,122
	9 days	0,507	0,320	0,018	0,020
	30 days	4,111	1,912	0,368	0,347
	100 days	2,149	0,821	0,029	0,016
Ovary	24 h	3,386	0,916	0,524	0,082
	9 days	2,466	1,208	0,359	0,112
	30 days	2,730	1,523	0,390	0,176
	100 days	2,135	2,037	0,377	0,358
Bone Marrow	24 h	1,750	0,879	0,036	0,022
	9 days	1,323	1,668	0,035	0,047
	30 days	1,202	0,215	0,045	0,017
	100 days	1,065	0,902	0,016	0,007
Faeces	24 h	2,319	0,193	0,607	0,193
	9 days	0,100	0,061	0,100	0,061
	30 days	0,060	0,027	0,060	0,027
	100 days	0,057	0,016	0,057	0,016
Urine	24 h	0,075	0,044	0,002	0,001
	9 days	0,047	0,025	0,002	0,001
	30 days	0,035	0,001	0,001	0,000
	100 days	0,006	0,006	0,001	0,000

Figure 7.1. Mice weight evolution up to 30 days after CeO_2 NPs administration. n = 20, 15, and 10 at days 1, 9, and 30, respectively.

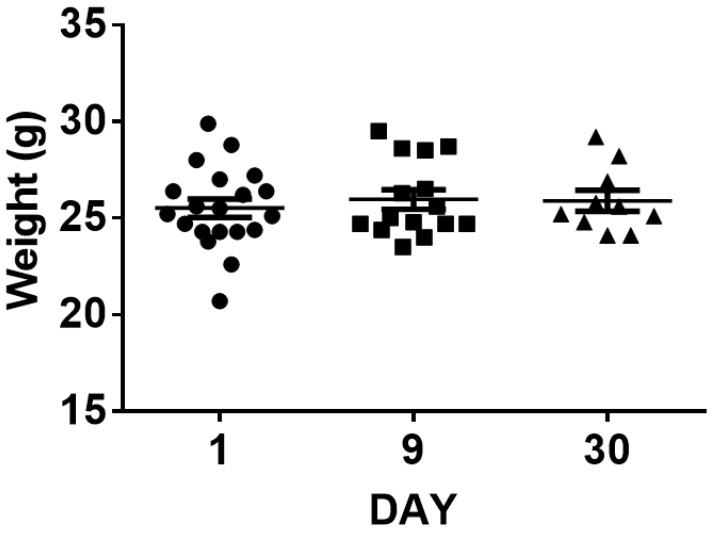
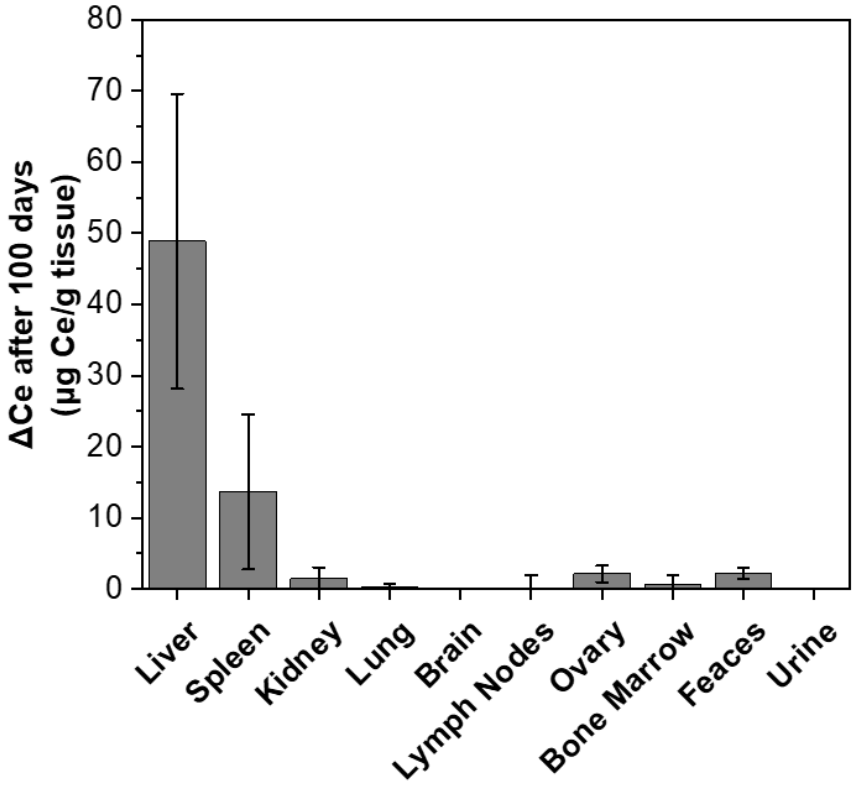


Figure 7.2. Cerium excretion in µg Ce/g tissue between day 1 and day 100.



7.3 ANNEX C: Articles

7.3.1 The Interactions between Nanoparticles and the Innate Immune System from a Nanotechnologist Perspective

nanomaterials

MDPI

Review

The Interactions between Nanoparticles and the Innate Immune System from a Nanotechnologist Perspective

Lena M. Ernst [1], Eudald Casals [2], Paola Italiani [3], Diana Boraschi [3,4,5] and Victor Puntes [1,6,7,*]

1 Vall d'Hebron Research Institute (VHIR), 08035 Barcelona, Spain; lena.montana@vhir.org
2 School of Biotechnology and Health Sciences, Wuyi University, Jiangmen 529020, China; wyuchemecm@126.com
3 Institute of Protein Biochemistry and Cell Biology (IBBC), National Research Council (CNR), 80131 Napoli, Italy; paola.italiani@ibbc.cnr.it (P.I.); diana.boraschi@ibbc.cnr.it (D.B.)
4 Shenzhen Institute of Advanced Technology (SIAT), Chinese Academy of Sciences (CAS), Shenzhen 518055, China
5 Stazione Zoologica Anton Dohrn, 80121 Napoli, Italy
6 Institut Català de Nanociència i Nanotecnologia (ICN2), CSIC and The Barcelona Institute of Science and Technology (BIST), Campus UAB, 08193 Barcelona, Spain
7 Institució Catalana de Recerca I Estudis Avançats (ICREA), 08010 Barcelona, Spain
* Correspondence: victor.puntes@vhir.org

Abstract: The immune system contributes to maintaining the body's functional integrity through its two main functions: recognizing and destroying foreign external agents (invading microorganisms) and identifying and eliminating senescent cells and damaged or abnormal endogenous entities (such as cellular debris or misfolded/degraded proteins). Accordingly, the immune system can detect molecular and cellular structures with a spatial resolution of a few nm, which allows for detecting molecular patterns expressed in a great variety of pathogens, including viral and bacterial proteins and bacterial nucleic acid sequences. Such patterns are also expressed in abnormal cells. In this context, it is expected that nanostructured materials in the size range of proteins, protein aggregates, and viruses with different molecular coatings can engage in a sophisticated interaction with the immune system. Nanoparticles can be recognized or passed undetected by the immune system. Once detected, they can be tolerated or induce defensive (inflammatory) or anti-inflammatory responses. This paper describes the different modes of interaction between nanoparticles, especially inorganic nanoparticles, and the immune system, especially the innate immune system. This perspective should help to propose a set of selection rules for nanosafety-by-design and medical nanoparticle design.

Keywords: nanoparticles; immune system; innate immunity; inflammation; tolerance

check for updates

Citation: Ernst, L.M.; Casals, E.; Italiani, P.; Boraschi, D.; Puntes, V. The Interactions between Nanoparticles and the Innate Immune System from a Nanotechnologist Perspective. *Nanomaterials* **2021**, *11*, 2991. https://doi.org/10.3390/nano11112991

Academic Editors: Horacio Cabral and Thierry Rabilloud

Received: 16 September 2021
Accepted: 3 November 2021
Published: 6 November 2021

Publisher's Note: MDPI stays neutral with regard to jurisdictional claims in published maps and institutional affiliations.

Copyright: © 2021 by the authors. Licensee MDPI, Basel, Switzerland. This article is an open access article distributed under the terms and conditions of the Creative Commons Attribution (CC BY) license (https://creativecommons.org/licenses/by/4.0/).

1. Introduction

The immune system of higher vertebrates encompasses a collection of different specialized cells and specialized soluble molecules distributed throughout the body, being present in all organs and tissues, circulating in blood and lymph (to reach every corner of the body in case of need), and concentrated in some lymphoid organs (lymph nodes, spleen, bone marrow, where hematopoiesis takes place in adult life). These cells have been classified into two functional branches, namely innate and the adaptive immunity, which have different roles, complementing each other very efficiently in complex organisms such as mammals (simpler organisms such as invertebrates only display a perfectly efficient innate immunity). The innate immune system's role is to scan the body to remove apoptotic bodies, cell debris, and protein aggregates; recognize and eliminate pathogens or abnormal cells; and keep commensals outside tissues. Additionally, it promotes the repair of damaged tissue and is involved in the control of embryogenesis and delivery. We can say that the innate immune system is the actual immune system, active throughout evolution with conserved and very efficient defensive mechanisms. The other system, adaptive immunity, developed much

later as a complement of innate immunity, providing slower but more specific protective responses, good for long-living and mobile organisms that do not stably reside in the same environment [1]. The adaptive immune responses are tools for the innate immune system with subordinated or programmed functions—tools because they develop without making any decision [2]. It is the innate immune system that detects, categorizes, and triggers the immune response and, in the case of additional needs, calls for adaptive immunity to come in when the innate activation has reached a certain threshold level indicative of excessive danger and the need for more specific defensive tools.

These complex defensive actions that body tissues perform in response to harmful stimuli, such as pathogens or damaged cells, are described as inflammation. Inflammation requires an excess biological workout and therefore it is closely related to metabolism. Immunometabolism has become increasingly popular since the publication of Mathis and Shoelson's perspective in 2011 [3]. This is crucial in the context of interactions with nanoparticles (NPs), since they have been observed to have the capacity to increase or decrease reactive oxygen species (ROS), which directly correlates with the onset or remission of inflammation [4]. ROS are free radical molecules resulting from natural metabolism, which, when excessive and unregulated, may contribute to cell damage and aggravate human pathologies such as cancer [5], neurodegeneration, and stroke, among others [6].

Following the great oxidation event some 2.3 billion years ago, oxidation has been the leading force of metabolism. A delicate equilibrium between heat generation (enthalpy) and biological organization (entropy) was established, which allowed natural systems to decrease their free energy in a particular controlled fashion [7]. Deregulation of a living system, for instance, in the case of a disease, increases enthalpy generation at the expense of entropy. The system over-burns, which in biological terms is described as inflammation (literally *setting in flames*). Inflammation is correlated with a particular metabolic pathway, anaerobic glycolysis, providing higher energy power output, in which cells defend themselves from aggression. Furthermore, aerobic glycolysis, with a broken Krebs cycle, provides important metabolic intermediates and ROS [8]. Inflammation provokes the unbalance between endogenous production of free radicals and antioxidant defenses, resulting in oxidative stress [9]. While this metabolic defense mechanism is an ability of all eukaryotic cells, it is reasonable to imagine that, through evolution, some cells adapted the unbalanced energy equation to becoming professional defensive cells forming a whole discontinued system distributed across the body and responsible for the maintenance, defense, and repair of our biological tissues. In normal conditions, these cells have a patrolling role based on scanning and surveying tissues to eliminate senescent or damaged cells and become aggressive when encountering some possible dangers, capable of initiating, developing, and controlling inflammation.

The innate cell response is different, depending on the type of stimulus or combination of stimuli, the stimulus intensity (quantitative and temporal), the location of the innate cells (the tissue and its specialization), and the microenvironmental conditions. All these cues trigger a defined activation profile in innate cells, which is different based on the combination of microenvironmental conditions that have triggered it. Engineered NPs may share several characteristics of microbial agents, such as size and ordered molecular surface patterns, presenting "eat-me" or "eat-me-not" surface signals that favor or prevent macrophages from engulfing them. Thus, they are expected to develop complex and intense interactions with immunity. Bachmann et al. [10] showed that the immune system readily recognized antigen repetitive organization on the surface of viral particles.

In contrast, poor antigen organization does not induce an immune response. The same holds for complement (in particular C1q, an ancient version of immunoglobulins) [11], which recognizes ordered antigenic structures as those present on microorganisms but do not react to disordered patterns as those present in mammalian cell surfaces. The same has been observed with NP coatings [12]. These interactions mainly concern innate immunity, as responsible for detecting and categorizing foreign matter inside the body.

In order to navigate the described interactions between NPs and the immune system, it is recommendable to remember the different type of immune cells and their different functions (Figure 1). A major role in the innate immune system is played by macrophages, which in mammals develop some specialized functions depending on the tissue where they reside and are named accordingly: Langerhans cells in the skin, Kupffer cells in the liver, osteoclasts in the bone, microglia in the brain. Other innate immune cells are the innate lymphoid cells (ILCs), such as natural killer cells. ILCs contribute to patrolling tissues (abundant in the barrier tissues such as mucosal surfaces), identifying and killing/eliminating abnormal cells and microorganisms, and contributing to tissue development and homeostasis. Contrary to macrophages, they cannot phagocytose, but they are endowed with cytotoxic tools that literally kill the target. Similarly, mast cells are highly efficient defensive cells, abundant in all barrier tissues, endowed with an array of pre-formed proteolytic enzymes and other bioactive substances, which they release upon challenge and can detoxify snake and bee venoms, release factors that initiate/enhance a tissue-localized protective inflammatory reaction against parasites, and contribute to tissue repair and remodeling. Other important innate cells are neutrophils (short-lived, very abundant in the blood, highly phagocytic and inflammatory, strong producers of reactive oxygen species (ROS) in response to microbes), basophils (functionally similar to mast cells but residing in the blood), and eosinophils (with partially overlapping functions with mast cells and basophils, involved in response to multicellular parasites). Moreover, cells of adaptive immunity include T and B lymphocytes, which develop membrane receptors or antibodies able to recognize different pathogenic molecules/antigens specifically. In between, there are dendritic cells, which share with macrophages the capacity of taking up, processing, and presenting pathogen-derived antigens to adaptive immune cells, thereby enabling T and B cells to develop their antigen-specific membrane receptors and antibodies.

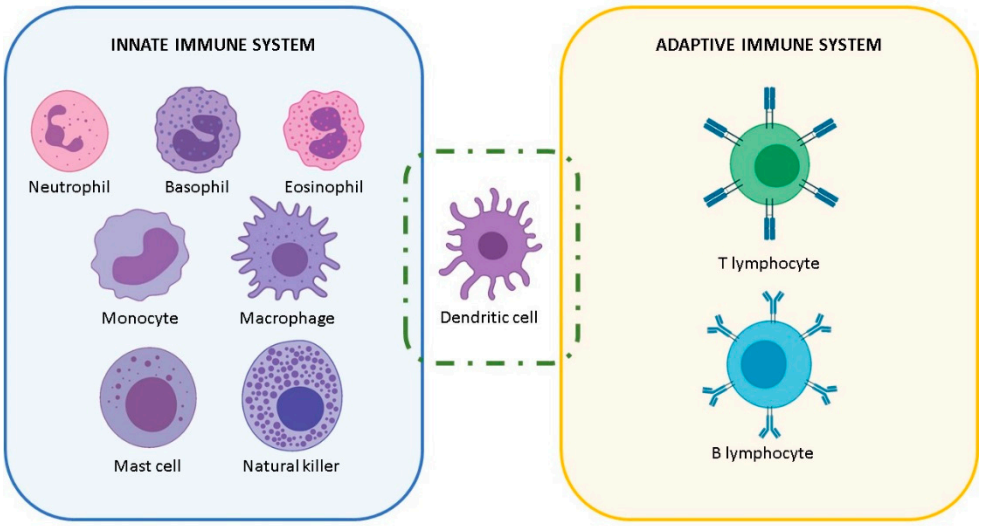


Figure 1. Representative classification of the most common mammalian immune cells.

The majority of the works on NP and immune system interactions [13] have focused on circulating blood monocytes (macrophage precursors) and tissue-resident macrophages [14]. Blood monocytes come from the bone marrow, while tissue macrophages can be a mixture of self-replicating cells that have populated the tissue during embryogenesis (developed from precursors in the yolk sac or fetal liver) and cells developed from blood monocytes that enter the tissue for replenishing the resident macrophage pool [15]. Macrophages present higher phagocytic activity than monocytes and can be easily identified based on size (monocytes are smaller than macrophages) and some biochemical markers (e.g., esterases) and surface molecules (e.g., CD14, CD16, CD68, CD11b, MAC-1) that are differentially expressed between the two cell types. The functional profile of monocytes and macrophages is exceptionally plas-

tic, as the role of these cells is that of rapidly reacting to different microenvironmental signals by adopting an appropriate activation profile, which will contribute to danger elimination and, eventually, instructing the subsequent adaptive immune responses.

2. The NP-Immune System Interactions

It is essential to realize that inorganic matter is commonly nanostructured and that NPs and nanostructures have naturally occurred on the planet's surface since its origin before life emerged. This suggests that the immune system of living organisms has developed in an environment rich in such structures and substances, and therefore it should know how to deal with them. However, since the advent of nanotechnology, we are building more artificial nanostructures and artificial combinations of nanostructures and molecules, which may result in stronger interactions with the immune system, beneficial or detrimental. They depend on the nature of the employed material and its evolution in the environment before encountering the immune cell. The observed interactions between NPs and the immune system can be classified as in Figure 2. It is essential to understand that the interaction of NPs and the immune system can be multifactorial; size, shape, and surface state (including composition, structure, charge. and hydrophilicity) are primary factors, together with the presence of bioactive moieties in the sample, or the promotion of chemical reactions resulting in immune activation. These factors are closely related to the NP evolution in different media, which may result into aggregation, dissolution, or associate with bystander (bio)molecules. All these factors should be taken into account to develop safe NPs and functional NPs.

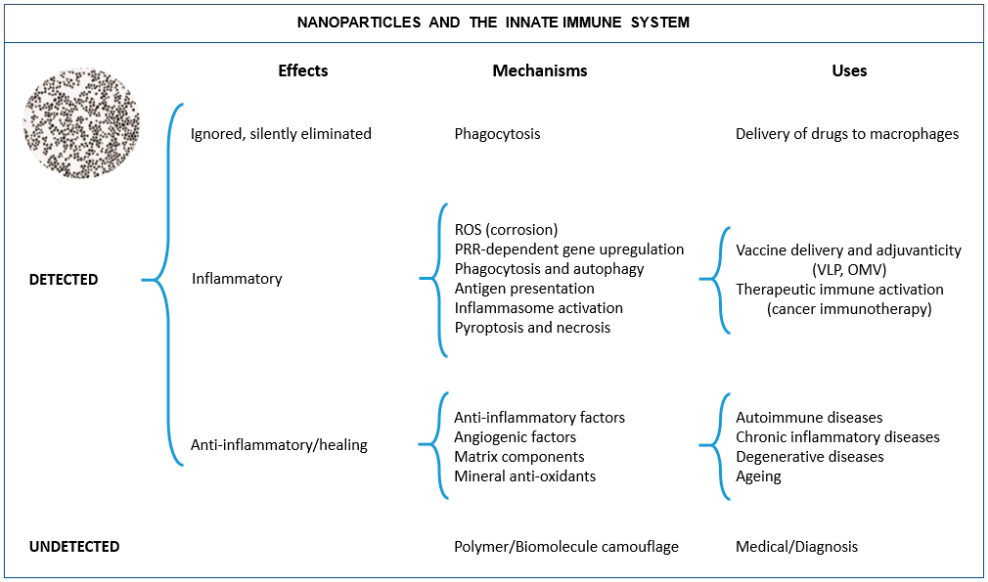


Figure 2. NP-immune system interactions. NPs can be undetected or detected by cells of the immune system, depending on different parameters such as their size, surface charge, and hydrophobicity/hydrophilicity of the surface coating. If detected, NPs can be either tolerated (either ignored or eliminated in a silent fashion, i.e., without inducing an inflammatory reaction) or generate an inflammatory response allowing for resolution of inflammation and tissue regeneration or an anti-inflammatory. With a proper NP design, these responses can be harnessed for developing different immunomodulating activities for medical exploitation (e.g., self-adjuvanted vaccines based on virus-like particles (VLPs), or outer membrane vesicles (OMVs), etc.).

2.1. When NPs Are Not Detected by the Immune System

The first scenario is when the NPs can escape from immune system detection. Indeed, the progress in the construction of synthetic nanostructures as delivery vehicles, contrast agents, or medical devices has allowed for the development of NPs able to escape the immune system and reach their target without inducing an undesirable inflammatory reac-

tion. In order to escape from pattern recognition receptors inserted in the cell membrane of immune cells, or opsonization by complement molecules or antibodies (which mark foreign/dead cells for recycling, thereby enhancing phagocytosis), the use of polymers to camouflage the NP surface has been thoroughly developed. In pharmacology, polyethylene glycol (PEG) and polyvinylpyrrolidone (PVP) have been the most used polymers to stealthily NPs from the immune system [13,16,17], historically developed together with the liposomal formulation of antineoplastic drugs, such as in the case of Doxil® and, more recently, mRNA vaccine platforms [16]. Studies showed that these polymer functionalized NPs may appear invisible (stealth) to the immune system [17,18] by mimicking non-dangerous biological structures. As a consequence, the PEG coating increased the half-life of organic and inorganic NPs in the bloodstream from minutes to hours [19,20], similar to previous observations with PEGylated proteins [21]. Similarly, oligosaccharide- and peptide-derived NP coatings seem to afford escape from the immune system and allow for longer circulation times. Nevertheless, these coatings can reduce/delay opsonization and phagocytosis, but they do not completely prevent it. Thus, for example, the development of anti-PEG antibodies has been reported in several patients, which led to faster clearance of subsequent doses of PEG-coated formulations [22–24]. To circumvent these problems, researchers have explored the possibility of coating NPs with natural substances that can more finely deceive the immune system, for instance, by coating NPs with albumin or serum mixtures. As far as proteins are not denatured, and the resulting object is not too big, NPs seem to pass undetected [25].

The different coatings employed to escape immune system detection are listed in Table 1.

Table 1. Coatings employed to avoid immune detection.

Surface Coating	Nanoparticle Core	References
Albumin (rat, mouse, or human)	CeO_2 NPs as an anti-inflammatory mineral substance	[26–29]
	Abraxane as an albumin-based nanoparticle for chemotherapeutic delivery	[30]
	Au NPs for tumor targeting	[19]
Polyethylene glycol (PEG)	SiO_2 NPs for evasion of phagocytic clearance	[20]
	Polystyrene NPs for evasion of phagocytic clearance	[31]
Retinol	Polyethylenimine (PEI) NPs for drug delivery	[25]
CD47	Polystyrene NPs for evasion from phagocytic clearance	[31,32]
Erythrocyte membrane fragments	Poly(lactic-co-glycolic acid) (PLGA) NPs for drug delivery	[33]

Another way of camouflaging NPs from immune elimination is using coatings with proteins that are downregulatory immune signals. This is the case of the CD47 protein, a marker of "self" and "eat-me-not" that is expressed on all cell membranes [34]. In the work of Rodriguez et al. [32], the attachment of "self" peptides computationally designed from human CD47 protein onto polystyrene NPs achieved a delayed macrophage-mediated clearance of NPs in mice. In addition, this increased the circulation time of the NPs and enhanced the drug delivery to lung adenocarcinoma xenografts. Likewise, Hu et al. [33] coated PLGA NPs with a red blood cell (RBC)-membrane shell. These RBC-based polymeric NPs also showed a longer circulation half-life and sustained in vivo drug release compared with that achieved by using PEG-coated NPs. The coating with specific "self" molecules can also be used for the opposite reason, i.e., to induce an immune system activation by coating NPs with endogenous danger-associated molecular patterns. As an example, Aldossari et al. [35] coated AgNPs with high-density lipoprotein (HDL), which is recognized by scavenger receptors (SR-B1) expressed by macrophages. Once administered to mice, HDL-coated AgNPs provoked the recruitment of inflammatory cells, whereas SR-B1-deficient mice showed reduced cell recruitment. This strategy allowed the antimicrobial activity of AgNPs to be enhanced by targeting delivery. This indicates how important the NP coating is to escape the immune system, where a large body of knowledge has been developed to allow NPs to serve as drug delivery vehicles.

2.2. When NPs Are Detected by the Immune System and Tolerated

When the immune system detects NPs, they can be tolerated or induce an activation. Being tolerated means that NPs are silently removed, without inducing inflammation, as if they were protein aggregates, apoptotic cells, or cellular debris. This can be controlled mainly by modulating NP size, surface charge, and hydrophobicity/hydrophilicity of their surface [13,16,17,32,33], where small sizes, hydrophilicity, and negative surface charges often result in tolerable NPs [36]. In general, one can say that NPs below 4–6 nm can pass undetected and undergo rapid renal clearance after i.v. administration [37]. As the NP diameter increases, NPs become the target of the different immune cells. NPs of virus-like size (a few tens to a few hundreds of nm) can be endocytosed without triggering inflammation [12]. Larger objects, of micrometric size, like bacteria, are phagocytosed, while for sizes larger than 10–20 microns, objects are encapsulated [38].

This has critical consequences for the biodistribution of NPs inside the body. NPs are transported and accumulated in different organs depending on the administration route, their physicochemical properties, and their detection by the immune system. Accordingly, after intravenous (i.v.) injection, common NPs are often filtered in the liver by hepatocytes [17,18] or eventually Kupffer cells (the liver macrophages) depending on if they are detected or pass undetected by the immune system [31]. The first studies of biodistribution of colloidal particles (a few hundred nm) were reported in the 1970s in the *Journal of the Reticuloendothelial Society* (now *Journal of Leukocyte Biology*). Singer et al. [39] and Adlersberg et al. [40], by treating mice with i.v. and i.p. colloidal Au, found that after one hour, 90% of the administered dose was accumulated in the liver and 10% in the rest of the body (mainly kidneys). Subsequent histological studies with similar colloidal gold particles i.p. administered found them in the liver and lymph nodes primarily localized inside macrophages [41]. These results were later confirmed by numerous studies of the pharmacokinetic and biodistribution of different NPs. Sadauskas et al. [42], using AuNPs of different sizes (below 40 nm), showed that Kupffer cells were central in accumulating NPs once they entered the body. Similar results were also obtained with metal oxides, quantum dots, carbon nanostructures, etc. [43]. Yokel et al. [44] administered citrate capped nanoceria (5, 15, 30, and 55 nm) at 50 and 100 mg/kg bw i.v. into Sprague-Dawley rats and measured Ce content over time (1 h, 20 h, and 30 days). Remarkably, in all these works and many others, no inflammation or systemic injury was observed, except at larger doses (>100 mg/kg bw). Accordingly, we have observed by mass spectroscopy that after i.v. administration of albumin-conjugated nanoceria (CeO_2) at low doses (0.1 mg/kg bw), twice a week during two weeks, in control and fibrotic Wistar rats, that most of the Ce is in the liver (84% of the administered dose after one hour and 75% eight weeks after administration) [26].

This non-inflammatory capture of NPs can be exploited for harnessing these phagocytic immune cells to transport NPs towards the target area, be it a wound, an infection, or a tumor. For such delivery, circulating monocytes have been proposed as a sort of Trojan Horse or Cellular Shuttle, since they naturally migrate from the blood to the sites of damage and disease. Hence, they can be loaded with NPs to be transported through the body [45,46]. Thus, Choi et al. [47] explored the use of monocytes containing AuNPs for transport into tumor regions for subsequent photothermal therapy. This study showed the phagocytosis of AuNPs by both monocytes and macrophages and their recruitment into the tumor. Oude-Engberink et al. [48] showed the accumulation of monocytes laden with iron oxide NPs (30 nm) in the affected cerebral sites in a rat model of experimental neuroinflammation. More recently, Moore et al. [49], using a microfluidic in vitro model, showed increased activity of monocytes/macrophages to transport NP across a confluent endothelial cell layer, advancing in the design of cellular shuttles loaded with NPs. This tolerated elimination of NPs may limit the dispersibility of NPs inside the body. However, the immune system is by itself an important therapeutic target where nanocarriers can efficiently transport drugs assisting immunotherapy.

2.3. When NPs Are Detected by the Immune System and Not Tolerated

Many reports show that NPs may induce harmful immune responses and toxicity. NPs can induce an inflammatory immune activation because of aggregation or dissolution or because they accidentally carry immune-activating moieties (such as endotoxin, detergents, allergens, or cationic molecules). These biological effects are rather independent of the composition, size, or shape of the individual NP, described as extrinsic factors of NP toxicity [4]. Similarly, the organization of molecular epitopes in a non-conventional form (upon adhesion of the NP surface) may generate new antigens or allergens. The activation of the immune system induced by NPs can be classified as follows:

2.3.1. NP-Induced Oxidative Stress

The more universal inflammatory reaction to NPs corresponds to the most non-specific and rapid defense mechanism of macrophages, the overproduction of reactive oxygen species (ROS), which results in oxidative stress, responsible of lipid oxidation and DNA damage and, eventually, structural alterations, DNA mutations, and cell death. ROS refers to biogenic free radical molecules resulting from natural metabolism characterized by being highly oxidant. These free radicals are involved in different critical physiological processes, such as gene expression, signal transduction, growth regulation, and, significantly, inflammation, where high ROS concentrations are needed to sustain the energetic demands of a proinflammatory immune response [50].

Accordingly, independently of composition, large aggregates of TiO_2 [51], Al_2O_3 [52], and Fe_2O_3 [53] NPs showed a similar capacity to increase oxidative stress. Moreover, the corrosion process of metallic NPs itself produces a high concentration of free radicals, which may trigger an inflammatory immune response [54–56]. These processes are often neglected in NPs made up of bulk non-biodegradable materials. However, biodegradation of Ag, Fe_3O_4, and CdSe/ZnS NPs due to enzymatic or hydrolytic activities in lysosomes [57,58] have been described. Even the physiological disintegration of AuNPs through oxidative etching by cysteine and chlorine has been described [59–61]. Similarly, carbon nanotubes (CNTs) have been observed to dissolve in vivo through enzymatic catalysis [62]. Subsequently, an increased number of reports has established relationships between observed inflammatory effects after NP exposure and NP disintegration [63–66]. Related to that, it is worth mentioning the works of Burello et al. [67] and Zhang et al. [55]. They developed theoretical and experimental models to predict the oxidative stress potential of oxide NPs by looking at their bandgap energy and their ability to perturb the intracellular redox state. Note that NP dissolution may become a source of toxic cations. For instance, in the early 2000s, the studies of Derfus et al. [68] and Kirchner et al. [69] showed that the released Cd ions were responsible for the intracellular oxidation and toxicity caused by CdSe NPs. Similar effects were found later when comparing the toxicity of Ni NP and ions as a function of time [70].

2.3.2. When Phagocytosis Is Not Sufficient

When the immune system detects a foreign object, phagocytosis is the first mechanism for elimination that comes into play. However, when the object is too big (usually larger than 10–20 μm), rather than engulfing it, the immune cells start spreading on it to form a layer of cells that secludes the object from the rest of the tissue and initiate a chemical defense against the material that, if not non-biodegradable, is permanently kept secluded into a fibrous capsule or granuloma.

Historically, chronic inflammation has been observed in the case of penetration of non-biodegradable (persistent) large size (micrometric) particles in the lungs, as the well-known cases of particle-induced granulomatosis such as silicosis and asbestosis [71]. This is because when a phagocytic cell fails to digest these particles, phagolysosomal rupture, the release of lysosomal enzymes and particles, and subsequent activation of the inflammasome and other cytoplasmic sensing mechanisms may happen, thereby triggering inflammation. This may lead, as the material persists, to chronic inflammation, perma-

nent oxidative stress, tissue damage, and alterations that favor tumorigenesis in the long term. Brandwood et al. [72] found that murine macrophages phagocytosed inert carbon fiber-reinforced carbon particles up to 20 microns in diameter, but larger particles were not engulfed and became surrounded by aggregations of macrophages. This reaction may have pathological aspects; fibromas and granulomas are non-functional neo-tissues, similar to scars, that may hamper the organ functions and be active, i.e., growing, for a long time. In some instances, the reaction can be overtly pathological, as in the case of long fibrous materials. Accordingly, when Poland et al. [73] instilled high doses of multiwalled carbon nanotubes between the membranes lining the lungs and abdominal organs in mice, they found that long straight nanotubes caused inflammation and lesions in membrane cells similar to those leading to cancer, just like asbestos fibers [74]. Similarly, Ag nanospheres did not elicit any immune response or toxicity, while Ag nanowires can elicit a high inflammatory response, directly correlated to nanowire length, in murine macrophages [75]. The same effects were observed by Ji et al. [76] in THP-1 cells when comparing nanoceria nanorods and high aspect ratio nanoceria nanowires at high doses and aggregation states. This suggests that the needle-like shape of NPs is prone to provoke inflammation. It has been observed that macrophages engulfing needle-shaped crystals and fibers end up getting pierced by the needle-like structures and, consequently, start inflammation [77]. Parental NPs usually are never grown to these sizes, but uncontrolled aggregation can transform objects of tens of nm to tens of μm.

2.3.3. NPs, Intendedly or Accidentally, Can Display Antigens, Allergens, or Toxins

The unintended or accidental absorption of biomolecules onto the NP surface may be a cause of concern. NPs may associate with specific bio-molecules, toxic by-standers, or pollutants, and present them to the immune system in an ordered pattern, thereby mimicking microorganisms and triggering the innate immune reaction of the host.

It is important to note that NPs have a strong tendency to adsorb many different molecules (hetero-aggregation) at their surface due to their high surface energy. Consequently, they are usually surrounded by a molecular coating, either provided intentionally (NP functionalization) and/or spontaneously by molecules present in the environment, forming the NP biocorona. These coatings also take part in the NP morphology and functions. The consequences of this are diverse; NPs can be good molecular aggregators and substrates for molecules to be presented to the immune system.

Among essential immunoactive biomolecules present in the environment, bacterial endotoxin is one of the most common and abundant. Endotoxins (also known as lipopolysaccharides (LPSs)) are large molecules present in the outer membrane of Gram-negative bacteria, able to elicit strong innate/inflammatory immune responses. Endotoxin is a ubiquitous environmental contaminant and can be present in all chemicals and glassware used in laboratories, even after sterilization (depyrogenation is needed to get rid of it). The presence of endotoxin, if not recognized, can be responsible for many of the in vitro and in vivo effects attributed to NPs [78]. Our study [79] showed that the endotoxin present on AuNPs turned those NPs from inactive to highly inflammatory and able to induce secretion of IL-1β in human primary monocytes. This could be an underlying factor in inflammatory responses and toxic effects associated with other metallic NPs and carbon nanomaterials [80,81]. Hence, special attention is needed to avoid endotoxin contamination when preparing NPs, which includes working in endotoxin-free conditions and glassware depyrogenation [82].

In other cases, the toxic ingredient may come from the formulation or derived chemicals employed during NPs preparation. If the synthesis process does not involve proper purification steps, the use of such NP samples may entail deleterious responses due to excess surfactants or unreacted precursors. This is the case of PEI molecules, a common NP stabilizer to enhance NP endocytosis, but with safety concerns due to the attachment to the negatively charged cell membranes that modify permeability and compromise viability [83]. Indeed, it is well-established that positively charged macromolecules can cause higher

toxicity and immune activation than their neutral or negatively charged counterparts, as in the case of monolayer-coated silicon nanoparticles [84]. Similar is the case of amphipathic molecules such as cetyltrimethyl ammonium bromide (CTAB), employed in preparing Au nanorods [85], which act as a detergent to lyse cell membranes. Another example is in the work of Dowding et al. [86]. These authors prepared different nanoceria NPs using the identical precursor (cerium nitrate hexahydrate) through a similar wet chemical process but using other bases: NH_4OH, which yields negatively charged nanoceria, or hexamethylenetetramine (HMTA), which yields positively charged nanoceria at neutral pH. Results showed that HMTA-nanoceria NPs were readily taken into endothelial cells and reduced cell viability at a 10-fold lower concentration than the other NPs, which showed no toxicity.

Another type of immunoactive molecule that NPs can adsorb is allergens. This is unlikely to happen in the case of NPs since the concentration of allergens in the environment is very low, and the NP surface would be passivated before encountering them. However, it must be taken into account. Note that it has been reported that car combustion emission microparticles, when coated by pollen grains, enhance allergenic responses [87]. Radauer et al. [88] observed the formation of a stable allergen coating around NPs when exposed to different types of allergens (Der p1 and Bet v1), enhancing allergic responses against them. A recent review about the potential of NPs to trigger allergies via adsorption of allergens can be found in reference [89]. Here, it is essential to remark that allergy, understood as an anomalous immune response towards substances that are generally tolerated, has never been observed for engineered nanomaterials per se.

Regarding immune effects induced by biomolecules adsorbed on the NP surface, another possible source of inflammation comes from the potential modification of the structure of proteins upon adsorption at the NP surface [90]. Lynch et al. [91] pointed out how partial protein misfolding at the NP surface may result in the exposure of protein fractions usually buried in the core of the native structure. These cryptic epitopes may be recognized by immune cells and trigger inappropriate defensive reactions. Accordingly, in the work of Falagan [92], such modifications of the adsorbed proteins structure have been indicated as responsible for the long-term toxicity observed after a single low-dose exposure of AuNPs.

2.3.4. NPs Presenting Vaccine Antigens and Working as Vaccine Adjuvants

Regarding the intentional use of NPs for vaccination, conjugation of antigens to NPs can help both attain a more efficient presentation of poorly immunogenic soluble antigens and provide an adjuvant effect targeted to innate immunity (the NP as a foreign agent) [12]. An interesting example is the development of AuNP-based virus-like particles (VLPs), where the NP replaces the virus core, which scaffolds the proteic capsid structure [93]. Typically, capsid proteins need the highly negatively charged dense core of DNA/RNA to self-assemble properly. This core can be replaced by dense and highly negatively charged AuNPs. Nikura et al. [93] demonstrated that the size and shape of AuNP-VLPs allowed for shaping of the in vitro and in vivo immune response in terms of the production of antibodies against West Nile virus. This implies that by modulating the NP size and shape, and consequently the arrangement of viral proteins on the NP surface, it could be possible to obtain highly effective and efficient vaccines. NPs can also be employed as vaccine adjuvants by exploiting their capacity to target and modulate the activity of innate immune cells. For a long time, vaccines were prepared by precipitation of antigens within some matrix, initially bread crumbs (in the XIX century), and currently alum powder, where the antigens are absorbed, forming aggregates that vary in size from 1 to 20 μm, acting as an antigen depot [94]. In this way, slow release of antigens is achieved, prolonging antigen presence, improving its processing and presentation. Other NP aggregates have been used as adjuvants. Skarastina et al. [95] used silica NPs (10–20 nm) as adjuvants for the hepatitis B vaccine in a mouse model. The monodisperse silica NPs formed heterogeneous aggregates larger than 1 μm after formulation, resulting in the same IgG2a/IgG1 ratios as in the case of immunization with alum as an adjuvant. Other nanostructure used as

vaccine adjuvants are nano-sized emulsions (sometimes called lipidic NPs). This is the case of the oil-in-water MF59 emulsion, which is used as an adjuvant, mainly for influenza vaccines (Flaud®, Novartis) and has been licensed in more than 20 countries. The MF59 adjuvant allows for significant cross-reactivity against viral strains and reduces antigen concentration to 50–200-fold lower doses [96].

The induction of inflammatory responses with non-pathogenic triggers has also been proposed as a preventive approach against exposure to unknown pathogens. Behind this concept, preventive activation of the innate immunity, there is the capacity of innate immune cells to develop a different response to a challenge as a consequence of previous contact with a different threat, a capacity known as innate memory [97,98]. All innate immune cells are able to develop a long lasting memory, despite their short lifespan in circulation. The reason lies mainly on the fact that the precursors in the bone marrow can be primed by a trigger and generate circulating immune cells with a different capacity to react against threats, as currently shown in monocytes/macrophages. Thus, after having previously experienced an inflammatory activation, the innate immune system becomes more efficient in preventing the rooting of newly incoming pathogens. For instance, this has been observed in the case of the administration of bacille calmette-guerin (BCG), the vaccine for tuberculosis, which increases resistance to other diseases [99]. The generation of innate memory thus represents an alternative, or better a complement, to the highly specific adaptive memory induced by vaccines. The strategy of innate memory induction leads to outcomes (enhanced protection) that have advantages (wider range of protection) and disadvantages (more unpredictable and less controllable side effects). Despite the controversy regarding safety, NPs can be used as adjuvants for the non-specific amplification of immune responses, and, even more, they can be excellent tools for generating or modulating innate memory [100]. In this regard, administration of AuNPs alone was observed to have little/no impact on the subsequent capacity of human monocytes to mount an innate/inflammatory response to a microbial challenge (LPS) [101]. However, the co-administration of AuNPs, or Fe_3O_4NPs, with memory-inducing microbial agents (e.g., LPS, BCG, muramyl dipeptide (MDP), Helicobacter pylori) led to a modulation of the innate memory response induced by the microbial agents depending on the priming stimulus and the NP type, shape, and size [102]. The implication is that vaccination with antigens and NPs could bring about a protective specific immunity based on adaptive immune memory and a non-specific innate memory induced by the antigen-NP combination.

The proinflammatory activation effects are listed in Table 2. In all these aspects, the uncontrolled proinflammatory activation of the immune system is, in principle, a common source of NP toxicity. In contrast, controlled activation can be employed for vaccination and other modes of defense against pathogens.

Table 2. Inflammatory activation induced by NPs.

NPs That Cause Inflammation		
Category	**Surfactant**	**References**
Inflammation induced by by-standers	Cetyltrimethyl ammonium bromide (CTAB)	[85]
	Hexamethylenetetramine (HMT)	[103]
Inflammation induced by pollutants	Bacterial endotoxin (LPS)	[78,79]
	Allergens	[88,89]
Category	**Mechanism**	**References**
Inflammation induced by the core	Non biocompatible size/shape	[72–76]
	Excess of aggregation/agglomeration	[51–53,96,102,104]
	Chemical transformations and corrosion	[54–70,102]
Category	**Surfactant**	**References**
Inflammation induced by the coating (bioactive molecules, VLPs…)	Virus like particles (VLP)	[93]
	Antigen/ordered peptides/proteins coatings	[91,92,100,105]
	Cationic polymers	[83]

2.4. When NPs Act as Enzymes and in This Way Can Modulate Immune Reactions

Rare-earth oxide NPs have been found to be biocompatible antioxidants able to buffer excess ROS in physiological conditions, showing powerful anti-inflammatory effects. Mineral antioxidants may offer superior activity to currently available substances due to their enhanced bioavailability and stability, longer tissue residence time, and resistance to biological degradation [106]. These features can be exploited in many diseases based on excessive immune/inflammatory activation, such as autoimmune diseases, chronic inflammation, organ rejection, asthma and other allergic diseases, neurodegenerative pathologies (Alzheimer's disease, Parkinson's disease), and aging [106]. They have been described as engineered inorganic materials with enzyme-like activities, especially cerium oxide NPs, nanoceria [106,107]. Nanoceria has been reported to display superoxide dismutase (SOD)-like activity (conversion of superoxide anion into hydrogen peroxide and finally oxygen) [108], catalase-like activity (conversion of hydrogen peroxide into oxygen and water) [109,110], peroxidase-like activity (conversion of hydrogen peroxide into hydroxyl radicals) [111], as well as NO scavenging ability [103]. Consequently, nanoceria has been shown to safely down-regulate oxidative stress by scavenging the excess of ROS in diseases such as retinal degeneration [112,113], neurological disorders (including Alzheimer's disease, Parkinson's disease, and ALS) [114–116], ischemia [117], cardiopathies [118], diabetes [119], gastrointestinal inflammation [120], liver diseases [26–28], and cancer [121,122], as well as in regenerative medicine [123] and tissue engineering [124], with better performance than other antioxidant substances in both efficacy and efficiency. Interestingly, nanoceria become active at high ROS concentrations. Otherwise, at homeostatic ROS levels, the NPs become inactive. This is because several free radicals have to be simultaneously absorbed onto the NP surface in order to be recombined into non-radical adducts, a condition that only happens for high ROS concentrations. In other words, the ROS scavenging capacities of nanoceria are ROS concentration dependent. With time, these NPs dissolve into innocuous ions, which are excreted via the urinary route [19]. The solid NPs have been observed to be excreted through the hepatobiliary route [26,125].

This aspect is significantly different from the previous ones, where activation of the immune system results in inflammatory responses. In this case, the enzyme-like catalytic activity of rare earth NPs results in anti-inflammatory activity. The different observed responses are listed in Table 3.

Table 3. Immune responses to NP exposure.

Category	Nanoparticle Core	Surface Coating	References
NPs that pass unnoticed	Au NPs	Polyethylene glycol (PEG)	[19]
	SiO_2 NPs	Polyethylene glycol (PEG)	[20]
	Polyethylenimine (PEI) NPs	Retinol	[25]
	Polystyrene NPs	CD47 or PEG	[31,32]
		Bovine serum albumin (BSA)	[46]
	Polymeric NPs	Erythrocyte membrane fragments	[33]
	Abraxane	Human serum albumin (HSA)	[30]
NPs that are tolerated	Au NPs	Sodium citrate	[42,92]
		Disordered peptidic coatings	[47]
	CeO_2 NPs	Rat serum albumin (RSA)	[44]
	Polystyrene NPs	Poly-L-lysine	[46]
	Fe_3O_4 NPs	Dextrane	[48]
	SiO_2 NPs	3-Aminopropyltriethoxysilane (APTES)	[49]

Table 3. *Cont.*

Category	Nanoparticle Core	Surface Coating	References
Immunoactive NPs with inflammatory activity	Au NPs	Peptides/proteins	[55,58,93,105]
		Bacterial endotoxin (LPS)	[78]
		Cetyltrimethyl ammonium bromide (CTAB)	[85]
		Allergens	[88]
		Poly(acrylic acid) (PAA)	[92]
		Polyethylene glycol (PEG)	[92]
	Ag NPs	High-density lipoprotein (HDL)	[35]
		Sodium citrate	[58,65,74]
	Alumina NPs	Fetal bovine serum (FBS)	[52]
	CeO_2 NPs	Hexamethylenetetramine (HMT)	[86]
		Polyethylenimine (PEI)-polyethylene glycol (PEG)	[122]
	Gadolinium endohedral metallofullerenols	Polyhydroxy	[80]
	Silica NPs	Hepatitis B virus core protein	[104]
Immunoactive NPs with anti-inflammatory activity	CeO_2 NPs	Murine serum albumin	[26–29]
		Polyethylene glycol (PEG)	[117]
		Gelatin	[124]

3. NP Evolution and Transformations in the Exposure Media

The interaction between NPs and the immune system strongly depends on the conditions in which such interaction occurs (route of exposure, co-exposure with other agents) and on the characteristics of both NPs and the host immune system. Here we have presented the variety of immune responses to NPs and how these responses can help us design immuno-active and immune-benign NPs, which could either avoid immune recognition and activation in order to persist in the body long enough for completing their theranostic tasks or directly interact with immune cells for triggering inflammatory or anti-inflammatory responses as desired for therapeutic purposes. Indeed, the scientific community is still struggling with the apparent contradiction of similar materials being toxic and non-toxic (even beneficial) at the same time. This paradox can be attributed to undescribed effects of NP modifications during their dispersion in the working media, such as aggregation and corrosion. The main modifications NPs may suffer during their dispersion in different media are shown in Figure 3. Basically, NPs can be coated with molecules (e.g., hydrophilic polymers) to both pass undetected by the immune system and avoid aggregation (1). They can also be coated with soluble antigenic molecules to induce a response against them (2). In the opposite direction, when dispersed in physiological media, NPs can aggregate (3) and adsorb other molecules present in the medium (e.g., protein corona) (4) or both (5). In addition, depending on the core composition, NPs can be used as ROS scavengers, thereby down-regulating inflammatory responses (6), or they can dissolve and act as an ion reservoir that may increase the level of oxidative stress and generate an inflammatory response (7).

NPs have different ways to minimize their high surface energy, basically aggregation and corrosion. These are common phenomena in nature, widely studied by geochemistry, where a NP is an intermediate state between a micrometric particle and the dissolved ions. Thus, NPs may aggregate or associate with coating molecules in different media. They may also disintegrate through corrosion (defined as the chemical degradation of a solid material) and dissolution.

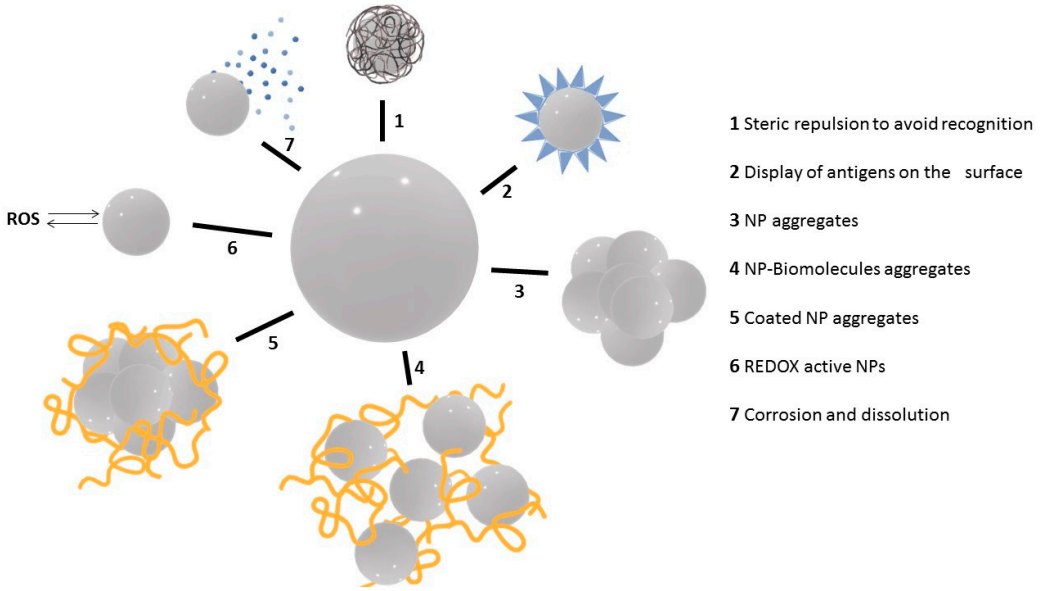


Figure 3. Intended or spontaneous NP modifications and their impact on immune responses.

Aggregation deserves particular attention. NPs are colloidally stable by repulsive electrostatic or steric forces or a combination of both. Aggregability depends on intrinsic NP parameters such as morphology, surface coating, and charge, and extrinsic parameters such as electrolyte concentration, pH, presence of organic matter, etc. Aggregation is common in physiological environments where NPs aggregate to submicrometric or micrometric sizes when not properly stabilized. To avoid it, one has to provide repulsive forces to the NP surface, either by electrostatic (high surface charge) or steric (entropic) means, usually provided by large soluble molecules associated with the NP surface; otherwise, they will aggregate and their unique physicochemical properties that arise at the nanoscale (quantum confinement, superparamagnetism, extreme catalytic activity, etc.) progressively lost. Note that aggregation entails modifications in terms of specific surface area, concentration, mobility, and dosing. Protein adsorption, the formation of a protein corona, is a particular aggregation phenomenon between NPs and proteins present in the dispersion media. It is a dynamic process in which, initially, proteins adsorb and desorb at the surface, followed by a set of re-organizational arrangements, which make this absorption more stable and finally irreversible [126,127]. This depends on NP size, surface state, type of protein, and protein-NP incubation media and conditions, where sophisticated functional patterns can be obtained [128]. The most straightforward strategy to cope with this issue is to passivate the NP surface in a controlled manner, e.g., by albuminization, PEGylation, or addition of PVP. These strategies usually decrease aggregation, even in high salt media, and the adsorption of microenvironmental biomolecules on the NP surface.

In addition to aggregation, chemical transformations, corrosion, and dissolution can also be a cause of immune activation via the alteration for the cellular redoxome, and the delivery of toxic cations. In this regard, the nanochemist or nanoengineer needs to control the redox potential (and the oxidative/reductive environment) where the NP will be stored, employed, and disposed of. In this regard, using NPs at their higher valence state is recommendable when possible [14] (passivating the surface with a continuous layer of oxide is sometimes an alternative). The chemical transformation and dissolution of NPs, which can cause immune activation or toxicity, is fundamental to determine NP fate and reduce its presence and persistence in the environment.

4. Concluding Remarks

After considering the different interactions NPs may have with the immune system, one can draw indications on how NPs have to be designed to control these interactions and

consequent responses. Indeed, while many NP functions can be attributed to their core structure, the surface coating defines much of their bioactivity. By controlling the nano-bio interface, NPs can be designed to be safe and innocuous or active and have therapeutic benefits. From the NP point of view, and for the nanochemist and the nanoengineer, the NP immunological properties can be summarized as depicted in Figure 4. The composition of the NP core determines its chemical potential and catalytic activity, while the surface coating largely determines its bioactivity. NPs can aggregate, either with other NPs or with macromolecules present in the physiological media (e.g., biocorona), or they can dissolve, being redox-active and acting as an ion reservoir, consequently increasing the levels of oxidative stress.

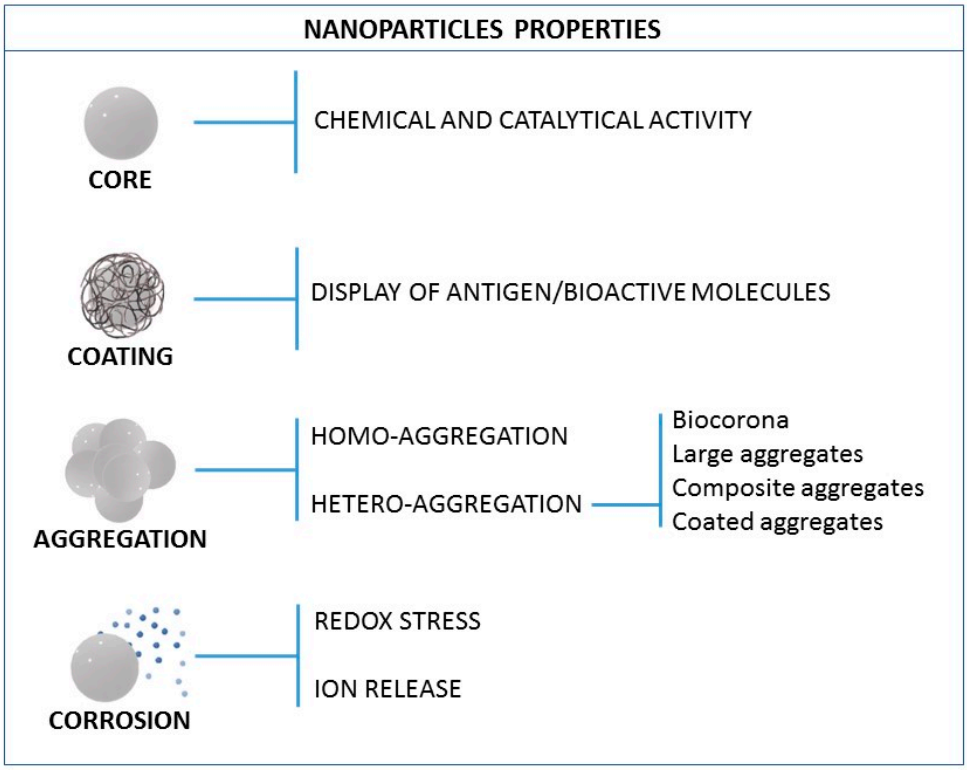


Figure 4. The NP properties that can impact the immune system.

In order to address the NP immune interactions, one has first to deal with the instability of the NP surface, and it should be passivated before introduction into biological systems. Otherwise, they may spontaneously aggregate, resulting in objects of increased size and decreased dose. Polymeric coatings have traditionally been the most commonly employed materials for such purposes. However, this surface engineering is sometimes costly and involves multi-step synthesis approaches, sometimes in the organic phase. One simple and effective solution could be to promote NP solubility in physiological media by pre-albuminization during the preparation process [118,119,128], a similar approach employed by Abraxane®, one of the first approved nanomedicines [30]. In addition to providing colloidal stability and avoiding opsonization, NP coatings can be designed to directly interact with the immune system, such as CD47 [32] for avoiding complement activation, LPS for inducing innate/inflammatory activation [79], or viral proteins for vaccination [95]. Finally, NPs that belong to the family of natural antioxidants, such as nanoceria that catalytically scavenge free radicals (ROS in the context of inflammation), provide powerful immunomodulatory effects.

Thus, by mainly playing with surface characteristics, it is possible to adjust the NP physicochemical characteristics (aggregation, surface display of given biomolecules, chemical stability) and consequently their modes of interaction with the immune system.

Author Contributions: V.P., L.M.E., E.C., P.I. and D.B. wrote the manuscript. L.M.E. also prepared the figures and managed references together with E.C. All authors have read and agreed to the published version of the manuscript.

Funding: This research was funded by the EU Commission H2020 project PANDORA (GA 671881; to D.B., P.I. and V.P.). Additional funds were provided by the EU Commission H2020 project ENDONANO (GA 812661; to P.I. and D.B.), the Italian MIUR InterOmics Flagship projects MEMORAT and MAME (to D.B. and P.I.), the Italian MIUR/PRIN-20173ZECCM (to P.I.), the CAS President's International Fellowship Programme (PIFI; award 2020VBA0028; to D.B.), Spanish Ministerio de Ciencia, Innovación y Universidades (MCIU) (RTI2018-099965-B-I00, AEI/FEDER, UE), and Generalitat de Catalunya (2017-SGR-1431) (V.P.).

Conflicts of Interest: The authors declare no conflict of interest. The funders had no role in the design of the study; in the collection, analyses, or interpretation of data; in the writing of the manuscript; or in the decision to publish.

References

1. Flajnik, M.F.; Kasahara, M. Origin and evolution of the adaptive immune system: Genetic events and selective pressures. *Nat. Rev. Genet.* **2010**, *11*, 47–59. [CrossRef]
2. Iwasaki, A.; Medzhitov, R. Control of adaptive immunity by the innate immune system. *Nat. Immunol.* **2015**, *16*, 343–353. [CrossRef]
3. Mathis, D.; Shoelson, S.E. Immunometabolism: An emerging frontier. *Nat. Rev. Immunol.* **2011**, *11*, 81. [CrossRef]
4. Casals, E.; Gusta, M.F.; Piella, J.; Casals, G.; Jiménez, W.; Puntes, V. Intrinsic and Extrinsic Properties Affecting Innate Immune Responses to Nanoparticles: The Case of Cerium Oxide. *Front. Immunol.* **2017**, *8*, 970. [CrossRef]
5. Reczek, C.R.; Chandel, N.S. The Two Faces of Reactive Oxygen Species in Cancer. *Annu. Rev. Cancer Biol.* **2017**, *1*, 79–98. [CrossRef]
6. Chen, Q.; Wang, Q.; Zhu, J.; Xiao, Q.; Zhang, L. Reactive oxygen species: Key regulators in vascular health and diseases. *Br. J. Pharmacol.* **2018**, *175*, 1279–1292. [CrossRef]
7. Ritort, F. The Noisy and Marvelous Molecular World of Biology. *Inventions* **2019**, *4*, 24. [CrossRef]
8. O'Neill, L.A. A broken krebs cycle in macrophages. *Immunity* **2015**, *42*, 393–394. [CrossRef]
9. Pizzino, G.; Irrera, N.; Cucinotta, M.; Pallio, G.; Mannino, F.; Arcoraci, V.; Squadrito, F.; Altavilla, D.; Bitto, A. Oxidative Stress: Harms and Benefits for Human Health. *Oxid. Med. Cell. Longev.* **2017**, *2017*, 8416763. [CrossRef]
10. Bachmann, M.F.; Rohrer, U.H.; Kündig, T.M.; Bürki, K.; Hengartner, H.; Zinkernagel, R.M. The influence of antigen organization on B cell responsiveness. *Science* **1993**, *262*, 1448–1451. [CrossRef]
11. Bachmann, M.F.; Jennings, G.T. Vaccine delivery: A matter of size, geometry, kinetics and molecular patterns. *Nat. Rev. Immunol.* **2010**, *10*, 787–796. [CrossRef]
12. Bastús, N.G.; Sánchez-Tilló, E.; Pujals, S.; Farrera, C.; López, C.; Giralt, E.; Celada, A.; Lloberas, J.; Puntes, V. Homogeneous Conjugation of Peptides onto Gold Nanoparticles Enhances Macrophage Response. *ACS Nano* **2009**, *3*, 1335–1344. [CrossRef]
13. Moghimi, S.M.; Szebeni, J. Stealth liposomes and long circulating nanoparticles: Critical issues in pharmacokinetics, opsonization and protein-binding properties. *Prog. Lipid Res.* **2003**, *42*, 463–478. [CrossRef]
14. Hume, D.A. The mononuclear phagocyte system. *Curr. Opin. Immunol.* **2006**, *18*, 49–53. [CrossRef]
15. Gordon, S.; Plüddemann, A. The Mononuclear Phagocytic System. Generation of Diversity. *Front. Immunol.* **2019**, *10*, 1893. [CrossRef]
16. Peracchia, M.T.; Harnisch, S.; Pinto-Alphandary, H.; Gulik, A.; Dedieu, J.C.; Desmaële, D.; d'Angelo, J.; Müller, R.H.; Couvreur, P. Visualization of in vitro protein-rejecting properties of PEGylated stealth polycyanoacrylate nanoparticles. *Biomaterials* **1999**, *20*, 1269–1275. [CrossRef]
17. Gref, R.; Lück, M.; Quellec, P.; Marchand, M.; Dellacherie, E.; Harnisch, S.; Blunk, T.; Müller, R.H. 'Stealth' corona-core nanoparticles surface modified by polyethylene glycol (PEG): Influences of the corona (PEG chain length and surface density) and of the core composition on phagocytic uptake and plasma protein adsorption. *Colloids Surf. B Biointerfaces* **2000**, *18*, 301–313. [CrossRef]
18. Hou, X.; Zaks, T.; Langer, R.; Dong, Y. Lipid nanoparticles for mRNA delivery. *Nat. Rev. Mater.* **2021**, *10*, 1–17.
19. Veronese, F.M.; Pasut, G. PEGylation, successful approach to drug delivery. *Drug Discov. Today* **2005**, *10*, 1451–1458. [CrossRef]
20. Harris, J.M.; Chess, R.B. Effect of pegylation on pharmaceuticals. *Nat. Rev. Drug Discov.* **2003**, *2*, 214–221. [CrossRef]
21. Perrault, S.D.; Walkey, C.; Jennings, T.; Fischer, H.C.; Chan, W.C.W. Mediating Tumor Targeting Efficiency of Nanoparticles Through Design. *Nano Lett.* **2009**, *9*, 1909–1915. [CrossRef]
22. He, Q.; Zhang, J.; Shi, J.; Zhu, Z.; Zhang, L.; Bu, W.; Guo, L.; Chen, Y. The effect of PEGylation of mesoporous silica nanoparticles on nonspecific binding of serum proteins and cellular responses. *Biomaterials* **2010**, *31*, 1085–1092. [CrossRef]
23. Abuchowski, A.; McCoy, J.R.; Palczuk, N.C.; van Es, T.; Davis, F.F. Effect of covalent attachment of polyethylene glycol on immunogenicity and circulating life of bovine liver catalase. *J. Biol. Chem.* **1977**, *252*, 3582–3586. [CrossRef]

24. Richter, A.W.; Akerblom, E. Antibodies against polyethylene glycol produced in animals by immunization with monomethoxy polyethylene glycol modified proteins. *Int. Arch. Allergy Appl. Immunol.* **1983**, *70*, 124–131. [CrossRef]
25. Cheng, T.-L.; Wu, P.-Y.; Wu, M.-F.; Chern, J.-W.; Roffler, S.R. Accelerated Clearance of Polyethylene Glycol-Modified Proteins by Anti-Polyethylene Glycol IgM. *Bioconjug. Chem.* **1999**, *10*, 520–528. [CrossRef]
26. Verhoef, J.J.F.; Carpenter, J.F.; Anchordoquy, T.J.; Schellekens, H. Potential induction of anti-PEG antibodies and complement activation toward PEGylated therapeutics. *Drug Discov. Today* **2014**, *19*, 1945–1952. [CrossRef]
27. Zhang, Z.; Wang, C.; Zha, Y.; Hu, W.; Gao, Z.; Zang, Y.; Chen, J.; Zhang, J.; Dong, L. Corona-Directed Nucleic Acid Delivery into Hepatic Stellate Cells for Liver Fibrosis Therapy. *ACS Nano* **2015**, *9*, 2405–2419. [CrossRef]
28. Oldenborg, P.-A.; Zheleznyak, A.; Fang, Y.-F.; Lagenaur, C.F.; Gresham, H.D.; Lindberg, F.P. Role of CD47, as a Marker of Self on Red Blood Cells. *Science* **2000**, *288*, 2051–2054. [CrossRef]
29. Rodriguez, P.L.; Harada, T.; Christian, D.A.; Pantano, D.A.; Tsai, R.K.; Discher, D.E. Minimal "Self" peptides that inhibit phagocytic clearance and enhance delivery of nanoparticles. *Science* **2013**, *339*, 971–975. [CrossRef]
30. Hu, C.-M.J.; Zhang, L.; Aryal, S.; Cheung, C.; Fang, R.H.; Zhang, L. Erythrocyte membrane-camouflaged polymeric nanoparticles as a biomimetic delivery platform. *Proc. Natl. Acad. Sci. USA* **2011**, *108*, 10980–10985. [CrossRef]
31. Aldossari, A.A.; Shannahan, J.H.; Podila, R.; Brown, J.M. Scavenger receptor B_1 facilitates macrophage uptake of silver nanoparticles and cellular activation. *J. Nanoparticle Res.* **2015**, *17*, 313. [CrossRef]
32. Seong, S.Y.; Matzinger, P. Hydrophobicity: An ancient damage-associated molecular pattern that initiates innate immune responses. *Nat. Rev. Immunol.* **2004**, *4*, 469–478. [CrossRef]
33. Bastús, N.G.; Casals, E.; Vázquez-Campos, S.; Puntes, V. Reactivity of engineered inorganic nanoparticles and carbon nanostructures in biological media. *Nanotoxicology* **2008**, *2*, 99–112. [CrossRef]
34. Choi, H.S.; Liu, W.; Misra, P.; Tanaka, E.; Zimmer, J.P.; Itty Ipe, B.; Bawendi, M.G.; Frangioni, J.V. Renal clearance of quantum dots. *Nat. Biotechnol.* **2007**, *25*, 1165–1170. [CrossRef]
35. Sperling, R.A.; Casals, E.; Comenge, J.; Bastús, N.G.; Puntes, V.F. Inorganic engineered nanoparticles and their impact on the immune response. *Curr. Drug Metab.* **2009**, *10*, 895–904. [CrossRef]
36. Qie, Y.; Yuan, H.; von Roemeling, C.A.; Chen, Y.; Liu, X.; Shih, K.D.; Knight, J.A.; Tun, H.W.; Wharen, R.E.; Jiang, W.; et al. Surface modification of nanoparticles enables selective evasion of phagocytic clearance by distinct macrophage phenotypes. *Sci. Rep.* **2016**, *6*, 26269. [CrossRef]
37. Singer, J.M.; Adlersberg, L.; Sadek, M. Long-term observation of intravenously injected colloidal gold in mice. *J. Reticuloendothel. Soc.* **1972**, *12*, 658–671.
38. Adlersberg, L.; Singer, J.M. The fate of intraperitoneally injected colloidal gold particles in mice. *J. Reticuloendothel. Soc.* **1973**, *13*, 325–342.
39. Williams, R.J.; Bradley, N.J. Distribution of intraperitoneal gold colloid (198-Au). *Acta Med. Austriaca* **1989**, *16*, 50–54.
40. Sadauskas, E.; Wallin, H.; Stoltenberg, M.; Vogel, U.; Doering, P.; Larsen, A.; Danscher, G. Kupffer cells are central in the removal of nanoparticles from the organism. *Part. Fibre Toxicol.* **2007**, *4*, 10. [CrossRef]
41. Casals, E.; Vázquez-Campos, S.; Bastús, N.G.; Puntes, V. Distribution and potential toxicity of engineered inorganic nanoparticles and carbon nanostructures in biological systems. *TrAC Trends Anal. Chem.* **2008**, *27*, 672–683. [CrossRef]
42. Yokel, R.A.; Tseng, M.T.; Dan, M.; Unrine, J.M.; Graham, U.M.; Wu, P.; Grulke, E.A. Biodistribution and biopersistence of ceria engineered nanomaterials: Size dependence. *Nanomed. Nanotechnol. Biol. Med.* **2013**, *9*, 398–407. [CrossRef]
43. Oro, D.; Yudina, T.; Fernandez-Varo, G.; Casals, E.; Reichenbach, V.; Casals, G.; de la Presa, B.; Sandalinas, S.; Carvajal, S.; Puntes, V.; et al. Cerium oxide nanoparticles reduce steatosis, portal hypertension and display anti-inflammatory properties in rats with liver fibrosis. *J. Hepatol.* **2016**, *64*, 691–698. [CrossRef]
44. Mehta, K.; Lopez-Berestein, G.; Hersh, E.M.; Juliano, R.L. Uptake of liposomes and liposome-encapsulated muramyl dipeptide by human peripheral blood monocytes. *J. Reticuloendothel. Soc.* **1982**, *32*, 155–164.
45. Thiele, L.; Rothen-Rutishauser, B.; Jilek, S.; Wunderli-Allenspach, H.; Merkle, H.P.; Walter, E. Evaluation of particle uptake in human blood monocyte-derived cells in vitro. Does phagocytosis activity of dendritic cells measure up with macrophages? *J. Control. Release* **2001**, *76*, 59–71. [CrossRef]
46. Choi, M.-R.; Stanton-Maxey, K.J.; Stanley, J.K.; Levin, C.S.; Bardhan, R.; Akin, D.; Badve, S.; Sturgis, J.; Robinson, J.P.; Bashir, R.; et al. A Cellular Trojan Horse for Delivery of Therapeutic Nanoparticles into Tumors. *Nano Lett.* **2007**, *7*, 3759–3765. [CrossRef]
47. Oude Engberink, R.D.; Blezer, E.L.; Hoff, E.I.; van der Pol, S.M.; van der Toorn, A.; Dijkhuizen, R.M.; de Vries, H.E. MRI of monocyte infiltration in an animal model of neuroinflammation using SPIO-labeled monocytes or free USPIO. *J. Cereb. Blood Flow Metab.* **2008**, *28*, 841–851. [CrossRef]
48. Moore, T.L.; Hauser, D.; Gruber, T.; Rothen-Rutishauser, B.; Lattuada, M.; Petri-Fink, A.; Lyck, R. Cellular Shuttles: Monocytes/Macrophages Exhibit Transendothelial Transport of Nanoparticles under Physiological Flow. *ACS Appl. Mater. Interfaces* **2017**, *9*, 18501–18511. [CrossRef]
49. Viola, A.; Munari, F.; Sanchez-Rodriguez, R.; Scolaro, T.; Castegna, A. The Metabolic Signature of Macrophage Responses. *Front. Immunol.* **2019**, *10*, 1462. [CrossRef]
50. Noel, A.; Maghni, K.; Cloutier, Y.; Dion, C.; Wilkinson, K.J.; Halle, S.; Tardif, R.; Truchon, G. Effects of inhaled nano-TiO_2 aerosols showing two distinct agglomeration states on rat lungs. *Toxicol. Lett.* **2012**, *214*, 109–119. [CrossRef]

51. Yoon, D.; Woo, D.; Kim, J.; Kim, M.; Kim, T.; Hwang, E.; Baik, S. Agglomeration, sedimentation, and cellular toxicity of alumina nanoparticles in cell culture medium. *J. Nanoparticle Res.* **2011**, *13*, 2543–2551. [CrossRef]
52. Zhu, X.; Tian, S.; Cai, Z. Toxicity Assessment of Iron Oxide Nanoparticles in Zebrafish (Danio rerio) Early Life Stages. *PLoS ONE* **2012**, *7*, 9. [CrossRef] [PubMed]
53. Liu, J.; Sonshine, D.A.; Shervani, S.; Hurt, R.H. Controlled Release of Biologically Active Silver from Nanosilver Surfaces. *ACS Nano* **2010**, *4*, 6903–6913. [CrossRef]
54. Zhang, H.; Ji, Z.; Xia, T.; Meng, H.; Low-Kam, C.; Liu, R.; Pokhrel, S.; Lin, S.; Wang, X.; Liao, Y.-P.; et al. Use of Metal Oxide Nanoparticle Band Gap to Develop a Predictive Paradigm for Oxidative Stress and Acute Pulmonary Inflammation. *ACS Nano* **2012**, *6*, 4349–4368. [CrossRef]
55. Semerád, J.; Filip, J.; Ševců, A.; Brumovský, M.; Nguyen, N.H.A.; Mikšíček, J.; Lederer, T.; Filipová, A.; Boháčková, J.; Cajthaml, T. Environmental fate of sulfidated nZVI particles: The interplay of nanoparticle corrosion and toxicity during aging. *Environ. Sci. Nano* **2020**, *7*, 1794–1806. [CrossRef]
56. Sabella, S.; Carney, R.P.; Brunetti, V.; Malvindi, M.A.; Al-Juffali, N.; Vecchio, G.; Janes, S.M.; Bakr, O.M.; Cingolani, R.; Stellacci, F.; et al. A general mechanism for intracellular toxicity of metal-containing nanoparticles. *Nanoscale* **2014**, *6*, 7052–7061. [CrossRef]
57. Jiang, X.; Miclăuş, T.; Wang, L.; Foldbjerg, R.; Sutherland, D.S.; Autrup, H.; Chen, C.; Beer, C. Fast intracellular dissolution and persistent cellular uptake of silver nanoparticles in CHO-K1, cells: Implication for cytotoxicity. *Nanotoxicology* **2015**, *9*, 181–189. [CrossRef]
58. Wiley, B.; Herricks, T.; Sun, Y.; Xia, Y. Polyol Synthesis of Silver Nanoparticles: Use of Chloride and Oxygen to Promote the Formation of Single-Crystal, Truncated Cubes and Tetrahedrons. *Nano Lett.* **2004**, *4*, 1733–1739. [CrossRef]
59. Kim, K.-H.; Kim, J.-U.; Cha, S.-H.; Lee, J.-C. Reversible Formation and Dissolution of Gold Nanoparticles through Turning On and Off Sequences of UV Light. *J. Am. Chem. Soc.* **2009**, *131*, 7482–7483. [CrossRef]
60. Xia, Y.; Xiong, Y.; Lim, B.; Skrabalak, S.E. Shape-controlled synthesis of metal nanocrystals: Simple chemistry meets complex physics? *Angew. Chem. Int. Ed. Engl.* **2009**, *48*, 60–103. [CrossRef] [PubMed]
61. Allen, B.L.; Kichambare, P.D.; Gou, P.; Vlasova, I.I.; Kapralov, A.A.; Konduru, N.; Kagan, V.E.; Star, A. Biodegradation of Single-Walled Carbon Nanotubes through Enzymatic Catalysis. *Nano Lett.* **2008**, *8*, 3899–3903. [CrossRef] [PubMed]
62. Franklin, N.M.; Rogers, N.J.; Apte, S.C.; Batley, G.E.; Gadd, G.E.; Casey, P.S. Comparative toxicity of nanoparticulate ZnO, bulk ZnO, and $ZnCl_2$, to a freshwater microalga (Pseudokirchneriella subcapitata): The importance of particle solubility. *Environ. Sci. Technol.* **2007**, *41*, 8484–8490. [CrossRef]
63. Auffan, M.; Rose, J.; Wiesner, M.R.; Bottero, J.Y. Chemical stability of metallic nanoparticles: A parameter controlling their potential cellular toxicity in vitro. *Environ. Pollut.* **2009**, *157*, 1127–1133. [CrossRef] [PubMed]
64. De Matteis, V.; Malvindi, M.A.; Galeone, A.; Brunetti, V.; De Luca, E.; Kote, S.; Kshirsagar, P.; Sabella, S.; Bardi, G.; Pompa, P.P. Negligible particle-specific toxicity mechanism of silver nanoparticles: The role of Ag+ ion release in the cytosol. *Nanomed. Nanotechnol. Biol. Med.* **2015**, *11*, 731–739. [CrossRef]
65. Wang, D.; Lin, Z.; Wang, T.; Yao, Z.; Qin, M.; Zheng, S.; Lu, W. Where does the toxicity of metal oxide nanoparticles come from: The nanoparticles, the ions, or a combination of both? *J. Hazard. Mater.* **2016**, *308*, 328–334. [CrossRef]
66. Burello, E.; Worth, A.P. A theoretical framework for predicting the oxidative stress potential of oxide nanoparticles. *Nanotoxicology* **2011**, *5*, 228–235. [CrossRef]
67. Derfus, A.M.; Chan, W.C.W.; Bhatia, S.N. Probing the Cytotoxicity of Semiconductor Quantum Dots. *Nano Lett.* **2004**, *4*, 11–18. [CrossRef]
68. Kirchner, C.; Liedl, T.; Kudera, S.; Pellegrino, T.; Muñoz Javier, A.; Gaub, H.E.; Stölzle, S.; Fertig, N.; Parak, W.J. Cytotoxicity of Colloidal CdSe and CdSe/ZnS Nanoparticles. *Nano Lett.* **2005**, *5*, 331–338. [CrossRef]
69. Zhou, C.; Vitiello, V.; Casals, E.; Puntes, V.F.; Iamunno, F.; Pellegrini, D.; Changwen, W.; Benvenuto, G.; Buttino, I. Toxicity of nickel in the marine calanoid copepod Acartia tonsa: Nickel chloride versus nanoparticles. *Aquat. Toxicol.* **2016**, *170*, 1–12. [CrossRef] [PubMed]
70. Heffner, D.K. The cause of sarcoidosis: The Centurial enigma solved. *Ann. Diagn. Pathol.* **2007**, *11*, 142–152. [CrossRef]
71. Brandwood, A.; Noble, K.R.; Schindhelm, K. Phagocytosis of carbon particles by macrophages in vitro. *Biomaterials* **1992**, *13*, 646–648. [CrossRef]
72. Poland, C.A.; Duffin, R.; Kinloch, I.; Maynard, A.; Wallace, W.A.H.; Seaton, A.; Stone, V.; Brown, S.; MacNee, W.; Donaldson, K. Carbon nanotubes introduced into the abdominal cavity of mice show asbestos-like pathogenicity in a pilot study. *Nat. Nanotechnol.* **2008**, *3*, 423. [CrossRef] [PubMed]
73. Stoehr, L.C.; Gonzalez, E.; Stampfl, A.; Casals, E.; Duschl, A.; Puntes, V.; Oostingh, G.J. Shape matters: Effects of silver nanospheres and wires on human alveolar epithelial cells. *Part. Fibre Toxicol.* **2011**, *8*, 36. [CrossRef] [PubMed]
74. Toybou, D.; Celle, C.; Aude-Garcia, C.; Rabilloud, T.; Simonato, J.-P. A toxicology-informed, safer by design approach for the fabrication of transparent electrodes based on silver nanowires. *Environ. Sci. Nano* **2019**, *6*, 684–694. [CrossRef]
75. Ji, Z.; Wang, X.; Zhang, H.; Lin, S.; Meng, H.; Sun, B.; George, S.; Xia, T.; Nel, A.E.; Zink, J.I. Designed Synthesis of CeO_2 Nanorods and Nanowires for Studying Toxicological Effects of High Aspect Ratio Nanomaterials. *ACS Nano* **2012**, *6*, 5366–5380. [CrossRef] [PubMed]
76. Fadeel, B. Hide and Seek: Nanomaterial Interactions with the Immune System. *Front. Immunol.* **2019**, *10*, 133. [CrossRef]

77. Li, Y.; Shi, Z.; Radauer-Preiml, I.; Andosch, A.; Casals, E.; Luetz-Meindl, U.; Cobaleda, M.; Lin, Z.; Jaberi-Douraki, M.; Italiani, P.; et al. Bacterial endotoxin (lipopolysaccharide) binds to the surface of gold nanoparticles, interferes with biocorona formation and induces human monocyte inflammatory activation. *Nanotoxicology* **2017**, *11*, 1157–1175. [CrossRef]
78. Li, Y.; Italiani, P.; Casals, E.; Valkenborg, D.; Mertens, I.; Baggerman, G.; Nelissen, I.; Puntes, V.F.; Boraschi, D. Assessing the Immunosafety of Engineered Nanoparticles with a Novel in Vitro Model Based on Human Primary Monocytes. *ACS Appl. Mater. Interfaces* **2016**, *8*, 28437–28447. [CrossRef]
79. Chen, Z.; Liu, Y.; Sun, B.; Li, H.; Dong, J.; Zhang, L.; Wang, L.; Wang, P.; Zhao, Y.; Chen, C. Polyhydroxylated metallofullerenols stimulate IL-1β secretion of macrophage through TLRs/MyD88/NF-κB pathway and $NLRP_3$ inflammasome activation. *Small* **2014**, *10*, 2362–2372. [CrossRef]
80. Chen, G.Y.; Yang, H.J.; Lu, C.H.; Chao, Y.C.; Hwang, S.M.; Chen, C.L.; Lo, K.W.; Sung, L.Y.; Luo, W.Y.; Tuan, H.Y.; et al. Simultaneous induction of autophagy and toll-like receptor signaling pathways by graphene oxide. *Biomaterials* **2012**, *33*, 6559–6569. [CrossRef]
81. Li, Y.; Italiani, P.; Casals, E.; Tran, N.; Puntes, V.F.; Boraschi, D. Optimising the use of commercial LAL assays for the analysis of endotoxin contamination in metal colloids and metal oxide nanoparticles. *Nanotoxicology* **2015**, *9*, 462–473. [CrossRef] [PubMed]
82. Kafil, V.; Omidi, Y. Cytotoxic impacts of linear and branched polyethylenimine nanostructures in a431 cells. *Bioimpacts* **2011**, *1*, 23–30.
83. Bhattacharjee, S.; de Haan, L.H.; Evers, N.M.; Jiang, X.; Marcelis, A.T.; Zuilhof, H.; Rietjens, I.M.; Alink, G.M. Role of surface charge and oxidative stress in cytotoxicity of organic monolayer-coated silicon nanoparticles towards macrophage NR8383 cells. *Part. Fibre Toxicol.* **2010**, *7*, 25. [CrossRef] [PubMed]
84. Alkilany, A.M.; Nagaria, P.K.; Hexel, C.R.; Shaw, T.J.; Murphy, C.J.; Wyatt, M.D. Cellular uptake and cytotoxicity of gold nanorods: Molecular origin of cytotoxicity and surface effects. *Small* **2009**, *5*, 701–708. [CrossRef] [PubMed]
85. Dowding, J.M.; Das, S.; Kumar, A.; Dosani, T.; McCormack, R.; Gupta, A.; Sayle, T.X.; Sayle, D.C.; von Kalm, L.; Seal, S.; et al. Cellular interaction and toxicity depend on physicochemical properties and surface modification of redox-active nanomaterials. *ACS Nano* **2013**, *7*, 4855–4868. [CrossRef]
86. Fujieda, S.; Diaz-Sanchez, D.; Saxon, A. Combined nasal challenge with diesel exhaust particles and allergen induces In vivo IgE isotype switching. *Am. J. Respir. Cell Mol. Biol.* **1998**, *19*, 507–512. [CrossRef]
87. Radauer-Preiml, I.; Andosch, A.; Hawranek, T.; Luetz-Meindl, U.; Wiederstein, M.; Horejs-Hoeck, J.; Himly, M.; Boyles, M.; Duschl, A. Nanoparticle-allergen interactions mediate human allergic responses: Protein corona characterization and cellular responses. *Part. Fibre Toxicol.* **2016**, *13*, 3. [CrossRef]
88. Martin, H.; Bettina, G.; Marlene, S.; Mark, G.; Albert, D. Immune Frailty and Nanomaterials: The Case of Allergies. *Curr. Bionanotechnol.* **2016**, *2*, 20–28.
89. Goy-López, S.; Juárez, J.; Alatorre-Meda, M.; Casals, E.; Puntes, V.F.; Taboada, P.; Mosquera, V. Physicochemical Characteristics of Protein–NP Bioconjugates: The Role of Particle Curvature and Solution Conditions on Human Serum Albumin Conformation and Fibrillogenesis Inhibition. *Langmuir* **2012**, *28*, 9113–9126. [CrossRef] [PubMed]
90. Lynch, I.; Dawson, K.A.; Linse, S. Detecting cryptic epitopes created by nanoparticles. *Sci. STKE* **2006**, *2006*, pe14. [CrossRef]
91. Falagan-Lotsch, P.; Grzincic, E.M.; Murphy, C.J. One low-dose exposure of gold nanoparticles induces long-term changes in human cells. *Proc. Natl. Acad. Sci. USA* **2016**, *113*, 13318–13323. [CrossRef]
92. Niikura, K.; Matsunaga, T.; Suzuki, T.; Kobayashi, S.; Yamaguchi, H.; Orba, Y.; Kawaguchi, A.; Hasegawa, H.; Kajino, K.; Ninomiya, T.; et al. Gold nanoparticles as a vaccine platform: Influence of size and shape on immunological responses in vitro and in vivo. *ACS Nano* **2013**, *7*, 3926–3938. [CrossRef]
93. Pulendran, B.; Arunachalam, P.S.; O'Hagan, D.T. Emerging concepts in the science of vaccine adjuvants. *Nat. Rev. Drug Discov.* **2021**, *20*, 454–475. [CrossRef] [PubMed]
94. Skrastina, D.; Petrovskis, I.; Lieknina, I.; Bogans, J.; Renhofa, R.; Ose, V.; Dishlers, A.; Dekhtyar, Y.; Pumpens, P. Silica nanoparticles as the adjuvant for the immunisation of mice using hepatitis B core virus-like particles. *PLoS ONE* **2014**, *9*, e114006. [CrossRef]
95. O'Hagan, D.T. MF59 is a safe and potent vaccine adjuvant that enhances protection against influenza virus infection. *Expert Rev. Vaccines* **2007**, *6*, 699–710. [CrossRef]
96. Boraschi, D.; Italiani, P. Innate Immune Memory: Time for Adopting a Correct Terminology. *Front. Immunol.* **2018**, *9*, 799. [CrossRef]
97. Mitroulis, I.; Ruppova, K.; Wang, B.; Chen, L.S.; Grzybek, M.; Grinenko, T.; Eugster, A.; Troullinaki, M.; Palladini, A.; Kourtzelis, I.; et al. Modulation of Myelopoiesis Progenitors Is an Integral Component of Trained Immunity. *Cell* **2018**, *172*, 147–161. [CrossRef]
98. Uthayakumar, D.; Paris, S.; Chapat, L.; Freyburger, L.; Poulet, H.; De Luca, K. Non-specific Effects of Vaccines Illustrated Through the BCG Example: From Observations to Demonstrations. *Front. Immunol.* **2018**, *9*, 2869. [CrossRef] [PubMed]
99. Barbosa, M.M.F.; Kanno, A.I.; Farias, L.P.; Madej, M.; Sipos, G.; Sbrana, S.; Romani, L.; Boraschi, D.; Leite, L.C.C.; Italiani, P. Primary and Memory Response of Human Monocytes to Vaccines: Role of Nanoparticulate Antigens in Inducing Innate Memory. *Nanomaterials* **2021**, *11*, 931. [CrossRef] [PubMed]
100. Della Camera, G.; Madej, M.; Ferretti, A.M.; La Spina, R.; Li, Y.; Corteggio, A.; Heinzl, T.; Swartzwelter, B.J.; Sipos, G.; Gioria, S.; et al. Personalised Profiling of Innate Immune Memory Induced by Nano-Imaging Particles in Human Monocytes. *Front. Immunol.* **2021**, *12*, 692165. [CrossRef] [PubMed]

101. Casals, E.; Zeng, M.; Parra-Robert, M.; Fernández-Varo, G.; Morales-Ruiz, M.; Jiménez, W.; Puntes, V.; Casals, G. Cerium Oxide Nanoparticles: Advances in Biodistribution, Toxicity, and Preclinical Exploration. *Small* **2020**, *16*, 1907322. [CrossRef]
102. Xu, C.; Qu, X. Cerium oxide nanoparticle: A remarkably versatile rare earth nanomaterial for biological applications. *Npg Asia Mater.* **2014**, *6*, e90. [CrossRef]
103. Korsvik, C.; Patil, S.; Seal, S.; Self, W. Superoxide dismutase mimetic properties exhibited by vacancy engineered ceria nanoparticles. *Chem. Commun.* **2007**, *10*, 1056–1058. [CrossRef] [PubMed]
104. Pirmohamed, T.; Dowding, J.; Singh, S.; Wasserman, B.; Heckert, E.; Karakoti, A.; King, J.; Seal, S.; Self, W. Nanoceria exhibit redox state-dependent catalase mimetic activity. *Chem. Commun.* **2010**, *46*, 2736–2738. [CrossRef] [PubMed]
105. Cafun, J.D.; Kvashnina, K.O.; Casals, E.; Puntes, V.F.; Glatzel, P. Absence of Ce3+ sites in chemically active colloidal ceria nanoparticles. *ACS Nano* **2013**, *7*, 10726–10732. [CrossRef] [PubMed]
106. Heckert, E.G.; Seal, S.; Self, W.T. Fenton-Like Reaction Catalyzed by the Rare Earth Inner Transition Metal Cerium. *Environ. Sci. Technol.* **2008**, *42*, 5014–5019. [CrossRef]
107. Dowding, J.; Dosani, T.; Kumar, A.; Seal, S.; Self, W. Cerium oxide nanoparticles scavenge nitric oxide radical ((NO)-N-center dot). *Chem. Commun.* **2012**, *48*, 4896–4898. [CrossRef]
108. Chen, J.P.; Patil, S.; Seal, S.; McGinnis, J.F. Rare earth nanoparticles prevent retinal degeneration induced by intracellular peroxides. *Nat. Nanotechnol.* **2006**, *1*, 142–150. [CrossRef]
109. Cai, X.; Sezate, S.A.; Seal, S.; McGinnis, J.F. Sustained protection against photoreceptor degeneration in tubby mice by intravitreal injection of nanoceria. *Biomaterials* **2012**, *33*, 8771–8781. [CrossRef]
110. Schubert, D.; Dargusch, R.; Raitano, J.; Chan, S.W. Cerium and yttrium oxide nanoparticles are neuroprotective. *Biochem. Biophys. Res. Commun.* **2006**, *342*, 86–91. [CrossRef]
111. D'Angelo, B.; Santucci, S.; Benedetti, E.; Di Loreto, S.; Phani, R.; Falone, S.; Amicarelli, F.; Cerù, M.P.; Cimini, A. Cerium Oxide Nanoparticles Trigger Neuronal Survival in a Human Alzheimer Disease Model By Modulating BDNF Pathway. *Curr. Nanosci.* **2009**, *5*, 167–176. [CrossRef]
112. Kalashnikova, I.; Mazar, J.; Neal, C.J.; Rosado, A.L.; Das, S.; Westmoreland, T.J.; Seal, S. Nanoparticle delivery of curcumin induces cellular hypoxia and ROS-mediated apoptosis via modulation of Bcl-2/Bax in human neuroblastoma. *Nanoscale* **2017**, *9*, 10375–10387. [CrossRef] [PubMed]
113. Kim, C.K.; Kim, T.; Choi, I.Y.; Soh, M.; Kim, D.; Kim, Y.J.; Jang, H.; Yang, H.S.; Kim, J.Y.; Park, H.K.; et al. Ceria nanoparticles that can protect against ischemic stroke. *Angew. Chem. Int. Ed. Engl.* **2012**, *51*, 11039–11043. [CrossRef] [PubMed]
114. Niu, J.L.; Azfer, A.; Rogers, L.M.; Wang, X.H.; Kolattukudy, P.E. Cardioprotective effects of cerium oxide nanoparticles in a transgenic murine model of cardiomyopathy. *Cardiovasc. Res.* **2007**, *73*, 549–559. [CrossRef]
115. Khurana, A.; Tekula, S.; Godugu, C. Nanoceria suppresses multiple low doses of streptozotocin-induced Type *1*, diabetes by inhibition of Nrf2/NF-κB pathway and reduction of apoptosis. *Nanomedicine* **2018**, *13*, 1905–1922. [CrossRef] [PubMed]
116. Colon, J.; Hsieh, N.; Ferguson, A.; Kupelian, P.; Seal, S.; Jenkins, D.W.; Baker, C.H. Cerium oxide nanoparticles protect gastrointestinal epithelium from radiation-induced damage by reduction of reactive oxygen species and upregulation of superoxide dismutase 2. *Nanomedicine* **2010**, *6*, 698–705. [CrossRef]
117. Parra-Robert, M.; Casals, E.; Massana, N.; Zeng, M.; Perramón, M.; Fernández-Varo, G.; Morales-Ruiz, M.; Puntes, V.; Jiménez, W.; Casals, G. Beyond the Scavenging of Reactive Oxygen Species (ROS): Direct Effect of Cerium Oxide Nanoparticles in Reducing Fatty Acids Content in an In Vitro Model of Hepatocellular Steatosis. *Biomolecules* **2019**, *9*, 425. [CrossRef] [PubMed]
118. Fernández-Varo, G.; Perramón, M.; Carvajal, S.; Oró, D.; Casals, E.; Boix, L.; Oller, L.; Macías-Muñoz, L.; Marfà, S.; Casals, G.; et al. Bespoken Nanoceria: An Effective Treatment in Experimental Hepatocellular Carcinoma. *Hepatology* **2020**, *72*, 1267–1282. [CrossRef]
119. Tarnuzzer, R.W.; Colon, J.; Patil, S.; Seal, S. Vacancy engineered ceria nanostructures for protection from radiation-induced cellular damage. *Nano Lett.* **2005**, *5*, 2573–2577. [CrossRef]
120. Li, H.; Liu, C.; Zeng, Y.-P.; Hao, Y.-H.; Huang, J.-W.; Yang, Z.-Y.; Li, R. Nanoceria-Mediated Drug Delivery for Targeted Photodynamic Therapy on Drug-Resistant Breast Cancer. *ACS Appl. Mater. Interfaces* **2016**, *8*, 31510–31523. [CrossRef] [PubMed]
121. Das, S.; Chigurupati, S.; Dowding, J.; Munusamy, P.; Baer, D.R.; McGinnis, J.F.; Mattson, M.P.; Self, W.; Seal, S. Therapeutic potential of nanoceria in regenerative medicine. *MRS Bull.* **2014**, *39*, 976–983. [CrossRef]
122. Marino, A.; Tonda-Turo, C.; De Pasquale, D.; Ruini, F.; Genchi, G.; Nitti, S.; Cappello, V.; Gemmi, M.; Mattoli, V.; Ciardelli, G.; et al. Gelatin/nanoceria nanocomposite fibers as antioxidant scaffolds for neuronal regeneration. *Biochim. Biophys. Acta-Gen. Subj.* **2017**, *1861*, 386–395. [CrossRef] [PubMed]
123. Muhammad, F.; Wang, A.; Qi, W.; Zhang, S.; Zhu, G. Intracellular Antioxidants Dissolve Man-Made Antioxidant Nanoparticles: Using Redox Vulnerability of Nanoceria to Develop a Responsive Drug Delivery System. *Appl. Mater. Interfaces* **2014**, *6*, 19424–19433. [CrossRef] [PubMed]
124. Casals, E.; Pfaller, T.; Duschl, A.; Oostingh, G.J.; Puntes, V. Time evolution of the nanoparticle protein corona. *ACS Nano* **2010**, *4*, 3623–3632. [CrossRef] [PubMed]
125. Casals, E.; Pfaller, T.; Duschl, A.; Oostingh, G.J.; Puntes, V. Hardening of the Nanoparticle Protein Corona in Metal (Au, Ag) and Oxide (Fe_3O_4, CoO and CeO_2) Nanoparticles. *Small* **2011**. [CrossRef] [PubMed]

126. Astorga-Gamaza, A.; Vitali, M.; Borrajo, M.L.; Suárez-López, R.; Jaime, C.; Bastus, N.; Serra-Peinado, C.; Luque-Ballesteros, L.; Blanch-Lombarte, O.; Prado, J.G.; et al. Antibody cooperative adsorption onto AuNPs and its exploitation to force natural killer cells to kill HIV-infected T cells. *Nano Today* **2021**, *36*, 101056. [CrossRef]
127. Ribera, J.; Rodríguez-Vita, J.; Cordoba, B.; Portolés, I.; Casals, G.; Casals, E.; Jiménez, W.; Puntes, V.; Morales-Ruiz, M. Functionalized cerium oxide nanoparticles mitigate the oxidative stress and pro-inflammatory activity associated to the portal vein endothelium of cirrhotic rats. *PLoS ONE* **2019**, *14*, e0218716. [CrossRef]
128. O'Shaughnessy, J.A.; Tjulandin, S.; Davidson, N. ABI-007 (ABRAXANE^{TM}), a Nanoparticle Albumin-Bound (nab) Paclitaxel Demonstrates Superior Efficacy vs Taxol in MBC: A Phase III Trial. In Proceedings of the 26th Annual San Antonio Breast Cancer Symposium, San Antonio, TX, USA, 3–6 December 2003. Abstract 44.

7.3.2 Exploring the Long-Term Tissue Accumulation and Excretion of 3 nm Cerium Oxide Nanoparticles after Single Dose Administration

antioxidants

MDPI

Article

Exploring the Long-Term Tissue Accumulation and Excretion of 3 nm Cerium Oxide Nanoparticles after Single Dose Administration

Lena M. Ernst [1], Laura Mondragón [1,2], Joana Ramis [1], Muriel F. Gustà [3,4], Tetyana Yudina [3], Eudald Casals [1,5], Neus G. Bastús [3,4], Guillermo Fernández-Varo [6], Gregori Casals [6,7], Wladimiro Jiménez [6,8] and Victor Puntes [1,3,4,9,*]

1 Vall d'Hebron Research Institute (VHIR), 08035 Barcelona, Spain
2 Josep Carreras Leukaemia Research Institute (IJC), 08916 Badalona, Spain
3 Institut Català de Nanociència I Nanotecnologia (ICN2), CSIC, The Barcelona Institute of Science and Technology (BIST), Campus UAB, Bellaterra, 08193 Barcelona, Spain
4 Networking Research Centre for Bioengineering, Biomaterials, and Nanomedicine (CIBER-BBN), Instituto de Salud Carlos III, 28029 Madrid, Spain
5 School of Biotechnology and Health Sciences, Wuyi University, Jiangmen 529020, China
6 Service of Biochemistry and Molecular Genetics, Hospital Clinic, Centro de Investigación Biomédica en Red de Enfermedades Hepáticas y Digestivas (CIBERehd), Institut d'Investigacions Biomèdiques August Pi i Sunyer (IDIBAPS), 08036 Barcelona, Spain
7 Department of Fundamental Care and Medical-Surgical Nursing, Universitat de Barcelona, 08007 Barcelona, Spain
8 Departament de Biomedicina, Universitat de Barcelona, 08007 Barcelona, Spain
9 Institució Catalana de Recerca i Estudis Avançats (ICREA), 08010 Barcelona, Spain
* Correspondence: victor.puntes@vhir.org

Abstract: Nanoparticle (NP) pharmacokinetics significantly differ from traditional small molecule principles. From this emerges the need to create new tools and concepts to harness their full potential and avoid unnecessary risks. Nanoparticle pharmacokinetics strongly depend on size, shape, surface functionalisation, and aggregation state, influencing their biodistribution, accumulation, transformations, and excretion profile, and hence their efficacy and safety. Today, while NP biodistribution and nanoceria biodistribution have been studied often at short times, their long-term accumulation and excretion have rarely been studied. In this work, 3 nm nanoceria at 5.7 mg/kg of body weight was intravenously administrated in a single dose to healthy mice. Biodistribution was measured in the liver, spleen, kidney, lung, brain, lymph nodes, ovary, bone marrow, urine, and faeces at different time points (1, 9, 30, and 100 days). Biodistribution and urinary and faecal excretion were also studied in rats placed in metabolic cages at shorter times. The similarity of results of different NPs in different models is shown as the heterogeneous nanoceria distribution in organs. After the expectable accumulation in the liver and spleen, the concentration of cerium decays exponentially, accounting for about a 50% excretion of cerium from the body in 100 days. Cerium ions, coming from NP dissolution, are most likely excreted via the urinary tract, and ceria nanoparticles accumulated in the liver are most likely excreted via the hepatobiliary route. In addition, nanoceria looks safe and does not damage the target organs. No weight loss or apathy was observed during the course of the experiments.

Keywords: nanoparticle biodistribution; nanopharmacokinetics; nanoceria; NP long-term accumulation; NP excretion; NP dissolution; nanosafety

check for updates

Citation: Ernst, L.M.; Mondragón, L.; Ramis, J.; Gustà, M.F.; Yudina, T.; Casals, E.; Bastús, N.G.; Fernández-Varo, G.; Casals, G.; Jiménez, W.; et al. Exploring the Long-Term Tissue Accumulation and Excretion of 3 nm Cerium Oxide Nanoparticles after Single Dose Administration. *Antioxidants* **2023**, *12*, 765. https://doi.org/10.3390/antiox12030765

Academic Editor: Peter Brenneisen

Received: 27 February 2023
Revised: 14 March 2023
Accepted: 16 March 2023
Published: 21 March 2023

Copyright: © 2023 by the authors. Licensee MDPI, Basel, Switzerland. This article is an open access article distributed under the terms and conditions of the Creative Commons Attribution (CC BY) license (https://creativecommons.org/licenses/by/4.0/).

1. Introduction

In the past years, immunometabolism has raised a genuine interest in the scientific community as a tool to control the immune system responses [1]. The immunomodulation

concept emerges from noticing that immune cells have different energetic demands depending on the required biological response. In general terms, the faster the energy is required, at higher power, the more free radicals (reactive oxygen species, ROS) are generated, and ATP production is enhanced, as it happens during inflammation [2]. This increased ROS production, enhances the chemical potential of cells to sustain their defensive response and consequent energy consumption in biosynthesis (cytokines and chemokines) and phagocytosis, led by fast and inefficient oxidation of glucose in the cytoplasm (anaerobic glycolysis) [2]. However, this increased ROS production is toxic, causing oxidative stress that results in the oxidation of proteins, lipids, DNA, and ultimately cell death [3]. Therefore, the modulation of immune cell metabolism is emerging as a tool to regulate deranged inflammatory immune responses. This can be achieved either by using antioxidants to control ROS and therefore cellular REDOX potential [4], or by cutting out fuel supply, as in ketogenic diets [5,6] or the use of metformin [7].

Indeed, the need to protect the organism from excess ROS has driven the interest in antioxidants for decades. In 1970, Linus Pauling published a book titled: "Vitamin C and the common cold" [8], describing the protective and anti-inflammatory properties of natural antioxidants. Since oxidative stress is intrinsic when homeostasis is broken, which occurs during disease, numerous epidemiological and mechanistic studies have shown the remarkable benefits of antioxidants in a wide variety of fields, such as autoimmune diseases [9], chronic inflammation [10], neurodegeneration [11], cancer [12], and infections [13]. Unfortunately, the benefits of antioxidants have not been harnessed yet for clinical use, despite the thorough clinical trials since then, which has been attributed to the poor drug-likeness of current available substances (instability, unspecific reactivity, and low bioavailability at the site of action), and consequently their poor pharmacokinetics (PK) profiles [14,15].

In this context, nanotechnology has shown us how mineral antioxidants, such as metal oxide nanoparticles, especially cerium oxide (CeO_2) nanoparticles (NPs), and nanoceria are safe and powerful anti-inflammatory substances [16–18] and seem to overcome these previous antioxidant PK limitations. Nanoceria is well known for its ability to scavenge ROS in biological systems, acting as an effective antioxidant and consequently anti-inflammatory substance [19]. It has been demonstrated to be highly soluble in biological media, present high bioavailability, disperse well in tissues, have therapeutic action at 50 to 250 micrograms/gram, and more importantly, while its chemical specificity is very low, scavenging different types of ROS (and reactive nitrogen species and reactive sulphur species) only in the case when an abnormally high (pathological) concentration of free radicals nanoceria is active, acting as a REDOX buffer [2]. Finally, as an inorganic catalyst, it can be used many times without being consumed, which allows it to work rather permanently at very low doses, offering chronic protection with a single administration. Accordingly, nanoceria efficacy has successfully been tested in a wide variety of disease models, mainly in inflammatory-related pathologies such as cardiac diseases [20], brain ischemia [21–23], diabetes [24], retinal dysfunction [25,26], liver inflammation [27,28], cancer [29], anaphylactic shock [30–32], acute [33] and chronic glaucoma [34], radiation-induced injuries [35,36], and neurodegeneration [37,38]. This ability of nanoceria to reduce ROS is crucial, because it avoids the direct damage derived from free radicals. In addition, it also has an important immunomodulatory effect, advocating for its use in medicine via its pharmaceutical development [39].

Despite these appealing therapeutic observations, there is still a fundamental open question: nanoceria's end of life inside the body and in the environment. To some extent, inorganic NPs are supposed to be non-biodegradable and known to accumulate in different tissues and remain there for a long time. It is well known that slow and inefficient clearance rates are displayed by inorganic matter, leading to long-term toxicity concerns due to accumulation. An example is the case of the so-called frustrated phagocytosis where inorganic matter induces chronic inflammation preluding cancer, as in the cases of silicosis or asbestosis, where hundreds of micrometre inorganic particles cause chronic granulomatosis [40].

Even if the inorganic matter causing these diseases is orders of magnitude larger than the currently employed NPs, this raises concerns about NP accumulation, aggregation, and excretion from the organism in extended periods.

Nanoparticle fate belongs to NP PK, the branch of pharmacology that studies drug administration, distribution, metabolization, and excretion. Nanoparticle PK significantly differs from the traditional small molecule PK, and thus emerges the need to create new tools and concepts to assess NP evolution and fate inside the body. Nanoparticle PK strongly depends on size, shape, surface state, and aggregation state. All these features influence nanoceria biodistribution, degradation, and excretion profile, and hence their therapeutic potential and safety.

Today, there are plenty of short-term NP biodistribution studies in the literature, but there is a lack of fate and excretion studies. Excretion is paramount in the development of a medicine. The primary natural excretion pathways from the body are via the liver to faeces, and kidneys to urine. Regarding kidney clearance, several studies show how very small NPs, smaller than 6 nm (in hydrodynamic diameter), can be readily cleared from the body via the urinary tract [41,42]. Note that glomerular filtration not only depends on size, but it also depends on molecule charge [43]. Kobayashi and co-workers [44] showed that glomerular filtration depended on whether the charge was positive or negative, showing enhanced filtration for cationic molecules. Other researchers reported similar observations on NP charge and size effects [42]. Clearance from the liver is more complex, leading to a slower elimination rate than urine excretion. This slow clearance rate is mediated by the hepatobiliary route. The clearance of NPs from the blood into the liver, and from the liver into faeces has been well described in the studies of Pr. Warren Chan [45,46].

In general, as expected, administrated nanoceria ended up accumulating mainly in the liver and spleen (around 90% of the injected dose) with smaller fractions accumulating in the kidneys and lungs, while the hepatobiliary route was the more often proposed excretion route [46]. It is important to understand that when administered, NPs must overcome different biological barriers before reaching their final destination. In short, the first natural barrier that NPs need to cross is the biological fluids, such as blood or lymph, sweat or tear, and the corresponding extracellular matrix, consisting of macromolecules (protein, vitamins), biological molecules (as saccharides) and minerals, that change in different tissues and compartments, and health status [47], which may promote NP aggregation and/or corrosion. The second natural barrier the NPs will encounter, in contrast to small molecules, is the immune system, which evolved to recognize molecular patterns from foreign substances and commensal organisms [48], labelling them with opsonins, and enhancing their uptake by phagocytic cells, such as splenic macrophages, or Kupffer cells in the liver. If NPs are recognized as foreign substances when entering the body, the immune response will reduce their plasma half-life, decreasing their efficiency in targeting different organs. As a third barrier, the microstructure of blood vessels and tissue also strongly determine NP biodistribution. Generally, NPs with hydrodynamic radii smaller than 6 nm are rapidly excreted through the urine while NPs with hydrodynamic radii between 6 and 200 nm are readily filtered in the liver. Larger ones are directly managed by the immune system in blood/lymph, and also tend to accumulate in the liver or other organs such as the lung or spleen [49].

In further detail, to study NP biodistribution, accumulation and excretion, the processes affecting NPs dispersion in the physiological medium have to be considered first [50]: aggregation, protein corona formation, and corrosion. NP aggregation and corrosion will affect NP quality, safety, and efficacy. First, blood and physiological media are highly saline. Hence, if NPs are stabilized by electrostatic repulsion, they will rapidly aggregate as soon as they enter in the highly electrolytic media. As a result, large aggregates (hundreds of nm) form and sediment, and they are not distributed further. These cases are not addressed in this work. Second, proteins in the media will interact with the NP surface. In this case, protein concentration is critical as high protein concentrations will lead to steric stabilization of NPs, while low concentrations will lead to agglomeration and aggregation

of NPs and proteins [50]. Finally, NPs can also undergo chemical transformations, as in the common case of corrosion (reactive chemical dissolution), leading to NP dissolution and the corresponding release of NP constituents. These three events usually coexist, and their rates depend on both NP characteristics and medium composition [51].

Regarding the encounter of NPs with the immune system, it is important to note that the immune system can detect molecular and cellular structures with a spatial resolution of a few nm, which allows for detecting molecular patterns expressed in a great variety of pathogens, including viral and bacterial proteins, and bacterial nucleic acid sequences [52], ranging from a few nm to a few hundred nm, as colloidal NPs, which suggests an intense interaction between both [53]. Thus, NPs can be recognized or pass undetected by the immune system. Once detected, they can be tolerated or induce defensive (pro-inflammatory) or anti-inflammatory responses. The different immune responses induced by NPs have been recently reviewed [53]. Basically, poor solubility, large sizes, and cationic charges at the surface or hydrophobic moieties are rather immunogenic, while small, negatively charged, and highly soluble NPs are relatively undetected and tolerated. In general, when needed, surface PEGylation helps to escape from immune detection [54,55]. Ideally, NPs should be designed to evade the immune system, allowing for penetration into the different body tissues unless the NP target is the immune system [53].

Finally, when considering intravenous (IV) administration, which is likely the most employed nanoceria administration route, it is essential to note that the main blood vessels and capillaries in the body have a continuous lining of endothelial cells with pores of 6 nm. In such conditions, small drug molecules, the vast majority of drugs, can diffuse in and out from the blood vessels into the lymph and vice versa, while the passive transport of large objects, such as proteins and NPs, through these pores, is negligible. Besides, fenestrated capillaries found in the intestine and endocrine and exocrine glands present 50–60 nm pores, while discontinuous capillaries, such as those found in the liver, spleen, and bone marrow, display pores ranging from 100 to 1000 nm, which are where NPs are commonly found [56]. Tight junctions deserve special attention, including the blood-brain barrier (BBB), placenta, retinal, and testis barriers, where pores smaller than 1 nm (400 Da) have been reported, preventing NP passive accumulation [57]. It is worth noting here that blood vessel and tissue permeability is altered during the course of diseases, facilitating the passive accumulation of NPs in the disease areas. This altered permeability can increase the concentration of NPs in those tissues by one order of magnitude [58]. This is the case of the enhanced permeability and retention (EPR) effect in solid tumours [59], where defective angiogenesis results in defective blood vessels with large endothelial pores (a few hundred nanometres) nurturing the tumour, which together with the absence of a functional lymphatic drain facilitates NP accumulation in the tumour [60]. Similarly, blood vessels and tissue porosity increase during inflammation, allowing NPs to accumulate in the inflamed area [37]. It is also important to note that functionalization with directing vectors may significantly change the nanoceria distribution, apparently more than size and aggregation state. Thus, nanoceria conjugated to fluorescein isothiocyanate [61] or edaravone [62] has been observed to cross the BBB. Here it is important to note that during neuroinflammation, caused by many brain diseases, together with growing tumours or traumatic brain injury, will allow NPs to permeate the BBB, allowing for the translocation of NPs, as in the case of Amyotrophic Lateral Sclerosis [63].

This study aims to explore 3 nm nanoceria long-term accumulation and excretion in healthy mice after a single IV administration and compare it with the related experiments. We also studied shorter-term accumulation and renal and faecal excretion in model rats, IV, and orally administered with nanoceria.

2. Materials and Methods

2.1. Model of the Effects of Protein Corona on Nanoceria Internalization and Intracellular Trafficking

The results reported by Mazzolini J. et al. [64] led them to speculate a model in which, in the presence of serum in the environment, the protein corona that formed around the nanoceria contains the proteins involved in cell adhesion and endocytic pathways. Among these adsorbed proteins, transferrin promotes nanoceria internalization through transferrin receptor clathrin-mediated endocytosis, followed by their storage in vesicles and the endosomal compartment. Under these conditions, cell division, viability, and metabolism are preserved, whereas in serum-free media, the absence of a protein corona around nanoceria induces plasma membrane disruption and metabolism changes.

2.2. CeO_2NPs Adsorption by Human Hepatocyte Cancer Cells

In a recent study, we reported that HepG2 cells, a human-derived cell cancer line, can internalize nanoceria [29]. In vitro experiments confirmed the uptake and retention of nanoceria by human hepatocyte cancer cells, mostly in endosome-like bodies. Human hepatocytes were exposed to CeO_2NPs (10 μg/mL) for 24 h and subjected to TEM analysis. NPs were strongly attached to the outer leaflet of the plasmatic membrane, free in the cytoplasm, and mostly inside numerous endosome-like bodies of diverse morphology.

2.3. Nanoceria Synthesis

Nanoceria was synthesized using a wet chemistry method based on the basic precipitation of cerium (III) nitrate hexahydrate ($Ce(NO_3)_3 \bullet 6\ H_2O$) in the presence of sodium citrate (SC). In detail, a TAMAOH solution (50 mL, 81 mM) was added to a 100 mL solution containing $Ce(NO_3)_3 \bullet 6\ H_2O$ (30 mM) and SC (60 mM). The final concentration was: 27 mM TMAOH, 10 mM $Ce(NO_3)_3 \bullet 6\ H_2O$, and 20 mM SC. The reaction mixture was left under stirring overnight at room temperature. Later, the mixture was transferred to a three-necked round-bottomed flask (250 mL) and left under refluxing at 100 °C for 4 h. The resulting mixture was a stable, well-dispersed solution of 3 nm nanoceria at a concentration of 1.72 mg/mL CeO_2.

Before use, the NPs solution was purified with 3 kDa centrifugal filter units (Amicon-Ultra-15 3K, Merck, Germany), and re-suspended in SC 2.2 mM.

2.4. Nanoceria Conjugation

MSA Conjugation

To prevent aggregation of the NPs in the bloodstream, and to avoid hypotonic shock, nanoceria was conjugated with albumin from mouse serum (MSA, Merck, Germany) in phosphate buffer (PB), 10 mM at 4 °C for 24 h before injection.

2.5. Nanoceria Characterization

2.5.1. Bacterial Endotoxin (LAL) Test

Both synthesis and purification of NPs were performed under sterile conditions and with non-pyrogenic material. To ensure safe NPs for animal administration, nanoceria was tested for LPS levels at Echevarne analysis laboratory (Barcelona, Spain).

2.5.2. Transmission Electron Microscopy (TEM)

Nanoceria was visualized using HRES-TEM (Tecnai F20 S/TEM). Ten μL of the as-synthesized solutions were drop-casted onto a carbon coated 200 mesh copper grid and left to dry for at least 24 h in the air at room temperature. The samples' average size and distribution were measured using Image J Analysis software by counting at least 2000 particles.

2.5.3. UV-Visible Spectra

UV-vis spectra were acquired with a Cary 60 spectrophotometer (Agilent Technologies, Santa Clara, CA, USA) in the 250–800 nm range, using 1.5 mL plastic cuvettes.

2.5.4. Dynamic Light Scattering (DLS) and ζ-Potential

Malvern ZetaSizer Nano ZS (Malvern instruments, Malvern, UK) operating at a light source wavelength of 532 nm and fixed scattering angle of 173° was used to measure NPs hydrodynamic size and ζ-Potential value. Measurements were conducted in 1 cm path cell and 25 °C. Three independent measures were performed.

2.5.5. X-ray Diffraction

XRD diffraction experiments were performed on a Malvern Panalytical Xpert Pro diffractometer, with Cu-Kα X-rays of wavelength (λ) = 1.5406 Å. The patterns were collected in the angle region between 20° and 95° (2θ).

2.6. In Vivo Study Design

All experimental procedures were conducted in strict accordance with the European (Directive 2010/63/UE) and Spanish laws and regulations (Real Decreto 53/2013; Generalitat de Catalunya Decret 214/97) on the protection of animals used for experimental and other scientific purposes, approved by the Vall d'Hebron Research Institute (VHIR) Ethical Experimentation Committee, and further validated by the authorized body of Generalitat de Catalunya (ref. n. 11357).

The experimental procedures conducted in Wistar rats were approved and performed according to the criteria of the Investigation and Ethics Committee of the Hospital Clínic Universitari (Barcelona, Spain), and validated by the authorized body of Generalitat de Catalunya (ref. n. 7907).

Animals received humane care according to the criteria outlined in the "Guide for the Care and Use of Laboratory Animals".

2.6.1. Long-Term Biodistribution in Healthy Mice

For long-term biodistribution study, 30 adult female BALB/C mice (Charles River Laboratories), of 25 g of body weight and 7 months-old at the time of NP administration, were housed 3 to 4 per cage with ad libitum access to food and water during a 12 h light/dark cycle. Mice were randomly divided into four groups. On day 0, four groups of six mice were IV (retro-orbital injection) administered in the ophthalmic venous sinus, under general anaesthesia using Isoflurane (5% for the induction phase and 2% for the maintenance phase), with a single dose of 5.7 mg/kg of body weight (bw) nanoceria conjugated with MSA in PB 10 mM, corresponding to the maximal volume that can be administered IV. Animals were sacrificed at different times after nanoceria injection: 1, 9, 30, and 100 days. The liver, spleen, kidneys, lung, brain, lymph nodes, ovaries, bone marrow, faecal content, and urine (collected in tared Eppendorfs) were collected and stored at −20 °C before elemental Cerium analysis.

2.6.2. Nanoceria Excretion in CCl_4-Treated Rats

The study was performed in male Wistar rats (Charles-River, Saint Aubin les Elseuf, France) with hepatic fibrosis induced by repetitive CCl_4 inhalation, as previously described [65]. The rats were fed ad libitum with standard chow and water containing phenobarbital (0.3 g L^{-1}) as the drinking fluid. The animals were exposed to CCl_4 vapor atmosphere twice a week for 16 weeks. Nanoceria (0.1 mg/kg bw) was injected twice a week for two consecutive weeks, starting at the seventh week after beginning CCl_4 administration. Nanoceria was dispersed in saline solution containing TMAOH ammonium salts (0.8 mM) and was administered as a bolus (500 µL) through the tail vein. After the last dose of nanoceria, the animals were placed in metabolic cages and 24 h urine and faeces measurements were performed at 3, 21, 42, and 56 days after nanoceria administration.

2.6.3. Confocal Imaging of Nanoparticles in Mice Liver

Adult female BALB/cAnNRj mice (Janvier) were 19–22 g and 6–7 weeks old at the time of NP administration. They were housed three to four per cage with ad libitum access to food and water during a 12 h light/dark cycle. Nanoparticles for IV injections were conjugated with MSA in PB buffer 10 mM at 4 °C, 24 h before injection in order to prevent aggregation in the bloodstream.

Experimental procedure—Optical Microscopy of Tissue sections (see Supplementary Materials, SM).

2.6.4. Organ Distribution of Fe_3O_4NPs in CCl_4-Treated Rats

Please see the details of procedure in Supplementary Materials (SM).

2.6.5. Organ Biodistribution after Oral Administration in Healthy Rats

In this study, CeO_2NP mixed with polyethylene glycol were administered to healthy Wistar rats daily by intragastric gavage administration (3 mg/mL; 10 mg CeO_2/Kg of bw) for 14 consecutive days (n = 3). Nanoceria was administered mixed with PEG as a standard excipient for oral administration, and thus prevented strong nanoceria aggregation once SC was protonated in the acidic pH of the stomach. The cerium concentration was measured by ICP-MS, and the major organs and serum were collected 72 h after the last administration.

2.7. Cerium Content Determination

Digestions were carried out in Ethos™ Easy (Millestone, Sorisole, Italy), an advanced microwave digestion system. First, samples were defrosted and mixed in the digestion solution containing one part of concentrated nitric acid and two parts of water. Subsequently, the digestions were performed under a 200 °C cycle for 1.5 h. Thereafter, elemental cerium in tissue were analysed using ICP-MS (7900 ICPMS, Agilent, Santa Clara, CA, USA), in Chemical analysis service (UAB, Barcelona, Spain).

3. Results

We have been working with nanoceria in disease models for over 15 years. According to our experience and the current literature, nanoceria accumulates largely (close to 85–95% of the injected dose) in the liver and spleen. Interestingly, this occurs both in healthy and liver-diseased models, as in hepatocellular carcinoma [29] or liver steatosis [66]. Indeed, liver accumulation of NPs has been extensively described in the scientific literature. An extended work can be found in Ref. [45], where the clearance of the NPs from blood to the liver is reported. In all those cases, the administered nanoceria was given at different doses and administration schedules, and although the NPs derived from similar synthesis, they had different formulations (mainly surface state and aggregation state) and ended up in similar places. Here, an important point to keep in mind is that biodistribution inside the organs is heterogeneous. It often seems assumed that NPs are homogeneously distributed and only a fraction of the organs are employed for elemental analysis. However, organs are complex and host different tissues and cell types, and therefore biodistribution inside the organs is heterogeneous. In model cirrhotic rats, injected nanoceria (5 nm aggregated in 30 nm clusters as described in Ref. [66]), was found heterogeneously distributed in the liver, as shown in Figure 1A, indicating that organs have to be homogenized before a fraction is digested for elemental analysis. There is a quite interesting study [45] where the blood clearance mechanisms were examined in relation to the flow dynamic and cellular phenotype in addition to the vessel's microstructure. Here, the slower blood flow within the organs enhances the possibility of NP retention, which can help predict the accumulation regions inside an organ.

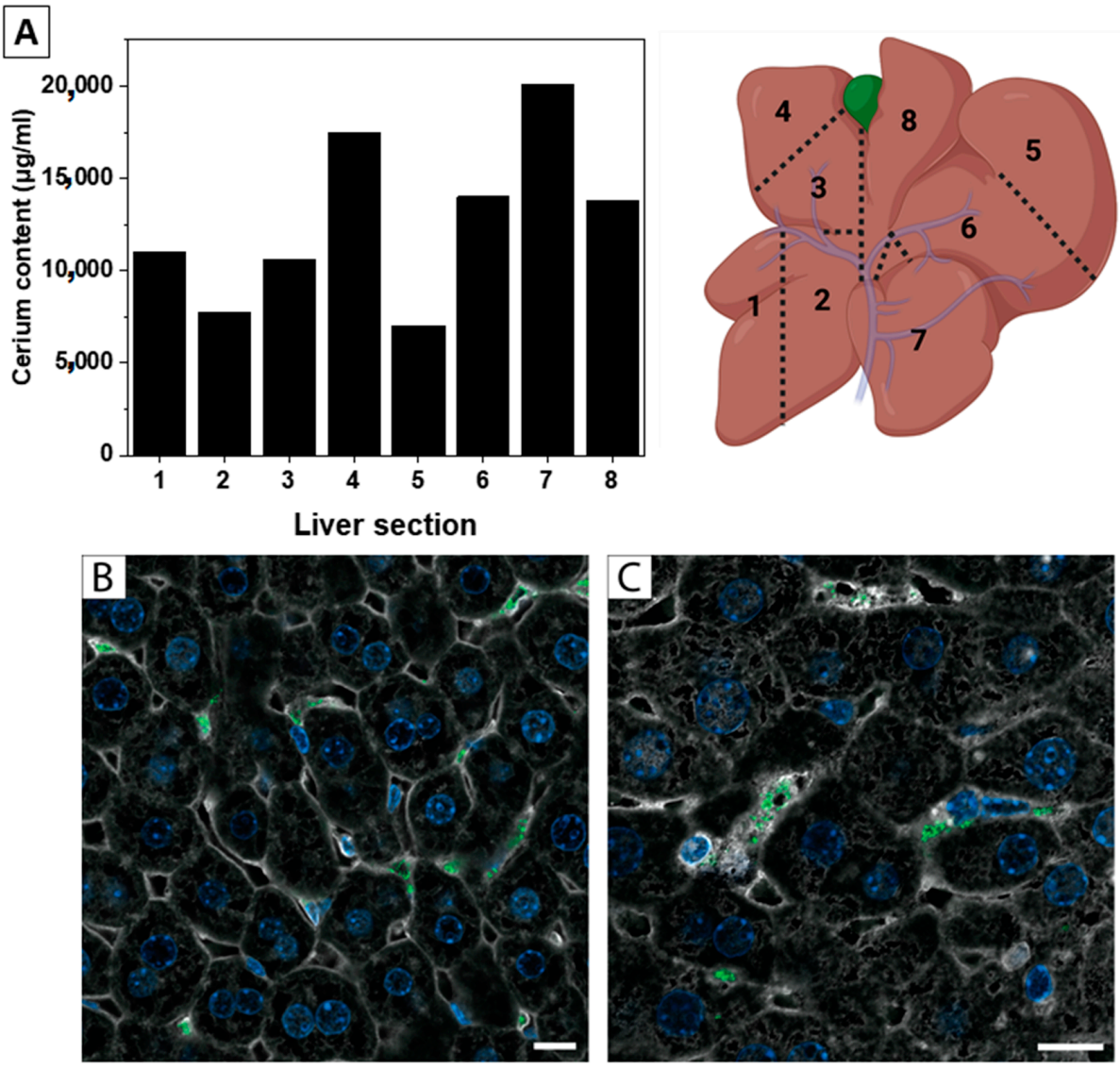


Figure 1. Hererogenicity in organ distribution. (**A**) Liver biodistibution of nanoceria 24 h after IV administration, and liver schema of the digested tissue sections. Liver was divided into 8 parts (schema), and Cerium content of each section is represented in the graph. (**B**,**C**) Confocal images of AuNPs in reflectance mode of a liver thin cut after IV administration of NPs to healthy mice at (**B**) 40× magnification and (**C**) 60× magnification. Actin (white), Hoechst (blue), and NPs (green). Scale bar = 10 µm.

Besides, the NPs can be processed by different types of cells. A clear example is the processing of NPs in the liver either by hepatocytes, described as the main responsible cells during hepatic filtration [67], or Kupffer cells, the resident macrophages in the liver, responsible for the elimination of apoptotic bodies, protein aggregates, and foreign matter [46]. However, we once observed selective capture of NPs by hepatic stellate cells in the mice liver after a single IV injection (Figure 1B). In this work, we employed 50 nm AuNPs so they could be observed in reflectance mode in the confocal microscope without the need for labels at the NP surface, which could affect their biodistribution. This is not expected to be a general trend or applicable to nanoceria, but this selective NP uptake illustrates a most likely widespread event.

Next, the fate of very small 3 nm non-aggregated nanoceria IV administered in healthy mice was assessed. Size is one of the parameters that has been the focus of understanding NPs biodistribution, accumulation, and clearance. As a first observation, it has been postulated that the bigger the NPs are, the narrower their organ distributions [49]. Size may also have a substantial impact on NP integrity. Cerium ions are made insoluble by oxidation at basic pH, and once nanoceria is dispersed at neutral pH, in the REDOX conditions of living systems, its thermodynamic fate is to reduce back and dissolve in the form of Ce^{3+} ions (see the Pourbaix diagram in Suplemmentary Materials [68]. This generally does not happen due to a remarkably high activation energy for cerium oxide crystal dissolution [69]. However, this activation energy decreases with size, ultra-small NPs being prone to dissolution, facilitating biodegradation. Indeed, the curvature radii of NPs with a diameter 30 nm or below become progressively unstable [70]. Therefore, the smaller the NP, the faster its degradation would be. Note that the estimated minimal thermodynamically stable nanoceria crystal size is about 1.9 nm in diameter [69], which leaves 3 nm NPs on the verge of dissolution. Indeed, rapid nanoceria dissolution has been reported inside late endosomes and endolysosomes [71], and at acidic pH during colorimetric detection of analytes [72].

Nanoceria was synthesized in sterile conditions by basic precipitation of cerium nitrate using a classical hydrothermal approach. Sodium citrate (SC) was used as a complexing and stabilizing agent, and TMAOH was used as a base. A stable colloidal solution of ~3 nm non-aggregated naked surface NPs was obtained [25] and described in Figure 2. Note that a precise description of NP features is critical in controlling the interactions at the nano–bio interface [73]. Morphology and size distribution analysed by high-angle annular dark-field scanning transmission microscopy (HAADF-STEM) and High-Resolution transmission electron microscopy (HRES-TEM) (Figure 2A) indicates the formation of non-aggregated 2.5 ± 0.5 nm quasi-spherical nanoceria particles of high uniformity and narrow size distribution (Figure 2A, insert). The X-ray diffraction patterns of the NPs confirm that the sample displays a pure fluorite single-phase (face-cantered cubic, fcc) crystal structure (Figure 2D). The broadness of the diffraction peaks indicates an ultra-small crystal size, where the Scherrer equation confirms the NP size of ~3 nm. The UV-visible spectrum of nanoceria shows a distinct absorption band at 283 nm with a characteristic bandgap of 3.11 eV (the bulk is 3.19 eV) (Figure 2B and inset). This reduced bandgap manifests the oxygen vacancies that nanoceria accumulates at its surface as it decreases in size. These oxygen vacancies determine nanoceria catalytic behaviour (oxygen vacancies are active sites) and nanocrystal stability (the more oxygen vacancies, the closer to dissolution). The zeta potential indicates that after purification and re-dispersion of nanoceria in 2.2 mM SC, particles are negatively charged (-38.9 ± 16.7 mV, at pH = 9.23 and a conductivity of 0.33 mS cm^{-1}) (data not shown). Hydrodynamic diameter and stability in simulated physiological media (DMEM, 10% FBS, pH 7.4) were measured by dynamic light scattering (DLS) and shown in Figure 2C, where as-synthesized nanoceria shows monomodal distribution peaking at 3.96 ± 0.89 nm (PDI = 0.35). As expected, the results show nanoceria aggregation within 24 h in DMEM due to surface charge screening because of the high ionic strength of the media. Nanoceria conjugation with albumin prevented NP aggregation, and a slightly increased hydrodynamic diameter, peaking at 6.28 ± 1.6 nm (PDI = 0.47), was observed. Interactions of nanoceria with proteins in physiological media were previously well described [74]. Because of that, we recommend NPs stabilization in the serum before inoculation, murine or rat serum in case of mice and rats, respectively, normally at a final 1 to 10 mg/mL protein concentration, which also prevents rapid renal clearance of NPs < 6 nm.

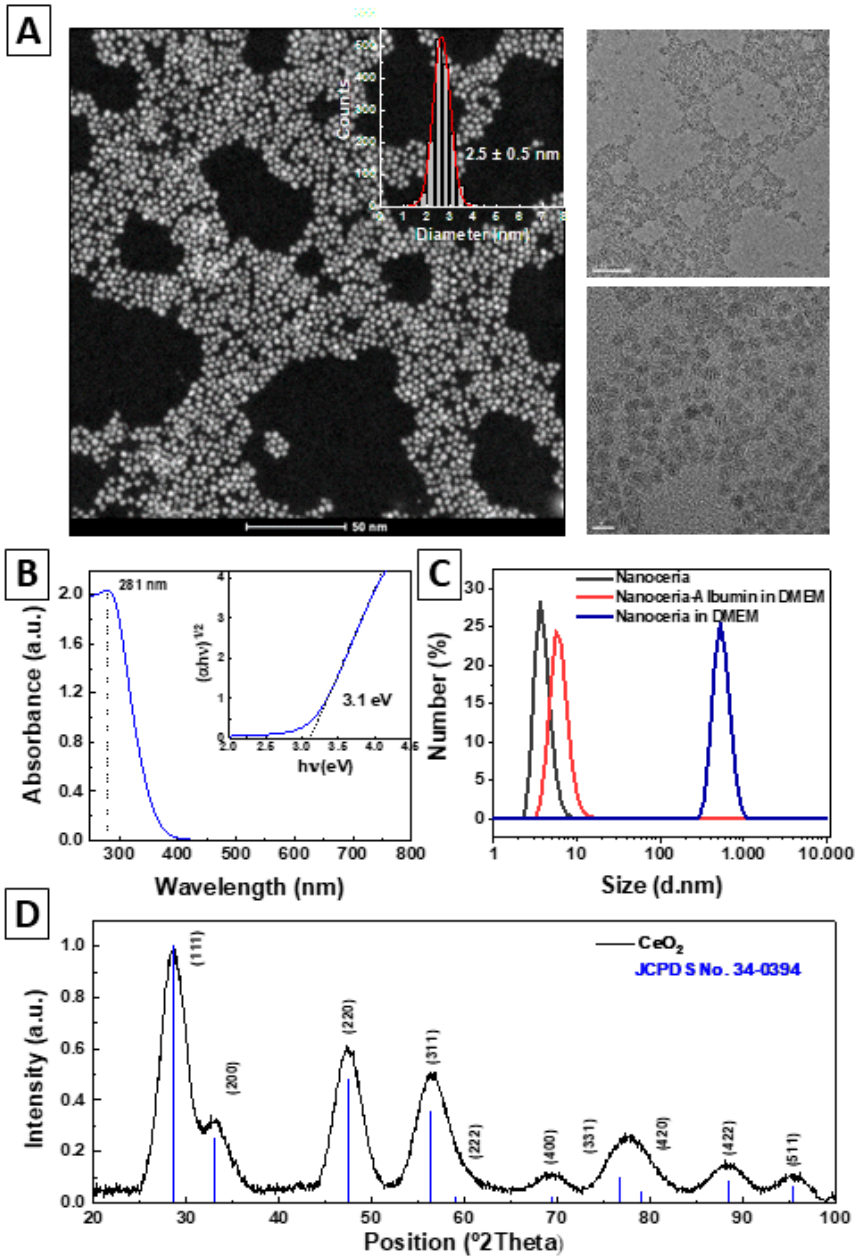


Figure 2. Synthesis and characterization of nanoceria. (**A**) HAADF-STEM images (left) and size distribution (insert), and HRES-TEM images (right). Scale bars are 50, 50, and 5 nm, respectively. (**B**) UV-visible spectrum of the nanoceria and optical bandgap energy determined by Tauc equation (insert). (**C**) The hydrodynamic diameter profile measured by dynamic light scattering of nanoceria (black), nanoceria-albumin in DMEM (red), and nanoceria in DMEM (blue). (**D**) X-ray diffraction pattern of the as-synthesized nanoceria and JCPDS No. 34-0394 standards.

In order to determine the biodistribution of the nanoceria, 4 groups of 5 mice each were IV administered with 5.7 mg/kg of body weight (bw) single dose of nanoceria and they were euthanized at different times after injection: 1, 9, 30, and 100 days. Although the most employed vein for administration is the lateral tail vein, we here chose retro-orbital injection in the ophthalmic venous sinus in the back of the eye socket. The reason is that administration in the secondary vein network improves the biocompatibility and prevents adverse infusion reactions. Thereafter, ICP-MS was used to determine cerium concentrations in the liver, spleen, kidney, lung, brain, lymph nodes, ovaries, bone marrow, urine, and faeces. During the experiments, all animals showed a healthy weight and

appearance, and normal activity without lethargy or apathy after NP administration (see Figure S1).

As expected, the results showed the main accumulation of nanoceria in the liver, and spleen (82%, and 5% of the injected dose (ID), respectively) (Figure 2, Table S1). Cerium was not detected in the brain and showed extremely low levels in the other organs, although the presence could be observed in the kidneys, lungs, lymph nodes, ovaries, and bone marrow. With time, Ce concentration in the different organs progressively diminished. The most significant elimination was observed in the liver with a reduction from 82% to 40% of ID between day 1 and day 100. The spleen was the second organ with more accumulation, but the clearance rate was slower (see the excretion rates for the different organs in Figure S2). In the kidney, lung, bone marrow, and ovaries there was low accumulation, and slow clearance rates could also be observed. The striking difference between the liver and the rest may indicate that while there exists a ready mechanism for NP excretion in the liver, NP macrophage accumulation in the same liver or other organs leads to much slower excretion. Interestingly, on day 30, cerium concentration increased in the lymph nodes, which may indicate some re-distribution at longer times. This rebound effect is also observed shortly after initial kidney accumulation (W. Jiménez, unpublished observations). Traditionally, the spleen has attracted little attention in pharmacology, because of its minor role in "classical" drug disposition and/or excretion, but this is changing for "new" generation drugs (nanoparticles, recombinant proteins, and monoclonal antibodies) [75]. For example, Demoy et al. demonstrated the pivotal role of spleen marginal zone macrophages in the uptake of polystyrene NPs [76]. We hypothesize then that in our case, a small portion of nanoceria could have been retained in spleen macrophages, which are known to be a slower clearance route, as discussed below.

The results suggest that the main clearance route is hepatobiliary elimination, showing a ≈60% decrease of nanoceria in the liver and ≈50% inside the body 100 days after injection. This hypothesis is also supported by the observed cerium content in the faecal samples. Interestingly, the excretion is enhanced in the first 24 h after injection, also showing the highest peak of cerium content in the collected faeces. With time, cerium is also detected in urine. Due to nanoceria's hydrodynamic diameter (Figure 2C), surface charge, and core density, it is highly improbable that particles undergo renal clearance. Besides, in other studies, no significant urine excretion was reported [77]. For this reason, these traces could be ionic cerium coming from nanoceria dissolution. All in all, this suggests elimination by the two main described mechanisms: (i) renal excretion of cerium ions and (ii) hepatobiliary elimination of CeO_2 NPs.

Despite the reduced number of time points in Figure 3, we fitted the evolution of cerium content inside the liver, or in all measured organs (AMO) vs. time to standard PK models, where small drugs diffuse rather passively through the body following a first-order reaction kinetics that can be described by an exponential decay of cerium concentration with time. We here use one exponential term for one model compartment and two exponential terms for two model compartments (see Suplemmentary Materials) [78,79]. As peripheral distribution is not expected to be significant with NPs, one would expect monomodal exponential decay behaviour. Divergence from this behaviour indicates how the system eliminates cerium in a more active form (Figure 4). In addition, it appears that after the ninth day and ahead, there is a rather monotonous decrease in the cerium concentration, which could be due to a slow excretion of slowly generated cerium ions. On one side, different nanoceria fractions may coexist, and some nanoceria may stay permanently in the body captured inside tissue macrophages or blood monocytes. On the other side, nanoceria should completely dissolve with time in biological conditions regardless of location, accounting for the slow monotonous ceria concentration decrease observed at long times. A physiologically based pharmacokinetic modelling of nanoceria systemic distribution in rats [80] showed similar results, especially the different NP fate depending on admin route, surface, size, and physicochemical properties.

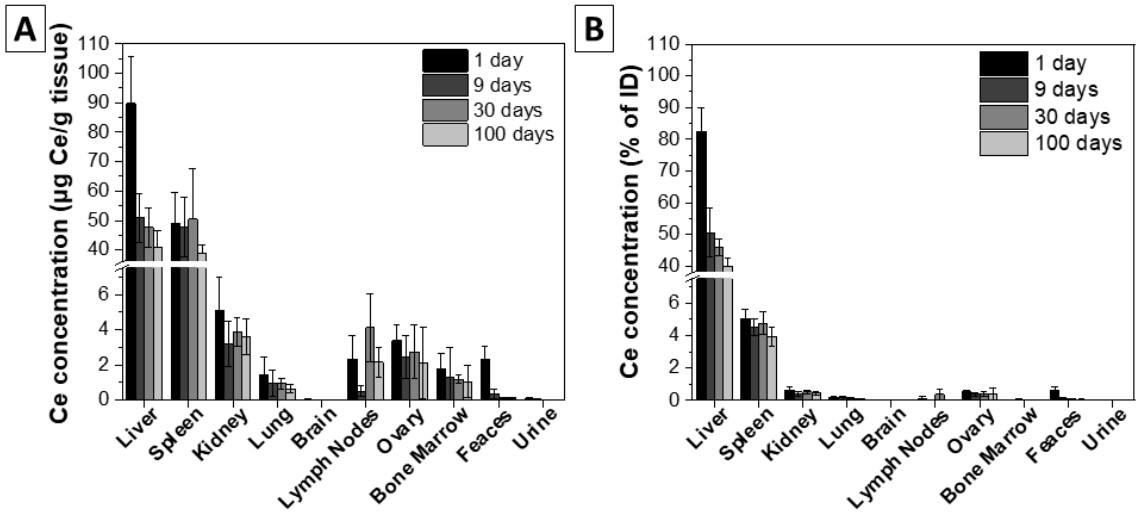


Figure 3. Organ cerium concentration measured by ICP-MS 1, 9, 30, and 100 days after single nanoceria IV administration (5.7 mg/Kg body weight). (**A**) Cerium concentration (µg Ce/g tissue). (**B**) Cerium as a percentage of the injected dose. $n = 5$.

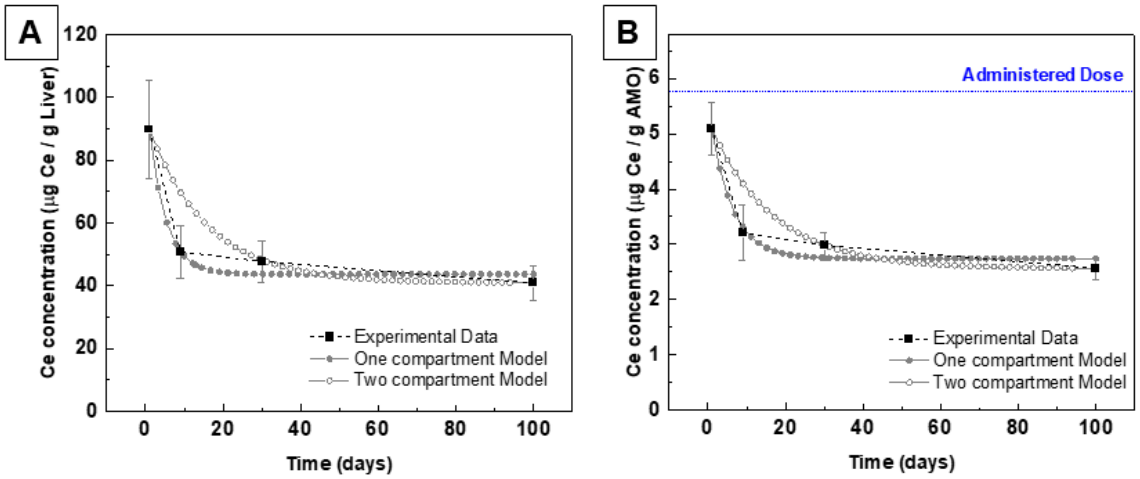


Figure 4. Pharmacokinetics of the CeO_2 NPs after IV post-injection at 1, 9, 30, and 100 days in the liver (**A**) and in all measured organs (AMO) (**B**). Black squares are experimental data, solid grey circles are the one-compartment model fitting, and the hollow grey circles are the two-compartment model fitting. Blue lines are the administered dose.

In another study, to compare if biodistribution was different in healthy or diseased pre-clinical models, we set rats in metabolic cages where cerium was also recovered in the urine and faeces during the experimental timeline. The experimental time in the metabolic cages was reduced for animal welfare. This study used Wistar rats with hepatic fibrosis induced by repetitive CCl_4 inhalation and water containing phenobarbital as the drinking fluid. The animals were injected through the tail vein with nanoceria (0.1 mg/Kg bw) twice a week for two consecutive weeks, starting in the seventh week after the beginning of CCl_4 administration [66]. After the last dose of nanoceria, animals were placed in metabolic cages to measure cerium concentration for 24 h urine and faeces deposition at 3, 21, 42, and 56 days. As shown in Figure 5, while the cerium faecal content decreases exponentially, a rather monotonous cerium concentration was observed in urine, supporting a slow and progressive nanoceria dissolution into cerium ions and its corresponding renal excretion [81]. As commented before, ultra-small ceria, close to the thermodynamic crystal stability limit, at neutral or acidic pH, is prone to dissolution.

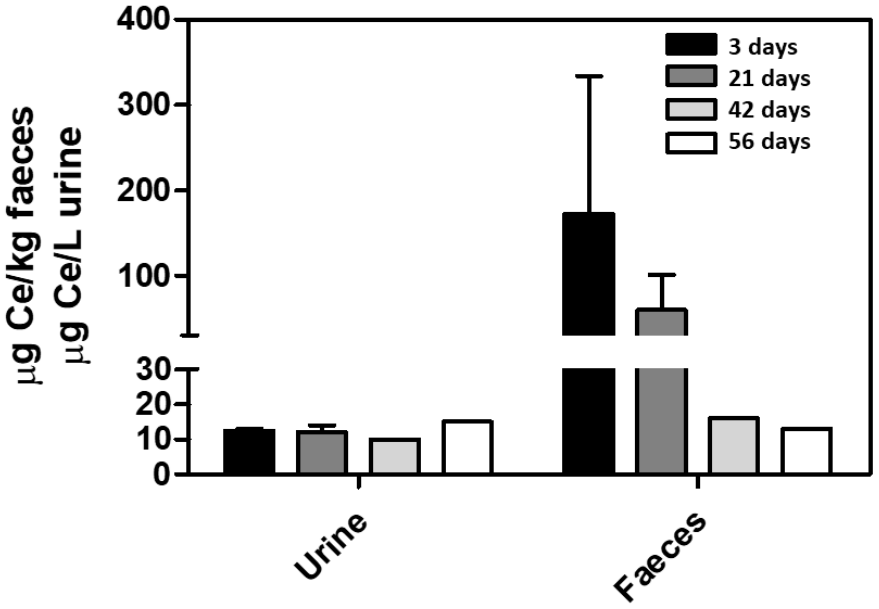


Figure 5. Nanoceria excretion in rats. Cerium concentration was measured by ICP-MS in urine and faeces from CCl_4-treated rats 3, 21, 42, and 56 days after IV nanoceria administration (0.1 mg/Kg bw) twice weekly for two weeks. $n = 3$.

These results are supported by other studies, where after IV injection of NPs with similar size and surface coating they were localized in both Kupffer cells and hepatocytes [82]. Note that both cells have phagocytic capacities, although hepatocytes are directly implicated in the pathway for biliary excretion (NPs found here will be potentially excreted to the bile), whereas Kupffer cells can only eliminate nanoceria via intracellular degradation. Importantly, the Kupffer cells uptake of nanoceria is often accompanied by a mild and transient activation of the immune system [82], calling for a careful examination of the immunogenic properties of designed NPs.

Regarding long-term accumulation of nanoceria, we would like to highlight the studies of Yokel et al. [83,84], where a large dose of 30 nm cubic nanoceria (87 mg/Kg bw) was IV administered to rats, and thereafter an exhaustive accumulation and excretion study was reported on days 1, 7, 30, and 90. In this case, nanoceria was again primarily accumulated in the spleen, liver, and bone marrow. Interestingly, NPs clearance from blood was studied for two weeks and it showed that less than 1% of the nanoceria was removed, and there was a small decrease of particles in any tissue over 90 days. Besides, while we have never observed significant NP in blood a few hours after injection (data not shown), in this study there is a significant cerium blood content after 90 days, which could indicate particle endocytosis by blood cells. This difference among the results is most likely due to the divergence between the physicochemical properties of the used nanoceria (large vs. small size, aggregated vs. non-aggregated, and spherical vs. cubic). Interestingly, although biodistribution and target organs are similar, excretion profiles seem to differ widely. Here, one could hypothesize that NPs that reach the liver and are processed by hepatocytes will be shuttled outside of the body via the hepatobiliary route while NPs that are phagocytosed by resident macrophages, Kupffer cells in the liver, will stay in the macrophages permanently (and if the macrophage dies, another macrophage will engulf the remains) while NPs may slowly dissolve generating Ce^{3+} ions that are excreted via the urinary tract (Figure 6).

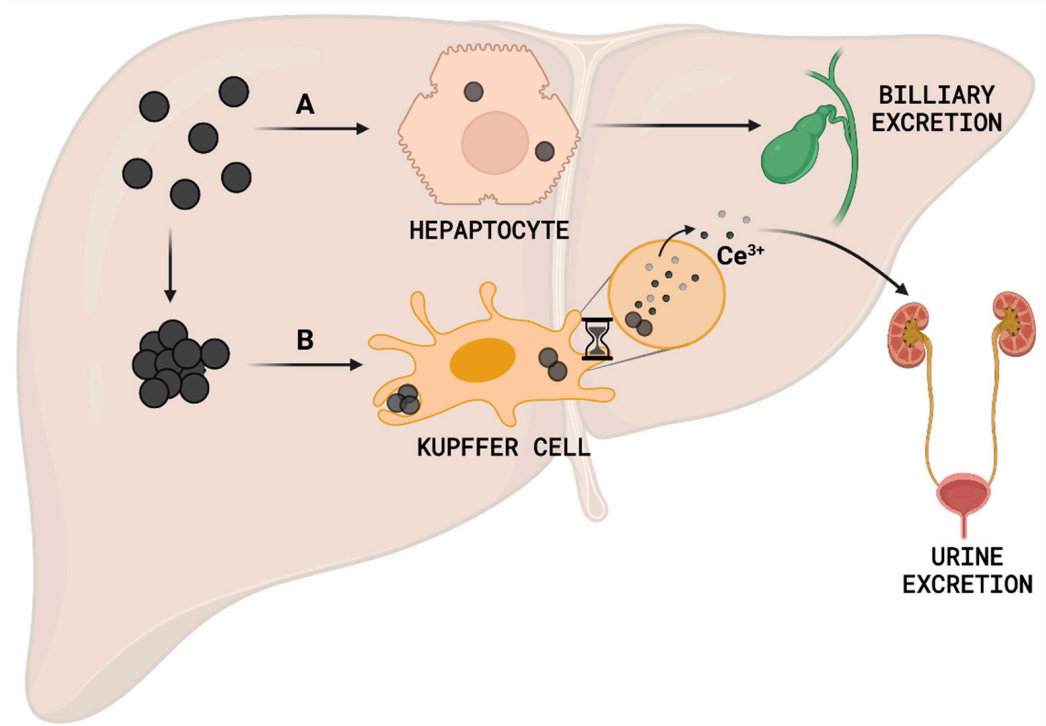


Figure 6. Hypothetical in vivo management of 3 nm nanoceria. After liver accumulation, (**A**) hepatocytes rapidly process non-immunogenic nanoceria to the biliary excretion, (**B**) while nanoceria detected by Kupffer cells will remain inside the cell until it completely dissolves and the produced Ce^{3+} ions are then excreted via the urine.

We also explored oral administration. In this regard, nanoceria dispersed in a polyethene glycol solution were delivered to healthy Wistar rats daily by intragastric administration (10 mg CeO_2/Kg bw) for 14 days ($n = 3$). While most of the cerium was found in faeces, some of it entered the body and was observed in the same organs but at different concentrations than in the case of parenteral administration (Figure 7). Here we realised, that although PEG coating, exposure to rat gastrointestinal fluid promotes the rapid dissolution of the NPs into Ce^{3+} ions, which have been reported to act as Ca^{2+}, and can be absorbed in the body without long-term accumulation and therefore being excreted through the urine [85]. Dispersion of nanoceria in simulated acidic solution (pH 1.7) showed both NP aggregation due to the protonation of the SC at stomach pH and dissolution of the NPs. If we estimate the average time of residence in the stomach to be about two hours, it seems that after a rapid agglomeration, nearly half of the nanoceria dissolves and the rest remains as aggregates (see Figure S3). Gastric capsules for mice and rat models are difficult to acquire and administrate, thus, we are exploring lipid NP encapsulation for stomach crossing. Besides, the dissolution of particles to ions could explain the elimination through kidneys and its prominent accumulation in the lung, where Ce^{3+} ($CeCl_3$) IV administered to mice has been reported to accumulate [81] before renal excretion. There is a case report where a woman accidentally ingested about 1000 mL of a nanoceria-containing solution while working in an industrial setting where nanoceria (aggregated 20–40 nm NPs) was used as a polishing agent [86]. Cerium was detected both in blood and urine. The only symptoms that she presented were transient scattered red petechial, mainly in her face, and decreased plasma coagulation factors. Indeed, anticoagulant properties have been attributed to cerium ions and other rare earth metals [81,87], but not to their nanoscale counterparts, as far as we know.

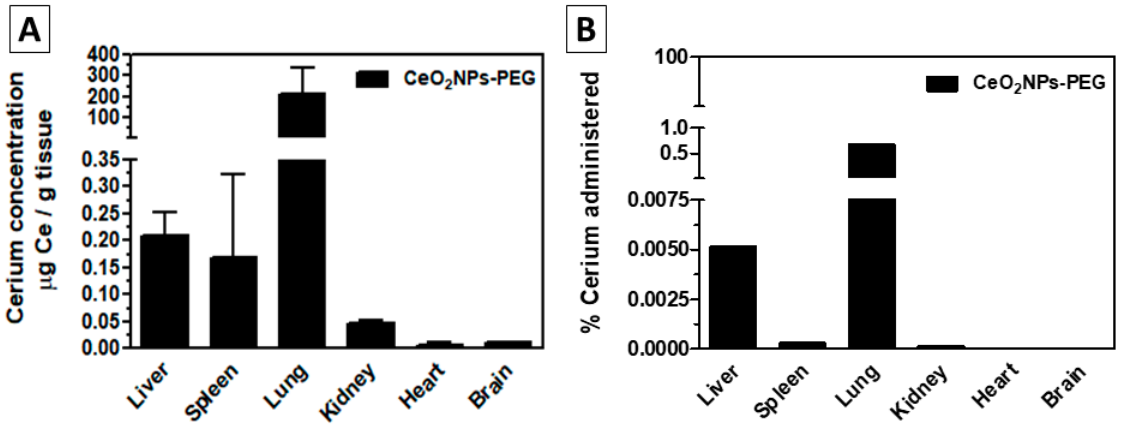


Figure 7. Organ biodistribution after oral administration of CeO_2-PEG coated nanoparticles (CeO_2NPs-PEG) in healthy rats. ICP-MS measured cerium concentration. CeO_2NPs-PEG were delivered daily by intragastric administration (10 mg CeO_2/Kg bw) for 14 days. Major organs and serum were collected 72 h after the last administration. (**A**) Cerium concentration in µg Ce/g tissue. (**B**) Cerium as a percentage of the administered dose. $n = 3$.

Finally, despite the numerous evidence, there is still the question if different NPs or different analytical techniques would confirm these generalities of NP biodistribution, including procedures, and experimental and conceptual approximations. Therefore, we employed the CCl_4-treated rats to observe the biodistribution of 8 nm NPs by magnetic resonance imaging (MRI), a technique displaying a high potential to localize NPs in vivo because of their high spatial resolution. Since nanoceria NPs lack paramagnetic properties, this protocol was performed using 8 nm Fe_3O_4NPs, which are somewhat similar, considering size, shape, and surface state, and a similar dose. We obtained sufficient resolution and contrast to assess Fe_3O_4NPs-induced signal intensity changes. The most pronounced changes, presented as an increase in signal intensity, were observed in the liver and spleen. These changes were apparent at the first image time point of 30 min after NPs injection (image not shown) and thereafter showed a progressive increase over 90 min (Figure S5), followed by a progressive decrease in signal intensity. Of note was that the brain image analyses revealed no changes during the observational period. Eight weeks after NPs administration the signal intensity was indistinguishable from that obtained in control rats (image not shown) (meaning that the iron concentration was below the limit of detection expected to be at 50% of the administered dose). These findings coincided with those obtained by analysing ICP-MS tissue Ce accumulation following nanoceria IV injection in fibrotic rats [66].

4. Conclusions

In conclusion, while it seems universal that a major capture of NPs happens in the liver and spleen, regardless of their difference in dose, morphology, aggregation, and surface state, or if they are taken by immune or filtering cells, the final tissue/cellular distribution and clearance rate from the body seems extremely dependent on those NP characteristics. In this model, NPs that will escape the immune system can be eliminated through the hepatobiliary route, whereas nanoceria captured by circulating monocytes or resident macrophages can dissolve and the cerium ions are excreted through the urine tract. The fact that it is slowly excreted from the body is promising for nanoceria medical development; however, the excretion rates are low and repeated dosing could lead to toxic accumulation [39]. Interestingly, in toxicity studies, no adverse effects were reported at concentrations much higher than the therapeutic ones, as reported after nanoceria oral administration of 1000 mg/Kg bw for 14 days [88], providing some room for repeated administration despite the slow excretion. Accumulation in the spleen also deserves special attention since much slower clearance rates have been observed. This could be related

to cell type interaction and to having monodisperse well characterized NPs that can be degraded. It is remarkable how, until now, nanoceria was reported to stay a long time inside the body and not be excreted, and has also been associated with mild pro-inflammatory activation. However, in this work, we demonstrate that non-immunogenic ultra-small highly soluble non-aggregated nanoceria is indeed excretable and biodegradable, paving the progress towards converting nanoceria into an active pharmaceutical ingredient.

All this data and considerations should help to better understand the PK of nanoceria to enable its successful translation to clinical use. Today, few inorganic NPs have reached clinical use: magnetite, Fe_3O_4, and amorphous silica, SiO_2, which is generally regarded as safe (GRAS) by the FDA [89]. Interestingly, both slowly dissolve in vivo into Fe^{2+} ions and salicylic acid, respectively. We expect that many other NPs will join the future pharmacopoeia, where nanoceria will play a significant role.

Supplementary Materials: The following supporting information can be downloaded at: https://www.mdpi.com/article/10.3390/antiox12030765/s1, Table S1: Cerium content by organ and days, given in μg Ce/g tissue and % of injected dose; Figure S1: Cerium excretion in μg Ce/g tissue between day 1 and day 100; Figure S2: Mice weight evolution up to 30 days after nanoceria administration; Figure S3: Dissolution of CeO2 Nanoparticles at pH 1.7; Figure S4: PourBoix diagram; Figure S5: The liver and spleen are major targets for nanoparticles in CCl4-treated rats; Extended Materials and Methods.

Author Contributions: Conceptualization, V.P. and L.M.E.; design, supervision and development of the mice in vivo experiments performed and the samples preparation for elemental analysis, L.M.; software, L.M.E., L.M., N.G.B. and G.F.-V.; formal analysis, L.M.E., N.G.B. and G.F.-V.; investigation, L.M.E., L.M., J.R., E.C., T.Y., G.F.-V. and M.F.G.; resources, G.C., W.J., M.F.G. and V.P.; data curation, L.M.E. and N.G.B.; writing—original draft preparation, L.M.E. and V.P.; writing—review and editing, L.M.E., N.G.B. and V.P.; supervision, W.J. and V.P.; project administration, W.J. and V.P.; funding acquisition, W.J. and V.P. All authors have read and agreed to the published version of the manuscript.

Funding: This research was obtained the financial support from the Spanish Ministerio de Ciencia, Innovación y Universidades (MCIU) (RTI2018-099965-B-I00, AEI/FEDER, UE) proyectos de I + D + I de programación conjunta internacional MCIN/AEI (CONCORD, PCI2019-103436) co-funded by the European Union and Generalitat de Catalunya (2017-SGR-1431). ICN2 is supported by the Severo Ochoa program from Spanish MINECO (SEV-2017-0706) and is funded by the CERCA Programme/Generalitat de Catalunya. L.M. thanks the financial support from AGAUR by means of the Grants for the incorporation of post-doctoral research staff into the Catalan science and technology system within the Beatriu de Pinós program (Grant No. 2016 BP 00350) and MICINN through the Ramón y Cajal program (RYC2019-026522-I). We would like to thank the Chemical Analysis Service at Autonomous University of Barcelona (SAQs, UAB, Barcelona, Spain) for the Ce content analysis developed. We acknowledge financial support from Dirección General de Investigación Científica y Técnica (Ministerio de Ciencia, Innovación y Universidades (RTI2018-094734-B-C21, to W. Jiménez), and Insituto de Salut Carlos III (FIS PI19-00774, to G. Casals and G. fernández-Varo).

Institutional Review Board Statement: The procedures that made use of mice in vivo models were approved by the Vall d'Hebron Research Institute (VHIR) Ethical Experimentation Committee and were further validated by the authorized body of Generalitat de Catalunya (approval code: ref. n. 11357).

Informed Consent Statement: Not applicable.

Data Availability Statement: The data presented in this study are available in the article and Supplementary Materials.

Conflicts of Interest: The authors declare no conflict of interest.

References

1. O'Neill, L.A.J.; Kishton, R.J.; Rathmell, J. A Guide to Immunometabolism for Immunologists. *Nat. Rev. Immunol.* **2016**, *16*, 553. [CrossRef]
2. Ernst, L.M.; Puntes, V. How Does Immunomodulatory Nanoceria Work? ROS and Immunometabolism. *Front. Immunol.* **2022**, *13*, 974. [CrossRef]
3. Auten, R.L.; Davis, J.M. Oxygen Toxicity and Reactive Oxygen Species: The Devil Is in the Details. *Pediatr. Res.* **2009**, *66*, 121–127. [CrossRef] [PubMed]
4. Morris, G.; Gevezova, M.; Sarafian, V.; Maes, M. Redox Regulation of the Immune Response. *Cell. Mol. Immunol.* **2022**, *19*, 1079–1101. [CrossRef] [PubMed]
5. Lin, J.; Huang, Z.; Liu, J.; Huang, Z.; Liu, Y.; Liu, Q.; Yang, Z.; Li, R.; Wu, X.; Shi, Z.; et al. Neuroprotective Effect of Ketone Metabolism on Inhibiting Inflammatory Response by Regulating Macrophage Polarization after Acute Cervical Spinal Cord Injury in Rats. *Front. Neurosci.* **2020**, *14*, 583611. [CrossRef] [PubMed]
6. Kesarwani, P.; Kant, S.; Zhao, Y.; Miller, C.R.; Chinnaiyan, P. The Influence of the Ketogenic Diet on the Immune Tolerant Microenvironment in Glioblastoma. *Cancers* **2022**, *14*, 5550. [CrossRef] [PubMed]
7. Bai, B.; Chen, H. Metformin: A Novel Weapon Against Inflammation. *Front. Pharmacol.* **2021**, *12*, 622262. [CrossRef]
8. Pauling, L. Vitamin C and the Common Cold. *Can. Med. Assoc. J.* **1971**, *105*, 448.
9. Mannucci, C.; Casciaro, M.; Sorbara, E.E.; Calapai, F.; di Salvo, E.; Pioggia, G.; Navarra, M.; Calapai, G.; Gangemi, S. Nutraceuticals against Oxidative Stress in Autoimmune Disorders. *Antioxidants* **2021**, *10*, 261. [CrossRef]
10. Arulselvan, P.; Fard, M.T.; Tan, W.S.; Gothai, S.; Fakurazi, S.; Norhaizan, M.E.; Kumar, S.S. Role of Antioxidants and Natural Products in Inflammation. *Oxid. Med. Cell Longev.* **2016**, *2016*, 5276130. [CrossRef]
11. Morén, C.; de Souza, R.M.; Giraldo, D.M.; Uff, C. Antioxidant Therapeutic Strategies in Neurodegenerative Diseases. *Int. J. Mol. Sci.* **2022**, *23*, 9328. [CrossRef] [PubMed]
12. Khansari, N.; Shakiba, Y.; Mahmoudi, M. Chronic Inflammation and Oxidative Stress as a Major Cause of Age-Related Diseases and Cancer. *Recent Pat. Inflamm. Allergy Drug Discov.* **2009**, *3*, 73–80. [CrossRef] [PubMed]
13. Chen, F.; Chen, L.; Liang, J.; Chen, Z.; Zhang, C.; Zhang, Z.; Yang, J. Potential Role of Superoxide Dismutase 3 (SOD3) in Resistance to Influenza A Virus Infection. *Antioxidants* **2023**, *12*, 354. [CrossRef] [PubMed]
14. Firuzi, O.; Miri, R.; Tavakkoli, M.; Saso, L. Antioxidant Therapy: Current Status and Future Prospects. *Curr. Med. Chem.* **2012**, *18*, 3871–3888. [CrossRef]
15. Benfeito, S.; Oliveira, C.; Soares, P.; Fernandes, C.; Silva, T.; Teixeira, J.; Borges, F. Antioxidant Therapy: Still in Search of the "Magic Bullet". *Mitochondrion* **2013**, *13*, 427–435. [CrossRef]
16. Nguyen, D.D.; Lai, J.Y. Synthesis, Bioactive Properties, and Biomedical Applications of Intrinsically Therapeutic Nanoparticles for Disease Treatment. *Chem. Eng. J.* **2022**, *435*, 134970. [CrossRef]
17. Sadidi, H.; Hooshmand, S.; Ahmadabadi, A.; Hoseini, S.J.; Baino, F.; Vatanpour, M.; Kargozar, S. Cerium Oxide Nanoparticles (Nanoceria): Hopes in Soft Tissue Engineering. *Molecules* **2020**, *25*, 4559. [CrossRef]
18. Yang, B.; Chen, Y.; Shi, J. Reactive Oxygen Species (ROS)-Based Nanomedicine. *Chem. Rev.* **2019**, *119*, 4881–4985. [CrossRef]
19. Xu, C.; Qu, X. Cerium Oxide Nanoparticle: A Remarkably Versatile Rare Earth Nanomaterial for Biological Applications. *NPG Asia Mater.* **2014**, *6*, e90. [CrossRef]
20. Niu, J.; Wang, K.; Kolattukudy, P.E. Cerium Oxide Nanoparticles Inhibits Oxidative Stress and Nuclear Factor-κB Activation in H9c2 Cardiomyocytes Exposed to Cigarette Smoke Extract. *J. Pharmacol. Exp. Ther.* **2011**, *338*, 53–61. [CrossRef]
21. Estevez, A.Y.; Pritchard, S.; Harper, K.; Aston, J.W.; Lynch, A.; Lucky, J.J.; Ludington, J.S.; Chatani, P.; Mosenthal, W.P.; Leiter, J.C.; et al. Neuroprotective Mechanisms of Cerium Oxide Nanoparticles in a Mouse Hippocampal Brain Slice Model of Ischemia. *Free Radic. Biol. Med.* **2011**, *51*, 1155–1163. [CrossRef] [PubMed]
22. Li, X.; Han, Z.; Wang, T.; Ma, C.; Li, H.; Lei, H.; Yang, Y.; Wang, Y.; Pei, Z.; Liu, Z.; et al. Cerium Oxide Nanoparticles with Antioxidative Neurorestoration for Ischemic Stroke. *Biomaterials* **2022**, *291*, 121904. [CrossRef] [PubMed]
23. Kim, C.K.; Kim, T.; Choi, I.-Y.; Soh, M.; Kim, D.; Kim, Y.-J.; Jang, H.; Yang, H.-S.; Kim, J.Y.; Park, H.-K.; et al. Ceria Nanoparticles That Can Protect against Ischemic Stroke. *Angew. Chem. Int. Ed.* **2012**, *51*, 11039–11043. [CrossRef] [PubMed]
24. Najafi, R.; Hosseini, A.; Ghaznavi, H.; Mehrzadi, S.; Sharifi, A.M. Neuroprotective Effect of Cerium Oxide Nanoparticles in a Rat Model of Experimental Diabetic Neuropathy. *Brain Res. Bull.* **2017**, *131*, 117–122. [CrossRef] [PubMed]
25. Badia, A.; Duarri, A.; Salas, A.; Rosell, J.; Ramis, J.; Gusta, M.F.; Casals, E.; Zapata, M.A.; Puntes, V.; García-Arumí, J. Repeated Topical Administration of 3 Nm Cerium Oxide Nanoparticles Reverts Disease Atrophic Phenotype and Arrests Neovascular Degeneration in AMD Mouse Models. *ACS Nano* **2023**, *17*, 910–926. [CrossRef] [PubMed]
26. Chen, J.; Patil, S.; Seal, S.; McGinnis, J.F. Rare Earth Nanoparticles Prevent Retinal Degeneration Induced by Intracellular Peroxides. *Nat. Nanotechnol.* **2006**, *1*, 142–150. [CrossRef]
27. Carvajal, S.; Perramón, M.; Oró, D.; Casals, E.; Fernández-Varo, G.; Casals, G.; Parra, M.; González de la Presa, B.; Ribera, J.; Pastor, Ó.; et al. Cerium Oxide Nanoparticles Display Antilipogenic Effect in Rats with Non-Alcoholic Fatty Liver Disease. *Sci. Rep.* **2019**, *9*, 12848. [CrossRef]
28. Córdoba-Jover, B.; Arce-Cerezo, A.; Ribera, J.; Pauta, M.; Oró, D.; Casals, G.; Fernández-Varo, G.; Casals, E.; Puntes, V.; Jiménez, W.; et al. Cerium Oxide Nanoparticles Improve Liver Regeneration after Acetaminophen-Induced Liver Injury and Partial Hepatectomy in Rats. *J. Nanobiotechnol.* **2019**, *17*, 112. [CrossRef]

29. Fernández-Varo, G.; Perramón, M.; Carvajal, S.; Oró, D.; Casals, E.; Boix, L.; Oller, L.; Macías-Muñoz, L.; Marfà, S.; Casals, G.; et al. Bespoken Nanoceria: An Effective Treatment in Experimental Hepatocellular Carcinoma. *Hepatology* **2020**, *72*, 1267–1282. [CrossRef]
30. Rice, K.M.; Selvaraj, V.; Manne, N.; Arvapalli, R.; Hambuchen, M. Cerium Oxide Nanoparticle Attenuates Lipopolysaccharide (LPS) Induced Acute Kidney Injury (AKI) and Acute Lung Injury (ALI) in Male Sprague Dawley Rats. *Nano Res. Appl.* **2018**, *4*, 8. [CrossRef]
31. Hashem, R.M.; Rashd, L.A.; Hashem, K.S.; Soliman, H.M. Cerium Oxide Nanoparticles Alleviate Oxidative Stress and Decreases Nrf-2/HO-1 in D-GALN/LPS Induced Hepatotoxicity. *Biomed. Pharmacother.* **2015**, *73*, 80–86. [CrossRef] [PubMed]
32. Cox, G.M.; Harrison, T.S.; McDade, H.C.; Taborda, C.P.; Heinrich, G.; Casadevall, A.; Perfect, J.R. Superoxide Dismutase Influences the Virulence of Cryptococcus Neoformans by Affecting Growth within Macrophages. *Infect. Immun.* **2003**, *71*, 173–180. [CrossRef] [PubMed]
33. Nguyen, D.D.; Yao, C.H.; Lue, S.J.; Yang, C.J.; Su, Y.H.; Huang, C.C.; Lai, J.Y. Amination-Mediated Nano Eye-Drops with Enhanced Corneal Permeability and Effective Burst Release for Acute Glaucoma Treatment. *Chem. Eng. J.* **2023**, *451*, 138620. [CrossRef]
34. Luo, L.J.; Nguyen, D.D.; Lai, J.Y. Harnessing the Tunable Cavity of Nanoceria for Enhancing Y-27632-Mediated Alleviation of Ocular Hypertension. *Theranostics* **2021**, *11*, 5447–5463. [CrossRef]
35. Colon, J.; Hsieh, N.; Ferguson, A.; Kupelian, P.; Seal, S.; Jenkins, D.W.; Baker, C.H. Cerium Oxide Nanoparticles Protect Gastrointestinal Epithelium from Radiation-Induced Damage by Reduction of Reactive Oxygen Species and Upregulation of Superoxide Dismutase 2. *Nanomedicine* **2010**, *6*, 698–705. [CrossRef]
36. Xu, P.T.; Maidment, B.W.; Antonic, V.; Jackson, I.L.; Das, S.; Zodda, A.; Zhang, X.; Seal, S.; Vujaskovic, Z. Cerium Oxide Nanoparticles: A Potential Medical Countermeasure to Mitigate Radiation-Induced Lung Injury in CBA/J Mice. *Radiat. Res.* **2016**, *185*, 516–526. [CrossRef]
37. D'Angelo, B.; Santucci, S.; Benedetti, E.; di Loreto, S.; Phani, R.A.; Falone, S.; Amicarelli, F.; Ceru, M.P.; Cimini, A. Cerium Oxide Nanoparticles Trigger Neuronal Survival in a Human Alzheimer Disease Model by Modulating BDNF Pathway. *Curr. Nanosci.* **2009**, *5*, 167–176. [CrossRef]
38. Pinna, A.; Malfatti, L.; Galleri, G.; Manetti, R.; Cossu, S.; Rocchitta, G.; Migheli, R.; Serra, P.A.; Innocenzi, P. Ceria Nanoparticles for the Treatment of Parkinson-like Diseases Induced by Chronic Manganese Intoxication. *RSC Adv.* **2015**, *5*, 20432–20439. [CrossRef]
39. Casals, E.; Gusta, M.F.; Piella, J.; Casals, G.; Jiménez, W.; Puntes, V. Intrinsic and Extrinsic Properties Affecting Innate Immune Responses to Nanoparticles: The Case of Cerium Oxide. *Front. Immunol.* **2017**, *8*, 970. [CrossRef]
40. Mossman, B.T.; Churg, A. Mechanisms in the Pathogenesis of Asbestosis and Silicosis. *Am. J. Respir. Crit. Care Med.* **2012**, *157*, 1666–1680. [CrossRef]
41. Longmire, M.; Choyke, P.L.; Kobayashi, H. Clearance Properties of Nano-Sized Particles and Molecules as Imaging Agents: Considerations and Caveats. *Nanomedicine* **2008**, *3*, 703. [CrossRef] [PubMed]
42. Soo Choi, H.; Liu, W.; Misra, P.; Tanaka, E.; Zimmer, J.P.; Itty Ipe, B.; Bawendi, M.G.; Frangioni, J.V. Renal Clearance of Nanoparticles. *Nat. Biotechnol.* **2007**, *25*, 1165. [CrossRef] [PubMed]
43. Comper, W.D.; Glasgow, E.F. Charge Selectivity in Kidney Ultrafiltration. *Kidney Int.* **1995**, *47*, 1242–1251. [CrossRef] [PubMed]
44. Kobayashi, H.; Le, N.; Kim, I.-S.; Kim, M.-K.; Pie, J.-E.; Drumm, D.; Paik, D.S.; Waldmann, T.A.; Paik, C.H.; Carrasquillo, J.A.; et al. The Pharmacokinetic Characteristics of Glycolated Humanized Anti-Tac Fabs Are Determined by Their Isoelectric Points. *Cancer Res.* **1999**, *59*, 422–430.
45. Tsoi, K.M.; Macparland, S.A.; Ma, X.Z.; Spetzler, V.N.; Echeverri, J.; Ouyang, B.; Fadel, S.M.; Sykes, E.A.; Goldaracena, N.; Kaths, J.M.; et al. Mechanism of Hard-Nanomaterial Clearance by the Liver. *Nat. Mater.* **2016**, *15*, 1212–1221. [CrossRef]
46. Poon, W.; Zhang, Y.N.; Ouyang, B.; Kingston, B.R.; Wu, J.L.; Wilhelm, S.; Chan, W.C. Elimination Pathways of Nanoparticles. *ACS Nano* **2019**, *13*, 5785–5798. [CrossRef]
47. Henke, E.; Nandigama, R.; Ergün, S. Extracellular Matrix in the Tumor Microenvironment and Its Impact on Cancer Therapy. *Front. Mol. Biosci.* **2020**, *6*, 160. [CrossRef]
48. Bachmann, M.F.; Rohrer, U.H.; Kündig, T.M.; Bürki, K.; Hengartner, H.; Zinkernagel, R.M. The Influence of Antigen Organization on B Cell Responsiveness. *Science* **1993**, *262*, 1448–1451. [CrossRef]
49. Sonavane, G.; Tomoda, K.; Makino, K. Biodistribution of Colloidal Gold Nanoparticles after Intravenous Administration: Effect of Particle Size. *Colloids Surf. B Biointerfaces* **2008**, *66*, 274–280. [CrossRef]
50. Barbero, F.; Russo, L.; Vitali, M.; Piella, J.; Salvo, I.; Borrajo, M.L.; Busquets-Fité, M.; Grandori, R.; Bastús, N.G.; Casals, E.; et al. Formation of the Protein Corona: The Interface between Nanoparticles and the Immune System. *Semin. Immunol.* **2017**, *34*, 52–60. [CrossRef]
51. Piella, J.; Bastús, N.G.; Puntes, V. Size-Dependent Protein-Nanoparticle Interactions in Citrate-Stabilized Gold Nanoparticles: The Emergence of the Protein Corona. *Bioconjug. Chem.* **2017**, *28*, 88–97. [CrossRef] [PubMed]
52. Bachmann, M.F.; Jennings, G.T. Vaccine Delivery: A Matter of Size, Geometry, Kinetics and Molecular Patterns. *Nat. Rev. Immunol.* **2010**, *10*, 787–796. [CrossRef] [PubMed]
53. Ernst, L.M.; Casals, E.; Italiani, P.; Boraschi, D.; Puntes, V. The Interactions between Nanoparticles and the Innate Immune System from a Nanotechnologist Perspective. *Nanomaterials* **2021**, *11*, 2991. [CrossRef] [PubMed]
54. Veronese, F.M.; Pasut, G. PEGylation, Successful Approach to Drug Delivery. *Drug Discov. Today* **2005**, *10*, 1451–1458. [CrossRef]
55. Milton Harris, J.; Chess, R.B. Effect of Pegylation on Pharmaceuticals. *Nat. Rev. Drug Discov.* **2003**, *2*, 214–221. [CrossRef]

56. Casals, E.; Vázquez-Campos, S.; Bastús, N.G.; Puntes, V. Distribution and Potential Toxicity of Engineered Inorganic Nanoparticles and Carbon Nanostructures in Biological Systems. *TrAC Trends Anal. Chem.* **2008**, *27*, 672–683. [CrossRef]
57. Kadry, H.; Noorani, B.; Cucullo, L. A Blood–Brain Barrier Overview on Structure, Function, Impairment, and Biomarkers of Integrity. *Fluids Barriers CNS* **2020**, *17*, 69. [CrossRef]
58. Wautier, J.L.; Wautier, M.P. Vascular Permeability in Diseases. *Int. J. Mol. Sci.* **2022**, *23*, 3645. [CrossRef]
59. Wu, J. The Enhanced Permeability and Retention (EPR) Effect: The Significance of the Concept and Methods to Enhance Its Application. *J. Pers. Med.* **2021**, *11*, 771. [CrossRef]
60. Ngoune, R.; Peters, A.; von Elverfeldt, D.; Winkler, K.; Pütz, G. Accumulating Nanoparticles by EPR: A Route of No Return. *J. Control. Release* **2016**, *238*, 58–70. [CrossRef]
61. Portioli, C.; Benati, D.; Pii, Y.; Bernardi, P.; Crucianelli, M.; Santucci, S.; Bentivoglio, M.; Passacantando, M. Short-Term Biodistribution of Cerium Oxide Nanoparticles in Mice: Focus on Brain Parenchyma. *Nanosci. Nanotechnol. Lett.* **2013**, *5*, 1174–1181. [CrossRef]
62. Bao, Q.; Hu, P.; Xu, Y.; Cheng, T.; Wei, C.; Pan, L.; Shi, J. Simultaneous Blood–Brain Barrier Crossing and Protection for Stroke Treatment Based on Edaravone-Loaded Ceria Nanoparticles. *ACS Nano* **2018**, *12*, 6794–6805. [CrossRef]
63. Subedi, L.; Venkatesan, R.; Kim, S.Y. Neuroprotective and Anti-Inflammatory Activities of Allyl Isothiocyanate through Attenuation of JNK/NF-KB/TNF-α Signaling. *Int. J. Mol. Sci.* **2017**, *18*, 1423. [CrossRef] [PubMed]
64. Mazzolini, J.; Weber, R.J.M.; Chen, H.S.; Khan, A.; Guggenheim, E.; Shaw, R.K.; Chipman, J.K.; Viant, M.R.; Rappoport, J.Z. Protein Corona Modulates Uptake and Toxicity of Nanoceria via Clathrin-Mediated Endocytosis. *Biol. Bull.* **2016**, *231*, 40–60. [CrossRef] [PubMed]
65. Clària, J.; Jiménez, W. Experimental Models of Cirrhosis and Ascites. In *Ascites and Renal Dysfunction in Liver Disease: Pathogenesis, Diagnosis, and Treatment*, 2nd ed.; Wiley-Blackwell: Hoboken, NJ, USA, 2007; pp. 215–226. [CrossRef]
66. Oró, D.; Yudina, T.; Fernández-Varo, G.; Casals, E.; Reichenbach, V.; Casals, G.; González de la Presa, B.; Sandalinas, S.; Carvajal, S.; Puntes, V.; et al. Cerium Oxide Nanoparticles Reduce Steatosis, Portal Hypertension and Display Anti-Inflammatory Properties in Rats with Liver Fibrosis. *J. Hepatol.* **2016**, *64*, 691–698. [CrossRef]
67. Kuntz, E.; Kuntz, H.-D. *Hepatology Textbook and Atlas*, 3rd ed.; Springer Berlin Heidelberg: Graz, Austria, 2008.
68. Pourbaix, M. *Atlas of Electrochemical Equilibria in Aqueous Solutions*, 1st ed.; Pergamon Press: Oxford, UK, 1966.
69. Plakhova, T.V.; Romanchuk, A.Y.; Yakunin, S.N.; Dumas, T.; Demir, S.; Wang, S.; Minasian, S.G.; Shuh, D.K.; Tyliszczak, T.; Shiryaev, A.A.; et al. Solubility of Nanocrystalline Cerium Dioxide: Experimental Data and Thermodynamic Modeling. *J. Phys. Chem. C* **2016**, *120*, 22615–22626. [CrossRef]
70. Auffan, M.; Rose, J.; Bottero, J.Y.; Lowry, G.V.; Jolivet, J.P.; Wiesner, M.R. Towards a Definition of Inorganic Nanoparticles from an Environmental, Health and Safety Perspective. *Nat. Nanotechnol.* **2009**, *4*, 634–641. [CrossRef]
71. Muhammad, F.; Wang, A.; Qi, W.; Zhang, S.; Zhu, G. Intracellular Antioxidants Dissolve Man-Made Antioxidant Nanoparticles: Using Redox Vulnerability of Nanoceria to Develop a Responsive Drug Delivery System. *ACS Appl. Mater. Interfaces* **2014**, *6*, 19424–19433. [CrossRef]
72. Galyamin, D.; Ernst, L.M.; Fitó-Parera, A.; Mira-Vidal, G.; Bastús, N.G.; Sabaté, N.; Puntes, V. Nanoceria Dissolution at Acidic PH by Breaking off the Catalytic Loop. *Nanoscale* **2022**, *14*, 14223–14230. [CrossRef]
73. Mülhopt, S.; Diabaté, S.; Dilger, M.; Adelhelm, C.; Anderlohr, C.; Bergfeldt, T.; de la Torre, J.G.; Jiang, Y.; Valsami-Jones, E.; Langevin, D.; et al. Characterization of Nanoparticle Batch-To-Batch Variability. *Nanomaterials* **2018**, *8*, 311. [CrossRef]
74. Casals, E.; Pfaller, T.; Duschl, A.; Oostingh, G.J.; Puntes, V.F. Hardening of the Nanoparticle–Protein Corona in Metal (Au, Ag) and Oxide (Fe_3O_4, CoO, and CeO_2) Nanoparticles. *Small* **2011**, *7*, 3479–3486. [CrossRef] [PubMed]
75. Cataldi, M.; Vigliotti, C.; Mosca, T.; Cammarota, M.R.; Capone, D. Emerging Role of the Spleen in the Pharmacokinetics of Monoclonal Antibodies, Nanoparticles and Exosomes. *Int. J. Mol. Sci.* **2017**, *18*, 1249. [CrossRef] [PubMed]
76. Demoy, M.; Andreux, J.P.; Weingarten, C.; Gouritin, B.; Guilloux, V.; Couvreur, P. In Vitro Evaluation of Nanoparticles Spleen Capture. *Life Sci.* **1999**, *64*, 1329–1337. [CrossRef] [PubMed]
77. Park, K.; Park, J.; Lee, H.; Choi, J.; Yu, W.J.; Lee, J. Toxicity and Tissue Distribution of Cerium Oxide Nanoparticles in Rats by Two Different Routes: Single Intravenous Injection and Single Oral Administration. *Arch. Pharm. Res.* **2018**, *41*, 1108–1116. [CrossRef]
78. Dubaj, T.; Kozics, K.; Sramkova, M.; Manova, A.; Bastús, N.G.; Moriones, O.H.; Kohl, Y.; Dusinska, M.; Runden-Pran, E.; Puntes, V.; et al. Pharmacokinetics of PEGylated Gold Nanoparticles: In Vitro-In Vivo Correlation. *Nanomaterials* **2022**, *12*, 511. [CrossRef]
79. Ahmed, T.A. Pharmacokinetics of Drugs Following IV Bolus, IV Infusion, and Oral Administration. *Basic Pharmacokinet. Concepts Some Clin. Appl.* **2015**, *10*, 53–98. [CrossRef]
80. Carlander, U.; Moto, T.P.; Desalegn, A.A.; Yokel, R.A.; Johanson, G. Physiologically Based Pharmacokinetic Modeling of Nanoceria Systemic Distribution in Rats Suggests Dose- and Route-Dependent Biokinetics. *Int. J. Nanomed.* **2018**, *13*, 2631–2646. [CrossRef]
81. Kawagoe, M.; Ishikawa, K.; Wang, S.C.; Yoshikawa, K.; Arany, S.; Zhou, X.P.; Wang, J.S.; Ueno, Y.; Koizumi, Y.; Kameda, T.; et al. Acute Effects on the Lung and the Liver of Oral Administration of Cerium Chloride on Adult, Neonatal and Fetal Mice. *J. Trace Elem. Med. Biol.* **2008**, *22*, 59–65. [CrossRef]
82. Yokel, R.A.; Hussain, S.; Garantziotis, S.; Demokritou, P.; Castranova, V.; Cassee, F.R. The Yin: An Adverse Health Perspective of Nanoceria: Uptake, Distribution, Accumulation, and Mechanisms of Its Toxicity. *Environ. Sci. Nano* **2014**, *1*, 406. [CrossRef]

83. Yokel, R.A.; Au, T.C.; MacPhail, R.; Hardas, S.S.; Butterfield, D.A.; Sultana, R.; Goodman, M.; Tseng, M.T.; Dan, M.; Haghnazar, H.; et al. Distribution, Elimination, and Biopersistence to 90 Days of a Systemically Introduced 30 Nm Ceria-Engineered Nanomaterial in Rats. *Toxicol. Sci.* **2012**, *127*, 256–268. [CrossRef]
84. Yokel, R.A.; Tseng, M.T.; Dan, M.; Unrine, J.M.; Graham, U.M.; Wu, P.; Grulke, E.A. Biodistribution and Biopersistence of Ceria Engineered Nanomaterials: Size Dependence. *Nanomedicine* **2013**, *9*, 398–407. [CrossRef] [PubMed]
85. Liang, Q.; Yin, H.; Li, J.; Zhang, L.; Hou, R.; Wang, S. Investigation of Rare Earth Elements in Urine and Drinking Water of Children in Mining Area. *Medicine* **2018**, *97*, e12717. [CrossRef] [PubMed]
86. Lu, Y.Q. Coagulation Disorders Following an Accidental Ingestion of Cerium Dioxide Nanoparticles. *Environ. Toxicol. Pharmacol.* **2021**, *82*, 103560. [CrossRef] [PubMed]
87. Funakoshi, T.; Furushima, K.; Shimada, H.; Kojima, S. Anticoagulant Action of Rare Earth Metals. *Biochem. Int.* **1992**, *28*, 113–119. [PubMed]
88. Lee, J.; Jeong, J.S.; Kim, S.Y.; Lee, S.J.; Shin, Y.J.; Im, W.J.; Kim, S.H.; Park, K.; Jeong, E.J.; Nam, S.Y.; et al. Safety Assessment of Cerium Oxide Nanoparticles: Combined Repeated-Dose Toxicity with Reproductive/Developmental Toxicity Screening and Biodistribution in Rats. *Nanotoxicology* **2020**, *14*, 696–710. [CrossRef]
89. GRAS Notices. Available online: https://www.cfsanappsexternal.fda.gov/scripts/fdcc/?set=GRASNotices&id=321&sort=GRN_No&order=DESC&startrow=1&type=column&search=Substance%C2%A4VARCHAR%C2%A4silica (accessed on 24 February 2023).

Disclaimer/Publisher's Note: The statements, opinions and data contained in all publications are solely those of the individual author(s) and contributor(s) and not of MDPI and/or the editor(s). MDPI and/or the editor(s) disclaim responsibility for any injury to people or property resulting from any ideas, methods, instructions or products referred to in the content.